



Evaluating biocompatible barrier films as encapsulants of medical micro devices

Jorge Mario Herrera Morales

► **To cite this version:**

Jorge Mario Herrera Morales. Evaluating biocompatible barrier films as encapsulants of medical micro devices. Materials. Université Grenoble Alpes, 2015. English. <NNT : 2015GREAS016>. <tel-01289295>

HAL Id: tel-01289295

<https://tel.archives-ouvertes.fr/tel-01289295>

Submitted on 16 Mar 2016

HAL is a multi-disciplinary open access archive for the deposit and dissemination of scientific research documents, whether they are published or not. The documents may come from teaching and research institutions in France or abroad, or from public or private research centers.

L'archive ouverte pluridisciplinaire **HAL**, est destinée au dépôt et à la diffusion de documents scientifiques de niveau recherche, publiés ou non, émanant des établissements d'enseignement et de recherche français ou étrangers, des laboratoires publics ou privés.

THÈSE

Pour obtenir le grade de

DOCTEUR DE L'UNIVERSITÉ GRENOBLE ALPES

Spécialité : **BIS - Biotechnologie, instrumentation, signal et imagerie pour la biologie, la médecine et l'environnement**

Arrêté ministériel : 7 août 2006

Présentée par

Jorge Mario HERRERA MORALES

Thèse dirigée par **François BERGER** et
encadrée par **Jean-Charles SOURIAU** et **David RATEL**

préparée au sein du **Laboratoire d'électronique des technologies de l'information (CEA-Leti)**
dans **l'École Doctorale Ingénierie pour la Santé, la Cognition et l'Environnement**

Evaluation de couches barrières biocompatibles pour l'encapsulation de dispositifs médicaux microélectroniques

Thèse soutenue publiquement le **23 novembre 2015**,
devant le jury composé de :

Dr. Alain RIPART

Conseiller scientifique, ex Senior VP&CSO SORIN CRM, Président

Dr. Christian BERGAUD

Directeur de recherche à LAAS-CNRS Toulouse, Rapporteur

Prof. George MALLIARAS

Professeur Ecole Nationale Supérieure des Mines, Rapporteur



Résumé (français):

Les dispositifs médicaux miniaturisés sont de plus en plus répandus dans le monde médical, car ils offrent de nouvelles opportunités de traitement et de surveillance. La miniaturisation des systèmes permet notamment une chirurgie minimalement invasive, une portabilité améliorée et une facilité d'utilisation. Parmi les exemples on peut mentionner les micro-stimulateurs cardiaques, les micro-implants cochléaires et les micro-capteurs ex-situ de glucose. Cependant, les micro-dispositifs implantables qui utilisent des technologies d'assemblage autres que les boîtiers métalliques sont encore à découvrir. La surveillance de paramètres physiologiques à l'aide de capteurs in-situ de pression et BioMEMS pourraient bénéficier des progrès faits sur les études d'encapsulation en couche mince destinées à protéger les micro-dispositifs de silicium contre la corrosion. En effet, une barrière qui empêche la diffusion et la pénétration des substances nocives est indispensable pour protéger à la fois le patient et le micro-dispositif. Les couches minces céramiques déposées par des procédés chimiques en phase vapeur sont de bons candidats grâce à leurs faibles perméabilités aux gazes, faibles réactivités chimiques et conformités de dépôt élevées. Cependant, dans des milieux biologiques représentatifs du corps humain, peu d'études ont été réalisées dans le domaine de la protection des dispositifs microélectroniques contre la corrosion.

Au cours de cette thèse, dix matériaux, choisis à l'issue d'une étude bibliographique, ont été étudiés: Al_2O_3 , BN, DLC, HfO_2 , SiC, SiN, SiO_2 , SiOC, TiO_2 et ZnO. Des couches ultrafines de ces matériaux (de 5 à 100 nm) ont été déposées par voie chimique en phase vapeur assisté par plasma (PECVD) ou par couches atomiques (ALD) sur des substrats silicium recouverts de matériaux généralement présents dans des dispositifs microélectroniques tels que le silicium cristallin, le cuivre, le tungstène nitrure et le poly-imide. Des mesures de cytotoxicité ont été réalisées et des tests de vieillissement ont été effectués pendant plusieurs semaines à des températures différentes dans une solution saline phosphatée (PBS) mais aussi dans une solution à base de sérum de veau fœtale (NaCl/SVF). Les changements dans la composition chimique et l'épaisseur ont été suivies par VASE, XPS et spectroscopie de masse d'ions secondaires à temps de vol (TOF-SIMS). Il a été montré que les couches de SiO_2 et de SiN (généralement utilisées pour la protection dans l'industrie de la microélectronique) n'étaient pas stables dans le PBS et le NaCl/SVF à 37°C, même si en revanche elles offraient une bonne barrière aux gazes. L' Al_2O_3 a lui montré une très bonne tenue en milieu salin et une remarquable herméticité mais en revanche, il s'est corrodé rapidement dans le NaCl/SVF. Les couches de DLC, SiOC et TiO_2 ont donné les meilleurs résultats de stabilité dans le PBS et le sérum de veau. Enfin, il a aussi été montré dans cette thèse que l'empilement TiO_2 sur Al_2O_3 offrait la meilleure efficacité comme barrière hermétique et diffusive pour la protection des microsystèmes de silicium contre la corrosion dans les milieux salins.

Title:

Selecting and evaluating biocompatible barrier films for protecting medical micro devices

Abstract:

Miniaturized medical devices are becoming increasingly adopted by doctors and patients because they enable new treatment and monitoring capabilities, minimally invasive surgery, improved portability and ease of use. Recent examples include micro pacemakers, micro cochlear implants and ex-situ micro glucose sensors. However, implantable micro devices employing packaging technologies other than metallic enclosures are yet to be seen. Physiological monitors such as in-situ pressure sensors and BioMEMS could profit significantly from advances in thin barrier films for corrosion protection of silicon micro devices. Coating films that stop the diffusion and permeation of harmful substances are necessary to protect both the patient and the micro device. Ceramic films deposited by chemical vapor deposition techniques are good candidates for this task due to their low permeability to gases, low chemical reactivity and high conformality. However, few studies are available about the corrosion protection offered by biocompatible coatings to microelectronic devices in representative biological environments.

Ten materials were selected in this thesis after a bibliographic study: Al₂O₃, BN, DLC, HfO₂, SiC, SiN, SiO₂, SiOC, TiO₂ and ZnO. Ultra-thin films of these materials (5-100 nm) were deposited by plasma enhanced chemical vapor deposition (PECVD) or atomic layer deposition (ALD) on substrates commonly found in electronic micro devices: crystalline silicon, copper, tungsten nitride and polyimide. *In vitro* cytotoxicity tests and degradation tests were performed for several weeks at different temperatures in Phosphate Buffer Saline (PBS) and NaCl supplemented with 10% Fetal Bovine Serum (NaCl/FBS). Changes in thickness and chemical composition were monitored by VASE, XPS and time-of-flight secondary ion mass spectroscopy (TOF-SIMS). It was found that SiO₂ and SiN films (generally used for protection in the microelectronics industry) are not stable in PBS and NaCl/FBS at 37°C, even though they act as good hermetic barriers. Al₂O₃ showed very good stability in saline solution and excellent behavior as gas barrier, but it was rapidly dissolved in NaCl/FBS. In contrast, films of DLC, SiOC and TiO₂ showed very low chemical reactivity in both mediums. Finally, it was shown that multilayers of TiO₂ on Al₂O₃ offer the best performance as hermetic and diffusion barriers for corrosion protection of silicon micro systems in saline environments.

Mots clés (français):

Biocompatibilité - Corrosion – Couche Barrière - Dispositif Médical Microélectronique

Keywords:

Biocompatible – Biodegradation – Corrosion – Barrier Film – Microelectronic Medical Device

To my dear people:

Melvis, Jorge, Andrés, Cris, Lili, Eli, Gabi, Manu, Ana,

and others who always support and encourage me.

Acknowledgements

I would like to thank to François Berger, Jean-Charles Souriau, Gilles Simon and David Ratel for their advice and constructive comments during these past three years.

I want to acknowledge as well the people of CEA and MINATEC that helped me with this research, especially: Olivier Renault, Jean-Paul Barnes, Anne-Marie Poupon, Corinne Perret, Stephane Cros, Arnaud Leroy, Patrick Boldrighini, Christophe Gaude, Armelle Danden, Stephane Ballerand, Olivier Pollet, Agathe Andre, Laurence Andreutti, Anne Roule, Tony Maindron, Olivier Girard, Laetitia Castagne, Myriam Assous, Edouard Deschaseaux, Nadine David, Catherine Brunet-Manquat, Gilles Poupon.

This work has been performed with the help of the “Plateforme Technologique Amont” (Grenoble, France) with the financial support of the “Nanosciences aux limites de la Nanoélectronique” Foundation and the CNRS Renatech network.

Table of contents

	Page
<u>Acknowledgements</u>	5
<u>Table of contents</u>	6
<u>List of Figures</u>	9
<u>List of Tables</u>	14
<u>Introduction</u>	16
<u>Chapter 1: Challenges of Biocompatible Packaging of Miniaturized Medical Devices</u>	18
1.1. Definition of biocompatibility	19
1.2. Regulations of Medical Devices	20
1.2.1. Regulations of Active Implantable Medical Devices	27
1.3. Packaging Requirements of Medical Micro Devices	30
1.3.1. Hermeticity	30
1.3.2. Compatibility with sterilization	33
1.3.3. Adhesion on substrate	33
1.3.4. Rounded edges	34
1.4. State of the Art of Miniaturized Medical Devices	35
<u>Chapter 2: Selection of Biocompatible Packaging Materials</u>	39
2.1. Strategy of selection	40
2.1.1. Scientific Literature	40

2.1.2. Databases	50
2.2. Method of Deposition	53
2.2.1. Chemical Vapor Deposition (CVD)	53
2.2.2. Atomic Layer Deposition (ALD)	58
2.3. Selected Materials	65
Chapter 3: Characterization and Evaluation of Materials	66
3.1. Characterization of materials	66
3.1.1. AFM	68
3.1.2. XRD	70
3.1.3. XRR	71
3.1.4. XPS	74
3.1.5. VASE	86
3.2. Biodegradation tests	87
3.2.1. Degradation tests in PBS heated to 67, 57 and 37°C with hot plate	89
3.2.2. Degradation tests in PBS heated to 67°C in oven	96
3.2.3. Biodegradation tests in 37°C NaCl/FBS	100
3.3. Biocompatibility tests	106
3.4. Diffusion Barrier tests	110
3.5. Helium permeability tests	112
3.6. Conclusion	119
Chapter 4: Test Vehicles	121
4.1. Test Vehicle VTB1	122
4.2. Test Vehicle VTB2	130
4.3. Test Vehicle VTB3	134
4.4. Test Vehicle VTB4	142
4.5. Conclusion	150

General Conclusion and Outlook	151
---------------------------------------	------------

Bibliography	155
---------------------	------------

Annexes	166
----------------	------------

A1. Characterization of thin films by VASE	166
---	------------

List of Figures

	Page
Summary of the systematic approach to a biological evaluation of medical devices as part of a risk management process. [6].....	22
Algorithm of ISO 10993-9 to establish the pertinence of degradation studies. [9]	26
Medical device development technology readiness-level (TRL) scale: from clean room to the patient bedside. [15]	29
Periodic table showing toxic elements typically found in silicon devices. [19]	30
Water vapor permeability of different classes of packaging materials and their predicted lifetime as function of thickness. [21]–[23]	31
Problems of covering of a silicone coating across sharp edges (Right) after conventional dicing of a silicon device (Left). [47], [48]	34
Evolution of artificial cardiac pacemakers. [50],[51]	35
A miniaturized camera developed by Medigus Ltd. [52], [54].....	36
Tear drop micro glucose sensor (NovioSense™). [55].....	36
Miniaturized intra ocular pressure sensor (SENSIMED Triggerfish®). [56].....	37
Methods of protecting Microsystems for human implantation: (a) Conformal layer or encapsulation, (b) Impermeable envelope or hermetic packaging. [18]	37
Gibbs energy of a metal at its interface with a solution. [75]	43
Pourbaix diagram of the titanium-water system. Marked region indicates physiological conditions. [81].....	46
Pourbaix diagram of Al-H ₂ O system. [89].....	47
Pourbaix diagram of Fe-H ₂ O system. [81].....	47
Insulating encapsulants proposed by the databases of CES EduPack®.....	51
Conductive materials proposed by the databases of CES EduPack®.....	52
The principle of thermal CVD. [100].....	53
Steps of a CVD process where SiO ₂ film is formed from SiH ₄ and O ₂ . [102], [103].....	54
Deposition rate of silicon films as a function of temperature and precursor. [101].....	55

Chemical vapor deposition process assisted by plasma discharge, a.k.a. PECVD.....	57
Stress deformation of thin films. [104]	57
Scheme of the principle of ALD to form an atomic monolayer of the desired film.	59
Temperature window for ALD. [101]	59
Adhesion test by cross-cut test method of silicon coupons coated with 100 nm SiC (Left) and 20 nm ZnO (Right).....	67
Schematic setup of AFM using laser beam deflection detection.	68
Topography of various deposited thin films as measured by AFM.	69
Graph of intensity versus diffracted direction of incident X-rays for various thin films deposited on silicon substrates.	70
XRR scan of a germanium thin film on silicon substrate [117].....	71
TEM images of a-CH film deposited on silicon.	73
General XPS of 20 nm Al ₂ O ₃ 250°C on silicon substrate.....	75
High resolution XPS of 20 nm Al ₂ O ₃ 250°C on silicon substrate.	75
General XPS of 50 nm BN 400°C on silicon substrate.....	76
High resolution XPS of 50 nm BN 400°C on silicon substrate.	76
General XPS of 100 nm SiC 350°C on silicon substrate.	77
High resolution XPS of 100 nm SiC 350°C on silicon substrate.....	77
General XPS of 100 nm a-CH 400°C on silicon substrate.....	78
High resolution XPS of 100 nm a-CH 400°C on silicon substrate.	78
Fitting of XPS of carbon 1s of DLC (a-CH) 400°C deposited on silicon substrate.....	79
General XPS of 20 nm HfO ₂ 300°C on silicon substrate.....	80
High resolution XPS of 20 nm HfO ₂ 300°C on silicon substrate.	80
General XPS of 100 nm SiN 400°C on silicon substrate.	81
High resolution XPS of 100 nm SiN 400°C on silicon substrate.....	81
General XPS of 100 nm SiO ₂ 400°C on silicon substrate.....	82
High resolution XPS of 100 nm SiO ₂ 400°C on silicon substrate.	82
General XPS of 100 nm SiOC 400°C on silicon substrate.	83
High resolution XPS of 100 nm SiOC 400°C on silicon substrate.	83
General XPS of 20 nm TiO ₂ 250°C on silicon substrate.	84

High resolution XPS of 20 nm TiO ₂ 250°C on silicon substrate.	84
General XPS of 20 nm ZnO 250°C on silicon substrate.	85
High resolution XPS of 20 nm ZnO 250°C on silicon substrate.	85
VASE measurements of thin films deposited on silicon coupons.	86
Thickness variations of different packaging layers immersed in PBS at 57°C.	90
TiO ₂ (Top) and SiC (Bottom) coupons after 8 weeks in 57°C PBS.	91
Thickness variation of SiN and SiO ₂ packaging layers immersed in 37°C PBS.	91
SiN coupons before (Left), after 8 days (Center) and 56 days (Right) in 37°C PBS.	92
SiO ₂ coupons after 56 days in 37°C PBS. Few apparent changes were visible.	92
Corrosion rates of SiN and SiO ₂ films in PBS heated on hot plate.	93
HiRes XPS of SiN film before (green) and after (red) 7 days in 57°C PBS.	94
HiRes XPS of SiO ₂ film before (green) and after (red) 7 days in 57°C PBS.	94
Photo (Left) and μphoto (Right) of ZnO coupon after 2 days in 37°C PBS.	95
Pourbaix diagram of the zinc-water system. [141]	95
Silicon coupons after 120 days in PBS heated to 67°C in closed oven.	96
VASE spectra of one Al ₂ O ₃ film before and after sterilization with EtO.	103
General XPS of Al ₂ O ₃ film before (left) and after (right) 27 days in NaCl/FBS.	104
General XPS of ZnO film before (blue) and after (red) 24h in NaCl/FBS medium.	104
Corrosion rates of SiN and SiO ₂ films in PBS and <i>in vivo</i> environments.	105
Scheme of the cytotoxicity test by the extraction method of ISO 10993-5.	107
Al ₂ O ₃ (Left) and SiOC (Right) films deposited on Kapton substrates.	115
Scheme of the gas permeameter developed by S. Cros et al. [165]	116
Cross section scheme of test vehicle VTB1 (Top) and upper view (Bottom).	122
Scheme of accelerated aging tests of VTB1 coupons.	123
Risk of saline solution infiltration between passive layer and RDL.	130
Scheme of cross section (Left) and upper view (Right) of test vehicle VTB2.	130
Micro photos of fabricated copper layers in VTB2 (Left) and VTB1 (Right).	133
Roughness of fabricated copper layers in VTB2 (Left) and VTB1 (Right).	133
Scheme illustrating the cross section of test vehicle VTB3 (Left). Top view of a VTB3 containing 12 metallic pads of sputtered WN (Right). Pad length is ~5 mm.	134

Accelerated aging tests of coated VTB3 coupons in hot saline solution.	135
WN layer of 100 nm after 2, 3 and 4 hours of soaking in 67°C PBS.....	136
ToF-SIMS of VTB3 coated with 20 nm TiO ₂ 200°C after 21 days in 67°C PBS.	139
Infiltration pits of VTB3 coated with 10 nm Al ₂ O ₃ + 20 nm TiO ₂ 200°C.....	140
ToF-SIMS over infiltration pit of VTB3 coated with 10 nm Al ₂ O ₃ + 20 nm TiO ₂ 200°C after 42 days in 67°C PBS. Metal layer of WN has disappeared in the pit.	140
Photos of unclean (Top) and clean (Bottom) VTB3 coupons protected with multilayer of (5 nm Al ₂ O ₃ + 5 nm TiO ₂) ⁴ deposited at 200°C after 5 days in 67°C PBS.....	141
Photos of VTB3s before and after soaking in Phosphate Buffered Saline at 67°C.	141
Generic process flow to create thin unsharpened silicon devices.	142
Process flow of the physicochemical etching method followed to soften die edges.	143
Process flow of our sequential dicing method for softening die edges.....	144
Profile obtained after isotropic etching with pure SF ₆ for a) 3 min (Top) and b) 6 min (Bottom) and hard mask removal.....	145
Thin silicon wafer glued to a glass carrier wafer.	146
Etch profile obtained after 50 μm of DRIE. Front-side was glued to a glass carrier.	146
Die chipping caused by blade dicing on a silicon wafer.	147
Dicing street obtained with V-shaped blade when a depth of 20 μm was intended.	148
Chamfered edges obtained by partial standard dicing followed by chamfered dicing (depth 20 μm) with a 30° V-shaped blade.....	148
Problem of alignment that occurred during the sequential blade dicing method.....	149
Schematic setup of a Variable Angle Spectroscopy Ellipsometry measurement.....	166
Orthogonal waves: A) linearly, B) circularly, C) elliptically polarized. [151]	167
The principle of ellipsometry measurements. [151].....	167
Dielectric function of rutile TiO ₂ on a spectral range from UV to IR. [151].....	169
Normal dispersion of a transparent material. [151].....	170
Anomalous dispersion of film in resonance with light of <450 nm. [151]	170
Optical constants of crystalline and amorphous Si in UV and visible region. [151]	171
Flowchart of the data analysis procedure in spectroscopic ellipsometry. [179]	172

VASE analysis of crystalline silicon. A) Experimental and model-generated Ψ and Δ . B) Refractive index and extinction coefficient.	173
VASE analysis of 20 nm Al_2O_3 250°C. A) Experimental and model-generated Ψ and Δ . B) Refractive index and extinction coefficient.	174
VASE analysis of 50 nm BN 400°C. A) Experimental and model-generated Ψ and Δ . B) Refractive index and extinction coefficient.	175
VASE analysis of 100 nm SiC 350°C. A) Experimental and model-generated Ψ and Δ . B) Refractive index and extinction coefficient.	176
VASE analysis of 110 nm DLC 400°C. A) Experimental and model-generated Ψ and Δ . B) Refractive index and extinction coefficient.	177
VASE analysis of 20 nm HfO_2 250°C. A) Experimental and model-generated Ψ and Δ . B) Refractive index and extinction coefficient.	178
VASE analysis of 100 nm SiN 400°C. A) Experimental and model-generated Ψ and Δ . B) Refractive index and extinction coefficient.	179
VASE analysis of 100 nm SiO_2 400°C. A) Experimental and model-generated Ψ and Δ . B) Refractive index and extinction coefficient.	180
VASE analysis of 100 nm SiOC 400°C. A) Experimental and model-generated Ψ and Δ . B) Refractive index and extinction coefficient.	181
VASE analysis of 20 nm TiO_2 250°C. A) Experimental and model-generated Ψ and Δ . B) Refractive index and extinction coefficient.	182
VASE analysis of 20 nm ZnO 250°C. A) Experimental and model-generated Ψ and Δ . B) Refractive index and extinction coefficient.	183

List of Tables

	Page
Guideline ISO 10993 for the biological evaluation and testing of medical devices. [6]	20
Biological evaluation tests for approval consideration of different categories of medical devices according to the standard ISO 10993. [6]	24
Thermodynamic stability of some metal oxides. [81]–[83]	42
Electrochemical series of various metals and elements at 298 K and 1 atm. [86], [87]	44
Tissue reactions around metallic implants. [90], [91]	48
Steps of ALD process between TMA and H ₂ O on top a silicon wafer. [108]	60
Comparison of deposition methods of thin films.[109]	62
Selected materials deposited by PECVD or ALD.....	65
Density, thickness and roughness of various thin films measured by XRR.	72
VASE analysis of various packaging films deposited on silicon coupons.	86
Acceleration factors for various temperatures according to the 10-degree model.....	87
Failure mechanism of electronic devices and associated activation energy [137].....	88
Aging test of packaging films in PBS solution heated to 67°C in convection oven.	98
Thin films deposited on silicon substrates for tests in 37°C NaCl/FBS.	101
Change of thickness (nm) after different degradation tests on silicon coupons.....	102
Cell viability of pure extracts collected from Si coupons coated with various films.....	108
Cell morphology caused by various films deposited on silicon coupons.	109
Cell viability of extracts collected from copper coupons coated with various barriers.	111
Helium Permeability of different packaging layers deposited on Kapton substrates.	117
Summary of evaluation tests performed on different packaging films.	119
Aging of VTB1 protected with different coatings after 7 days in 67°C PBS.	123
Best protective films of VTB1 after aging test in 67°C PBS.	128
Coating films deposited on VTB2 samples.....	131
VTB2 protected with different coatings before and after soaking in 67°C PBS.....	131

Photos of WN coupons with various coatings during soaking in PBS at 67°C. 136
ToF-SIMS depth profiles of Al₂O₃+TiO₂ coatings deposited on Si + 100 nm WN..... 138
Summary of evaluated barrier films for biocompatible packaging of silicon devices..... 152

Introduction

Picture consulting your doctor about a pain in the chest and he says “You need a pacemaker! But do not worry. Take these pills before going asleep and the micro pacemaker will get itself in place”. This fantastic tale may not be from a distant future, but a technology that could be available within two decades. Continuous progress in biocompatible barrier films for packaging medical micro devices shows promising results for this tale to become true.

In 2015, there are many wonderful electronic devices that a couple of decades ago would sound like fantasy: smartphones, tablets, autonomous vehicles, drones and so on. These devices are possible thanks to advances in the fabrication of Microsystems and Microprocessors. Gordon Moore stated fifty years ago that the number of components that can be put into Integrated Circuits doubles every two years. Such pace of miniaturization has brought affordable and powerful electronic devices to the general public. The traditional field of application of Micro technologies has been data computing and sensors, but there is a growing interest by physicians and industrialists to extend it to miniature medical devices. Such diversification has enabled already the creation of medical devices with a total volume smaller than one cubic centimeter such as micro pacemakers, cochlear implants, glucose sensors and intra ocular pressure sensors. In addition, novel treatments and therapies could be developed as for example is the case of Brain Computer Interfaces for quadriplegic patients.

However, most microelectronic devices contain toxic substances that are harmful for living organisms. Conversely, living organisms are detrimental to microelectronic devices. They detect the invasion of unknown foreign objects and attack them with an arsenal of biochemical reactions until they are neutralized. This rejection reaction towards foreign objects is troublesome for patients whose life depends on implantable medical devices. As consequence, implantable electronic devices must be very well encapsulated in order to guarantee a functional life of several years for the patient and the device.

The aim of this thesis was to enable the encapsulation of silicon microsystems for medical implants of several years. Ideally, package lifetimes of ten years or longer should be possible.

Our work consisted in selecting and evaluating biocompatible barrier films for packaging silicon devices intended for chronic medical implants. It will be presented in four chapters of this manuscript.

The first chapter explains current regulations of implantable medical devices and the legal requirements of materials used in the encapsulation of active implantable medical devices. It explains also the limits of current tests to help in the development of biocompatible and hermetic packaging materials for medical micro devices, and additional material requirements needed for compatibility with current micro fabrication technologies.

The reasons behind the selection of encapsulant materials and their methods of fabrication will be presented on the second chapter of this manuscript. This selection was made with the intention to help a joint laboratory between LETI and SORIN to develop implantable miniaturized integrated sensors for monitoring *in situ* different physiological parameters. One targeted application was a micro accelerometer and controller chip packaged inside a silicon box, which is embedded in a catheter, intended for heart beat monitoring. The encapsulant should protect this silicon box for more than 10 years even if there is infiltration of the catheter by the blood medium.

The methodology of evaluation of selected packaging materials is presented and discussed in the third and fourth chapters of this manuscript. The purpose was to develop degradation tests that predict as accurately as possible the *in vivo* aging of implanted materials and devices. At present, materials' degradation tests are mainly performed in saline solutions such as Ringer Lactate and Phosphate Buffered Saline heated to 90°C. It would be explored the relevance of such tests to predict the aging of encapsulant materials of medical micro devices.

We shall finish by drawing a general conclusion about selected packaging materials and to suggest an outlook on the subject of this thesis. It is expected our work will help to develop new encapsulant materials and technology bricks that will push for novel packaging and regulations of medical micro devices.

Chapter 1: Challenges of Biocompatible Packaging of Miniaturized Medical Devices

Devices made of one or more biocompatible materials and designed to perform specific functions in the body are commonly known as medical devices or implants. First medical implants were made by Egyptians thousands of years ago for dental prostheses. But it was not until the apparition of modern antibiotics and synthetic polymers on the 20th century that the number of applications for medical implants started to grow exponentially. Nowadays, some common medical devices include orthopedic prostheses; cardiovascular implants; neural implants, plastic and reconstructive implants, dental implants, ophthalmic systems including contact and intraocular lenses, catheters and drug-dispensing implants [1].

The medical devices sector in Europe employs 575 000 people hired by 25 000 companies, of which 95% are small and medium-sized enterprises. Total sales amount to €100 billion [2]. This big market is essential to the healthcare of European citizens and consequently strict regulations have been created with the aim of protecting the health of patients and ensuring the reliability of medical devices.

As there are many different types of medical implants, various norms have been created to homogenize their evaluation and testing by regulatory organizations such as the Food and Drug Administration in the United States, the Medicines and Healthcare products Regulatory Agency in the United Kingdom, and the Ministry of Social Affairs and Health in France. A general review of regulations for medical devices in Europe is presented initially in this chapter. Then, additional materials requirements for successful encapsulation of miniaturized Implantable Electronic Devices (IEDs) are discussed. The last part of this chapter is dedicated to review the state of the art of miniaturized IEDs.

Before discussion of regulations, a definition of the term *biocompatibility* is necessary.

1.1. Definition of biocompatibility

Biocompatibility can be defined as “the ability of a material to perform with an appropriate host response in a specific situation” [3], or as “the biological performance in a specific application that is judged suitable to that situation” [4]. Thus, a biocompatible material or biomaterial should coexist with the biological environment (patient) without causing undesirable effects in the frame of a specific biomedical application. According to the type of biological response caused on the host organism, biomaterials can be classified as:

- Inert biomaterials: elicit minor or no host response. In other words, they are capable to interact directly with biological systems like living tissue, biological fluids or cell cultures with minimal adverse reaction or rejection by the living organism. Medical grade titanium alloys, stainless steels, glass and alumina ceramics fall in this category.
- Interactive biomaterials: elicit specific, beneficial responses, such as cellular adhesion, tissue ingrowths, etc. Hydroxyapatite used to promote bone ingrowth and drug eluting stents belong to this group.
- Replant biomaterials: consist of native tissue, cultured *in vitro* from cells obtained previously from the specific implant patient. The nascent field of tissue engineering is mostly concerned with this type of materials.
- Viable biomaterials: contain or attract living cells that are treated by the host as normal tissue matrices and are actively reabsorbed or remodeled by the host. Biomaterials with a high bioresorption rate such as PHEMA (poly(2-hydroxyethyl methacrylate) or calcium phosphate (CaP) are considered viable [3].

The word undesirable was highlighted in the definition of biocompatibility because it means that the integrity of the patient and the medical implant ought to be desired. In order to enforce ethical behavior among fabricants of medical devices, various national and supranational regulatory organizations exist. Most export markets accept the norm ISO 10993 for the biological evaluation of medical implants and it will be reviewed in the next section.

1.2. Regulations of Medical Devices

The International Standards Organization (ISO) established the standard ISO 10993 to homogenize the biological evaluation and testing of all classes of medical devices (MDs) that have direct or indirect contact with patients. Unlike other standards of ISO, the standard ISO 10993 does not provide a rigid set of tests methods as this might result in unnecessary constraints on the development and use of novel medical devices, or a false sense of security in the general use of medical devices [5]. As consequence, the norm ISO 10993 is referred as Guideline or Standard Guideline. The standard guideline ISO 10993 is divided in 20 parts (Table 1).

Table 1: Guideline ISO 10993 for the biological evaluation and testing of medical devices. [6]

Part 1: Evaluation and testing within a risk management process
Part 2: Animal welfare requirements
Part 3: Tests for genotoxicity, carcinogenicity and reproductive toxicity
Part 4: Selection of tests for interactions with blood
Part 5: Tests for <i>in vitro</i> cytotoxicity
Part 6: Tests for local effects after implantation
Part 7: Ethylene oxide sterilization residuals
Part 8: WITHDRAWN: Clinical investigation of medical devices
Part 9: Framework for identification and quantification of potential degradation products
Part 10: Tests for irritation and skin sensitization
Part 11: Tests for systemic toxicity
Part 12: Sample preparation and reference materials
Part 13: Identification and quantification of degradation products from polymeric medical devices
Part 14: Identification and quantification of degradation products from ceramics
Part 15: Identification and quantification of degradation products from metals and alloys
Part 16: Toxicokinetic study design for degradation products and leachables
Part 17: Establishment of allowable limits for leachable substances
Part 18: Chemical characterization of materials
Part 19: Physico-chemical, morphological and topographical characterization of materials
Part 20: Principles and methods for immunotoxicology testing of medical devices in phosphate buffered saline

Each part of the norm outlines different biological tests to perform for a specific category of materials or medical devices. For example, a medical device that has contact with blood must pass the tests of hemotoxicity outlined by Part 4; a device in contact with living tissue has to pass a test of cytotoxicity outlined by Part 5; a device in contact with the skin has to pass a test of irritation and skin sensitization outlined by Part 10, etc.

It is important to stress that the standard guideline ISO 10993 covers only the testing of materials and medical devices that have direct or indirect contact with the patient's body, and it must be carried out as part of a structured biological evaluation program within a risk management process in accordance with the standard ISO 14971 [6]. The biological evaluation of medical devices as part of a risk management process is outlined in Figure 1.

The first step in the biological evaluation of medical devices is to obtain information about the identification and chemical characterization of the device or material concerned (further details about material characterization are provided in ISO 10993-18 and ISO 10993-19). If the combination of all materials, chemicals and processes has an established history of safe use in the intended application, then further characterization and biological evaluation might not be necessary [6]. If such precedent is not available, four criteria must be fulfilled for the material/device to pass the standard ISO 10993 without further biological tests:

1. First one is the criterion of familiarity. If the device/material is not the same as one previously approved for clinical use by competent authorities, the device/material must undergo biological tests to assess its toxicological risk.
2. If it is the same type of device/material as one already approved, it must prove its chemical composition is equivalent. If it is different from the approved device, a toxicological risk assessment must be performed.
3. Third criterion concerns the equivalence of manufacturing and sterilization of the material/device. If they are not the same as the ones used in the commercially available device, pertinent biological tests must be carried out.
4. The fourth and final criterion is the equivalence of contact with the body. If the body contact is not the same as in the previously approved device, the device/material must go through a toxicological risk assessment.

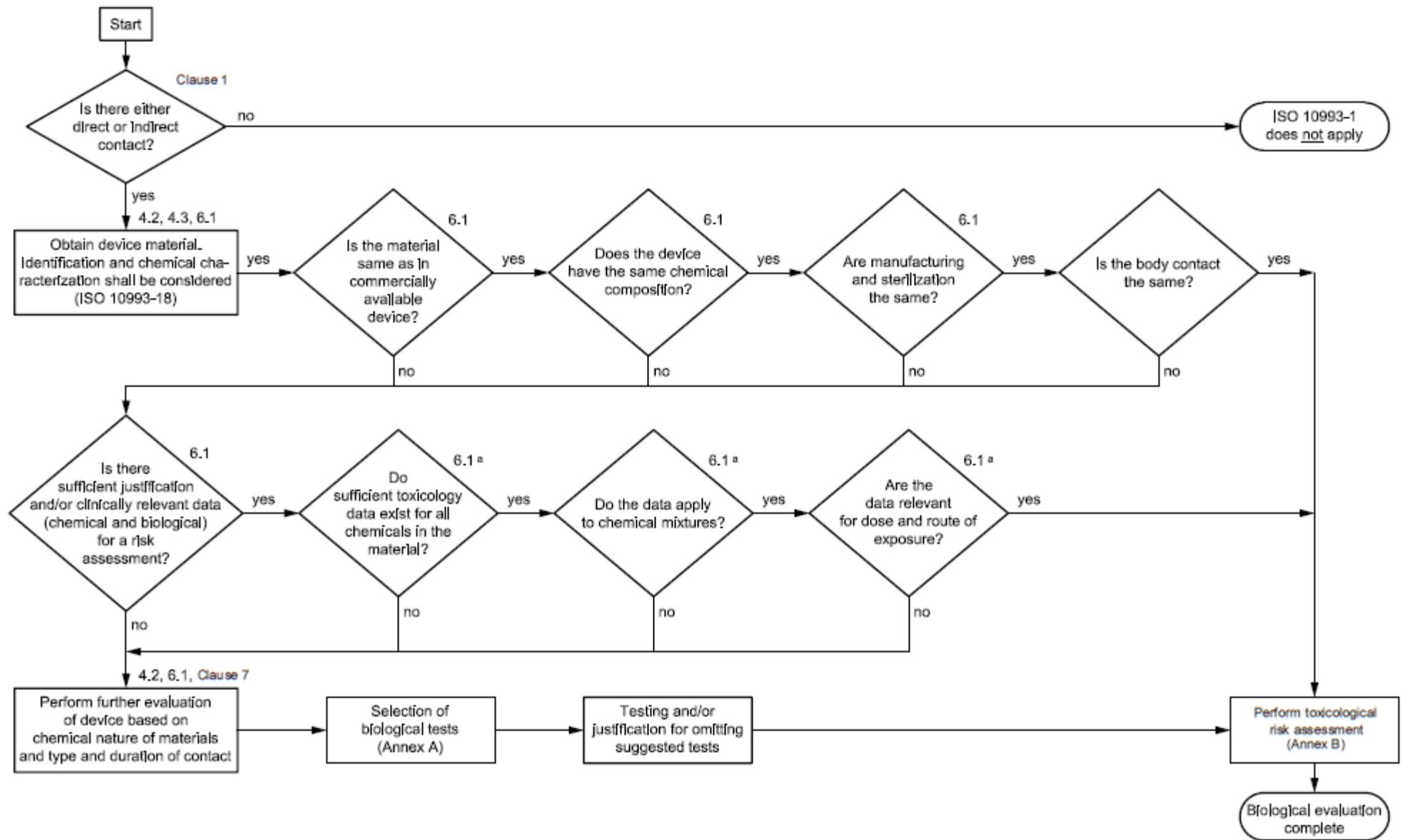


Figure 1: Summary of the systematic approach to a biological evaluation of medical devices as part of a risk management process. [6]

Material characterization is a crucial first step in the biological evaluation process. During the selection of materials for using in the manufacture of the device, the first consideration should be fitness for purpose with regard to the characteristics and properties of the material. Chemical, toxicological, physical, electrical, morphological and mechanical properties have to be considered.

The extent of required chemical characterization depends on the quality of data about clinical safety and toxicology, and on the nature and duration of body contact with the medical device. Chemical characterization should discover at least the constituent chemicals of the device and possible residual process aids or additives used in its manufacture. The identity and quantity of novel materials and chemicals present should be established. For devices that have known leachable chemical mixtures, potential synergies of the leachable chemicals should be considered. When the potential for degradation exists during manufacture, sterilization, transport, storage, or usage of the device, the presence and nature of degradation products must be characterized [5], [7].

In case there is not enough sufficient data from clinical essays, literature review or commercially available devices, a toxicological risk assessment is conducted. The first part consists in performing *in vitro* biocompatibility tests. If they are successful, *in vivo* biocompatibility tests might be performed if deemed necessary for that type of material or medical device. The battery of biological tests to perform *in vitro* or *in vivo* varies depending on the category of the material or medical device.

Medical devices and biomaterials can be categorized according to the nature and the duration of body contact. According to the nature of the body contact, a medical device can be classified as a surface device, external communicating device, or implant device. And according to the duration of body contact, medical devices are further classified as limited, prolonged or permanent. Materials or medical devices in contact with the body for less than 24 hours are considered devices of limited exposure (A). If the device has body contact for more than 24 hours but less than 30 days, it is considered a device of prolonged exposure (B). Devices whose cumulative body contact exceeds 30 days are considered permanent contact devices (C).

Table 2 resumes the biological tests for consideration of a given medical device according to the nature and duration of body contact. Generally, the longer the duration of body contact, the larger the body of evidence of biocompatibility must be to obtain regulatory approval for a medical device.

Table 2 is intended to be used as a guide by biomedical professionals who are appropriately qualified by training and experience as stipulated by the standard ISO/IEC 17025 [8]. They shall be able to interpret the requirements and judge the outcome of evaluation tests for each medical device, taking into consideration all the factors relevant to the device, its intended use and the current knowledge of the medical device provided by the scientific literature and clinical experience [7]. They might conclude in some cases that no tests are required if a safe history of usage of an equivalent medical device is available. Conversely, they ought to demand that novel materials and medical devices are orderly tested for biocompatibility.

Table 2: Biological evaluation tests for approval consideration of different categories of medical devices according to the standard ISO 10993. [6]

Medical device categorization by			Biological effect								
nature of body contact (see 5.2)	Contact	contact duration (see 5.3) A – limited (≤ 24 h) B – prolonged (> 24 h to 30 d) C – permanent (> 30 d)	Cytotoxicity	Sensitization	Irritation or intracutaneous reactivity	Systemic toxicity (acute)	Subchronic toxicity (subacute toxicity)	Genotoxicity	Implantation	Haemocompatibility	
Category											
Surface device		A	X ^a	X	X						
		B	X	X	X						
		C	X	X	X						
	Mucosal membrane	A	X	X	X						
		B	X	X	X						
		C	X	X	X		X	X			
	Breached or compromised surface	A	X	X	X						
		B	X	X	X						
		C	X	X	X		X	X			
External communicating device	Blood path, indirect	A	X	X	X	X				X	
		B	X	X	X	X				X	
		C	X	X		X	X	X		X	
	Tissue/bone/dentin	A	X	X	X						
		B	X	X	X	X	X	X	X		
		C	X	X	X	X	X	X	X		
	Circulating blood	A	X	X	X	X					X
		B	X	X	X	X	X	X	X	X	X
		C	X	X	X	X	X	X	X	X	X
Implant device	Tissue/bone	A	X	X	X						
		B	X	X	X	X	X	X	X		
		C	X	X	X	X	X	X	X		
	Blood	A	X	X	X	X	X		X	X	
		B	X	X	X	X	X	X	X	X	
		C	X	X	X	X	X	X	X	X	

^a The crosses indicate data endpoints that can be necessary for a biological safety evaluation, based on a risk analysis. Where existing data are adequate, additional testing is not required.

The materials used to construct medical devices might decompose chemically when exposed to a biological environment and form degradation products that may have a different behavior to the bulk material once exposed in the body [9]. The degradation of a material by a biological environment is known as biodegradation and it might compromise the safety and efficacy of a medical device if its hazard is not properly managed. For example, a material can be perfectly suitable and biocompatible for a specific short-term application, but unsuitable for prolonged or long-term implantations due to its degradation rate. For that reason, biodegradation must be identified and quantified with relevant tests for the materials in contact with the body for more than 24 hours.

Relevant degradation tests for a given material are summarized in the guideline ISO 10993-9 (Framework for identification and quantification of potential degradation products), which outlines the general principles followed by case specific tests described in ISO 10993-13 (polymers), ISO 10993-14 (ceramics) and ISO 10993-15 (metals and alloys) [9]. Figure 2 (page 26) of guideline ISO 10993-9 shows a flow chart to establish the pertinence of degradation studies. Degradation studies are necessary when new, unknown, or theoretically possible degradation products have been identified [9].

The aim of degradation studies is to assess the biological stability or biostability of the material when exposed to a model environment similar to the one found in its intended application, which is called service environment. The model environment is thus carefully selected to be representative of the anatomical location for the intended use of the device. Sometimes *in vitro* models do not reflect all aspects of the service environment, and *in vivo* models are employed. However, it is important to note that a biological environment is not absolutely required for the studies of degradation. The main requirement is that the model *simulates* the conditions of the service environment. For example, tests of degradation of materials in blood are difficult to implement due to problems of coagulation, so implants in contact with blood are typically evaluated using physiological isotonic electrolyte solutions such as 0.9% saline, Phosphate Buffer Saline (PBS) or Ringer's solution [10], [11].

In case degradation products are found by these studies, the level of biological tolerability for the host is determined based on their nature and concentration. This is primarily assessed through clinical experience and focused studies [9].

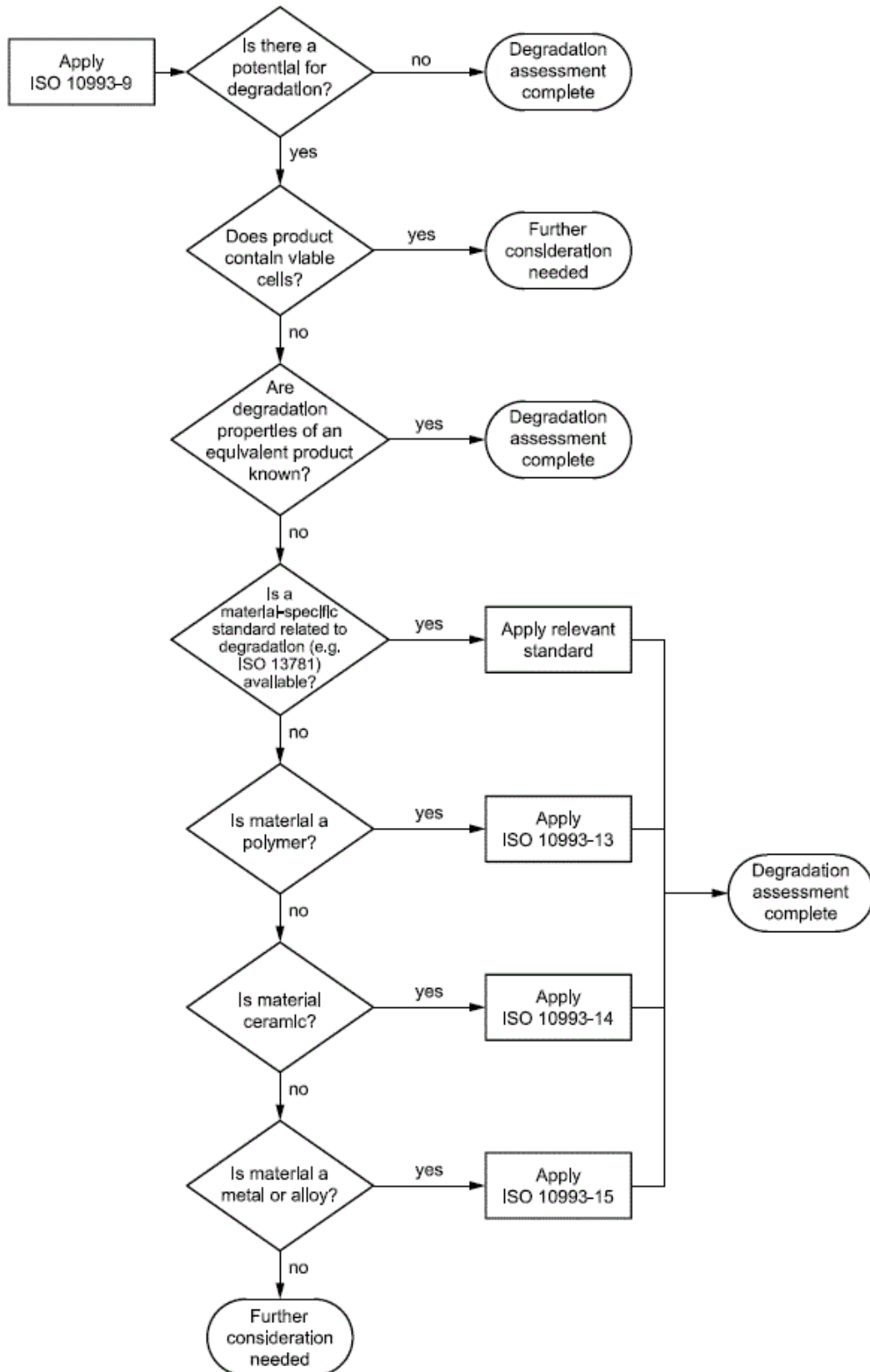


Figure 2: Algorithm of ISO 10993-9 to establish the pertinence of degradation studies. [9]

1.2.1. Regulations of Active Implantable Medical Devices

Active Medical Devices are a particular category in the group of medical devices. An active medical device is any medical device that relies for its functioning on a source of power other than the human body or gravity. An Active Implantable Medical Device (AIMD) is any active medical device which is intended to be totally or partially introduced, surgically or medically, into the human body or by medical intervention into a natural orifice, and which is intended to remain after the procedure. AIMDs include a wide range of devices, including pacemakers, defibrillators, cochlear implants, neurological stimulators, infusion pumps [12].

Standards for Active Medical Devices are based in Europe on directive 90/385/EEC by the European Communities and in the United States on regulation 21 CFR 860 by the Food and Drugs Administration (FDA). According to Council Directive 90/385/EEC, there are five essential requirements that must be met by AIMDs:

1. “The devices must be designed and manufactured in such a way that, when implanted under the conditions and for the purposes laid down, their use does not compromise the clinical condition or the safety of patients. They must not present any risk to the persons implanting them or, where applicable, to other persons.
2. The devices must achieve the performances intended by the manufacturer, that is be designed and manufactured in such a way that they are suitable for one or more of the functions as specified by him.
3. The characteristics and performances must not be adversely affected to such a degree that the clinical condition and safety of the patients or, as appropriate, of other persons are compromised during the lifetime of the device anticipated by the manufacturer, where the device is subjected to stresses which may occur during normal conditions of use.
4. The devices must be designed, manufactured and packed in such a way that their characteristics and performances are not adversely affected in the storage and transport conditions laid down by the manufacturer (temperature, humidity, etc.).
5. Any side effects or undesirable conditions must constitute acceptable risks when weighed against the performances intended” [12].

AIMDs are normally made from one or more biomaterials in direct contact with the body, and contain properly packaged electronic components like microchips, accelerometers and

antennas that are usually powered by lithium batteries [13]. For example, a pacemaker is a permanent AIMD that consists of a hermetically sealed titanium canister connected to polyurethane catheters in charge of delivering electrical stimulation to the heart. Medical grade titanium and polyurethane are both biomaterials widely used in implants due to their relatively biological inertness and proved biocompatibility [4]. If novel materials were used, pacemakers made of other materials than titanium and polyurethane must undergo biological tests of cytotoxicity, sensitization, intracutaneous reactivity, acute toxicity, subacute toxicity, genotoxicity, implantation and haemocompatibility (see Table 1). These tests are outlined by the standard guideline ISO 10993, parts 3–20, as well as the norms ISO 13485 and ISO 14971 for quality and risk management. With so many additional biological tests, it is understandable the aversion of medical manufacturers to introduce novel biomaterials in pacemakers or other AIMDs.

As AIMDs are designed to remain in direct contact with the body for long periods, they are subject to rigorous standards and requirements to protect the health and safety of patients. Such requirements are covered by ISO standards for quality such as the ISO 9000 series, which are complemented by market-specific standards (ISO 10993 for biocompatibility of medical devices, plus ISO 13485 and ISO 14971 for quality and risk management of medical devices), as well as local market regulations like for example the European Council Directive 93/42/EEC for medical devices and Council Directive 90/385/EEC for active implantable medical devices. The latter one by the European Economic Community is especially important because it regulates the market readiness and service parameters of AIMDs.

Market readiness is closely related to the Technology Readiness Level (TRL) scale created by the National Aeronautics and Space Administration (NASA) to estimate the maturity of any technology before being deployed in critical tasks [14]. Figure 3 shows a proposed Technology Readiness Level chart for medical devices [15].

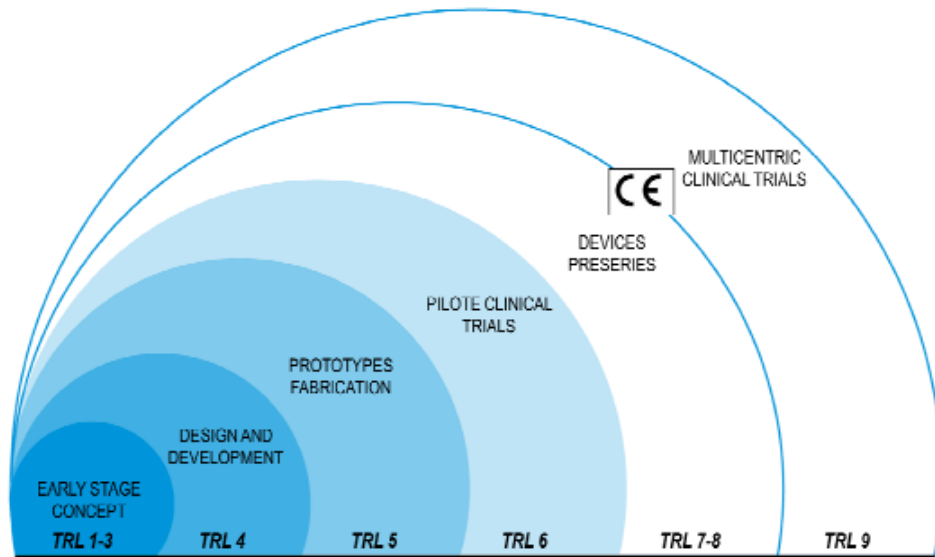


Figure 3: Medical device development technology readiness-level (TRL) scale: from clean room to the patient bedside. [15]

An AIMD that has demonstrated conformity with the five essential requirements previously discussed has passed then the phases of early stage concept (TRL 1-3), design development (TRL 4) and fabrication of prototypes (TRL 5). Such AIMD must be further evaluated in pilot clinical trials, which correspond to the sixth level of the TRL scale of medical devices (Figure 3). This level is a common bottleneck for the technological development of AIMDs as there are few institutes or clinics approved to conduct such trials [15]. CLINATEC is one of them.

If these pilot clinical trials performed on few patients are successful, the manufacturer can fabricate a pre-series of the AIMD (TRL 7-8) and seek approval from regulatory agencies like the European Community (“CE”) or the Food and Drugs Administration (FDA) to conduct multicenter clinical trials (TRL 9). If these clinical trials on larger populations are also successful, the AIMD is granted market approval and it can be sold to the general public.

Manufacturers of medical devices are afraid of being sued by patients due to problems of biocompatibility of materials. Most of them still remember the scandal of silicone implants that terminated French company Poly Implant Prothèse (PIP). However, it is important to remark that PIP voluntarily committed a violation of regulations of medical devices and its cheap silicone implants were not formally approved by health inspectors [16]. It is then in the economic interest of manufacturers to adhere strictly to the regulations of medical devices dictated by the European Community.

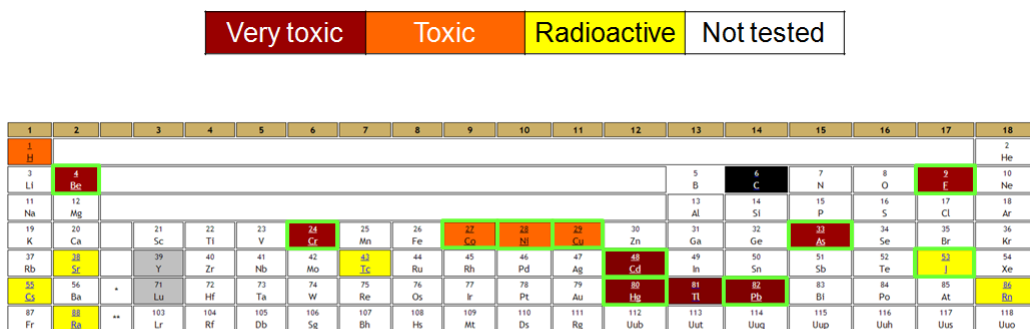
1.3. Packaging Requirements of Medical Micro Devices

The packaging of Microsystems for miniaturized medical devices poses several problems. Medical micro devices must ensure not only high reliability while simultaneously shrinking the size of the device, but also ensure long-term protection of the device. It is not uncommon nowadays to build miniaturized prototypes of implantable medical devices with useful lifetimes of ten years or more. However, it is not currently possible to guarantee packaging lifetimes of such span for micro devices [17], [18].

The main challenges that packaging materials must overcome to make possible long-term packaging of implantable Medical Microsystems are discussed in this section.

1.3.1. Hermeticity

Electronic circuits can be made of toxic materials. They may contain toxic semiconductors (e.g., gallium arsenide), insulators (e.g., beryllium oxide) or metals (e.g., copper, aluminum, lead) that are well known to be toxic [19]. Figure 4 shows a periodic table with chemical elements known to be toxic or radioactive, and it circles in green color the chemical elements typically found in electronic circuits. It can be seen that many chemical elements known for their toxicity are commonly present in silicon devices. Therefore, an encapsulant of medical micro devices must be not only highly conformal, but also a very good barrier against the diffusion of toxic substances arising from the device.



Source: <http://corrosion-doctors.org/Elements-Toxic/Elements.htm>

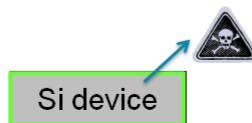


Figure 4: Periodic table showing toxic elements typically found in silicon devices. [19]

Besides being good barriers against the diffusion of toxic substances, materials used to encapsulate AIMDs need to have as well an extremely low permeability to water vapor to prevent corrosion of electronics. This imposes restrictions in the choice of packaging materials for devices that require a package lifetime of 10 years or more. Figure 5 shows the water vapor permeability of many common classes of packaging materials and their predicted lifetime at different thickness. By definition, materials with less than one day of sealing capacity are considered non-hermetic and permeable to water vapor, and they are indicated by the red line of Figure 5. It can be seen in Figure 5 that metals, ceramics, glasses or pure crystals are necessary to provide enough hermeticity for a package lifetime of at least 10 years, which is the intended target of modern implantable electronic devices. This is why electronic systems designed for prolonged use in severe environments are by default placed inside hermetically sealed containers made of metals, ceramics, pure crystals or glasses [20]. The reason behind it is that only these materials have low enough permeability against water vapor to maintain a low content of moisture in the internal cavity and achieve practical long-term packages [21].

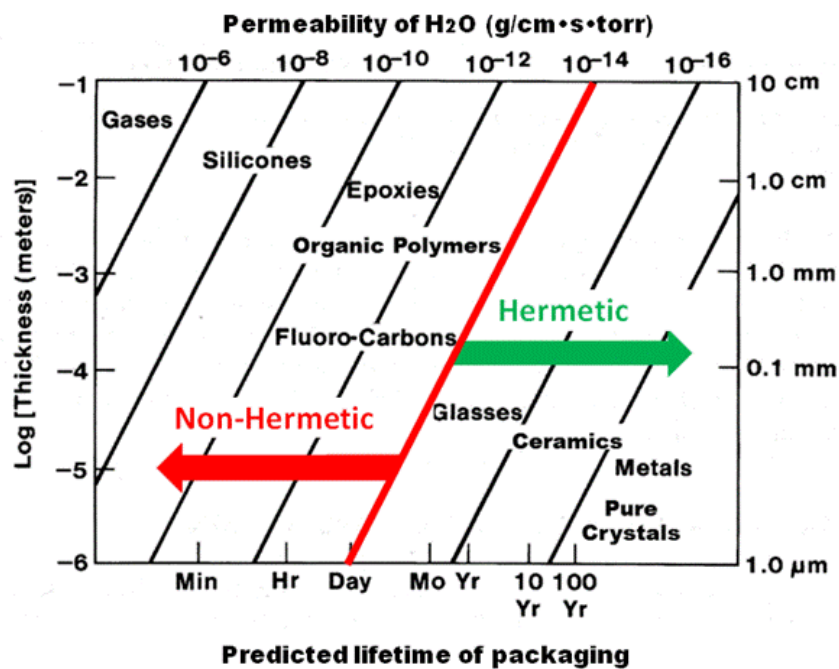


Figure 5: Water vapor permeability of different classes of packaging materials and their predicted lifetime as function of thickness. [21]–[23]

In the beginning of the microelectronics industry in the late 50's, the United States Department of Defense was one of the main promoters of hermetic packaging of electronic components for military applications in the severe conditions found inside missiles, airplanes and space exploration. The military standard MIL-STD-883 was thus created to standardize, among others, the evaluation of hermetic packages for microcircuits [24]. This technical standard defines hermeticity as the effectiveness of the seal of microelectronic devices with designed internal cavities to prevent the entry of reactive gases or contaminants [24, p. 81]. A hermetic seal is needed to protect the internal electronic components from contaminants like ions or moisture that can cause corrosion and circuit failure [25, p. 243]. The property of moisture to condense into liquid droplets is a function of pressure, temperature and the water vapor present in the air. At a given temperature and pressure, the water vapor concentration in the air at which liquid droplets start to condense is known as the dew point. The mathematical relation between temperature and the partial pressure of pure water at the standard dew point is described by the Antoine equation,

$$\log_{10} P = 8.07131 - \frac{1730.63}{233.426 + T} \quad \text{Eq. 1}$$

Where P is the water vapor pressure in torr and T is the temperature of water in degrees Celsius [26]. According to Antoine's Eq. 1, the water vapor pressure needed for liquid droplets to form at 0°C and one atmosphere with 100% relative humidity is 4.5 torr, which corresponds to a molar concentration of water molecules of 0.6% or 6000 parts per million. At levels below this percentage of water vapor, liquid drops are not able to form at 0°C. One could argue that devices used at temperatures higher than 0°C can tolerate higher levels of moisture. However, out of concern that some contaminants can cause condensation of liquid droplets before reaching the saturation dew point, 5/6 of the dew point at 0°C or 5000 ppm is usually taken as the acceptable limit of moisture in the internal cavity according to the qualification requirement of MIL-PRF-38534 and MIL-PRF-38535 [25, p. 119]. Most hermetic seals and packages are therefore designed to keep the internal cavity environment below 5000 ppm (i.e. 0.5%) of moisture throughout the service lifetime of the device.

1.3.2. Compatibility with sterilization

The cleanness of medical devices must be ensured by proper sterilization. Sterilization involves destruction of all forms of life by heat, irradiation, gas or chemical treatment [27]. Medical manufacturers of Active Implantable Medical Devices (AIMDs) such as pacemakers and neurostimulators currently prefer chemical sterilization with Ethylene Oxide (EtO) gas because it is effective, economical and performed at low temperatures (30-60°C) during few hours, which is ideal for heat and moisture sensitive materials and electronic components [28]. However, EtO is carcinogen and there are proposals to ban its usage in the sterilization of medical devices [29]. If EtO is banned, steam sterilization is probably the next best choice [30]. Though, it is typically performed for 20 min at 120°C, which forbids its application in many medical devices containing polymers. As most present packaging materials of MDs consist of polymers, there is additional interest to develop non-polymer packaging materials that can resist high temperatures for few hours.

A good advice from designers of MDs is to get an idea of your materials tolerance to sterilization when building early prototypes. Otherwise, there may be fewer or no options to change it when more advanced prototypes are fabricated [31].

1.3.3. Adhesion on substrate

Adhesion is defined as the process of attachment of a substance to the surface of another substance [32]. Packaging layers of implantable electronic devices must have excellent adhesion (that is, 0% of area removed by the tape test method ISO 2409:2013 [33]) to substrates typically used in the fabrication of Microsystems such as silicon and silicon oxide. Otherwise, there is early failure of the micro device as consequence of infiltration of water and ions inside the packaging, which conducts to loss of insulation resistance between conductive layers, corrosion of metals and loss of electrical contacts [25, p. 243], [34]–[37].

Adhesion requires energy that can come from chemical and/or physical linkages, the latter being reversible when enough energy is applied [32]. Chemical adhesion occurs when the atoms of two different surfaces form ionic, covalent, or hydrogen bonds [38]. Chemical linkages between the packaging layer and the substrate are preferred because they are not easily broken. In order to achieve them, chemical vapor deposition (CVD) and surface activation of substrates by plasma or chemical solutions can be used to obtain excellent adhesion between the encapsulant and substrate.

1.3.4. Rounded edges

Implantable medical devices are foreign to living organisms. When foreign bodies are present in biological tissue, the normal healing response of the organism to an external wound is changed. Such changed healing response is called Foreign-body reaction (FBR) and consists of adverse reactions like inflammation, tissue-encapsulation leading to isolation of the implant, or infection [39]. If such reaction is strong, the implant can cause chronic inflammation, pain, infection, and rejection by the body in a fibrous capsule. In some instances, post-surgery removal of the implant by the physicians becomes necessary. It is estimated that about 5% of medical implants become infected post-surgery [40].

It is known since 1976 that implants with sharp forms induce stronger FBRs [41]. Recent studies have further highlighted the importance of morphological characteristics like stiffness and sharpness on FBRs [42],[43]. Unfortunately, microelectronic devices are based on crystalline silicon wafers that are hard and brittle. Wafer dicing is normally done using conventional blade technology, which can cause chipping and cracking of the silicon device. Alternative dicing techniques include laser dicing [44] and plasma dicing [45].

The problem of sharpness of the implanted microelectronic device can be solved in some cases by embedding it in a soft biomaterial that resembles the mechanical properties of human tissue [46]. However, silicon dice sharp edges are problematic even when embedded in a soft biocompatible polymer because there is incomplete covering over the edges, which leads to local problems in biocompatibility (Figure 6) [47]. In order to minimize the FBR of implantable medical micro devices, a dicing or etching method to obtain rounder or softer edges is needed. Both methods were attempted during this thesis (page 142).

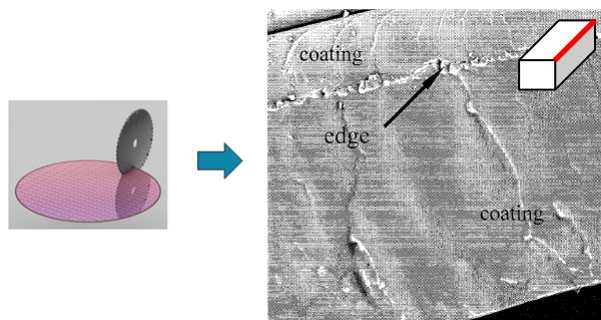


Figure 6: Problems of covering of a silicone coating across sharp edges (Right) after conventional dicing of a silicon device (Left). [47], [48]

1.4. State of the Art of Miniaturized Medical Devices

In the early 50's, some metals like titanium or stainless steel were already known to be inert biomaterials in orthopedic implants. The missing technology to fabricate portable Active Implantable Medical Devices (AIMDs) arrived in 1954 with the first commercial silicon transistor produced by Texas Instruments. Early enthusiasts began then to research and develop smaller AIMDs building upon technologies developed by the defense industry for the hermetic packaging of electronics. Packaging requirements of portable AIMDs were high like those of military hardware, but not because they had to work at extreme conditions of temperature and pressure, but because they had to ensure high reliability in the chemically aggressive and at the same time fragile environment found inside patients. It was not easy task to change the aim of hermetic electronic packaging from environments outer space to the relatively untested conditions of the human body. Early devices lasted only few hours and had to be regularly changed due to packaging failures and primitive battery technology [49]. Nevertheless, a new industry was born and soon enough AIMDs such as artificial cardiac pacemakers, cochlear implants, and neurological stimulators started to help patients in need of them. Figure 7 shows the evolution from the early 60's until nowadays of one type of AIMD, the artificial cardiac pacemaker.

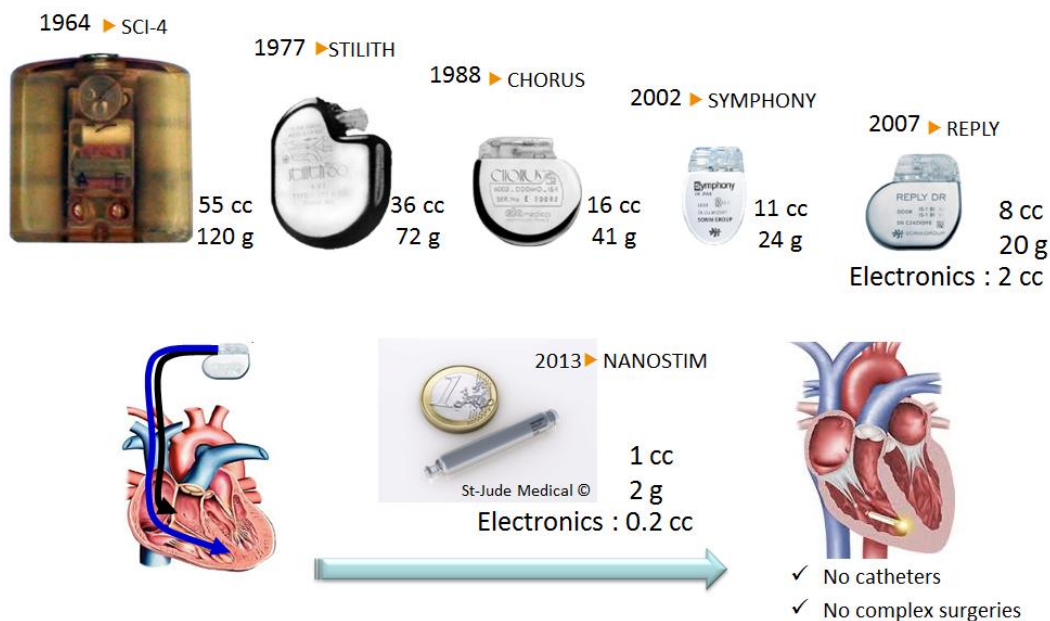


Figure 7: Evolution of artificial cardiac pacemakers. [50],[51]

It can be seen in Figure 7 a progressive tendency towards miniaturized devices. This trend of miniaturization can be observed as well in other active MDs such as cameras (Figure 8), cochlear implants, retina implants, ex-situ glucose sensors (Figure 9), multifunctional contact lenses (Figure 10) and neurostimulators [50],[52]. Miniaturized AIMDs enhance not only the portability and comfort of patients, but also enable new therapeutic treatments thanks to their ability to fit inside organs of the patient that are not available to conventional AIMDs. For example, the small size of modern leadless pacemakers allows implanting them directly in the heart. This eliminates the need for cardiac catheters, which are prone to complications such as dislocations and infections. The incidence of these complications is relatively low (about 4%), but taking into account that more than four million people around the world have implanted cardiac catheters [53], nearly 160 000 patients could benefit from miniaturized pacemakers. And this number does not include patients potentially attracted by the cosmetic appeal and extra comfort offered by leadless pacemakers.

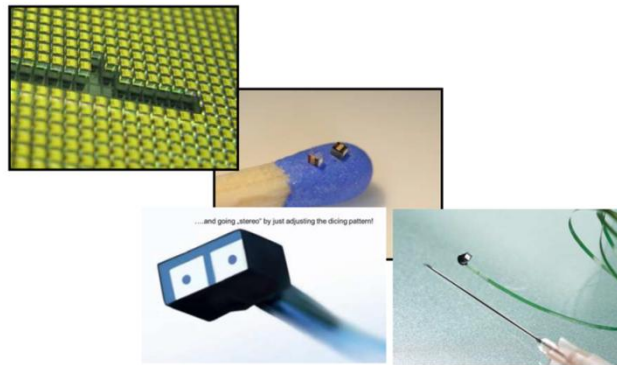


Figure 8: A miniaturized camera developed by Medigus Ltd. [52], [54]



Figure 9: Tear drop micro glucose sensor (NovioSense™). [55]

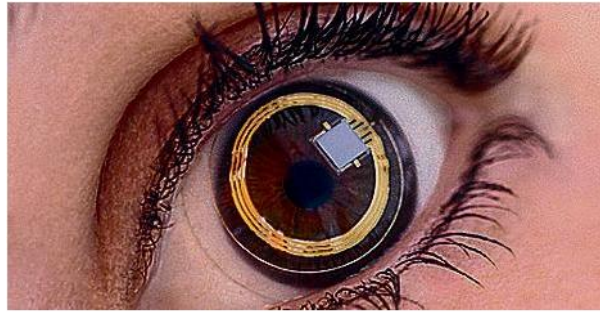


Figure 10: Miniaturized intra ocular pressure sensor (SENSIMED Triggerfish®). [56]

Miniaturized MDs contain highly integrated electronic circuits packaged either within a hermetic enclosure (e.g., pacemakers) or a conformal layer (e.g., the pressure sensor, glucose sensor and micro camera displayed above). Figure 11 illustrates these two methods of protecting Integrated Circuits (IC) and related components for human implantation [57], [18].

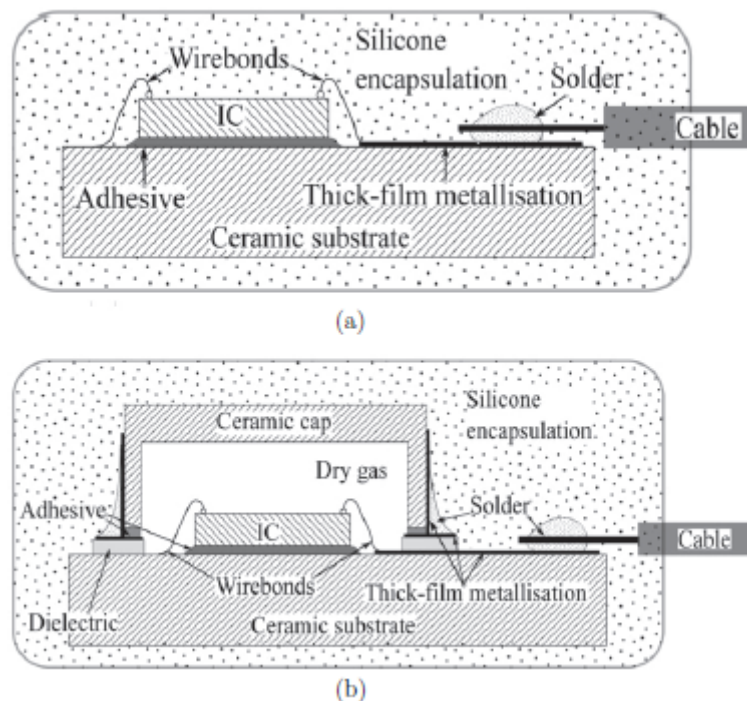


Figure 11: Methods of protecting Microsystems for human implantation: (a) Conformal layer or encapsulation, (b) Impermeable envelope or hermetic packaging. [18]

The conformal layer method has been widely employed in the microelectronics industry with encapsulants such as silicone and epoxy because it is less expensive and easier to implement than the method of impermeable envelopes. However, there are several failure modes present

in the encapsulation method that make difficult to predict the long-term behavior of the packaging [34]–[37], [57]. This is why modern MDs that are not implanted (e.g., the ex-situ micro glucose sensor of Figure 9) or that are in contact with the human body for few hours (e.g., the pressure sensor and micro camera showed before) are protected this way.

The hermetic packaging or impermeable envelope has been historically preferred for more demanding commercial and military applications because it is a mature technology developed since 1945, plus it is possible to guarantee the service lifetime of packages with internal cavities larger than 0.1 cm^3 [17]. For this reason, although pacemaker's size and weight have consistently reduced over the years to facilitate the portability and comfort of patients, they are still packaged in hermetically sealed titanium cans (Figure 7). However, such metallic canisters are expensive, rigid (which excludes its application to several biological sensors [46]) and can make up to 90% of the volume of the final medical micro device. Moreover, metallic enclosures obstruct practical transmission of data or wireless power, which is another trend followed by modern MDs [50], [52]. Some authors have proposed impermeable envelopes made of ceramics [58], [59] or even pure crystals like silicon [47], [60], but the cost of the impermeable envelope method remains high and has limited potential for further miniaturization.

In order to continue with the trends of miniaturization and functional diversification of AIMDs, it is necessary to develop a micro packaging method suitable for long-term human implantation. This need is frequently mentioned in the scientific literature [17], [61]–[63]. Such micro packaging method would enable placing novel miniaturized medical devices in close contact with the target site of implant during several years. This thesis' goal is to help in the development of such micro packaging method.

Chapter 2: Selection of Biocompatible Packaging Materials

It was seen in previous chapter that biocompatible packaging is most important for protecting both patient and medical device. In order to do this successfully, the packaging material must comply with various requirements (e.g., biocompatibility, hermeticity, compatibility with sterilization) that are regulated by international standards as well as local ones. The selection of suitable packaging materials is also restricted by the process of fabrication and the conditions of evaluation of medical devices.

Fabrication of Microsystems is performed in rigorously controlled areas called ‘clean rooms’ where there are ultra-low levels of airborne particles, microbes and volatile residues as well as small fluctuations in temperature, humidity and vibrations [64]. Novel active implantable medical devices like micro glucose monitors or retina implants require opening the packaging layer by physical or chemical etching to interact via an electrode with the outer environment [65]. However, this etching requirement imposes limits on the selection of packaging materials. For example, biocompatible materials such as silicones and epoxies are widely used for the encapsulation of medical implants [20], but they are avoided in most clean rooms due to contamination concerns about volatile residues [66]. Furthermore, these and similar polymer materials do not provide enough hermeticity for implantations longer than 24h [67].

Typically, packaging layers are made by chemical vapor deposition (CVD) techniques in the microelectronics industry. CVD techniques are preferred for the protection of Microsystems because they produce solid thin films ($<10\ \mu\text{m}$) of high conformal deposition and quality. Plus, they do so without releasing byproducts or using chemical substances like solvents, plasticizers, catalysts and accelerants that release volatile residues and contaminate the air of clean rooms [64, p. 50]. Examples of CVD passive layers widely used in microelectronics are silicon oxide, silicon nitride and silicon carbide. Packaging layers of Microsystems intended for prolonged and chronic medical implants should be fabricated by CVD techniques in order to be compatible with the fabrication environment of clean rooms.

Packaging of miniaturized IEDs in clean rooms at the wafer scale (that is, Wafer Level Packaging = WLP) enables not only a high degree of miniaturization thanks to passive thin films, but also a reduction of costs thanks to parallel encapsulation of numerous silicon devices. This way, WLP become economically interesting compared to traditional approaches

for the packaging of medical devices such as glass encapsulation or hermetic welded titanium canisters. These traditional approaches have limitations for further miniaturization and are not compatible with novel medical devices such as in-situ physiological monitors and Brain-Computer Interfaces.

The pressure to select suitable encapsulant materials for packaging novel medical devices has been increased recently. Medical regulatory bodies in Europe and North America have started demanding that whenever novel microelectronic devices (e.g., BioMEMS and physiological sensors) are used as part of or inside a medical device, it is mandatory to coat them with a biocompatible encapsulant that protects the patient in case the outer plastic or metallic housing containing the device fails or is infiltrated by external biological fluids.

This chapter reviews the materials typically used in the packaging of medical devices and taking into account the methods of fabrication available in clean rooms discusses the reasoning behind the selection of materials that are characterized and evaluated in later chapters.

2.1. Strategy of selection

Our strategy for selecting packaging materials of medical microsystems was divided in three stages. First stage consisted in searching in the scientific literature and materials databases for solid materials with reported excellent chemical stability, impermeability and biocompatibility. The second stage consisted in identifying among the previously selected materials those compatible with fabrication in standard clean rooms. The third and final stage consisted in selecting materials and fabrication recipes that could be readily deposited at CEA-LETI and MINATEC.

2.1.1. Scientific Literature

Many scientific articles and books were consulted for biocompatible materials for the encapsulation of medical devices. The most helpful resources were the books of J. Black (*Biological Performance of Materials: Fundamentals of Biocompatibility*, Marcel Dekker, 1999), D. F. Williams (*Fundamentals Aspects of Biocompatibility*, CRC Press, 1981) and B. D. Ratner (*Biomaterials Science*, Academic Press; 2012). Biocompatible materials constitute a relatively new field of study, characterized by the merge of multiple disciplines such as physics, chemistry, biology and medicine. Continuous progress in biomaterials has brought us

in the last century many successful medical implants such as orthopedic prostheses (e.g., knee and hip joint replacements); cardiovascular implants (e.g., artificial heart valves, stents and pacemakers); neural implants (e.g., cochlear implants and nerve stimulators); plastic and reconstructive implants (e.g., breast augmentation implants, maxillofacial reconstruction and injectable collagen for soft tissue augmentation); dental implants; ophthalmologic prostheses (e.g., contact and intraocular lenses); bladder stimulators; and drug-dispensing implants.

However, comparisons of biomaterials are misleading as one biomaterial can be perfectly suitable for a given application, but toxic for another. For example, aluminum and its oxides have been proven to cause minor tissue reactions in orthopedic implants, but it has also been reported an association between aluminum concentration in the brain and Alzheimer's disease [68]. Thus, the "biocompatibility" or chronic toxicity of a given material ought to be judged depending on which part of the body is implanted and for how long. This task is more difficult with permanent implants with lifetimes of >10 years because there is no practical way to ensure the device materials are stable for such span.

Taking into account that biocompatibility is a local property and that it depends on the duration of implantation, the "selection" of encapsulant materials for permanent "general" implantation is misguided. It is more practical to define an intended application. As this study was created to support a project of CEA-LETI to develop a miniaturized hermetic silicon box containing an accelerometer and IC for in-situ monitoring of the endocardial acceleration signal for >10 years [60], the intended application of encapsulant materials selected in this study was long-term cardiac implantation of silicon devices.

There are currently several materials that have been successfully employed in different biomedical devices and are considered generally as *biocompatible*. Some of them include:

- Polymers like Poly-Urethane, Parylene-C and Silicone [69],
- Ceramics or glasses like Pyrex[®], SiO₂, Si₃N₄, SiOC, ZrO₂ and ZnO [70]–[72],
- Diamond-like materials such as BN and amorphous carbon [73], [74]
- Noble metals and their alloys, [75]
- Medical grade Stainless Steels, [76]
- Titanium and their alloys [77],
- Some Cobalt-based alloys, [78]
- MP35N[®] (a Nickel-Cobalt-Chromium-Molybdenum alloy) [79].

From these materials, the most relevant for the protection of silicon micro devices for cardiac applications are solid materials impermeable to liquids and moisture. That is: Metals and Ceramics. Each one of these families of materials shall be examined in the next pages.

Metals

Most metals are readily corroded when placed in contact with saline solutions. Metallic corrosion can be defined as the reaction between a metal and its environment [75]. Pure metals are seldom found in nature. They are usually found in a corroded state such as oxide or sulfide, as part of an ore. Metallic corrosion is a spontaneous electrochemical process, driven by the higher thermodynamic stability of the metal compound produced, which is generally an oxide (Table 3) [80]. This is why metals are virtually never found in their pure state in nature, but rather combined in an ore as a metallic compound. To purify metals from ores, enormous amounts of energy must be supplied to reverse the reaction of oxidation.

Table 3: Thermodynamic stability of some metal oxides. [81]–[83]

Metal	Most stable oxide	Standard heat of formation ¹ (kcal/mol)
Tantalum	Ta ₂ O ₅	500.1
Niobium	Nb ₂ O ₅	422.1
Aluminum	Al ₂ O ₃	389.5
Chromium	Cr ₂ O ₃	267.4
Hafnium	HfO ₂	266.1
Zirconium	ZrO ₂	249.0
Titanium	TiO ₂	217.4
Vanadium	V ₂ O ₅	209.0
Silicon	SiO ₂	205.4
Iron	Fe ₂ O ₃	64.0
Gold	N/A	-12.0

¹ The standard molar heat of formation of a compound (ΔH_f^0) is equal to the enthalpy change (ΔH) when one mole of compound is formed from its constituent elements at 25°C and 1 atm [84].

Corrosion may occur in different environments, but it is aqueous corrosion that is most relevant for biomaterials, especially aqueous corrosion in saline environments where the concentration of NaCl is usually 0.9%. Water and salt ions provide a chemical environment where electrochemical reactions can take place. Electrochemical reactions need anodic and

cathodic sites to occur. A metal surface in a saline environment can have millions of micro-sized cathodes and anodes [80].

The metal is dissolved by an oxidation process at the anodic site, where it loses electrons as symbolized by the equation:



For the electrochemical reaction to continue there must be a balance of mass and electric charges. So, there must be a cathode where electrons are being consumed and a reduction reaction is taking place. Many different reactions of reduction can occur at the cathode, the two most common being the reduction of dissolved oxygen or hydrogen ions:



Eq. 3 takes place preferentially in aerated places where oxygen is readily available in aqueous solution, whereas Eq. 4 tends to occur in acid media. To avoid corrosion means finding ways to minimize or prevent the previous electrochemical reactions from occurring at the anode and cathode.

Let us consider the ideal case of a pure metal immersed in aqueous solution. Its anodic dissolution is given by Eq. 2. Atoms of the metallic surface are actually positive ions (a.k.a. cation) held together by the free electron cloud, with each cation sitting at the bottom of energy well [85]. A deeper energy well is available in the aqueous solution, which is the solvated metal cation surrounded by water molecules

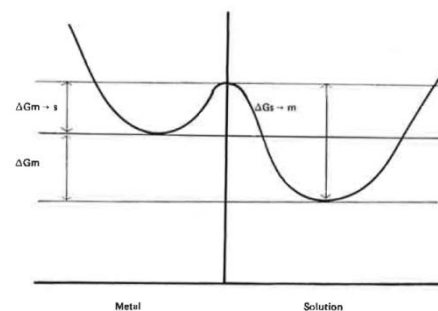


Figure 12: Gibbs energy of a metal at its interface with a solution. [75]

or other molecules like for example chloride anions. Figure 12 shows the Gibbs energy of a pure metal as function of its distance to the metal-solution interface. The solvated state of the cation is energetically favored compared to its state in the metallic surface and therefore the

Gibbs energy change for the dissolution process of the metal (ΔG_m) is negative. This means that anodic dissolution of metals is a thermodynamically spontaneous process [75].

When the anode is connected to a cathode by an external circuit so that electrochemical reactions described by Eq. 2–Eq. 4 may continue, a difference of voltage potential is established between them and it can be quantified by comparison with a reference. The reference is known as standard electrode and many types of them are available. A hydrogen standard electrode is typically used for this quantification. The cathode reaction that takes place with such electrode is described by Eq. 4 and results in the production of hydrogen gas. The potential difference between a metal and its solution determined by a standard hydrogen electrode is referred to as the single potential on the standard hydrogen scale [75].

When the single potential is measured at 25°C and concentration of 1 gram of metal salt per liter of solution, the potential is referred to as the standard or normal electrode potential. Comparison of several standard electrode potentials in a list known as the electrochemical series is most useful to predict the stability of metals and elements. Table 4 shows the electrochemical series of some metals and elements of interest.

Table 4: Electrochemical series of various metals and elements at 298 K and 1 atm. [86], [87]

Metal, compound	Half reaction	Standard potential (V)
Fluorine	$F_2 + 2 H^+ + 2 e^- \leftrightarrow 2 HF$	+3.05
Ozone	$O_3 + 2 H^+ + 2 e^- \leftrightarrow O_2 + 2 H_2O$	+2.08
Gold	$Au^+ + e^- \leftrightarrow Au$	+1.83
Hydrogen peroxide	$H_2O_2 + 2 H^+ + 2 e^- \leftrightarrow 2 H_2O$	+1.78
Oxygen, Hydrogen (acid)	$O_2 + 4 H^+ + 4 e^- \leftrightarrow 2 H_2O$	+1.23
Platinum	$Pt^{2+} + 2 e^- \leftrightarrow Pt$	+1.19
Silver	$Ag^+ + e^- \leftrightarrow Ag$	+0.80
Copper	$Cu^{2+} + 2 e^- \leftrightarrow Cu$	+0.34
Hydrogen	$2 H^+ + 2 e^- \leftrightarrow H_2$	0
Tungsten	$WO_3 + 6 H^+ + 6 e^- \leftrightarrow W + 3 H_2O$	-0.09
Nickel	$Ni^{2+} + 2 e^- \leftrightarrow Ni$	-0.25
Cobalt	$Co^{2+} + 2 e^- \leftrightarrow Co$	-0.28
Iron	$Fe^{2+} + 2 e^- \leftrightarrow Fe$	-0.44
Tantalum	$Ta^{3+} + 3 e^- \leftrightarrow Ta$	-0.60
Chromium	$Cr^{3+} + 3 e^- \leftrightarrow Cr$	-0.74
Zinc	$Zn^{2+} + 2 e^- \leftrightarrow Zn$	-0.76
Titanium	$Ti^{2+} + 2 e^- \leftrightarrow Ti$	-1.63
Aluminum	$Al^{3+} + 3 e^- \leftrightarrow Al$	-1.66
Silicon	$Si^{4+} + 4 e^- \leftrightarrow Si$	-2.14
Lithium	$Li^+ + e^- \leftrightarrow Li$	-3.04

Metals with negative standard potentials tend to give away electrons and to dissolve in aqueous solution as consequence. The more negative the standard potential, the stronger this tendency to give away electrons and act as reducing agent. Lithium, titanium and aluminum belong to this category. Conversely, metals with positive standard potentials are good receivers of electrons and do not dissolve easily. They are therefore good oxidizing agents. Gold, platinum, silver and copper belong to this category.

Metals like platinum and gold are known since ancient times for their chemical stability and durability. For example, gold does not corrode and so it was a symbol of immortality among pre-Columbian South American natives. Gold and platinum are consequently called “noble” metals because of their remarkable resistance to corrosion. However, noble metals’ elevated price and poor mechanical properties forbids their application in the majority of medical implants.

Luckily, some metals react with water to form an oxide that is very coherent, uniform and thermodynamically stable in aqueous solution under certain conditions [77]. Electrode potential-pH equilibrium diagrams (a.k.a. Pourbaix diagrams for their developer, Marcel Pourbaix) are useful to understand the extent of protection offered by this oxide layer to metals. Pourbaix diagrams indicate the most stable phase of a metal-solution system under certain environmental regions. The parallel dashed lines in such graphs indicate the stability region of water. For example, titanium is readily oxidized by water in the environment conditions found inside the human body (that is, pH 1.5–8.5) to form a stable and uniform film of TiO_2 (Figure 13). This oxide thin film of about 10 nm protects the bulk metal from further corrosion by the aqueous solution. In these cases, it is said that the metal is passive, or passivated [80].

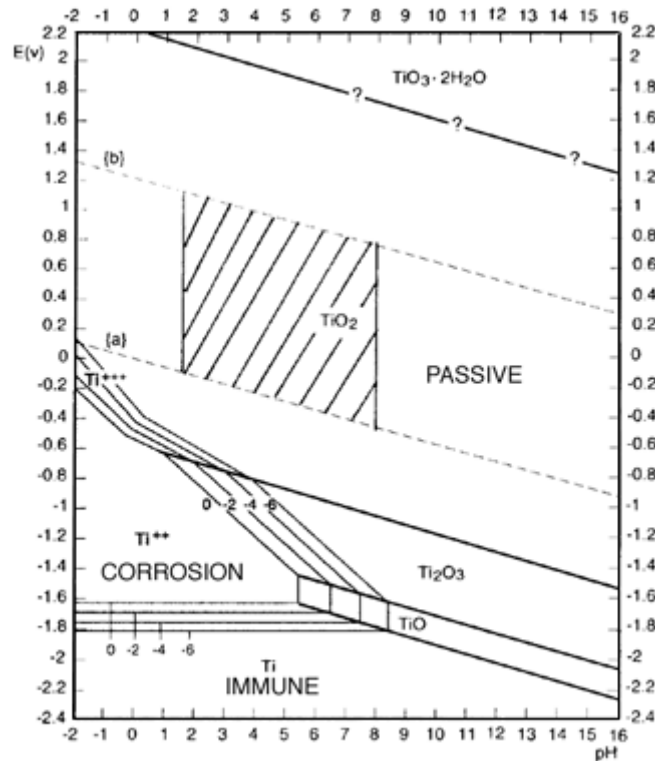


Figure 13: Pourbaix diagram of the titanium-water system. Marked region indicates physiological conditions. [81]

Conversely, there are metals that do not readily form passive layers in aqueous solutions. Metals at the top of Table 3 readily form passive layers, whereas those at the bottom form them much more slowly. At the top of Table 3, there are metals like tantalum, niobium and aluminum that readily form passive layers. Figure 14 shows the Pourbaix diagram of aluminum. It can be seen that although its passive layer is stable over a long range of applied potential, it is stable only on a small range of pH. It is important to remark that Pourbaix diagrams predict the thermodynamic stability of metallic chemical species in water, but they do not contain information about the speed at which such corrosion reactions occur. For example, aluminum is not stable outside the pH region from 5 to 7, but its corrosion takes place very slowly, in the order of few microns of metal dissolved per year in marine atmospheres [88].

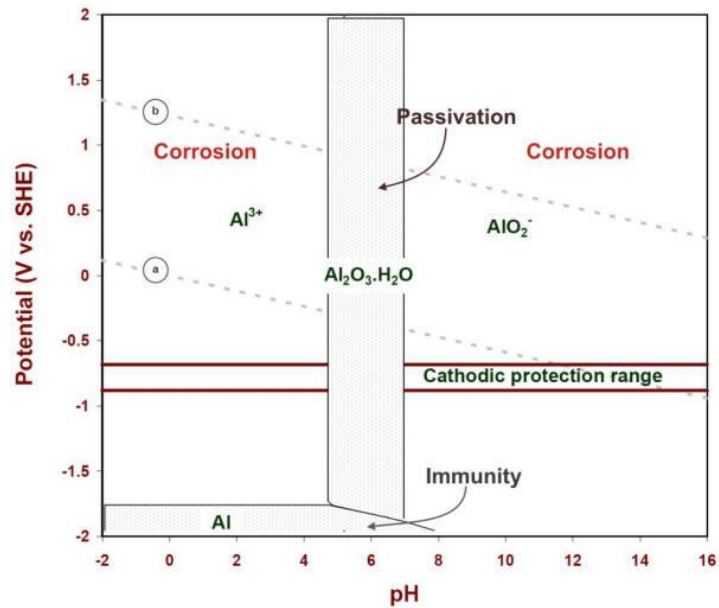


Figure 14: Pourbaix diagram of Al-H₂O system. [89]

Iron is one example of a metal that does not easily form passive layers. The Pourbaix diagram for the iron-water system is shown in Figure 15. It can be seen that iron undergoes corrosion in physiological environments (region defined between pH 1.5–8.5 and parallel dashed lines). At the bottom of Table 3, there is gold that forms an unstable oxide as indicated by the negative value of the heat of formation of its oxide. The thermodynamic instability of gold's oxide explains its extraordinary chemical inertness and also the difficulty of achieving good adhesion between gold and other passive layers.

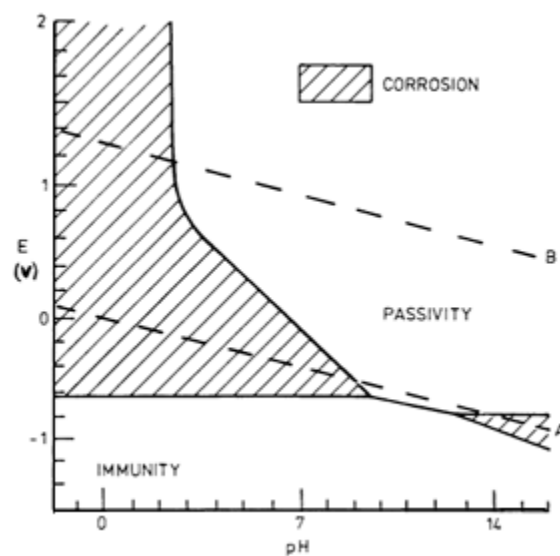


Figure 15: Pourbaix diagram of Fe-H₂O system. [81]

In general, the larger the heat of formation of a metal oxide, the more thermodynamically stable is the passive layer of the metal. The higher thermodynamic stability of the metal oxide produced means that enormous amounts of energy must be supplied to reverse this process of oxidation [81]. For that reason, most metallic biomaterials are based in noble metals or alloys of Ta, Nb, Cr, Zr and Ti [77], [79], [82], [75], [90]. These metals and their alloys are, for most practical purposes, biologically inert and produce minor or no adverse tissue reactions after implantation. Table 5 resumes the tissue reactions of humans to different metallic implants as part of orthopedic or dental prostheses.

Table 5: Tissue reactions around metallic implants. [90], [91]

Thickness of pseudo-membrane around implant		Type of reaction		
Minor reaction	Severe reaction	Vital <i>Minimal</i>	Capsule <i>Scar tissue</i>	Toxic <i>Tissue damage</i>
Ti alloys, stainless steels, CoCr alloys	Fe, Co, Cr, Ni, Mo, V, Mn, Incoloy	Ti, Nb, Pt, Ta, Zr and their alloys	Fe, Mo, Al, Au, Ag, stainless steels, CoCr alloys	Co, Cu, Ni, V

Metals that cause minimal adverse reactions are metals and alloys of Ti, Zr, Nb, Ta and Pt. The thermodynamic stability of their metal oxides makes them virtually chemically inert in biological environments and explains the minimal tissue reaction elicited by them [92]. On the other hand, metals of Co, Ni, Cu, and V cause severe tissue damage and are considered in general toxic to humans. In between these groups, there are metals that cause adverse tissue reactions (Fe, Mo, Al, Au, Ag, stainless steels and CoCr alloys), but they are effectively isolated by the host organism in a capsule of scar tissue to prevent further damage. Elemental release, surface oxide formation and oxide conformation are three important factors controlling the osseointegration of metallic implants [93]. Gold is essentially chemically inert in physiological conditions, but its lack of surface oxide renders difficult its osseointegration and it is eventually isolated in a scar tissue capsule (Table 5).

Relatively inexpensive metals that cause minor tissue reactions, like for example Titanium and Stainless Steel, are commonly employed to fabricate hermetic canisters for packaging AIMDs such as defibrillators and pacemakers. Such metallic envelopes are privileged for

commercial applications because they allow using standard microelectronics inside airtight environments and it is possible to predict the lifetime of packages $>0.1 \text{ cm}^3$ based on detected helium leak rates [17].

Ceramics

Ceramics can be made from several inorganic compounds and to have amorphous, crystalline or poly-crystalline structures. For example, glass is a type of ceramic with amorphous (non-crystalline) structure that is widely known. Silicon dioxide is the main constituent of glass and is considered a bioceramic. Biocompatible ceramics or bioceramics can be classified according to their reactivity as:

(1) Nearly inert ceramics: have minimal alteration of the surface in contact with biological tissue. One example is dense alumina ceramics. Usually; a thin capsule of 1–6 mm of fibrous tissue forms around the interface of alumina. Sometimes such capsule becomes too thick, so the ceramic orthopedic prosthesis becomes detached from the bone and there is failure of the medical device as consequence. To prevent this negative outcome, resorbable and controlled surface-active biomaterials were invented during the late 1960's.

(2) Totally resorbable ceramics: are typically made of CaO and P_2O_5 compounds, like for example $\text{Ca}_3(\text{PO}_4)_2$. These compounds slowly disintegrated within the body and the bioceramic is gradually infiltrated by local tissue. Thus, the material behaves similar to a native bone graft that favors bone in-growth.

(3) Controlled surface reactivity ceramics: are intended for rapid and permanent fixation of the implanted ceramic before fibrous encapsulation might isolate it from the body. These materials have relatively good mechanical properties and they are commonly called bioglasses because they possess a glass (i.e. amorphous) micro structure. If they are partially or fully crystallized, they are called bioactive glass-ceramic or bioglass-ceramics [75].

Ceramic films with amorphous structure are more interesting than poly-crystalline ceramics for the encapsulation of microelectronics because they do not have grain boundaries that may work as weak points for the infiltration of water or localized corrosion. This is why for the

hermetic encapsulants of this thesis, amorphous ceramics of the first category (nearly inert materials) were chosen. Some examples of nearly inert ceramics are SiO_2 , SiOC and ZrO_2 .

As silicon is a metalloid element that undergoes corrosion when present in saline solutions [18], [94], silicon devices have to be passivated by metal oxides or inert bioceramics to protect them from biodegradation. One approach suggested by Kotzar et al. [95] is to use relatively inert silicon compounds such as SiC , SiO_2 and Si_3N_4 as passive layers of Microsystems intended for medical devices. These materials are biocompatible according to guideline ISO 10993-5 and are readily available in standard clean rooms. Another approach is using some of the metallic oxides of Table 3 for corrosion protection of vulnerable substrates such as copper or stainless steel [96]–[98]. The former approach is already used in the microelectronics industry to protect silicon devices as part of BioMEMS applications, whereas the latter one is rather novel and it has not been tested for biocompatible packaging of microelectronic devices.

2.1.2. Databases

Some candidate materials for the encapsulation of microsystems were identified with the help of CES EduPack, which is a comprehensive group of databases of materials and process information developed by Granta Design©. It contains more than 3900 bulk materials including their most relevant material properties like electrical, mechanical, thermal, optical, chemical composition, durability and fabrication process.

Both insulating and conductive materials were consulted. This software allows choosing a range of values for various parameters of search such as: density, electrical resistivity, chemical stability / durability in different chemical environments, flammability and maximum and minimum service temperature, among others.

Insulating materials

Insulating materials with a solid structure were sought because high density is correlated with low porosity and low permeability to water vapor. Therefore materials with a density smaller than 1000 kg/m^3 , or 1.000 g/cm^3 were discarded. The maximum service temperature was chosen to be larger than 70°C because the encapsulant will be tested with accelerated aging tests at high temperatures. Plus, chemically inert materials with excellent durability in different chemical environments were desired. 54 materials out of 3900 bulk materials fulfilled the previous criteria. They are shown in Figure 16.

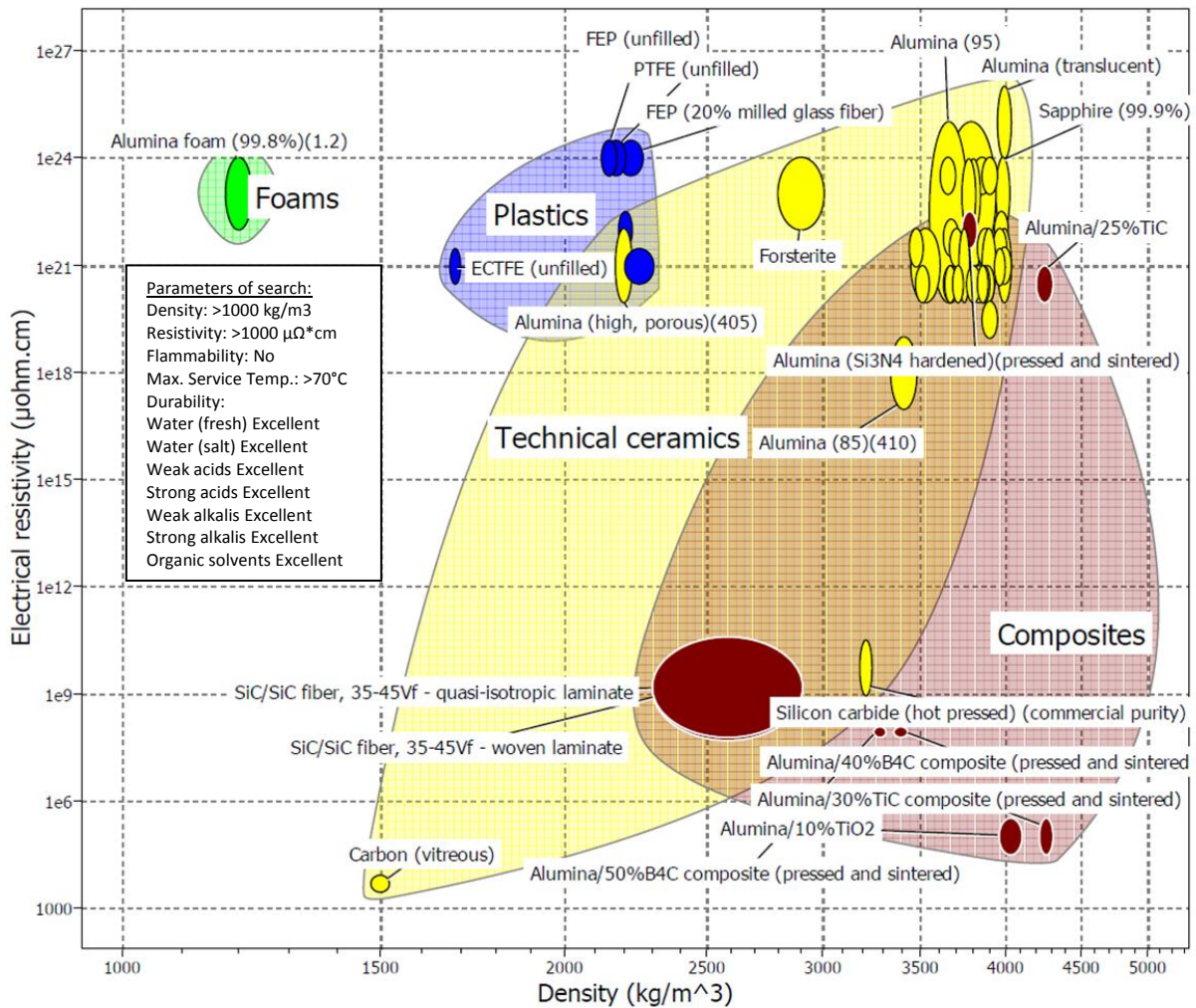


Figure 16: Insulating encapsulants proposed by the databases of CES EduPack®.

Materials located in the right upper corner of Figure 16 are more desirable because they have higher resistivity and density, which means they are probably good insulating impermeable barriers. Most of materials in Figure 16 are ceramics. 40 materials are alumina (Al_2O_3) or combinations of alumina with other materials such as TiO_2 , TiN , TiC , B_4C , SiO_2 , SiN , and ZrO_2 . Three materials are different formulations of silicon carbide (SiC). One material is glassy or vitreous carbon, a material renowned for its amorphous microstructure of sp^2 carbon [99]. And the other materials are fluorocarbon polymers such as PTFE (also known as Teflon®), FEP, ECTFE, and PFA.

However, fluorocarbon polymers are not compatible with fabrication in clean rooms due to concerns about the volatility of their chemical residues [64]. And glassy carbon is a material that cannot be readily deposited by Chemical Vapor Deposition [99]. But there is a material

closely related that can be: Diamond Like Carbon (DLC). DLC is a combination of amorphous sp^2 and sp^3 carbon with excellent chemical stability [99]. Taking into account previous limitations, the following materials were preselected as candidate materials for the encapsulation of medical microsystems:

- Alumina
- Titania
- Zirconia
- Hafnia
- Silicon carbide
- Silicon nitride
- Silicon oxide
- DLC

Conductive materials

109 conductive materials were suggested by the CES EduPack® databases and they are shown in Figure 17. As explained before, most of them are noble metals and alloys of metals that form a dense and uniform metal oxide passive layer, like for example Tantalum, Titanium, Zirconium, Chromium and Niobium.

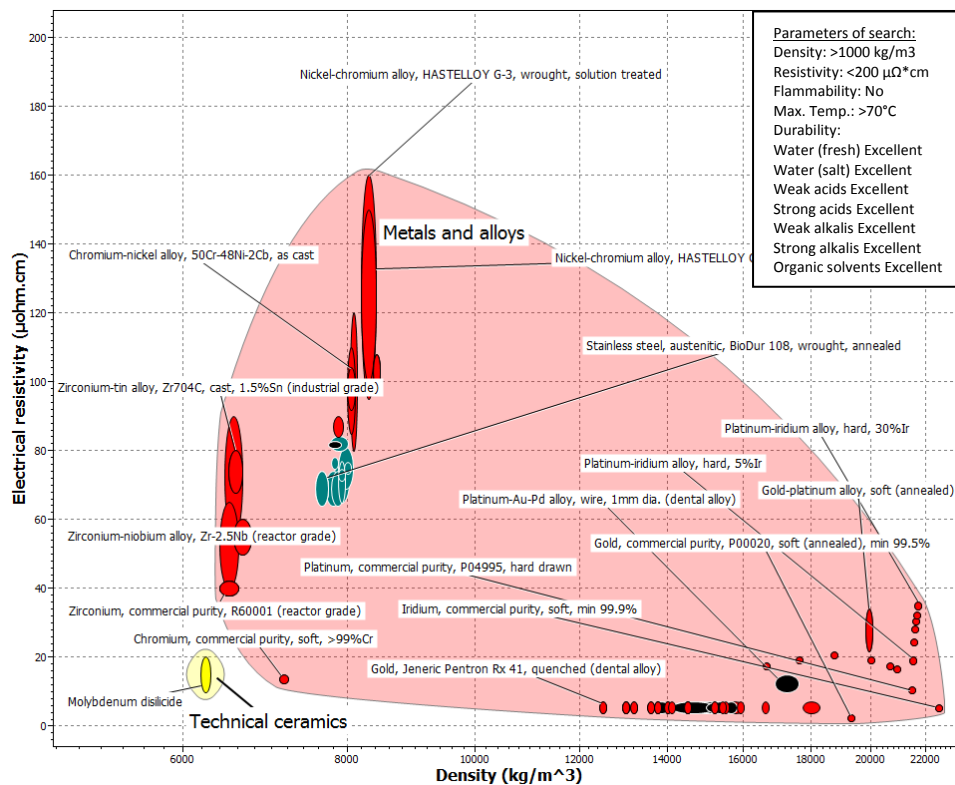


Figure 17: Conductive materials proposed by the databases of CES EduPack®.

However, noble metals and alloys such as stainless steel are forbidden in most clean rooms out of concern of metallic contamination in the fabrication of microsystems [64]. Fortunately, gold is tolerated in some clean rooms of CEA-LETI dedicated to MEMS technologies. Therefore, gold was selected for the fabrication of electrodes in the test vehicles of this thesis.

2.2. Method of Deposition

As previously discussed in Chapter 1, encapsulant materials readily deposited by chemical vapor deposition (CVD) methods are preferred in order to avoid concerns about contamination and particles volatility during the processes of micro fabrication in clean rooms. Another reason is that CVD produces thin films of high conformality and density with good adhesion on silicon substrates. CVD techniques can also coat holes and trenches with high aspect ratios (which is defined as the ratio of length to diameter of the trench). This last feature is extremely important to avoid the formation of micro cavities between the substrate and encapsulant, which can act as a point for the condensation of water and the beginning of corrosion processes. This section explains briefly the principles behind two CVD techniques employed in this thesis: Plasma Enhanced Chemical Vapor Deposition (PECVD) and Atomic Layer Chemical Vapor Deposition (ALD).

2.2.1. Chemical Vapor Deposition (CVD)

Chemical Vapor Deposition was invented in the 1920s as a method for growing thin solid films of dielectrics and semiconductors on the surface of a heated substrate by mixing flows of reactive gases. Figure 18 sketches the principle of thermal CVD. Ideally, the reactant gases do not react together in the gas phase (i.e. undergo homogeneous reaction) because this causes the formation of particulates

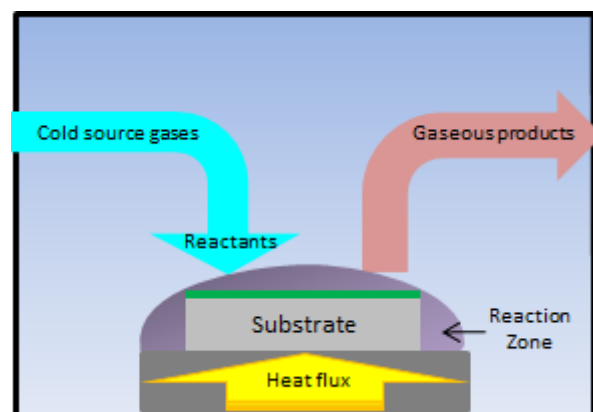


Figure 18: The principle of thermal CVD. [100]

that end up embedded in the growing film and affect its quality. The reactant gases should approach the heated surface and react with each other once they have impinged the surface to form a solid film of deposited material by a heterogeneous reaction [101].

A CVD process can be divided generally in seven steps (Figure 19). First step consists in the mass transport of the reactant gases to the surface on the substrate. Second step is homogeneous reactions that occur between reactant gases molecules as they are transported to the surface. Third step is the adsorption of the molecules to the surface. Fourth step is the diffusion of reactant molecules through the surface of the surface. Fifth step is nucleation and growth of film on the substrate as reactant molecules find each other and react on the surface. Sixth step is desorption of unreacted or produced gas molecules from the surface. Seventh step is evacuation of gaseous products by a vacuum pump from the reaction chamber [102].

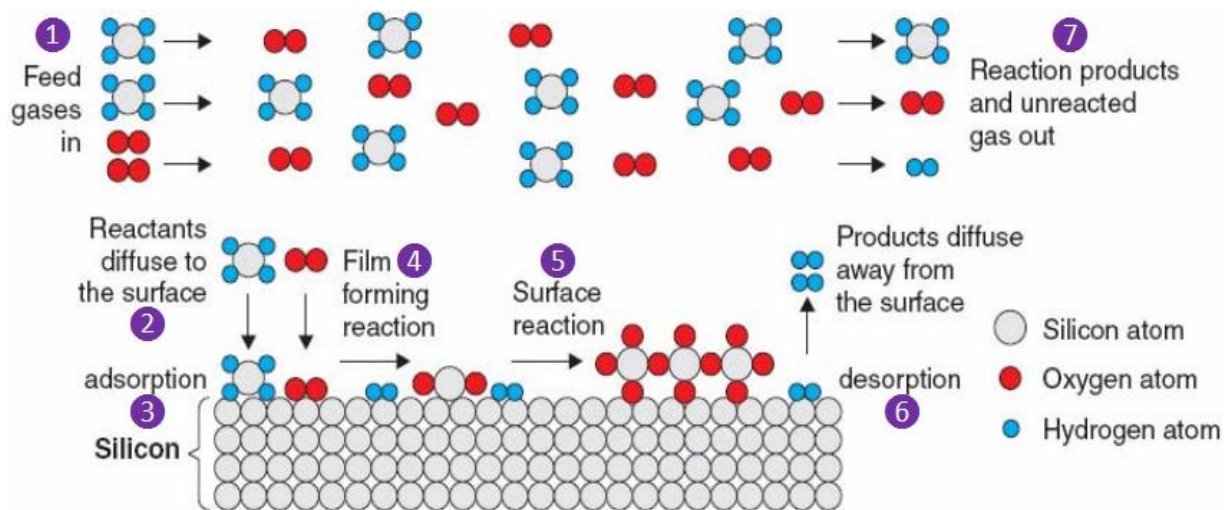
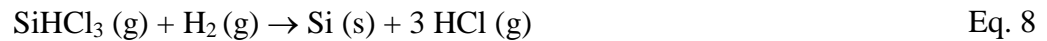
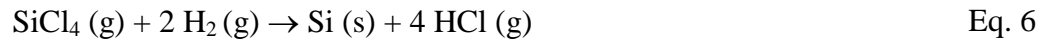


Figure 19: Steps of a CVD process where SiO₂ film is formed from SiH₄ and O₂. [102], [103]

The best reactant gases for a CVD process are usually the most reactive gases available because this allows high deposition rates at lower temperatures. For example, silicon was one of the first thin films to be deposited by thermal CVD because back then it was difficult to produce silicon substrates of high purity to build integrated circuits into them. Some of the reactant gases used to grow silicon films were:





The silicon film deposited by any of these four reactions can be single crystal, polycrystalline or amorphous, depending on the temperature of deposition. The plot of temperature versus film growth rate of these reactions is shown in Figure 20. Two different zones can be seen on each curve of Figure 20. The zone to the left of the curve (at higher temperatures) presents a line of smaller slope. This zone indicates the region where single crystal epitaxial films can be grown and is controlled by the mass transport of reactant gases to the surface. This means that the deposition rate is equal to the mass input rate into the reactor, which occurs at very high temperatures or pressures. The zone to the right of this region has a steeper slope and indicates a zone controlled by the kinetics of surface reactions and nucleation growth. This zone is favorable to grow amorphous or polycrystalline uniform films on substrates of complex topography [102].

It can be seen as well in Figure 20 that for a given temperature the highest and lowest growth rates are respectively obtained with SiH_4 and SiCl_4 . This is because the silicon tetrachloride molecule (SiCl_4) is the most stable of the four silicon precursors. Conversely, the silane molecule (SiH_4) is the least stable of the four [101].

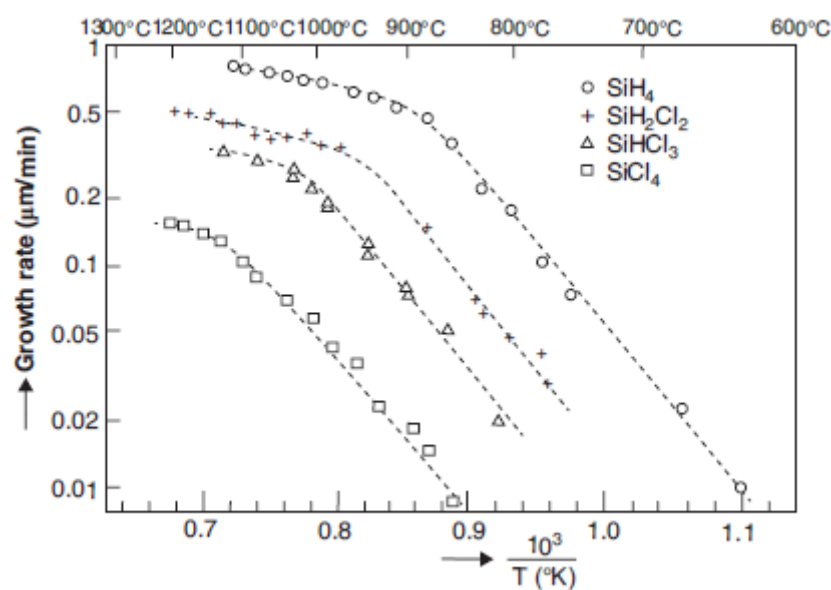


Figure 20: Deposition rate of silicon films as a function of temperature and precursor. [101]

Although the silane precursor allows depositing silicon films at lower temperatures and higher growth rates, the deposited films have poorer quality compared to those produced with the silicon tetrachloride precursor. This is because gas phase homogeneous reactions are also more likely to occur when silane is used as precursor. For this reason, silicon tetrachloride is preferred as the precursor of silicon films for most commercial applications of thermal CVD [101].

Besides quality, another important criterion for commercial applications of thermally activated CVD is temperature of deposition, which usually is inversely proportional to the film growth rate. As the substrate's surface has to be heated sufficiently enough to produce acceptable deposition rates of $>0.1 \mu\text{m}/\text{min}$ for commercial applications, temperatures $>800^\circ\text{C}$ are typically employed to obtain films of good quality with acceptable deposition rates. However, the high temperature needed to deposit dielectric films of good quality by thermal CVD limits its application in the field of packaging of electronics, where processes must be performed at temperatures lower than 400°C to prevent damaging the finished microelectronic device [64]. Research on ways to deposit films of good quality at temperatures lower than 400°C led to the development of plasma assisted CVD. Glow and plasma discharges can be used in some CVD reactions to produce thin films of good quality at relatively low temperatures.

Plasma Enhanced Chemical Vapor Deposition (PECVD)

Besides the nature of gas precursors, one way to reduce the temperature of deposition without compromising the quality of the film is to use plasma discharges to create highly reactive ionized species (free radicals) that react rapidly on the heated surface to produce the desired film (Figure 21). This is why this type of CVD is called plasma assisted or plasma enhanced. PECVD allows depositing polycrystalline or amorphous thin films of high quality at temperatures lower than 400°C . Another advantage is that mechanical properties of the film (e.g. mechanical stress) can be tailored by controlling the ion bombardment with the substrate bias voltage [102].

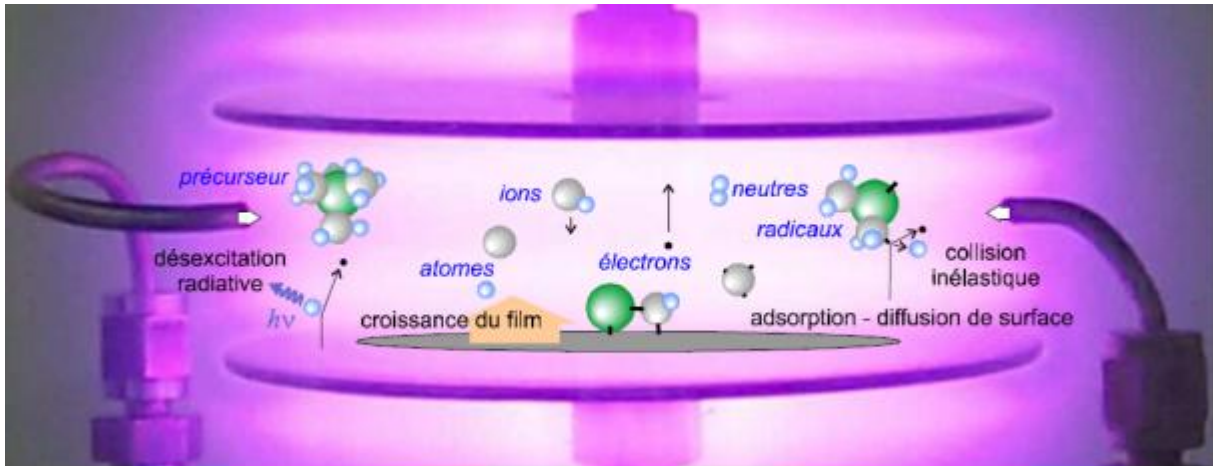


Figure 21: Chemical vapor deposition process assisted by plasma discharge, a.k.a. PECVD.

The reaction steps are the same to those for thermal CVD. The difference is that ionized chemical species allow lower deposition temperatures to be used. There are several issues to consider when plasma discharges are used to activate gaseous reactions. Reactive radicals created from the reactant gases do react more easily than their neutral precursors, but ions and hot electrons are also created in the process. They can impinge on the substrate and have positive and negative effects on the deposited film and substrate's surface. Ion bombardment typically causes compressive stress (Figure 22), which may densify the film and reduce the probability of cracking. But it can also produce charge defects in the film that lead to lower dielectric breakdown voltage [101]. Very large stress in films can lead to cracking and crazing, bowing of thin substrates, non-uniformity of phases and film/substrate separation [104]. Films of Cr, Ni, Ag, stainless steel, Cu and Al have typically tensile stress, whereas films of Nb, Ti, Zr and Hf have compressive stress. These differences are exploited to deposit dielectric multi-layer films with nearly zero net stress [105].

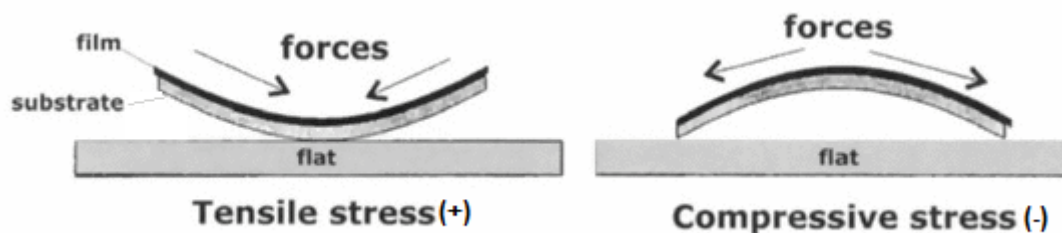


Figure 22: Stress deformation of thin films. [104]

The frequency of the electric field used to activate the plasma can greatly influence its properties. Frequencies of >80 MHz increase greatly the deposition rate but the film uniformity is affected when the size of topographic features reach one quarter wavelength.

To summarize, PECVD creates a mixture of ionized chemical species that does not exist in thermally activated CVD. This may lead to positive outcomes, but also negative ones. Some of the disadvantages of PECVD are [101]:

1. Film chemistry is not always easy to control.
2. Film density may be low compared to other techniques like thermal CVD.
3. Film conformality is poor.
4. Plasma uniformity, and hence film uniformity, are hard to achieve.

2.2.2. Atomic Layer Deposition (ALD)

Atomic layer deposition (ALD) is another variation of the family of CVD techniques. It was developed in the 1970s in Finland for electroluminescent flat panel displays from a technique called “atomic layer epitaxy”. Its Finnish inventor, Tuomo Suntola, created the technique in June 1974 and described the event as follows: “We had still an empty laboratory with just tables and chairs and a Periodic Table of the Elements hanging on the wall. Looking at the Periodic Table, and thinking of the overall symmetry in nature, to me came the idea of “serving” the complementary elements of a compound sequentially, one at a time, onto a surface. Monoatomic layers may be obtained if the complementary elements make a stronger bond with each other than they do with their own kind of atoms” [106].

In other words, ALD is a thin film growth technique based on sequential self-limiting surface reactions in which two complementary reactant vapors are supplied to a surface in alternating pulses. These reactions are self-limiting because only a certain amount of reactant vapor can be chemisorbed on the surface of the substrate for each pulse. As result, the film is grown one atomic layer at the time, and the technique is called Atomic Layer Deposition [101].

Suntola used initially elemental species (e.g., Ga and P), and exposed them sequentially to a heated surface to form a monolayer of the desired solid thin film. A vacuum pump was used to evacuate the chamber after each pulse of elemental species, and the cycle was repeated many times until reaching the desired thickness. The principle of this process is illustrated in Figure 23.

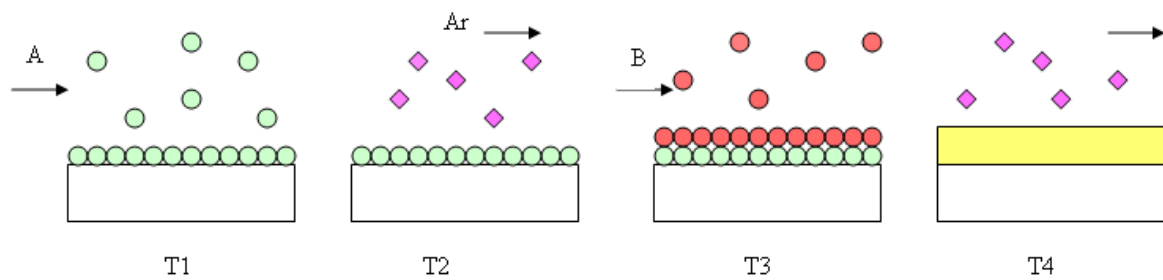


Figure 23: Scheme of the principle of ALD to form an atomic monolayer of the desired film.

Where T1: introduction of precursor A that is chemically adsorbed until saturation of surface.

T2: Purge with inert gas (argon).

T3: Introduction of precursor B that reacts with A to form one monolayer of film.

T4: Purge with inert gas (argon).

This way of growing thin films from elemental species is known as direct ALD. Later, Suntola suggested the same process could be performed using elemental compounds of elevated vapor pressures, such as halogen molecular species (e.g. TiCl_4 , AlCl_3) or organometallic compounds (e.g. trimethyl-aluminum or TMA).

As a chemical reaction between complementary elements/compounds is involved, the surface temperature is an important parameter. The concept of “temperature window” was introduced to explain the relationship between deposition rate and surface temperature (Figure 24).

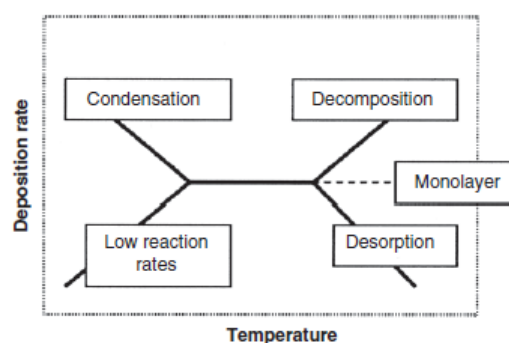


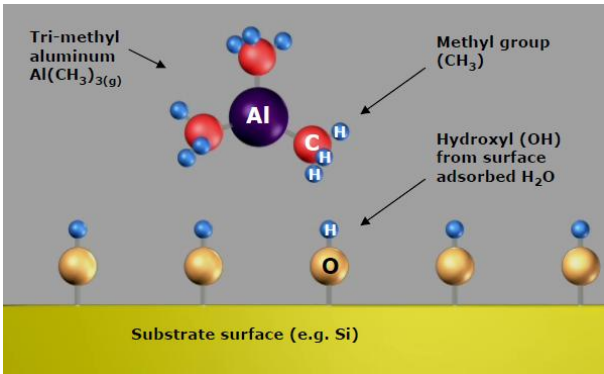
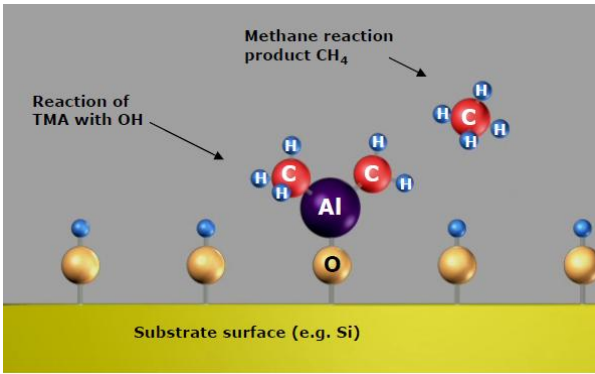
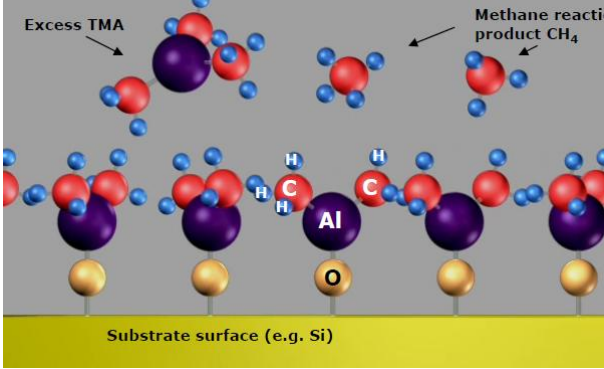
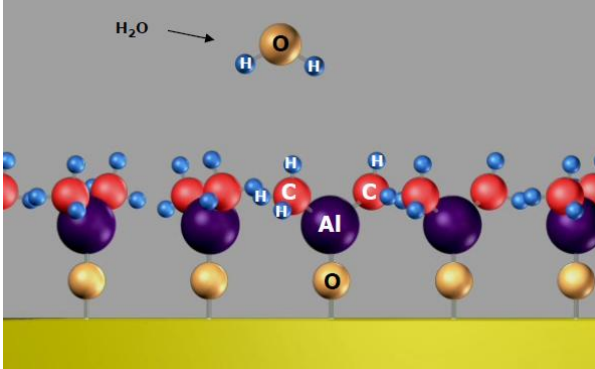
Figure 24: Temperature window for ALD. [101]

If the substrate temperature is very high, precursor A may decompose or desorb from the surface before having time to react. If temperature is too low, more than one layer may be

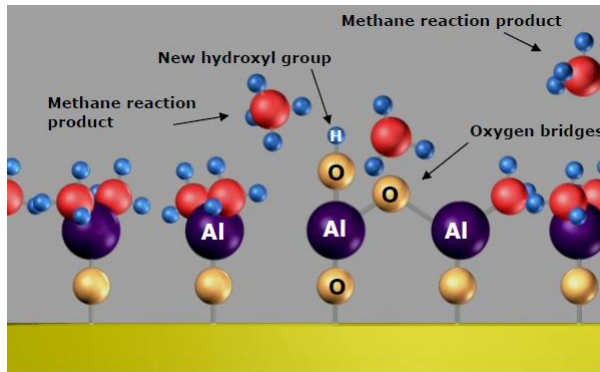
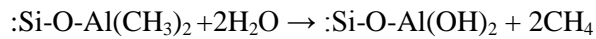
deposited on the surface (i.e. Condensation) or the reaction time may be too long to complete one monolayer.

As in the case of CVD, deposition temperatures can be lowered by using the most reactive gaseous reactants. For example, alumina thin films of good quality can be grown from TMA and water vapor at temperatures of 200°C. This process is described in Table 6. Although it is possible to grow alumina films at lower temperatures with some surge of carbon impurities due to incorporation of methane, the limiting step becomes the desorption rate of excess water molecules from the surface (step 6 of Table 6). Purge times of water of less than 1 s at 200°C can increase to 180 s at 33°C [107]. However, shorter purge times can be maintained down to room temperature by using more reactive oxidizing agents (e.g. ozone or oxygen radicals produced by plasma — see Top of Table 4) [101].

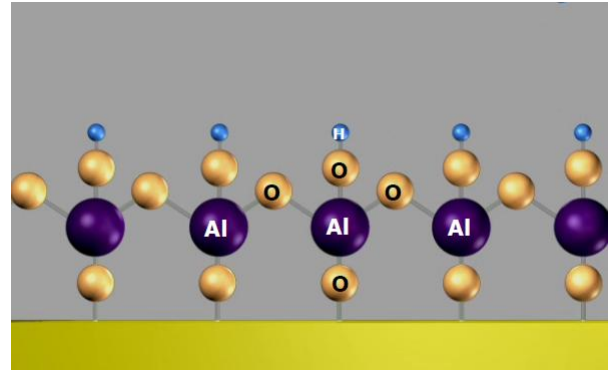
Table 6: Steps of ALD process between TMA and H₂O on top a silicon wafer. [108]

<p>1. Mass transport of TMA to wafer surface containing hydroxyl groups Si-O-H</p>  <p>Substrate surface (e.g. Si)</p>	<p>2. Reaction of TMA with substrate: $\text{Al}(\text{CH}_3)_3 + \text{:Si-OH} \rightarrow \text{:Si-O-Al}(\text{CH}_3)_2 + \text{CH}_4$</p>  <p>Substrate surface (e.g. Si)</p>
<p>3. TMA reacts with hydroxyl groups until surface is passivated. It does not react with itself, terminating the reaction at one layer.</p>  <p>Substrate surface (e.g. Si)</p>	<p>4. TMA and gaseous products are pumped away with inert gas (e.g. argon), and water molecules are pulsed into the chamber.</p> 

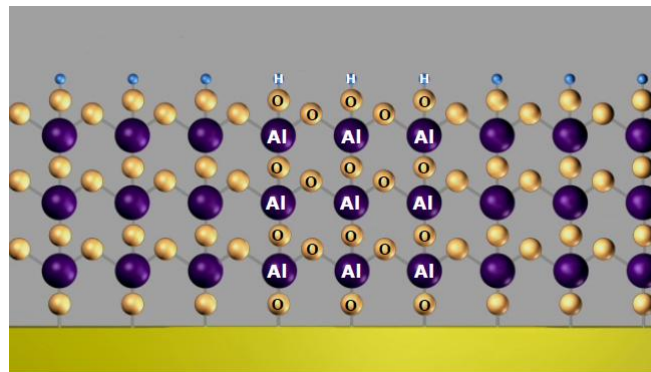
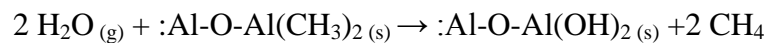
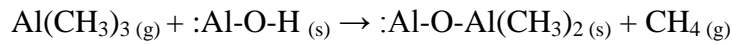
5. Creation of new hydroxyl groups by water:



6. Reaction products like methane and excess water are pumped away with inert gas.



7. Process is repeated for several cycles. Each cycle requires one pulse of TMA and one pulse of H₂O, and purging with argon in-between pulses. Two reaction steps occur in each cycle:



The time necessary for one cycle of ALD is $t = T_1 + T_2 + T_3 + T_4$ (Figure 23) and takes usually from 3 to 300 sec. This time per cycle depends on various factors like temperature, pressure, substrate geometry, and frequency and nature of plasma discharges. For example, it takes us 150 deposition cycles to form a film of 20 nm Al₂O₃ by thermal ALD at 200°C with TMA and H₂O as precursors, which amounts to roughly 60 min or 0.33 nm/min. This is relatively fast compared with other ALD films such as TiO₂, which requires little more than four hours depositing 20 nm at 200°C. This equals ~0.1 nm/min.

Low deposition rates of ALD (in comparison with CVD techniques of ~0.1 μm/min) have limited its commercial usage to devices of high added value. For example, high-k thin films like HfO₂ for transistors <45 nm made by Intel© and Passive Integrated Connected Substrates like super capacitors by IPDIA©.

Table 7 compares various thin film deposition techniques. It can be seen that ALD and CVD techniques are better suited for the deposition of highly conformal (step coverage) and dense packaging films, which are properties necessary for medical micro devices.

Table 7: Comparison of deposition methods of thin films.[109]

Method	ALD	MBE	CVD	Sputtering	Evaporation	PLD
Thickness Uniformity	good	fair	good	good	fair	fair
Film Density	good	good	good	good	poor	good
Step Coverage	good	poor	varies	poor	poor	poor
Interface Quality	good	good	varies	poor	good	varies
Number of Materials	fair	good	poor	good	fair	poor
Low Temp. Deposition	good	good	varies	good	good	good
Deposition Rate	fair	poor	good	good	good	good
Industrial Applicability	good	fair	good	good	good	poor

MBE = molecular beam epitaxy, PLD = pulsed laser deposition.

Though ALD produces thin films of high density and excellent conformality at relatively low temperatures (<300°C), maximum one atomic layer of <0.1 nm is deposited per cycle [101]. As one deposition cycle lasts 30–300 seconds in standard ALD reactors, it takes 4–40 hours to deposit a coating of 50 nm.

Although it is impractical to grow films larger than 50 nm this way, it is been reported that the best protection of substrates sensitive to moisture is provided by thicker ALD films [110], [111]. Some state of the art reactors called spatial ALD systems can complete one deposition cycle in ~1 second, greatly reducing the time needed to deposit ALD films of >50 nm [112]. It is expected that these new machines will render more attractive ALD for various industrial applications such as Organic Solar Cells and OLEDs where thicker ALD films are desirable for atmospheric protection of delicate electronic devices [113].

However, ALD films may appear amorphous and turn to crystalline after a given thickness [97]. Crystalline layers are undesirable for packaging applications because the interfaces between crystals serve as weak points for infiltration of saline water and subsequent corrosion of the underlying substrate. Besides, delamination from substrate is worse for ALD films thicker than 50 nm [97], [110]. And delamination of coatings from medical devices is a recurrent point of failure in present packaging technologies [114], [115].

Hence, a good balance between high density, high deposition rates, low content of crystals and good adhesion on substrate is needed to achieve effective barrier coatings deposited by ALD for corrosion protection of IEDs.

Results

2.3. Selected Materials

Taking into consideration the points made throughout this chapter, ten materials were selected to deposit by ALD or PECVD (Table 8). Films were deposited by either Atomic Layer Deposition (ALD) in a Fiji F200 machine from Cambridge Nanotech Inc. or by Plasma-enhanced Chemical Vapor Deposition (PECVD) in a Centura 5200 from Applied Materials Inc. Fabrication details can be found elsewhere [71]–[73], [95], [96], [116]. Film thicknesses were chosen smaller than 100 nm in most cases to facilitate characterization of films by spectroscopy techniques and shorten the time needed for corrosion protection tests. Deposition temperatures were chosen inferior to 400°C to be compatible with packaging of Integrated Circuits based on CMOS technology.

Table 8: Selected materials deposited by PECVD or ALD.

Material	Width (nm)	Fabrication	Precursors	Temp. (°C)
Al ₂ O ₃	10–40	ALD	Al ₂ Me ₆ , H ₂ O	90–250
HfO ₂	10–40	ALD	HfCl ₄ , Hf(NMe ₂) ₄ , H ₂ O	200–300
TiO ₂	10–40	ALD	Ti(NMe ₂) ₄ , H ₂ O	100–250
ZnO	10–40	ALD	Zn(C ₂ H ₅) ₂ , H ₂ O	250
SiN	100–500	PECVD	SiH ₄ , NH ₃ , N ₂	400
SiO ₂	100–500	PECVD	SiH ₄ , N ₂ O	400
SiOC	100–500	PECVD	SiMe ₄ , O ₂ , He	400
SiC	100–500	PECVD	SiMe ₄ , He	350
DLC (a-CH [*])	100–500	PECVD	C ₃ H ₆ , He	400
BN	50–100	PECVD	B ₂ H ₆ , NH ₃ , N ₂	400

* Amorphous Hydrogenated Carbon films (50% C, 50% H), a type of DLC films.

Coupons with deposited films were kept inside a nitrogen chamber until measurements or tests were performed.

Chapter 3: Characterization and Evaluation of Materials

This chapter deals on the characterization of deposited materials and the impact of their morphological properties on their performance as barrier films for the encapsulation of silicon devices. First half contains the different analytic techniques employed to characterize the surface and bulk structure of deposited materials. The latter half of this chapter concerns the evaluation of films in light of several requirements such as biocompatibility, chemical stability, biostability and impermeability.

As there were many candidate packaging layers, a screening method for selecting the best packaging layer was implemented on coupons. Our screening methodology consisted of evaluating selected packaging layers by:

- (1) Biodegradation and accelerated aging tests in a saline solution that simulates the service environment of blood serum.
- (2) Helium gas permeability measurements to evaluate the hermeticity of the packaging layers to external gases like moisture.
- (3) Cytotoxicity and morphology tests to validate the biocompatibility of deposited films.
- (4) Diffusion barrier tests to assess the effectiveness of the selected films to stop toxic/corrosive substances from escaping/entering the device.

3.1. Characterization of materials

Thin films of 10–500 nm of encapsulant materials selected in Chapter 2 (page 65) were deposited as full sheet layers on 200 mm polished Si(100) p-type wafers supplied by MEMC Korea Company©. Unless specified in this manuscript, deposition temperatures of packaging films are those given in page 65 and 250°C for films of Al₂O₃, HfO₂ and TiO₂.

Coupons of size 2.0x1.5 cm² were diced from coated wafers. The surface of each coupon was 3.0 cm², which was judged a convenient size for the tests of cytotoxicity, biodegradation and accelerated aging.

Adhesion of films on silicon coupons was evaluated as excellent according to the cross-cut test method ISO 2409:2013 [33]. Results for silicon coupons coated with a film of 100 nm SiC and 20 nm ZnO are shown in Figure 25. It can be seen that 0% of film area was removed after applying and removing the scotch tape from the cross pattern. Similar results were obtained for other films listed on page 65.

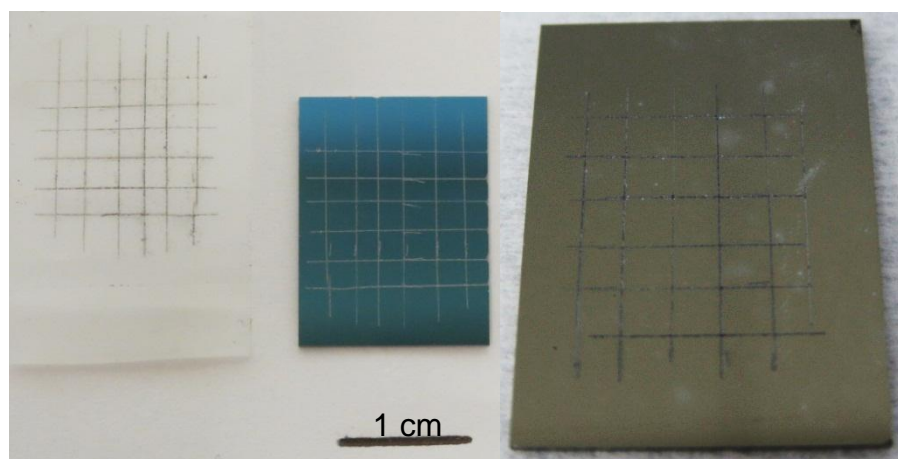


Figure 25: Adhesion test by cross-cut test method of silicon coupons coated with 100 nm SiC (Left) and 20 nm ZnO (Right).

Coupons were cleaned prior to characterization by rinsing them with 18.2 M Ω •cm De-Ionized (DI) water, followed by acetone, isopropyl alcohol and DI water. A nitrogen blow gun was used to dry the coupons before being dehydrated on a hot plate at 125°C for 15 minutes.

Deposited films on coupons were then characterized by Atomic Force Microscopy (AFM) for surface roughness; X-Ray Diffraction (XRD) for the crystalline structure; X-Ray Reflectometry (XRR) for the film density; X-ray Photo-electron Spectroscopy (XPS) for the chemical composition of the surface; Variable Angle Spectroscopy Ellipsometry (VASE) for the refractive index and film thickness.

These measurements help to elucidate the chemical composition, uniformity, roughness, density, thickness and optical properties of deposited films. This information will be useful in correlating the results obtained from the evaluation tests (cytotoxicity, accelerated aging, gas permeability) with the material properties of films.

Due to the large number of characterization techniques, results and discussion of each technique are given just after the explanation of its principle and experimental method.

3.1.1. AFM

Atomic Force Microscopy (AFM) is a type of Scanning Probe Microscopy to measure the topography of solid materials with sub-nanometer resolution. It is possible to measure the hardness and roughness of a sample surface with the help of a mechanical probe coupled to a beam laser reflected on the reverse side of the cantilever (Figure 26). The cantilever has a nanometer probe that displaces up and down the Z-axis as it is swiped across the sample. The reflection of the laser beam on the back of the cantilever follows these oscillations along the vertical axis, which are collected by a photodiode detector and analyzed by a computer.

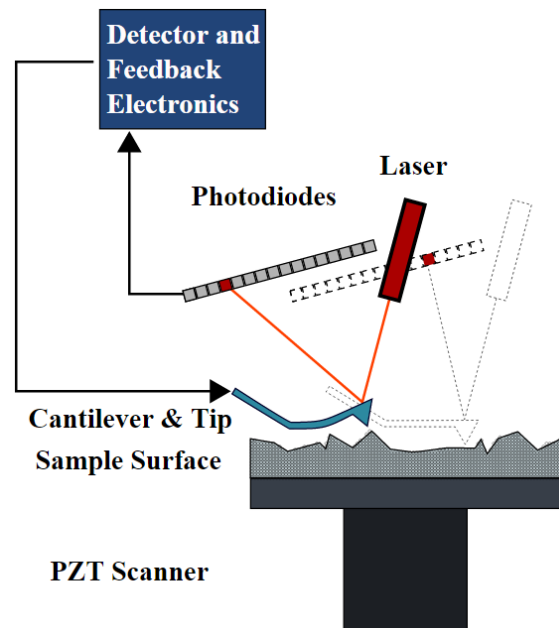


Figure 26: Schematic setup of AFM using laser beam deflection detection.

AFM measurements were performed inside a Bruker Dimension Icon Glovebox®, which provided acoustic and atmospheric isolation inside a non-reactive environment of <1 ppm moisture and oxygen content. A tip of BudgetSensors© model Tap300Al was employed in the cantilever. Data treatment and analysis were carried out in a machine of Nanoscope Analysis©. A scan area of $5 \times 5 \mu\text{m}^2$ was measured.

The topography and Root Mean Squared Roughness (Rq) of various encapsulant thin films is shown in Figure 27. The roughness of crystalline silicon wafers was 0.26 nm. Deposited films of Al_2O_3 , BN, a-CH, SiOC and TiO_2 are uniform and conformal to the silicon substrate as demonstrated by Rq values <1 nm. The Rq of HfO_2 is also smaller than 1 nm, but some protuberances are visible on its surface. This may be due to non-conformal growth of the film, or contamination particles present on the sample at the time of measurement. The former case seems more plausible. Films of SiC, SiO_2 , SiN and ZnO have root mean squared roughness (Rq) values >1 nm, indicating they are not as uniform as the former films.

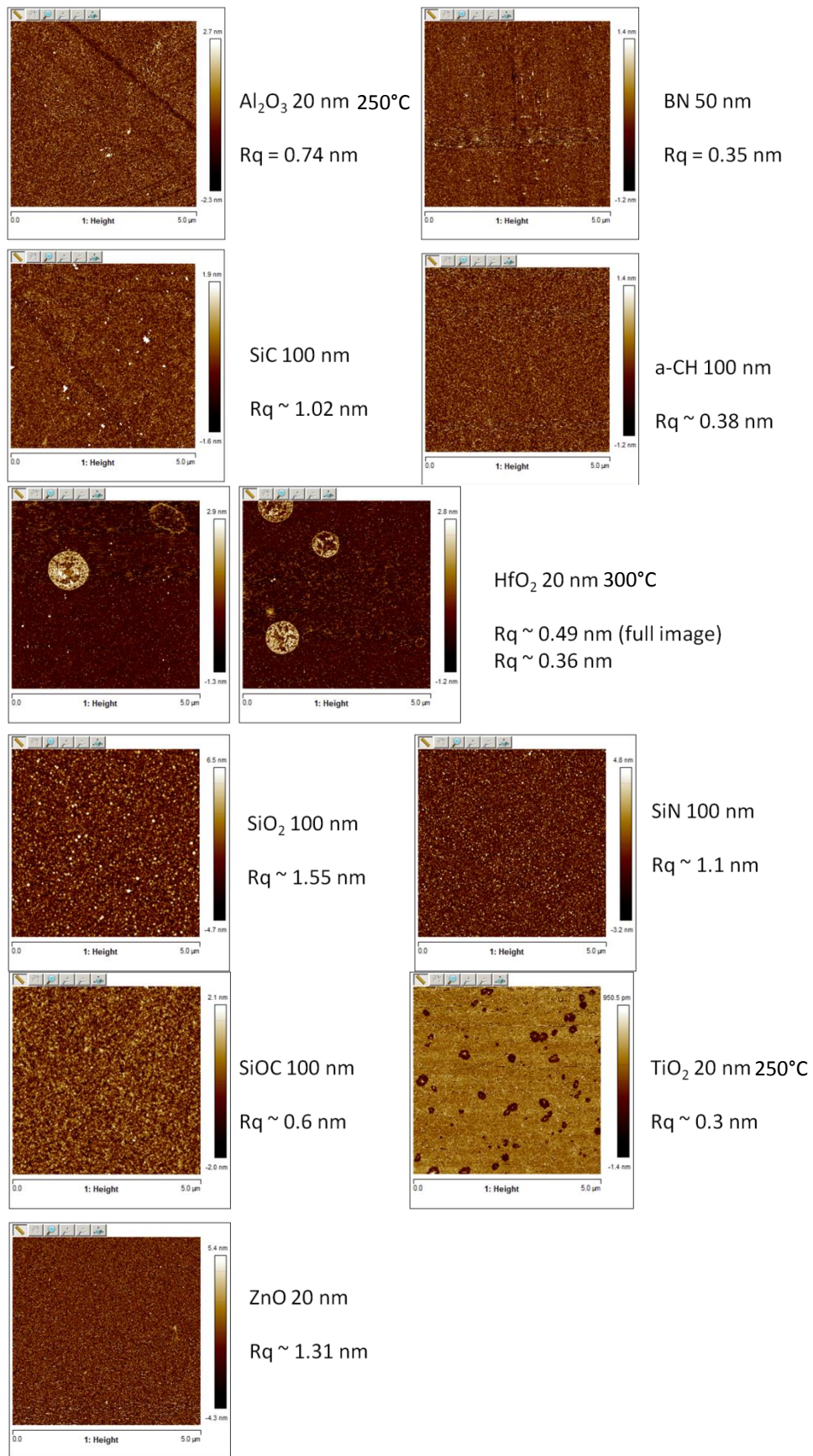


Figure 27: Topography of various deposited thin films as measured by AFM.

3.1.2. XRD

X-Ray Diffraction (XRD) crystallography is employed to characterize the crystalline structure of materials. The crystalline atoms of the analyzed material cause the diffraction of incident X-rays in specific directions. The angles and intensities of the diffracted x-rays beams are then mathematically analyzed to reconstruct the three-dimensional distribution of electrons and atoms within crystals. If the material is not crystalline, there are not specific peaks present in a diagram of diffracted angle versus intensity.

XRD measurements were analyzed by Grazing Incidence X-ray Diffractometry in a Bruker D5000®, with angle of incidence 2° and Co K_α radiation. Results are shown in Figure 28. The small and wide peak around 70° present in all patterns corresponds to the crystalline silicon substrate (100). Most patterns given in Figure 28 have no characteristic Bragg peaks, indicating that the deposited films are X-ray amorphous. The exception is ZnO film. The deposited ZnO film has the wurtzite crystalline structure, a type of non-centrosymmetric hexagonal crystal system where each atom is tetrahedrally coordinated. The surface of measured samples was 3 cm^2 . The Bruker D5000® XRD machine employed for the measurements works better with samples of $>4 \text{ cm}^2$. This is why there are some small peaks in Figure 28 due to background noise introduced by the substrate holder.

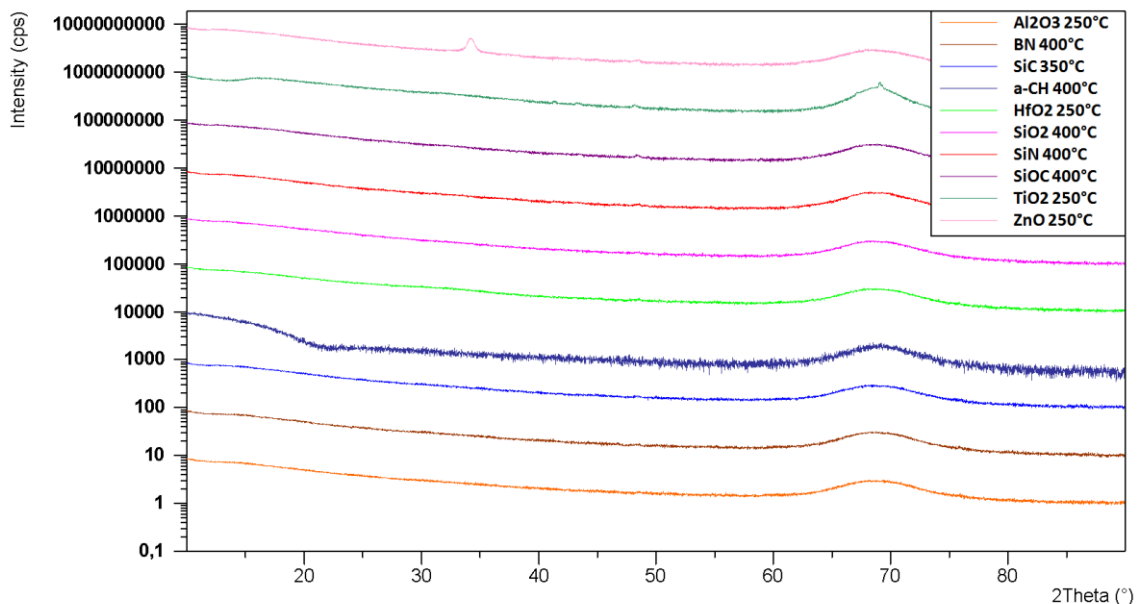


Figure 28: Graph of intensity versus diffracted direction of incident X-rays for various thin films deposited on silicon substrates.

3.1.3. XRR

X-ray Reflectometry (XRR) measures the reflectance of a sample as function of the grazing incidence angle of X-rays. The scan obtained is fitted according to the Fresnel equations to find the density, thickness and roughness of the measured film. One example of a germanium thin film deposited on silicon can be seen in Figure 29. The slope of the figure can be fitted to find the roughness at the bottom of the film. The period of the oscillations is equal 2π divided by the film thickness. And the amplitude of the oscillations provides information about the difference in density between the film and the substrate [117].

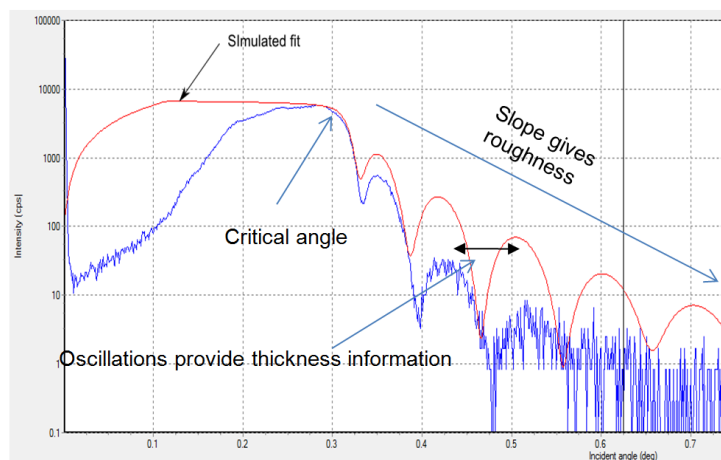


Figure 29: XRR scan of a germanium thin film on silicon substrate [117].

A Bruker D8FABLINE® machine was employed for XRR measurements of deposited films. Cu K α radiation of 8.05 keV was used. Experimental errors of $\pm 5\%$ can be expected for density, thickness and roughness estimations obtained from fitting the XRR scans. Table 9 resumes the results of density, roughness and thickness obtained by fitting XRR scans of various deposited films.

Thickness values were similar to those obtained by spectroscopic ellipsometry for equivalent films. Roughness estimations are consistent with those obtained by AFM within a margin of error of 0.5 nm. The exception to this was SiC film that has a roughness value of 3.5 nm, which is quite different from the roughness of 1.0 nm obtained by AFM. This is because AFM measures the upper roughness of deposited films, whereas XRR estimates the roughness of the lower part of the film, at its interface with the substrate. As films were deposited on a 2–3

nm film of native silicon oxide, this difference suggests a rough interface between the SiC film and silicon oxide. The opposite case is the film of SiO₂ that has No value of roughness Assigned (N/A), indicating a smooth interface with the substrate.

Table 9: Density, thickness and roughness of various thin films measured by XRR.

Film	Thickness (nm)	Density (g/cm ³)	Roughness (nm)
HfO ₂ 250°C	18.0	9.8	0.3
ZnO 250°C	22.1	5.3	1.8
TiO ₂ 250°C	16.2	4.3	0.5
TiO ₂ 200°C	22.0	3.9	0.7
TiO ₂ 100°C	20.1	3.7	0.6
Al ₂ O ₃ 250°C	23.9	3.1	0.5
SiN 400°C	99.0	2.5	0.8
SiOC 400°C	450	2.1–2.3	-
SiO ₂ 400°C	103.2	2.2	N/A
BN 400°C	89.8	1.5–1.7	0.7
SiC 350°C	100.4	1.4	3.5
DLC 400°C	500	1.2–1.4	-

Films of HfO₂, ZnO, TiO₂ and Al₂O₃ deposited by ALD have the highest densities among measured films. They are thus better candidates for the hermetic packaging of electronic devices, provided they are chemically stable in harsh environments.

As TiO₂ is a material well known for being biocompatible, dense and conformal [77], TiO₂ samples deposited at three different temperatures were measured by XRR to determine if there was a significant decrease of film density at lower temperatures. The best deposition temperature for TiO₂ in terms of density (compared to a theoretical value of 4.3 g/cm³ [118]) is between 200 and 250°C.

Measured densities for SiN, SiO₂ and SiC films deposited by PECVD are consistent with values reported in the literature for similar recipes [64], [119, p. 745]. They are overall lower than densities measured for ALD films.

It was not possible to fit precisely the XRR scans of SiOC, BN and DLC (a-CH) films. SiOC film density was very close to that of silicon (2.33 g/cm^3) and the two materials were not completely dissociated. BN and DLC films had a gradient of density along the Z-axis perpendicular to the substrate's surface. BN film density was between 1.5 and 1.7 g/cm^3 , and DLC film density was between 1.2 and 1.4 g/cm^3 .

Transmission electron microscopy (TEM) images confirmed DLC films have a gradient of density (Figure 30). The zone closer to the interface with air has a higher density and therefore a darker color in the TEM pictures, suggesting its density is higher and probably 1.4 g/cm^3 . It can be seen as well in Figure 30 an irregular line present between the zone close to the surface and bulk DLC. This is expected from a DLC film containing unsaturated sp^2 carbon bonds that were oxidized by adsorption of oxygen [120]–[123].

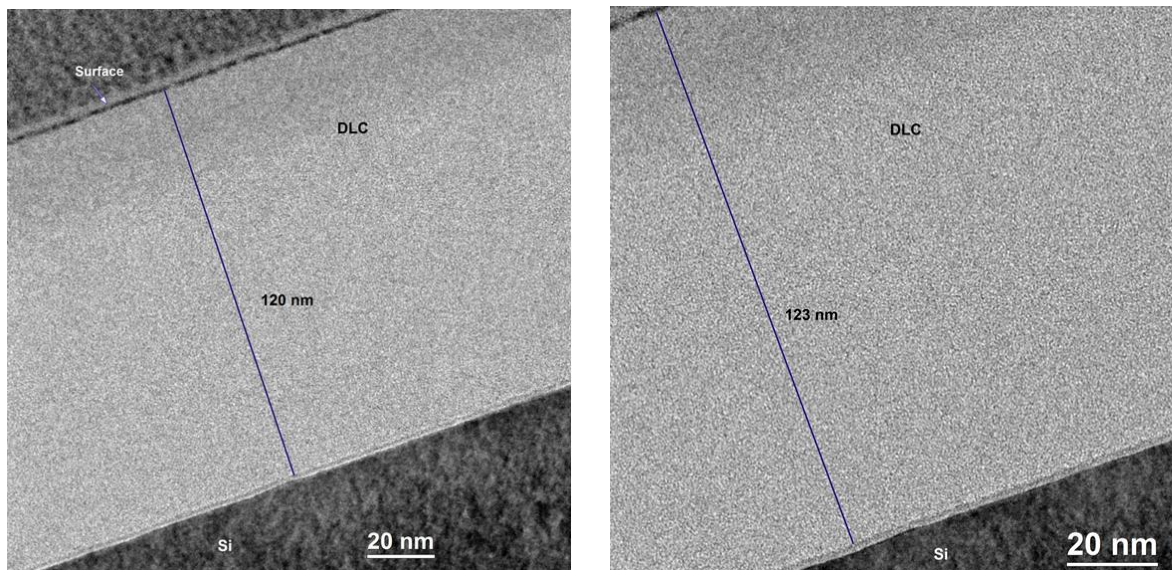


Figure 30: TEM images of a-CH film deposited on silicon.

3.1.4. XPS

X-ray induced Photoelectron Spectrum (XPS) analysis is a quantitative spectroscopic technique for studying the surface chemistry of a material. It is capable of measuring the elemental composition, empirical formula, chemical state and electronic state of the elements within a material. In XPS, photoelectron spectra are acquired by irradiating the material surface with a beam of high energy photons or x-rays and measuring the kinetic energy of the photo-electrons liberated from the sample's upper layers. As the mean free path of electrons in solids is few nanometers, detected photoelectrons belong to the first 10 atomic layers of the surface in most materials and as result the technique is called surface sensitive. The data obtained from the photoelectrons is presented as a graph of intensity (units: counts per second) versus electron energy (units: eV). This graph is called the X-ray induced Photoelectron Spectrum (XPS) and contains various peaks in different locations representing the Binding Energy (BE) and chemical state of released electrons. The energies and intensities of the photoelectron peaks allow the identification and quantification of all elements (except for hydrogen) and molecules present on the material's surface [124].

XPS measurements were performed with $K\alpha$ radiation of Aluminum (monochromatic, excitation 1486.6 eV, spot size 100 μm) at a collection angle of 45° relative to the surface normal vector, giving a penetration depth of 6.7 nm in a SiO_2 reference. 63% of the intensity was emitted below 3 nm. The energetic resolution of high resolution spectra is 0.5 eV.

XPS spectra of thin films of Table 9 were taken before any tests (initial), after sterilization with ethylene oxide (EtO) and after soaking for 27 days in saline solution (9 g/L NaCl) supplemented with 10% volume of Fetal Bovine Serum (NaCl/FBS, see page 100 for details).

Al₂O₃

From the initial general XPS of Al₂O₃ 250°C (Figure 31), it can be seen there is contamination of its surface with carbon atoms (C1s 17.8%) and some traces of silicon (Si2p <0.1%). The concentration of oxygen atoms (O1s 59.0%) includes also atoms arising from atmospheric contamination. The ratio Al/O is smaller than 2:3 not only as consequence of adventitious carbon atoms arising from natural contamination, but also due to incorporation of methane (CH₄) and flaking of organic contaminants in the ALD chamber [101]. HiRes XPS (Figure 32) confirmed that carbon 1s binding energies come mainly from organic molecules type (-CH₂CH(OH)-)_n [125], which is consistent with incorporation of methane in the film during deposition. A film density lower than the value for pure Al₂O₃ (3.95 g/cm³) is expected. The ratio Al/O was not affected by sterilization with ethylene oxide (Figure 32), however Al₂O₃ film disappeared after 27 days of biodegradation tests in NaCl/FBS (page 104).

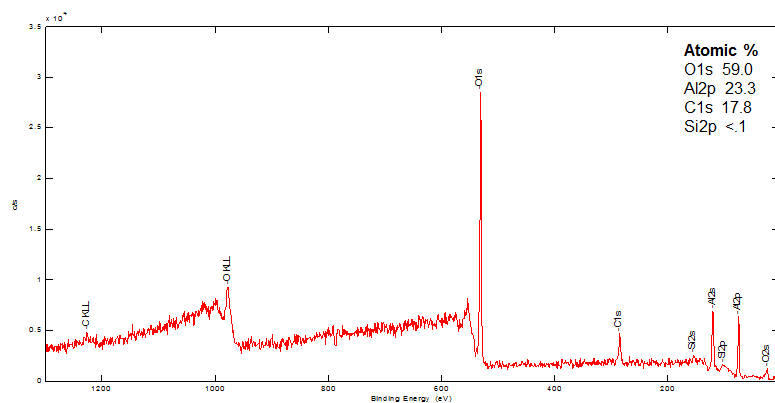


Figure 31: General XPS of 20 nm Al₂O₃ 250°C on silicon substrate.

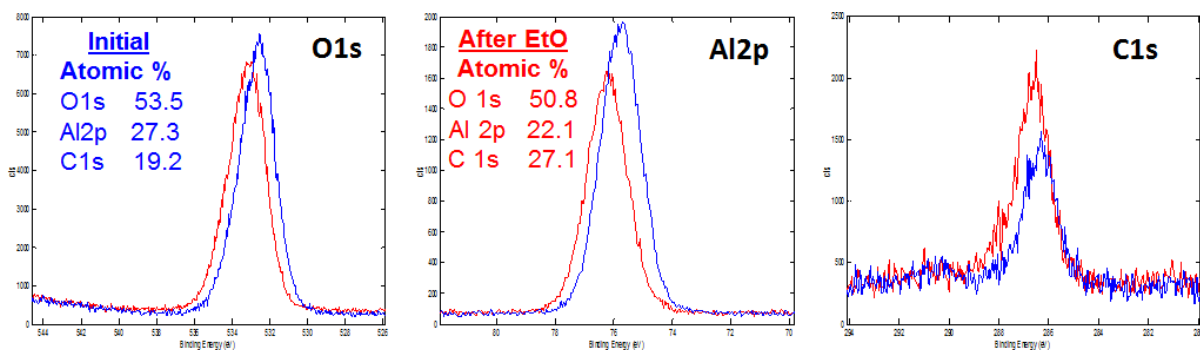


Figure 32: High resolution XPS of 20 nm Al₂O₃ 250°C on silicon substrate.

BN

The initial general XPS of BN 400°C (Figure 33) shows a relatively high content of carbon (C1s 27.4%) and oxygen (O1s 16.6%) atoms are present on the surface. The ratio of B/N is far below 1:1 stoichiometry. High resolution spectra (Figure 34) confirmed that the surface is oxidized (B-Ox) and sterilization with EtO did not change the stoichiometry of the film. High resolution spectra of N1s show that N atoms have two chemical states: bonded to boron (B-N) and oxide groups (N-Ox). The N-Ox is shifted to higher binding energies, indicating there is probably an upper layer of B-Ox and below it a layer of N-Ox that interfaces with a lower layer of B-N. XPS results after NaCl/FBS indicate that BN is not stable in such medium.

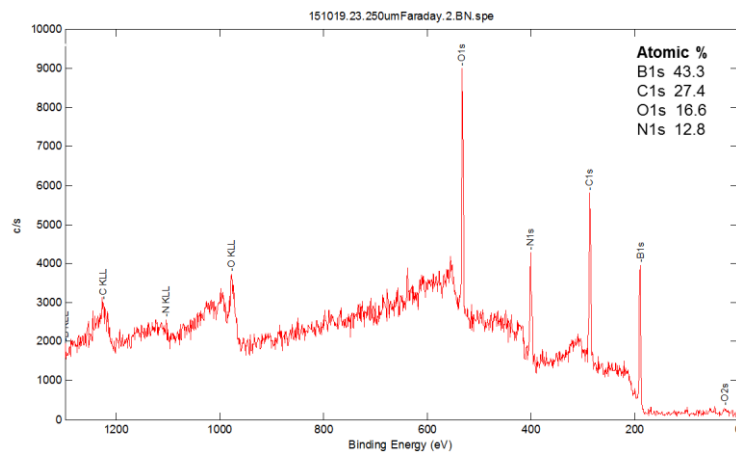


Figure 33: General XPS of 50 nm BN 400°C on silicon substrate.

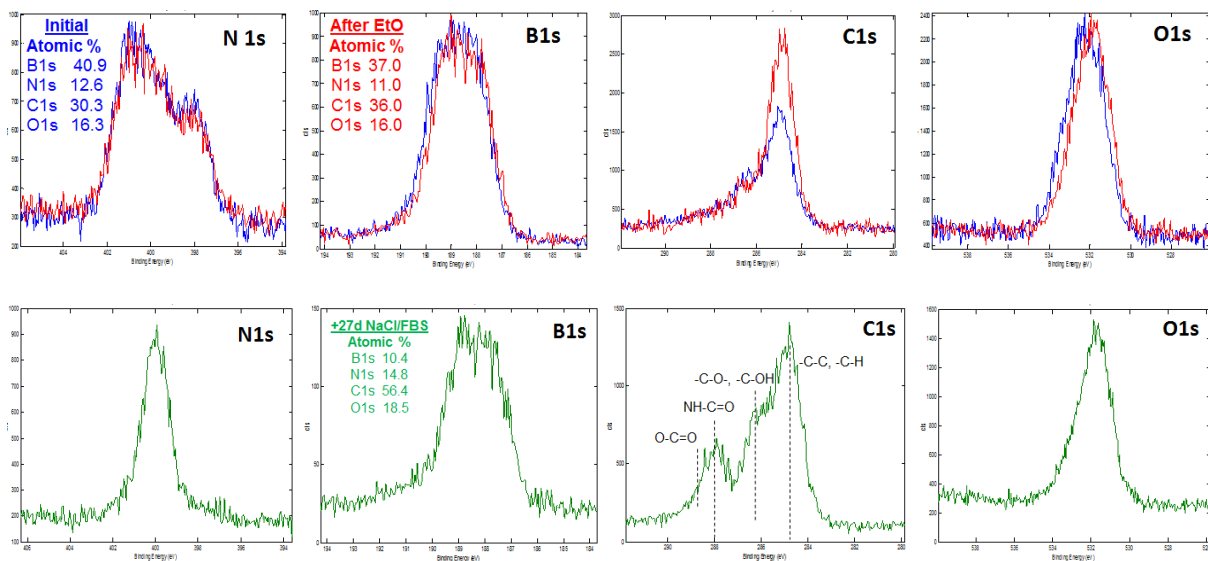


Figure 34: High resolution XPS of 50 nm BN 400°C on silicon substrate.

SiC

General XPS of 100 nm SiC 350°C (Figure 35) shows there is oxidation of the surface (O1s 16.6%) and presence of nitrogen (N1s 6.8%). HiRes XPS of Si2p (Figure 36) confirmed that silicon is bounded to carbon as Si-C [126]. HiRes XPS of C1s is shifted to higher energies, indicating the presence of chemical states of C-O-C (B.E. ~286 eV) and O-C=O (B.E. ~288.5) [127]. This suggests that surface's carbon is not only bound to silicon as Si-C, but also as Si-C-O-C and Si-C-O₂. This is not surprising as the recipe used for SiC (precursors Si(CH₃)₄ and He) is very similar to the recipe of SiOC (precursors Si(CH₃)₄, O₂ and He). SiC film was not significantly affected by sterilization with EtO and biodegradation test in NaCl/FBS.

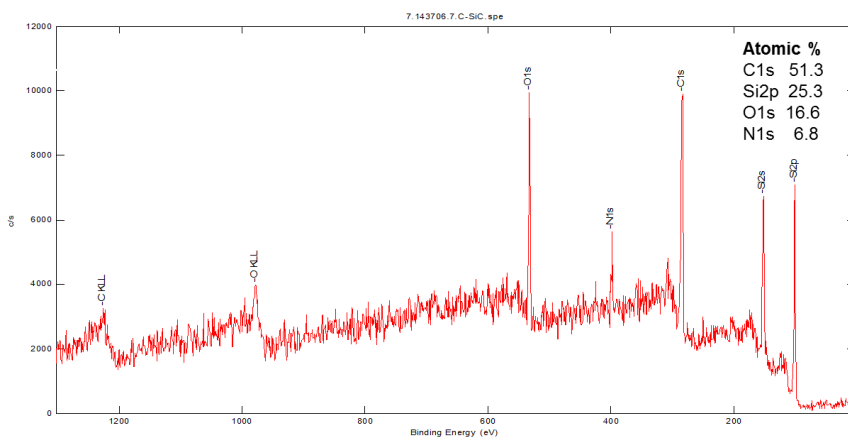


Figure 35: General XPS of 100 nm SiC 350°C on silicon substrate.

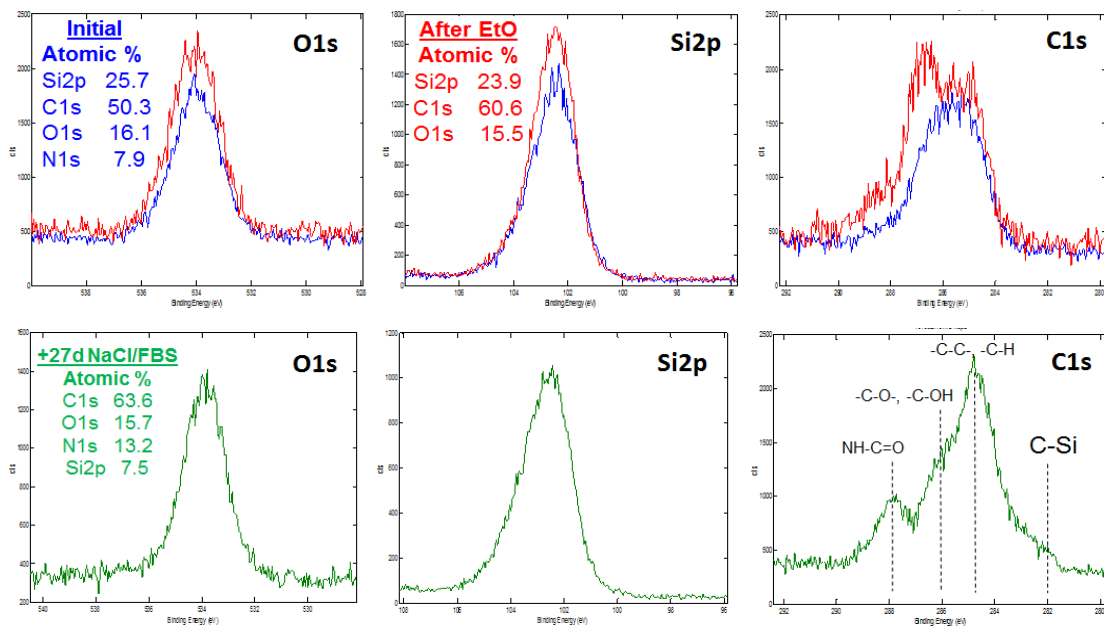


Figure 36: High resolution XPS of 100 nm SiC 350°C on silicon substrate.

DLC

The general XPS of 100 nm a-CH 400°C deposited on silicon substrate is shown in Figure 37. There is oxidation of the surface (O1s 16.2%). HiRes XPS of carbon 1s is slightly modified after sterilization with EtO (green arrow in Figure 38), indicating the appearance of C-O bonds (~286 eV). This is consistent with the well-known behavior of ethylene oxide as alkylating agent [128]. HiRes XPS measurements after biodegradation tests in NaCl/FBS do not suggest DLC film was degraded by such medium.

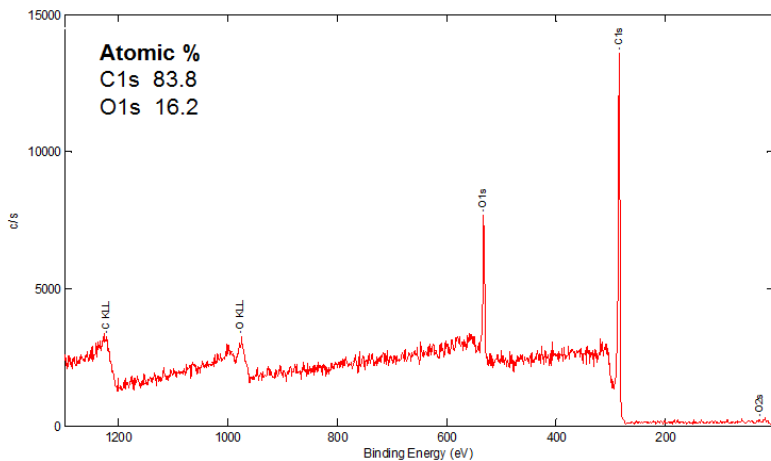


Figure 37: General XPS of 100 nm a-CH 400°C on silicon substrate.

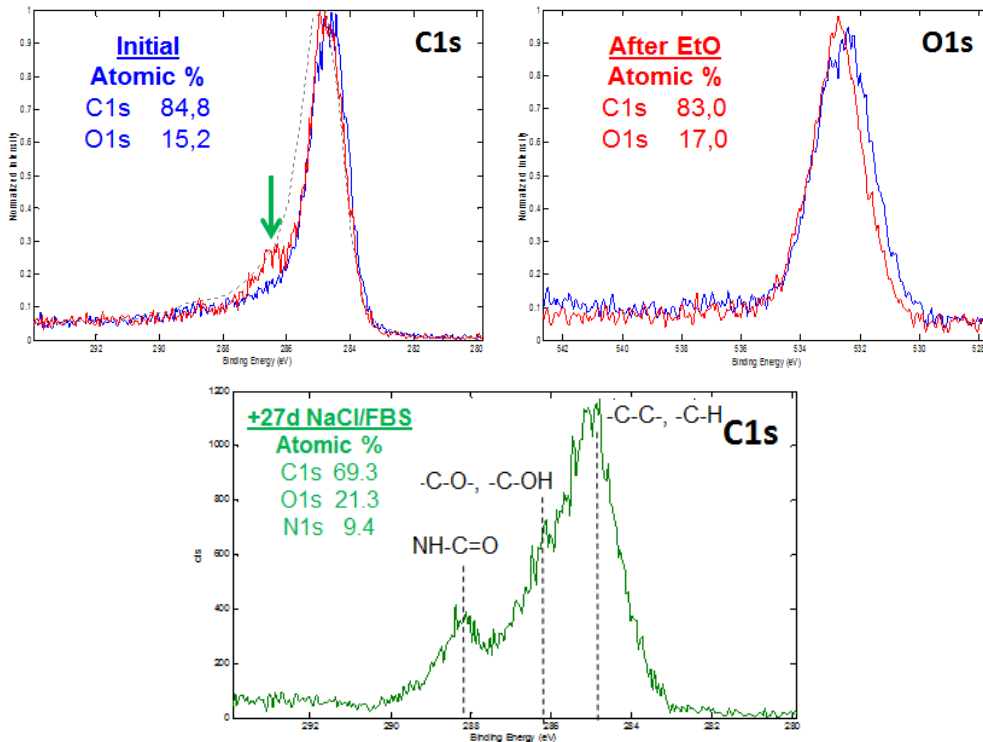


Figure 38: High resolution XPS of 100 nm a-CH 400°C on silicon substrate.

Figure 39 shows XPS measurements performed at Ultra High Vacuum conditions and heating to 450°C for 20 min in order to estimate an accurate ratio of sp² to sp³ carbon without interference of adventitious atmospheric carbon. Software CasaXPS® was used for fitting the peaks. The estimated percentages of sp² and sp³ carbon are respectively 83% and 16%. The remaining 1% corresponds to C-O bonds. This ratio of sp² to sp³ carbon remained constant even after biodegradation tests in NaCl/FBS for 27 days, indicating the excellent chemical stability of deposited DLC films.

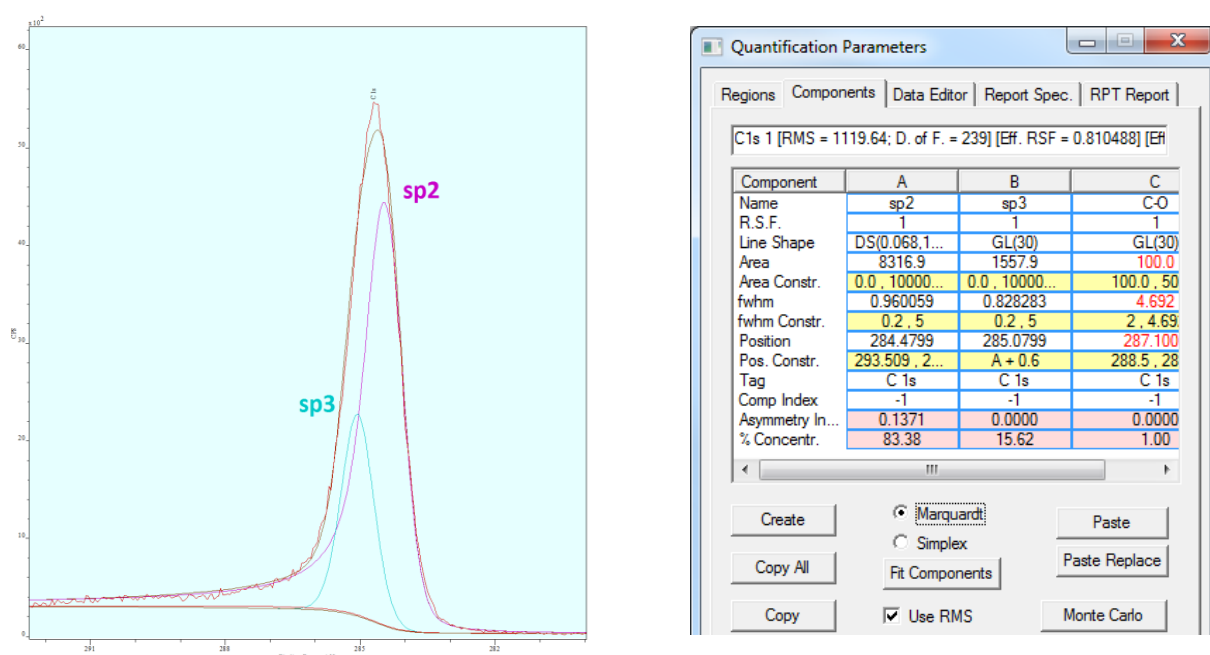


Figure 39: Fitting of XPS of carbon 1s of DLC (a-CH) 400°C deposited on silicon substrate.

HfO₂

The general XPS spectrum of HfO₂ 300°C is shown in Figure 40. The content of silicon atoms on the surface (Si2p 4.3%) has two possible explanations. First one is that the film is thinner than 6-7 nm and the silicon substrate is detected in XPS measurements. VASE and XRR measurements confirmed that the film thickness was 18–20 nm, so this explanation can be discarded. The second one is that there was contamination with silicon compounds during film deposition or afterwards. It is known in the literature that the temperature of deposition affects the thickness of the interfacial SiO_x layer formed between Si and HfO₂ [129, p. 117]. Since HfO₂ is a poor diffusion barrier for water, water adsorbed on its surface can diffuse down to the silicon substrate and contributes to regrowth of the interfacial SiO_x layer at

temperatures ranging from 200°C to 400°C. In addition, impurities in HfO₂ films enhance interfacial reactions with silicon such as inter-mixing and Si out-diffusion [129].

A relatively high content of oxygen (O1s 44.0%) and carbon (C1s 36.0%) are seen in Figure 40, indicating a high content of carbon impurities. HiRes XPS of C1s and O1s in Figure 41 indicate the presence of metal oxides (529–530 eV), organic C-O (531.5–532 eV), and SiO₂ (532.9 eV) chemical bonds [130]. The binding energy of Hf4f in Figure 41 after EtO and biodegradation tests in NaCl/FBS are consistent with the chemical state of HfO₂ [131].

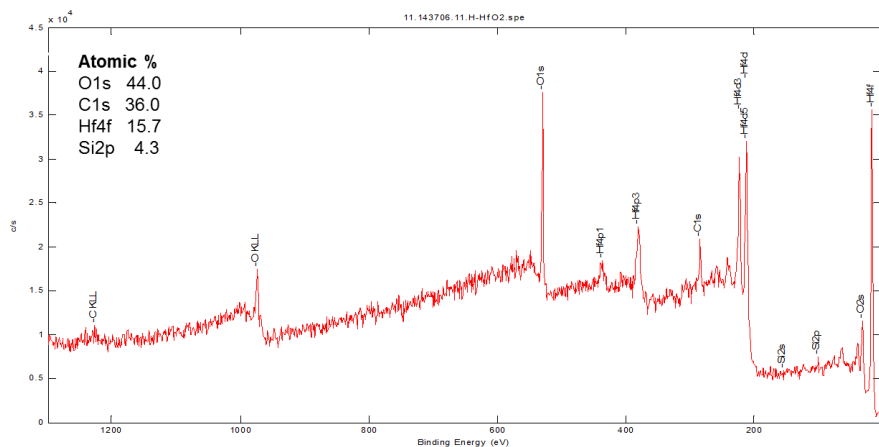


Figure 40: General XPS of 20 nm HfO₂ 300°C on silicon substrate

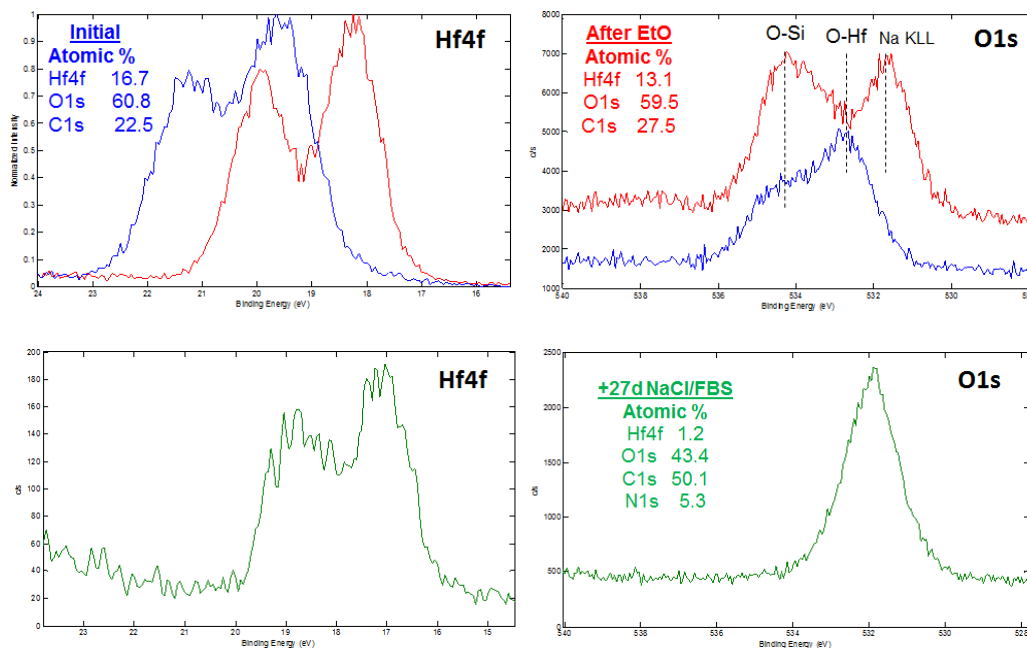


Figure 41: High resolution XPS of 20 nm HfO₂ 300°C on silicon substrate.

SiN

General XPS of SiN (Figure 42) shows there is strong oxidation of the surface as the atomic percentage of O1s is larger than N1s and Si2p. Figure 43 shows that peaks of Si2p and N1s have a binding energy consistent with chemical bonds of Si–N [126],[132]. But the base of Si2p peak is shifted toward higher energies indicating a non-negligible content of Si atoms in the chemical state of SiO₂. HiRes XPS of O1s indicates also that most oxygen atoms exist as SiO₂ [130]. This means that deposited film of SiN has been oxidized to SiO₂ near its surface. A small fraction of adventitious sp³ carbons are bound to oxygen atoms as C-O-C.

SiN film was not affected by sterilization with EtO. But it was degraded by biodegradation test in NaCl/FBS as new chemical bonds were established between nitrogen and protein groups. SiO₂ bonds disappeared after biodegradation test.

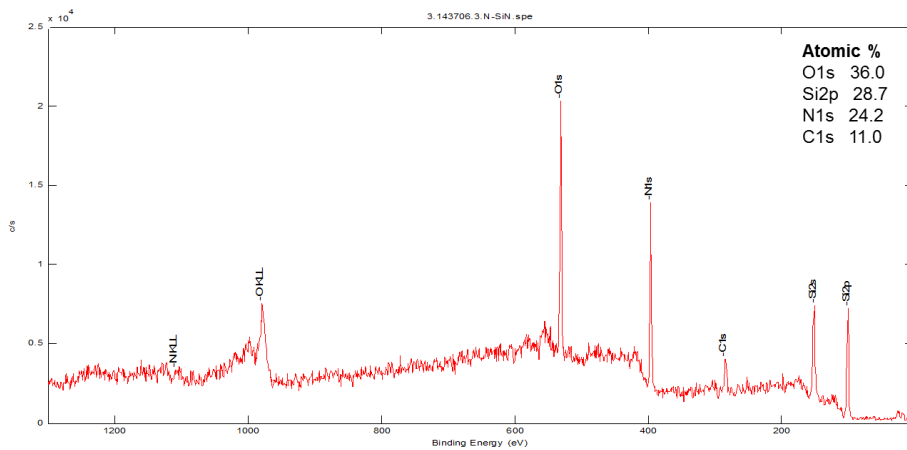


Figure 42: General XPS of 100 nm SiN 400°C on silicon substrate.

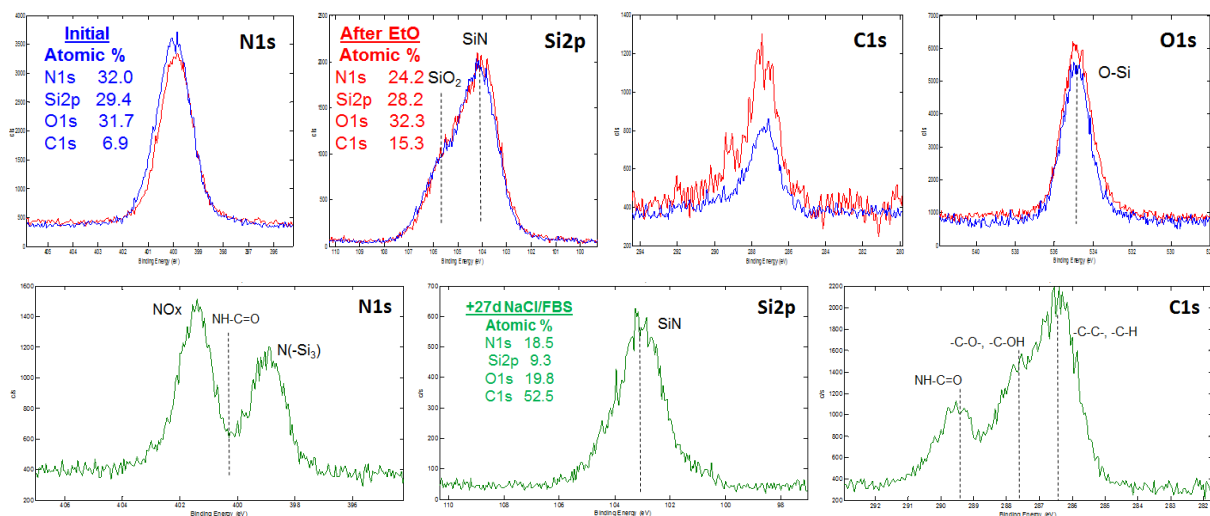


Figure 43: High resolution XPS of 100 nm SiN 400°C on silicon substrate.

SiO₂

The general XPS of 100 nm SiO₂ 400°C on silicon substrate can be seen in Figure 44. The ratio of Si/O is near the stoichiometric value of 1:2. This ratio does not change after sterilization with EtO, although there is an increase of carbon content consequent with the alkylating behavior of EtO (Figure 45). HiRes XPS of Si2p and O1s confirmed that most silicon and oxygen atoms are in the chemical state of SiO₂.

HiRes XPS of O1s and C1s after biodegradation test in NaCl/FBS shows there are new chemical bonds between them and functional groups of proteins such as NH-C=O and -C-O-, but most atoms of silicon and oxygen remain in the chemical state of SiO₂.

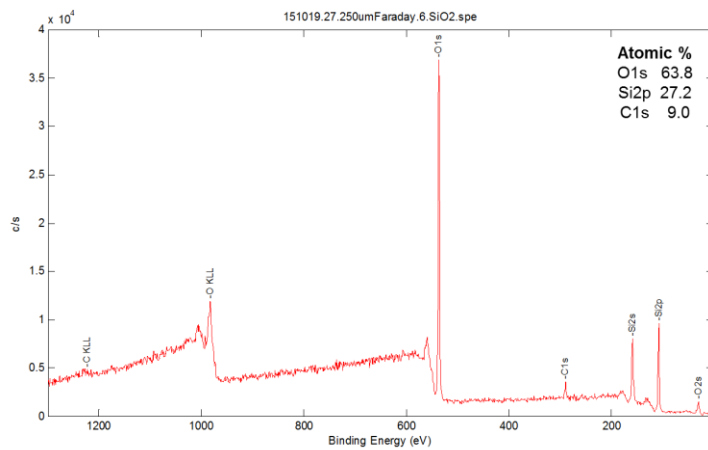


Figure 44: General XPS of 100 nm SiO₂ 400°C on silicon substrate.

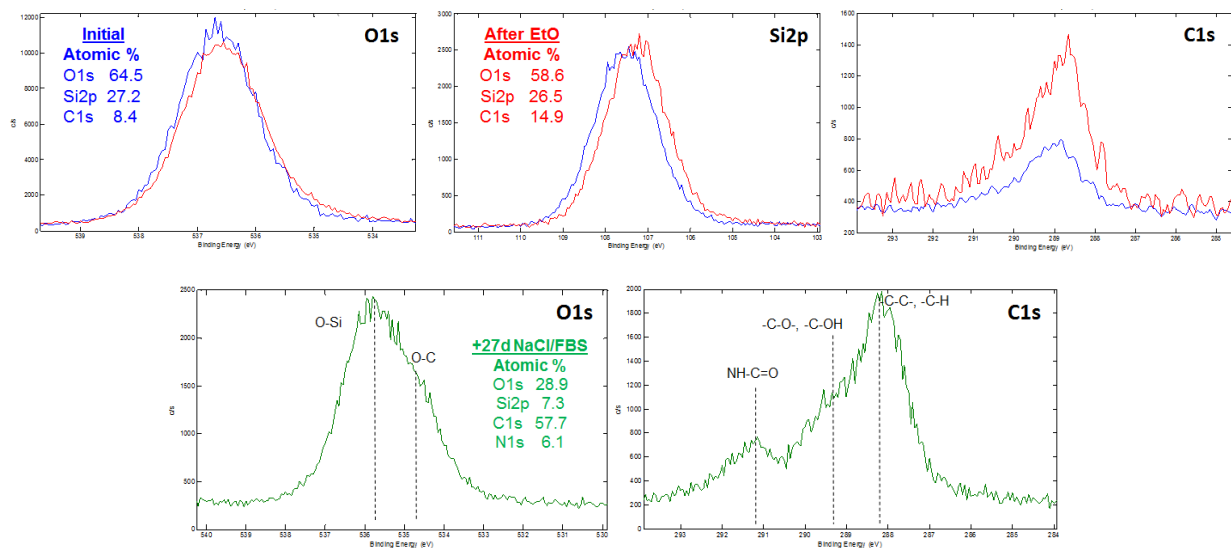


Figure 45: High resolution XPS of 100 nm SiO₂ 400°C on silicon substrate.

SiOC

General XPS of 100 nm SiOC 400°C on top of silicon is shown in Figure 46. The content of carbon is relatively low considering the sample was exposed to the atmosphere and a layer of 1–2 nm of adventitious carbon was present. The atomic percentages are not very different from those found for the SiO₂ film. HiRes XPS of Si2p in Figure 47 displays a binding energy of 103.5 eV, which is the exact value expected for the chemical state of SiO₂ [126]. However, HiRes XPS of O1s shows a BE higher than the value expected for SiO₂ (532.9 eV), and closer to the BE for organic C=O (~533 eV) [130]. This means the film is made mostly of SiO₂ with some C=O and C-O-C groups present on the surface. SiOC film was not negatively affected by sterilization with EtO or biodegradation tests in NaCl/FBS.

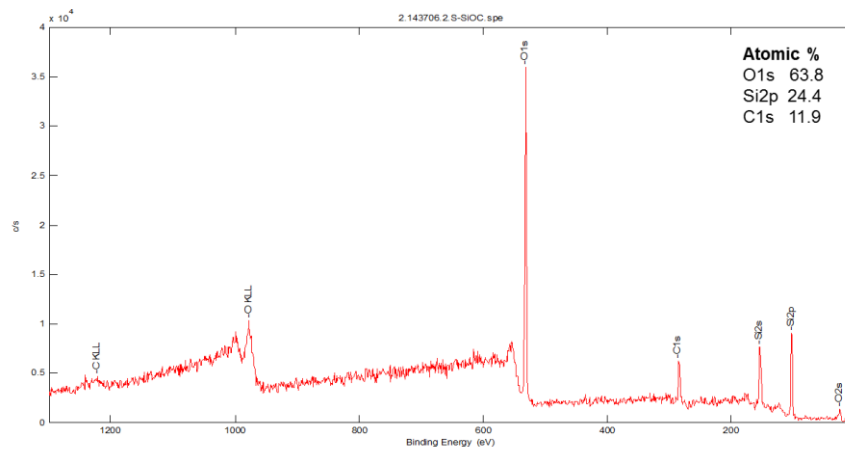


Figure 46: General XPS of 100 nm SiOC 400°C on silicon substrate.

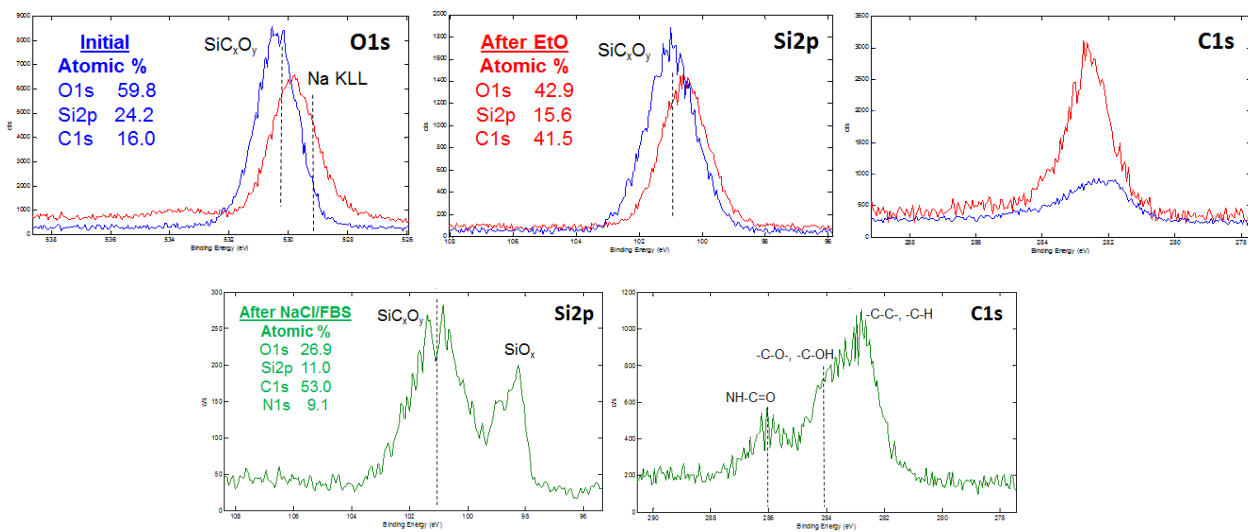


Figure 47: High resolution XPS of 100 nm SiOC 400°C on silicon substrate.

TiO₂

The general XPS of 20 nm TiO₂ 250°C (Figure 48) shows a ratio of Ti/O near the ideal stoichiometry of 1:2. The content of carbon 1s (25.2%) is higher than in films of Al₂O₃ (17.8%) and ZnO (22.7%), indicating there is a significant amount of carbon impurities in this TiO₂ film. HiRes XPS of initial Ti2p in Figure 49 confirms that titanium atoms are in the chemical state of TiO₂ (theoretical BE 458.5 eV) [133]. HiRes XPS of O1s has a peak left-shifted at 530.1 eV, which is consistent with the presence of metal oxides (529–530 eV) and some chemical states of organic C-O. HiRes XPS of C1s indicates a majority of C-C bonds along some organic C-O-C bonds.

XPS results after EtO and NaCl/FBS indicated the film is chemically stable in both cases.

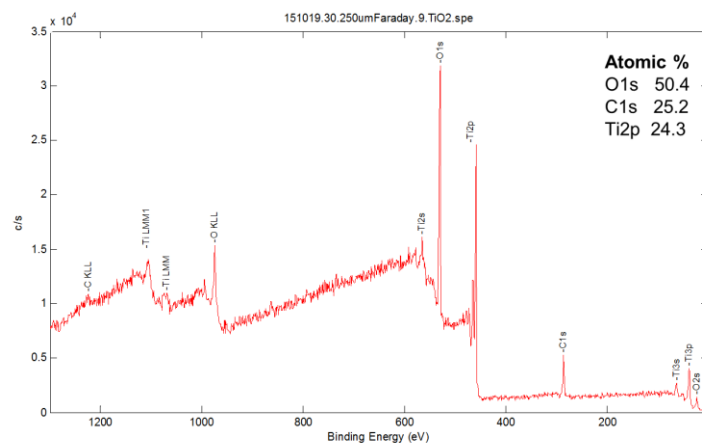


Figure 48: General XPS of 20 nm TiO₂ 250°C on silicon substrate.

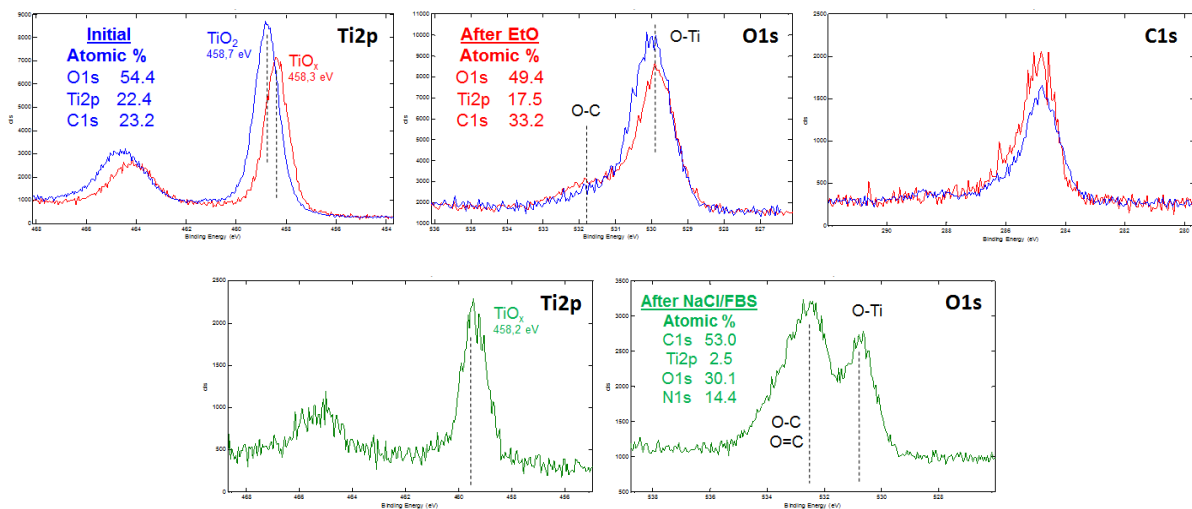


Figure 49: High resolution XPS of 20 nm TiO₂ 250°C on silicon substrate.

ZnO

The general XPS of 20 nm ZnO 250°C deposited on silicon is shown in Figure 50. There is strong oxidation of the surface, with a ratio of Zn/O smaller than one. HiRes XPS of O1s (Figure 51) suggests oxygen is bound mainly as metal oxide, but also in minor proportion as organic C-O. HiRes XPS of C1s confirms there are C-O-C bonds present in small proportion. The peak of Zn2p3 is symmetrically centered around 1021.5 eV, indicating most zinc atoms exist as ZnO [134]. Other than the contamination introduced by the adventitious atmospheric carbon, this film of ZnO has small amount of impurities and its density should be close to its theoretical value. XRR and XRD measurements (page 70) confirmed the purity of ZnO films. As deposited ZnO layers were not stable in saline solution after 24h, XPS measurements after sterilization with EtO and biodegradation tests in NaCl/FBS were not performed.

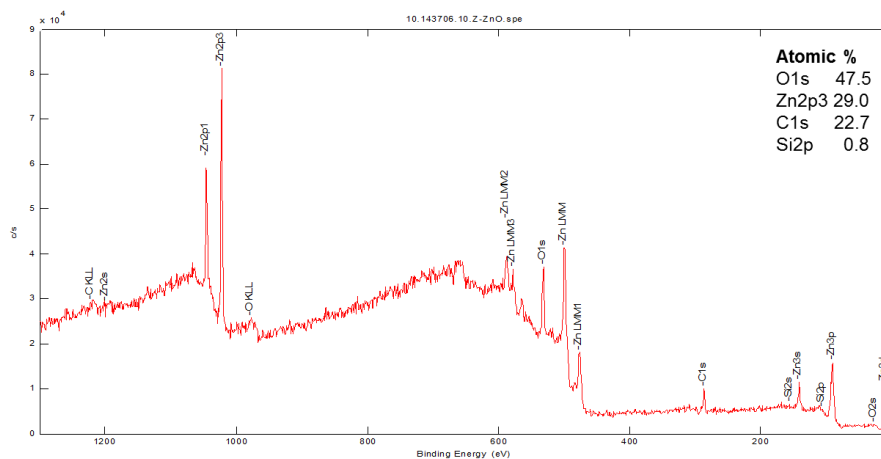


Figure 50: General XPS of 20 nm ZnO 250°C on silicon substrate.

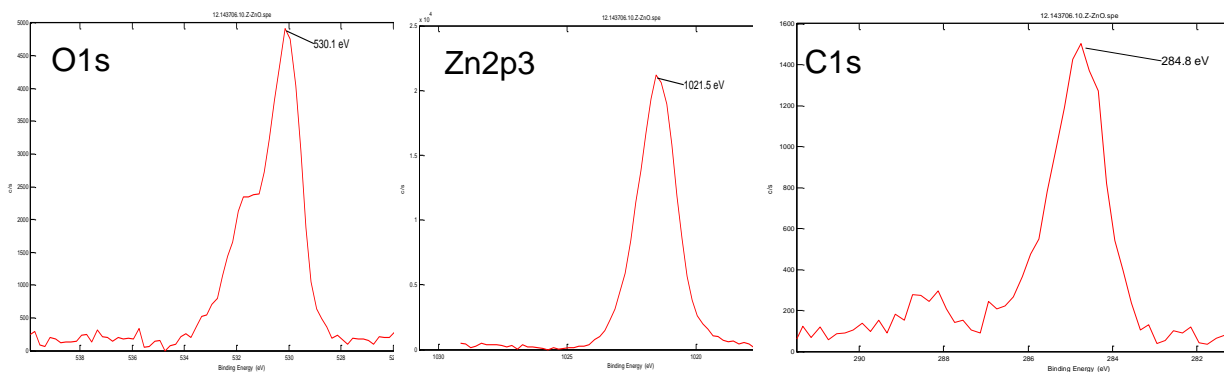


Figure 51: High resolution XPS of 20 nm ZnO 250°C on silicon substrate.

3.1.5. VASE

Variable Angle Spectroscopy Ellipsometry (VASE) measurements were performed with an ellipsometer of the rotating analyzer type M-2000DI® by J.A. Woollam Co., Inc. Spectroscopic measurements were made in the wavelength range of 190–1700 nm with 5 nm intervals at an incident angle of 55–75°. The Mean Squared Error (MSE) of data fitting was smaller than 5.0 in most cases, which implies a very good fit. Experimental errors of 0.1–1.0 nm can be expected for estimated values of film thickness.

Materials of page 65 were deposited on crystalline silicon coupons of size 2.0x1.5 cm² and measurements were taken at the center of the coupon with the help of a paper support with alignment marks (Figure 52). Table 10 resumes VASE results of some deposited thin films. Optical constants are given at 633 nm. More details can be found in the Annexes (page 166).

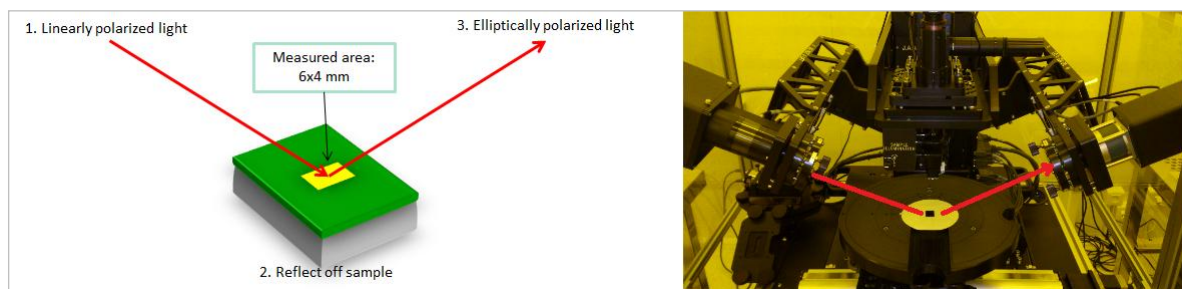


Figure 52: VASE measurements of thin films deposited on silicon coupons.

Table 10: VASE analysis of various packaging films deposited on silicon coupons.

Film	Fabrication	Fitted range (nm)	MSE	Thickness (nm)	Roughness (nm)	n	k
Al ₂ O ₃	ALD 250°C	190–1700	1.0	19.6	0.39	1.62	0
HfO ₂	ALD 250°C	600–1700	0.9	19.9	0.10	2.03	0.66
TiO ₂	ALD 250°C	400–1700	2.3	15.4	0.21	2.64	0.25
ZnO	ALD 250°C	400–1700	1.1	20.6	1.14	1.92	0
SiN	PECVD 400°C	190–1700	2.6	100.0	0.95	1.87	0.0037
SiO ₂	PECVD 400°C	190–1700	2.9	98.6	0.28	1.46	0
SiOC	PECVD 400°C	400–1700	1.4	98.1	0.20	1.42	0
SiC	PECVD 350°C	400–1700	2.8	98.6	0.79	1.84	0
DLC	PECVD 400°C	400–1700	3.4	111.1	6.3	1.81	0.12
BN	PECVD 400°C	400–1700	3.7	47.2	0.30	1.99	0.022

3.2. Biodegradation tests

Accelerated lifetime tests are necessary to ensure reliable encapsulation of medical devices for several years at body temperature of 37°C. There are different ways to estimate the Acceleration Factor (AF) of high temperature aging tests. The model most commonly used in biomedical packaging is known as the model of the “10-degree rule”. The 10-degree rule is based on the experimental observation that the reaction rate of polymeric reactions doubles with every increment of ten degrees [135]. That is:

$$AF = 2^{\Delta T/10} \quad \text{Eq. 9}$$

In Eq. 9, ΔT is the difference between the temperature of test (a.k.a. temperature of stress) and the temperature of use of the device. The acceleration factor and equivalent time at 37°C according to Eq. 9 for various temperatures are given in Table 11. From Table 11, it can be seen that three months at 90°C is equivalent to a lifetime of roughly ten years according to the 10-degree model.

Table 11: Acceleration factors for various temperatures according to the 10-degree model.

Temperature (°C)	Acceleration Factor (AF)	Real time (day)	Equivalent time at 37°C (day)
37	1	90	90
57	4	90	360
67	8	90	720
90	39.4	90	3546

Another way to estimate accelerated aging factors is using the Arrhenius model. The Arrhenius model treats the degradation rate of some performance parameter as a pseudo-first order reaction [136, p. 287]. According to Arrhenius model, the AF of such reaction is:

$$AF = \exp\left(\frac{E_a}{k} \left(\frac{1}{T_{use}} - \frac{1}{T_{stress}}\right)\right) \quad \text{Eq. 10}$$

Where E_a is the energy of activation (eV), k is the Boltzmann constant ($8.617 \cdot 10^5$ eV K⁻¹), T_{use} is 37°C for medical devices, and T_{stress} is the temperature of the accelerated aging test. The most important factor to estimate the AF in Eq. 10 is the activation energy required for that process to occur. Different activation energies for various failure mechanisms of microelectronic devices have been computed and published. Table 12 lists activation energies for various failure mechanisms commonly seen in electronic devices [137].

Table 12: Failure mechanism of electronic devices and associated activation energy [137].

Failure mechanism	Activation energy (eV)
Oxide effects	0.3–0.5
Silicon defects (Bulk)	0.3–0.5
Corrosion in humid air	0.4–0.8
Assembly defects	0.5–0.7
Electro migration	0.6–0.9
Mask/Photoresist defects	0.7
Contamination	1.0
Unknown	0.7

The activation energy for a failure mechanism induced by corrosion in humid air is not known precisely [18]. Let us assume a value of 0.6 eV for this process based on the data reported by Weick *et al.* [138]. According to the Arrhenius model, an aging test performed at 67°C that failed due to this mechanism has an AF of 7.2. This is slightly smaller than the value predicted by the 10-degree model in Table 11. Now, if the activation energy is assumed to be 0.7 eV, the aging test's AF becomes 10.1 at 67°C, which is considerable higher than the AF listed in Table 11. Due to this incertitude about the activation energy of corrosion of micro-devices in humid environments, the Med-Tech industry prefers to employ the 10-degree model for the prediction of lifetimes of medical devices [135].

It is been reported in the literature that the 10-degree model should not be used for temperatures larger than 60–70°C [135], [139]. The validity of the 10-degree rule for aging tests at higher temperatures is a recurrent subject of discussion. Medical doctors consider that tests at temperatures higher than 40°C are not relevant to predict the long-term response of implanted medical devices because physiological environments never exceed that value. On the other hand, people from the microelectronics industry are so used to accelerate aging tests

and short cycles of fabrication that they employ temperatures as high as 90°C to predict lifetimes of >10 years for medical devices. As this thesis was prepared in close collaboration with medical researchers of CLINATEC, it was decided to follow an approach between these two opinions. So accelerated aging tests at temperatures <70°C were preferred. The goal was to perform the aging tests at conditions as similar as possible to the real conditions encountered by the medical device.

In biomedical laboratories, the term “degradation” and “biodegradation” tests are employed to designate aging tests performed in simulated and biological environments, respectively. A saline solution of Phosphate-Buffer Saline (PBS) that simulates the chemical environment found in human blood serum was chosen for “degradation” tests of packaging layers in this study. They were performed at 67°C, 57°C and 37°C. Additionally, “biodegradation” tests were performed in a saline solution of 0.9 wt% NaCl supplemented with 10% volume of Fetal Bovine Serum (FBS) at 37°C.

3.2.1. Degradation tests in PBS heated to 67, 57 and 37°C with hot plate

Four coupons of each packaging layer were placed on the bottom of a borosilicate petri dish and PBS solution poured over them until a fixed level of ~80% the total volume. The PBS solution was supplied by Euromedex Inc. as a 0.2 µm-filtered 10X solution containing KH_2PO_4 10.6 mM, $\text{Na}_2\text{HPO}_4 \cdot 2\text{H}_2\text{O}$ 30.0 mM, NaCl 1.54 M and dissolved to 1X with bi-distilled water of 18.2 MΩ·cm. Heating was performed on a hot plate whose temperature was set to 54-60°C as measured by a portable electronic thermometer with an accuracy of ±0.1°C. This temperature range is reported here as 57°C.

The PBS solution was changed completely every week and losses due to evaporation of solution during the week were compensated by additions of DI water until reaching the original level of liquid in order to maintain the ionic concentration constant.

Coupons were removed from the PBS solution and cleaned with DI water, a soft tissue and a nitrogen blow gun before all thickness measurements. Those materials showing problems of corrosion or a significant change in thickness over time at 57°C were further evaluated by aging tests at 37°C. The goal was to determine if such corrosion problems would occur at 37°C as well.

Aging tests by immersion in PBS at 37°C were performed on a hot plate. Here as well, it was difficult to precisely regulate the temperature of the hot plate. The temperature of the PBS

solution was measured in the range of 34–40°C. Such temperature range is reported here as 37°C.

To quantify the stability of each packaging layer, the film thickness variation of each coupon was monitored over time by Variable Angle Spectroscopic Ellipsometry (VASE). Estimated errors of film thickness varied between 0.1 and 1.0 nm. For example, the average thickness of 15 coupons coated with 14.0 nm ALD TiO₂ (according to the manufacturer of the Fiji F200™ machine) was 13.9±0.1 nm and all samples had a MSE smaller than 2. However, the main difficulty to monitor the change of film thickness over time was to measure exactly the same location on the coupon. It was noticed that shifting the measured area by 0.2 cm resulted in film thickness differences of 0.5–2.0 nm. Hence, a measurement error of ±2.0 nm can be expected when measuring the variation of film thickness over time.

Results and discussion

The thickness variations of different packaging layers after 4–8 weeks of immersion in 57°C PBS are plotted in Figure 53. The change of thickness was computed as the current minus the original (day 0) thickness for each coupon. Values plotted in Figure 53 are the average of four coupons measured per material. SiN coupons had disappeared after two weeks of soaking in 57°C PBS. Hence, this value was not plotted in the graph.

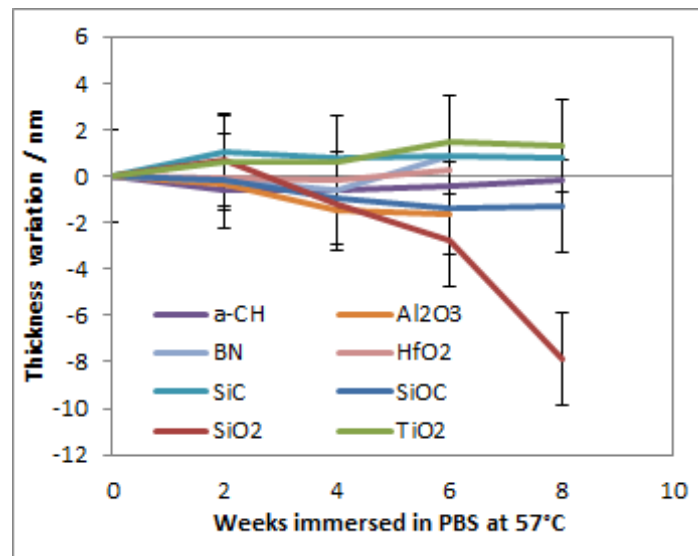


Figure 53: Thickness variations of different packaging layers immersed in PBS at 57°C.

The small increase of thickness of some packaging layers in Figure 53 is probably due to precipitation of salts on top of the coupons and to the accuracy of our measurements being ±2

nm. It can be seen as well that there are packaging layers which pass our criteria of stability of a film thickness variation smaller than 2 nm after 6–8 weeks in PBS at 57°C. They are Al₂O₃, HfO₂, TiO₂, SiC, SiOC, BN and a-CH. Unspoiled coupons of TiO₂ and SiC after 8 weeks in 57°C PBS are shown in Figure 54.

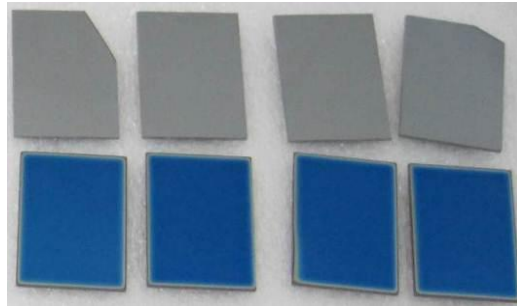


Figure 54: TiO₂ (Top) and SiC (Bottom) coupons after 8 weeks in 57°C PBS.

Those packaging layers whose thickness loss was larger than two nanometers after 6–8 weeks of immersion in 57°C PBS were considered unstable. This is the case for SiN and SiO₂ packaging layers. They were therefore tested in 37°C PBS to determine if a similar behavior was observed. The results of these tests are plotted in Figure 55.

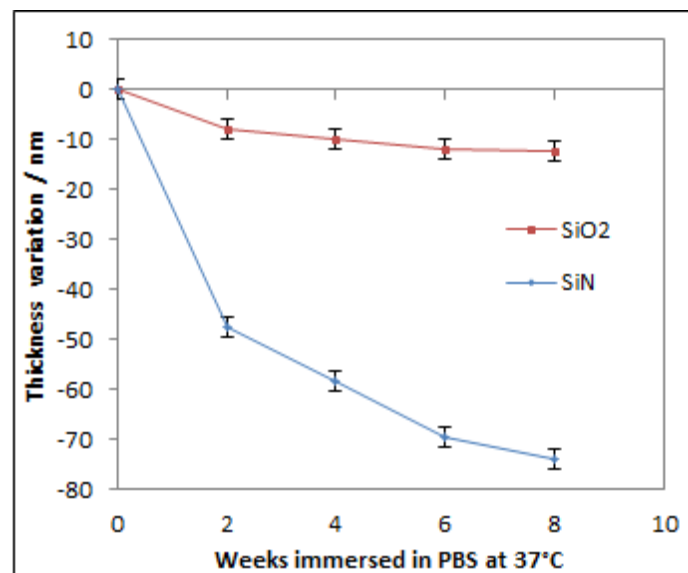


Figure 55: Thickness variation of SiN and SiO₂ packaging layers immersed in 37°C PBS.

It can be concluded from Figure 55 that SiN films are not stable in 37°C PBS. The decomposition of SiN does not follow a straight line, but it tends toward a limit value. Such

deviation from linearity is probably due to the formation of a layer richer in oxygen that passivates of the SiN layer from further chemical reactions [138].

It was noticed that the frequency of renewal of the PBS solution is an important factor in its chemical aggressiveness. If the PBS solution is changed completely every week and losses due to evaporation of solution during the week are compensated by additions of DI water, a decomposition line of SiN like that of Figure 55 can be expected.

Corrosion of SiN coupons was visible after few days of immersion in 37°C PBS (Figure 56). On the other hand, SiO₂ coupons deteriorated slowly and more uniformly in the same conditions (Figure 57).

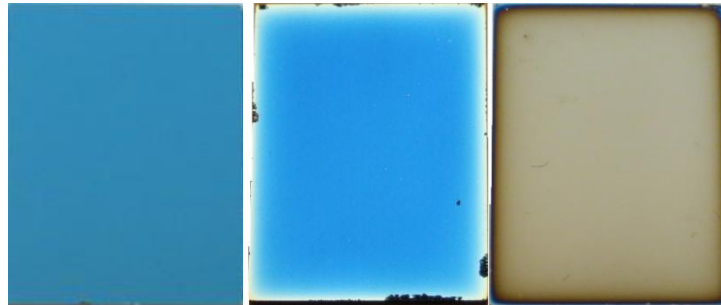


Figure 56: SiN coupons before (Left), after 8 days (Center) and 56 days (Right) in 37°C PBS.

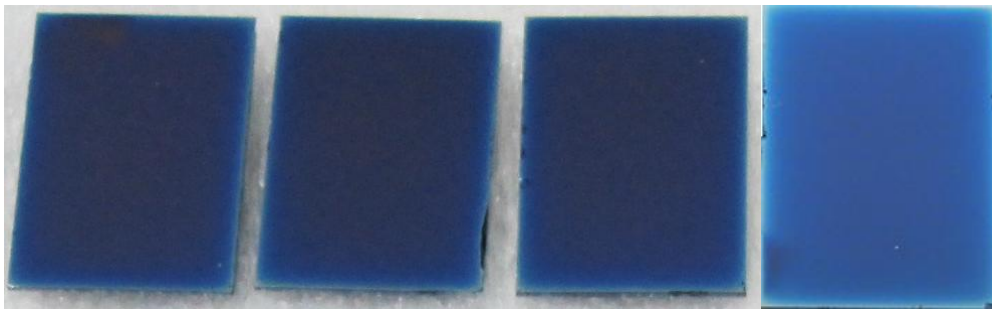


Figure 57: SiO₂ coupons after 56 days in 37°C PBS. Few apparent changes were visible.

Although corrosion is typically associated with metals, it can be defined in general as the deterioration of materials by chemical interaction with its environment [140]. The amount of corrosion loss in thickness over time is called the corrosion rate. Corrosion rates of SiN and SiO₂ films in PBS solution heated to 67, 57 and 37°C on a hot plate are plotted in Figure 58.

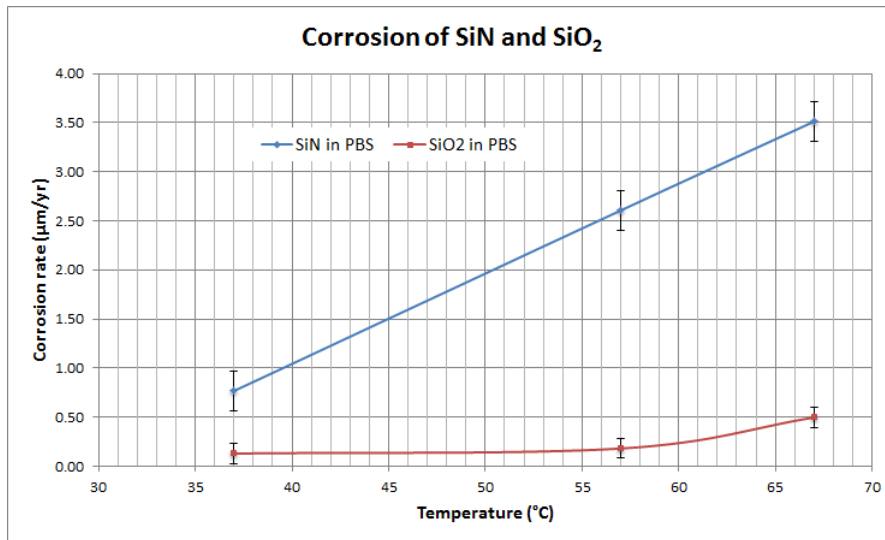
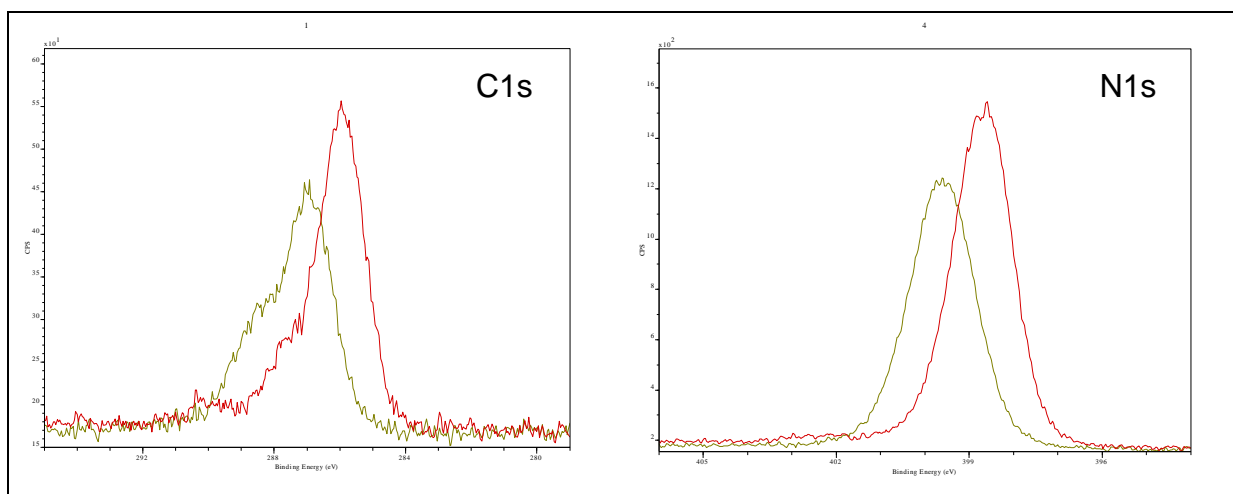


Figure 58: Corrosion rates of SiN and SiO₂ films in PBS heated on hot plate.

A corrosion rate of 0.10 ± 0.05 µm per year in 37°C PBS was found for SiO₂ packaging layers deposited by PECVD at 400°C with SiH₄ and N₂O as precursors. A corrosion rate of 0.77 ± 0.05 µm per year in 37°C PBS is expected for a SiN film deposited by PECVD at 400°C from SiH₄, NH₃, N₂ as precursors. This is consistent with values reported by Osenbach *et al.* for SiN:H films prepared by PECVD at 360°C from similar precursors [34].

High resolution XPS measurements of SiN coupons after 7 days in 57°C PBS (Figure 59) showed the chemical bonds of its surface had an important shift (1.0 eV) to lower binding energies, indicating there was a significant transfer of charge from Si atoms to negative chemical species due to the formation of new chemical bonds. The negative chemical species were probably chloride ions.



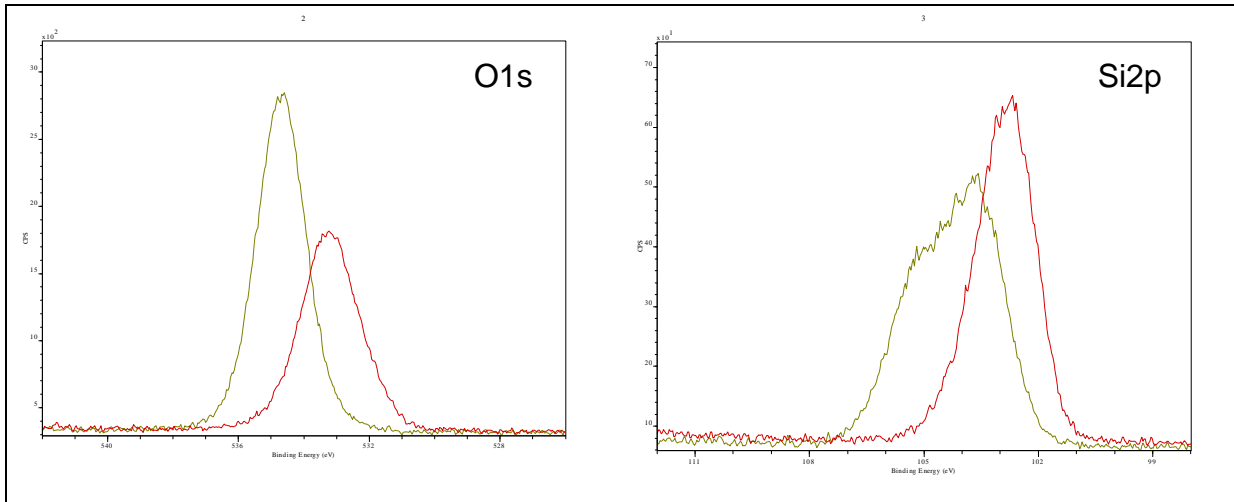


Figure 59: HiRes XPS of SiN film before (green) and after (red) 7 days in 57°C PBS.

In comparison with SiN, HiRes XPS of SiO₂ (Figure 60) showed there was a smaller transfer of charge (0.5 eV) from Si atoms to negative chemical species, indicating its surface was less distorted by soaking in PBS solution.

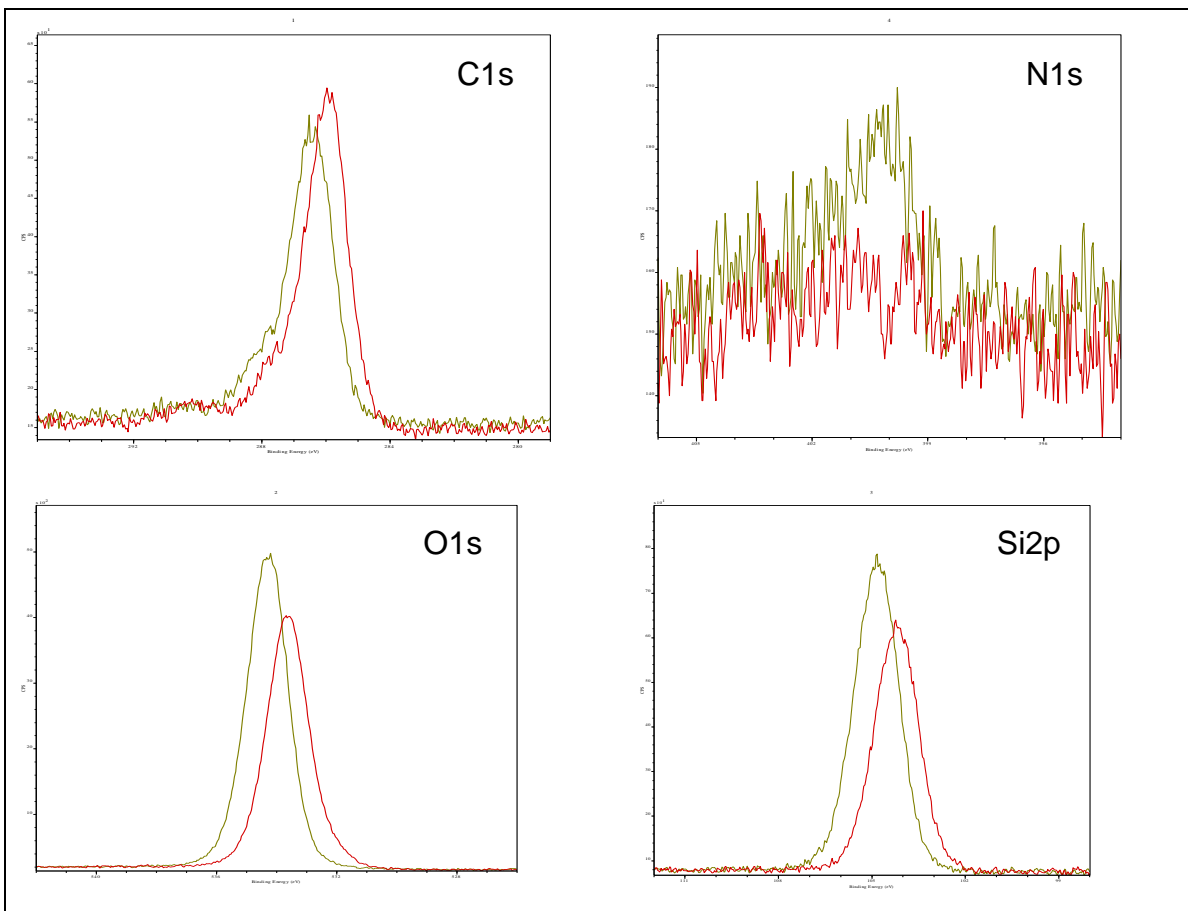


Figure 60: HiRes XPS of SiO₂ film before (green) and after (red) 7 days in 57°C PBS

ZnO films were rapidly dissolved by PBS and the original film was gone after a couple of days (Figure 61). Pourbaix diagram of the zinc and water system predict that Zn^{2+} is the most stable chemical species at pH 7 (Figure 62). Therefore, thin films of ZnO are not recommended for encapsulation of electronic devices in aqueous environments.

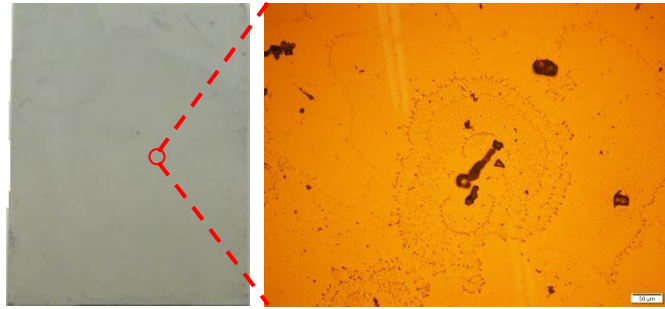


Figure 61: Photo (Left) and μ photo (Right) of ZnO coupon after 2 days in 37°C PBS.

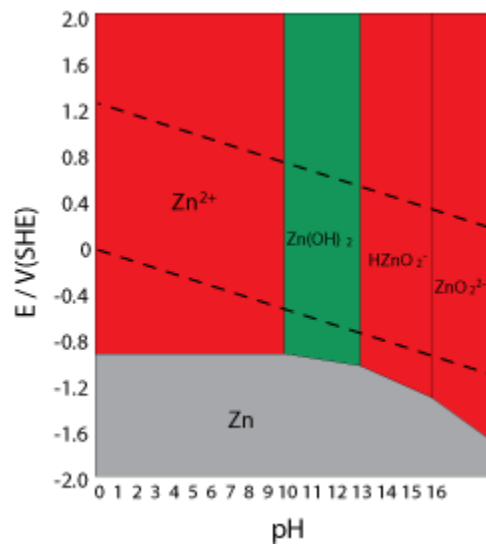


Figure 62: Pourbaix diagram of the zinc-water system. [141]

3.2.2. Degradation tests in PBS heated to 67°C in oven

Four coupons of each packaging film were placed on the bottom of plastic containers of 50 cm³ made from Per-Fluor-Alkoxy copolymer (PFA) by VITLAB GmbH. PFA is extremely hydrophobic and chemically inert material suitable for degradation tests [142]. Saline solution poured on them was same PBS solution detailed in the previous section. Heating was performed on a convection oven whose temperature was set to 67°C within an accuracy of $\pm 0.1^\circ\text{C}$. Losses of liquid due to evaporation were insignificant, so PBS solution was not replenished with DI water. Coupons were removed from PBS and cleaned with acetone, isopropyl alcohol and DI water before observations and thickness measurements.

In parallel, the corrosion rate of crystalline silicon (p-type, 1–50 ohm*cm) was determined by gravimetric measurements of 20 coupons (size 2.00*1.50*0.0725 cm³) before and after soaking in PBS at 67°C for 120 days.

Results and discussion

Clear signs of corrosion were visible on the coupons after 120 days in 67°C PBS (Figure 63). The rainbow colors visible on some coupons have been reported for uncoated implantable silicon devices by D.J. Edell *et al.* and indicate corrosion of silicon [143, p. 568]. The average corrosion rate of crystalline silicon coupons in 67°C PBS was $17.0 \pm 4.2 \text{ mg m}^{-2} \text{ day}^{-1}$. This corresponds to $2.66 \pm 0.66 \text{ }\mu\text{m/yr}$ when a density of 2.33 g/cm^3 is assumed for silicon [144].

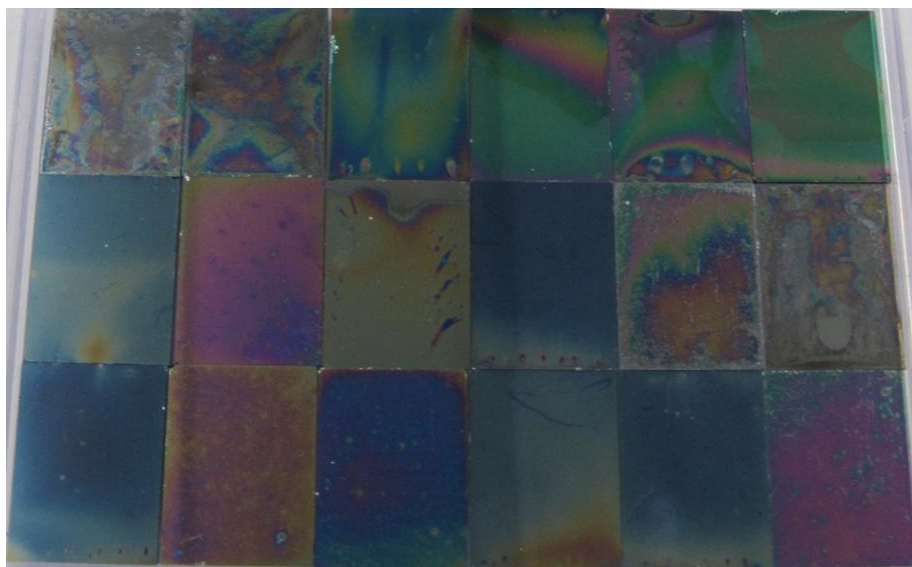


Figure 63: Silicon coupons after 120 days in PBS heated to 67°C in closed oven.

This value is smaller than the corrosion rate of $11.2 \mu\text{m}/\text{yr}$ reported by D. Zhou *et al.* in Bicarbonate Buffered Saline at 57°C [145, p. 23], and of $12 \mu\text{m}/\text{yr}$ reported by D. J. Edell *et al. in vivo* for p+ silicon coupons implanted subcutaneously and in the subdural space of a New Zealand rabbit [143, p. 568]. The chemical composition of these experiments is not well detailed by the authors, so it is difficult to explain the different corrosion rates. It is clear, however, that silicon [143] and silicon oxide [146] have higher corrosion rates *in vivo* and they should be thoroughly encapsulated for usage in implantable medical devices.




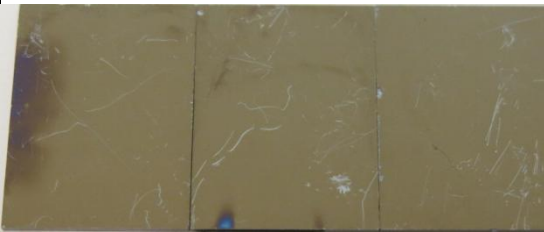


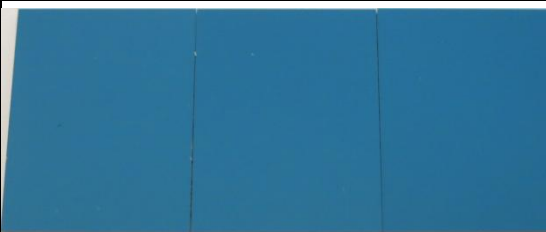
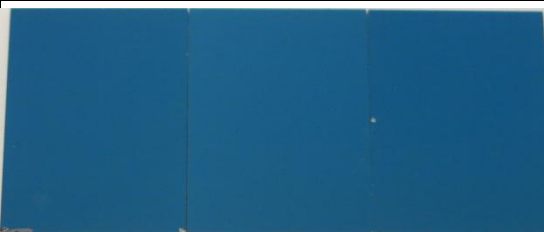
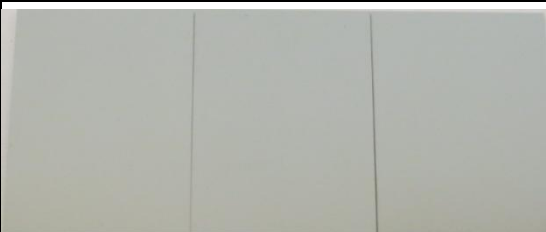


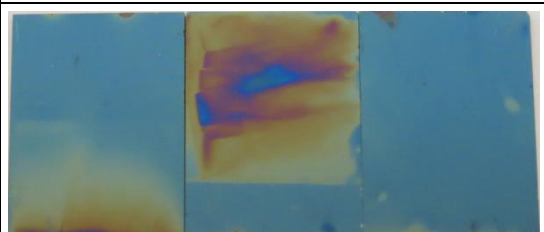
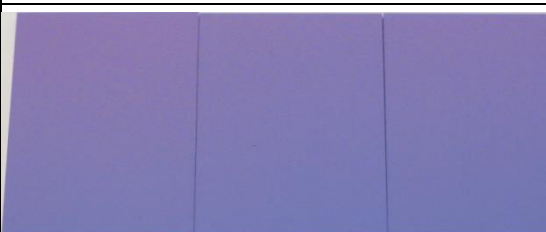
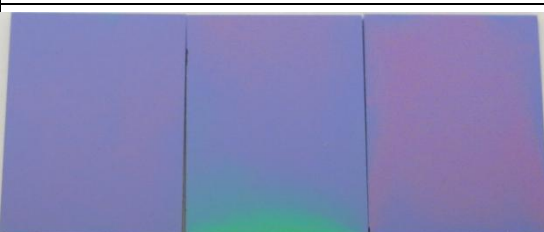
Table 13 shows various packaging films before and after soaking them in 67°C PBS for 70 days. Among films deposited by PECVD, only DLC and SiOC did not have signs of corrosion and their thickness remained stable after immersion in 67°C PBS for 70 days. ALD films of Alumina and Titania did not show visible changes. VASE measurements confirmed there were no significant changes of thickness for these films.

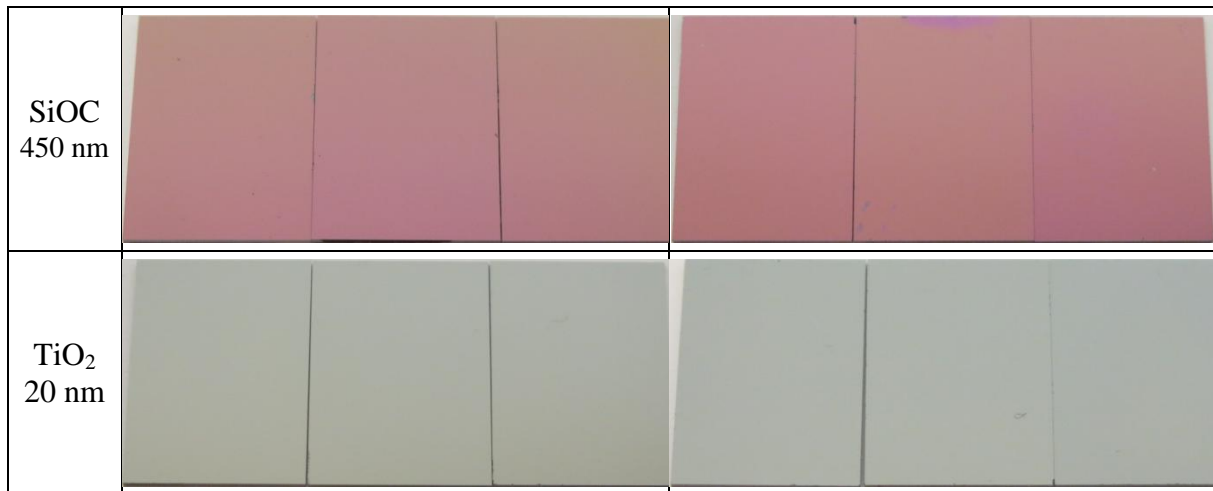
Thin films of BN, SiC, SiO_2 and SiN had clear signs of corrosion. It was also clear from VASE measurements that the optical properties and composition of films was severely affected by this aging test.

Corrosion rates of $2.0 \pm 0.2 \mu\text{m}/\text{yr}$ for SiN and $0.10 \pm 0.06 \mu\text{m}/\text{yr}$ for SiO_2 films were obtained in PBS heated to 67°C in the oven. Although higher temperatures typically produce faster reaction rates, corrosion rates of SiO_2 and SiN films in 67°C PBS inside the oven were 23–46% lower than those obtained in 57°C PBS on a hot plate (see again Figure 58).

Smaller corrosion rates of aging tests in the oven are probably due to lower aeration and hence lower concentration of dissolved oxygen available for corrosion reactions. It is well known that corrosion of materials is strongly influenced by the amount of dissolved oxygen in the fluid [147]. Lower aeration in body fluids explains as well why some ceramics like SiN have lower corrosion rates *in vivo* [148], [146].

Table 13: Aging test of packaging films in PBS solution heated to 67°C in convection oven.

Film	Initial	+ 70 days in 67°C PBS
Al ₂ O ₃ 20 nm		
BN 50 nm		
SiC 100 nm		
DLC 100 nm		
HfO ₂ 20 nm		
SiN 100 nm		
SiO ₂ 500 nm		



Conclusion

An aging test method to quantify the degradation of packaging layers in a solution that simulates the human blood has been proposed. This aging test method is well adapted for the screening of biocompatible packaging layers. Further tests to measure the biodegradation of packaging layers in biological mediums such as FBS (Fetal Bovine Serum) are interesting to provide a good comparison of corrosion rates *in vitro* and *in vivo*.

Films of Al₂O₃, TiO₂, SiOC and DLC were chemically inert to aging tests in PBS solution heated to 67°C in oven. The irregular and inhomogeneous corrosion of other films suggests that chemical etching of films occurs at such high temperature. It is unlikely such etching would take place at 37°C. Therefore, films of BN, HfO₂, SiC, SiO₂ and SiN should not be discarded as encapsulation films of medical devices based on results of aging tests performed at temperatures of 67°C or higher.

3.2.3. Biodegradation tests in 37°C NaCl/FBS

A reliable micro packaging method needs to know rather precisely the degradation rates of packaging films in chemical environments similar to implantation. PBS solution is not enough to model the interaction between the surface of implanted materials and biomolecules such as peptides and proteins [11]. It is thus necessary to design materials degradation experiments that closely resemble the conditions found by medical implants.

The biodegradation tests presented here were designed to quantify the degradation rate of packaging thin films in a biological medium representative to cardiac implants: a saline solution of 0.9% NaCl supplemented with Fetal Bovine Serum (FBS). The globular protein Bovine Serum Albumin (BSA) is a major component of FBS, and it has been reported by Hedberg et al. that saline solutions supplemented with BSA are more chemically aggressive than simple PBS [76]. As few studies are available about the degradation rates of ceramic thin films in biological environments [76], we decided to evaluate selected packaging films in the biological medium of NaCl/FBS in order to study their behavior in chemical conditions more representative of *in vivo* implants.

Ten materials reported in the literature as compatible with biological applications were studied: Al₂O₃, BN, Diamond Like Carbon, HfO₂, SiC, SiN, SiO₂, SiOC, TiO₂ and ZnO [95][149][71][72][96]. Thin films of these materials were deposited on wafers of polished p-type silicon (100). Coupons of size 20x15 mm² were diced from these wafers.

Table 14 resumes the different films deposited by either Atomic Layer Deposition (ALD) in a Fiji F200 machine from Cambridge Nanotech Inc. or Plasma-Enhanced Chemical Vapor Deposition (PECVD) in a Centura 5200 machine from Applied Materials Inc. Samples were kept inside a nitrogen chamber until the biodegradation tests were performed.

Prior to the biodegradation tests, coupons were submitted to a typical cleaning protocol with ethanol and a common detergent soap used in biological laboratories, Triton X-100. Next, coupons underwent a standard cycle of sterilization with Ethylene Oxide (EtO) consisting of 180 min of preconditioning at 50% relative humidity and 240 min of exposure.

Table 14: Thin films deposited on silicon substrates for tests in 37°C NaCl/FBS.

Material	Avg. thickness /nm	Fabrication
Al ₂ O ₃	20	ALD 250°C
HfO ₂	20	ALD 250°C
TiO ₂	20	ALD 250°C
ZnO	20	ALD 250°C
SiN	100	PECVD 400°C
SiO ₂	500	PECVD 400°C
SiOC	450	PECVD 400°C
SiC	100	PECVD 350°C
BN	50	PECVD 400°C
DLC (a-CH)	100	PECVD 400°C

Biodegradation tests were performed for four weeks at 37°C in a NaCl solution (0.9 g/L) supplemented with 10% volume of Fetal Bovine Serum (FBS). This biological medium was changed every 48 hours. Coupons were sterilized by immersion in ethanol at 70°C, De-Ionized (DI) water and irradiation with UV light (250 nm) before being re-immersed in a new saline FBS medium.

Changes in thickness and chemical composition were monitored before and after each test by Variable Angle Spectroscopic Ellipsometry (VASE) and X-ray Photon electron Spectroscopy (XPS). Prior to measurements, sample coupons were rinsed sequentially with DI water, acetone, isopropyl alcohol and DI water. A nitrogen blow gun was used to remove the excess of water from coupons, before being dehydrated on a hot plate at 125°C for 15 min.

The film thickness of each coupon was determined by VASE. Experimental errors of ±2 nm can be expected for thickness measurements due to the difficulty of locating exactly the same spot on the coupon.

XPS measurements were performed with Ka1 radiation of Aluminum (excitation 1486.6 eV, spot size 100 µm) at a collection angle of 45° relative to the surface normal vector, giving a penetration depth of 6.4 nm in SiO₂. 63% of the intensity was emitted below 3 nm.

Results and discussion

The variation of film thickness for the different materials is presented in Table 15. Each value is the average change of thickness of three coupons rounded to the nearest unit.

Table 15: Change of thickness (nm) after different degradation tests on silicon coupons.

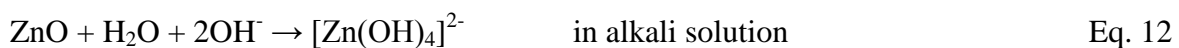
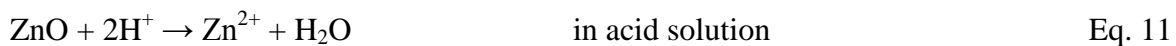
Film	Cleaning with ethanol and soap	Sterilization with EtO	27 days in 37°C NaCl/FBS
20 nm TiO ₂	0	0	0
50 nm BN	0	0	0
100 nm DLC	0	0	0
20 nm HfO ₂	0	0	0
100 nm SiC	⇒	⇒	⇒
450 nm SiOC	0	0	0
500 nm SiO ₂	0	0	-15
100 nm SiN	0	0	-50
20 nm Al ₂ O ₃	0	0	a
20 nm ZnO	-7	-7	b

^a Film disappeared after 27 days of test.

^b Film disappeared after 1 day of test.

Cleaning with ethanol and soap

All films, except ZnO, were stable to the cleaning protocol with ethanol and detergent. A change of thickness of 7 nm was detected for the ZnO coupons after this cleaning procedure. This loss of thickness is probably due to the amphoteric behavior of zinc oxide that produces soluble ions in alkali and acid solutions [150, p. 640] :



Sterilization with EtO

The sterilization procedure with EtO did not produce a significant change of thickness or chemical composition of coupons; even for coupons of ZnO. Parameters psi and delta of ellipsometry spectroscopic are very sensitive to changes of thickness and morphological

structure of thin films [151]. These parameters did not change after the sterilization procedure with EtO, indicating the films were not affected by this procedure. One example of a film unchanged after sterilization with EtO is shown in Figure 64.

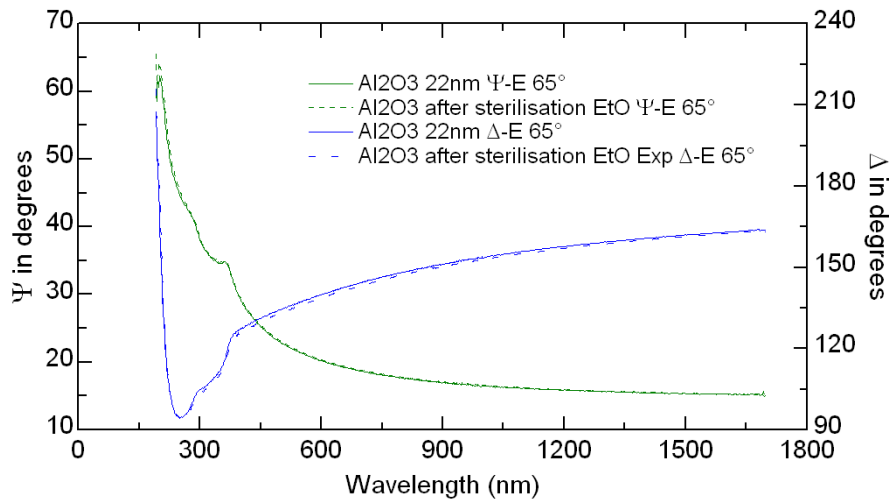


Figure 64: VASE spectra of one Al_2O_3 film before and after sterilization with EtO.

Immersion in 37°C NaCl/PBS

Biodegradation tests in saline solution supplemented with FBS had a negative impact on coupons of Al_2O_3 , SiN, SiO_2 , and ZnO. Especially for Al_2O_3 and ZnO films that disappeared completely (Figure 65 and Figure 66). By linear extrapolation from degradation rates in the NaCl/FBS medium, average dissolution rates of deposited films are 8 $\mu\text{m}/\text{yr}$ for ZnO, 0.7 $\mu\text{m}/\text{yr}$ for SiN, 0.3 $\mu\text{m}/\text{yr}$ for Al_2O_3 , and 0.2 $\mu\text{m}/\text{yr}$ for SiO_2 films. Similar values have been reported for *in vivo* degradation tests of PECVD silicon nitride and silicon oxide [146], [152].

These film dissolution rates, although apparently small, are problematic for the corrosion protection of metallic redistribution layers in microelectronic components with openings in the packaging film (e.g. biosensors), because they allow infiltration of corrosive liquid mediums inside the silicon device and device failure occurs as consequence [25]. For implants where the life of the patient depends on the correct functioning of the medical device, these dissolution rates are not acceptable as the chemical inertness of the packaging film must be guaranteed.

XPS measurements confirmed the decomposition of Al_2O_3 , SiN , SiO_2 , and ZnO films in 37°C NaCl/FBS . In general, a surface enrichment in Na , Cl and Si atoms was recorded after the degradation tests in both biological mediums. The XPS lines of Zn (Figure 66) and Al (Figure 65) disappeared after one day and 27 days immersed in the NaCl/FBS medium, respectively.

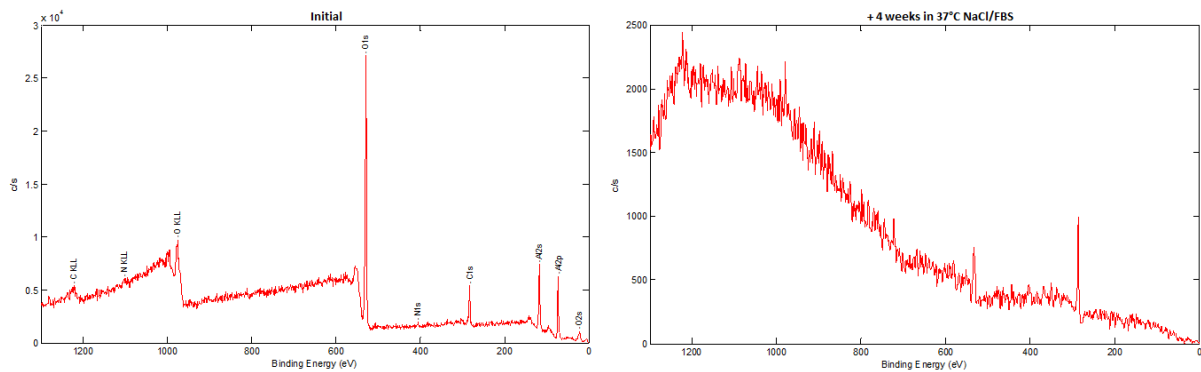


Figure 65: General XPS of Al_2O_3 film before (left) and after (right) 27 days in NaCl/FBS .

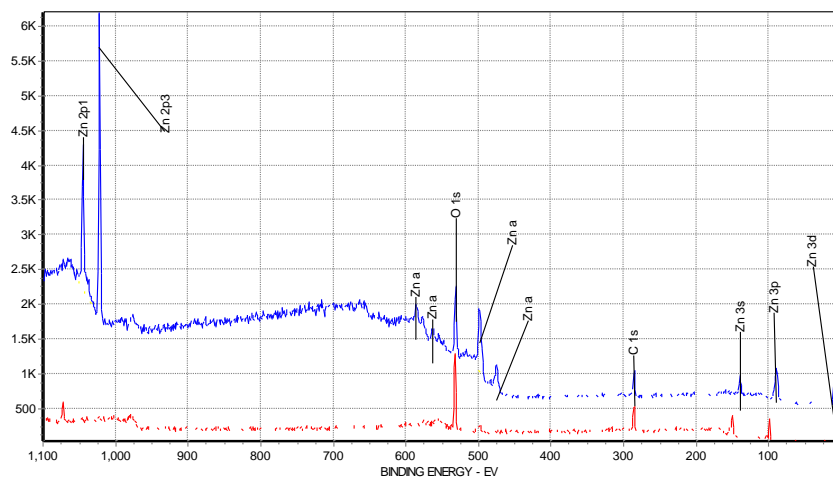


Figure 66: General XPS of ZnO film before (blue) and after (red) 24h in NaCl/FBS medium.

Results of accelerated degradation tests in $>57^\circ\text{C}$ PBS are not necessarily representative of the real conditions faced by packaging materials in physiological environments (Figure 67). On one hand, they overestimate greatly the dissolution rates of SiN films compared to *in vivo* dissolution rates reported by Maloney *et al.* [146].

On the other hand, they fail to predict the decomposition of Al_2O_3 films in complex biological environments like the NaCl/FBS medium (Figure 65). They also underestimate by a factor of >4 the dissolution rate of SiO_2 compared to *in vivo* rates reported by Maloney *et al.* [143],

which explains the smaller than *in vivo* corrosion rates obtained for Si coupons in PBS at 67°C (page 98).

Therefore, extrapolation of results of accelerated degradation tests in PBS should be done carefully, especially when predicting the aging behavior of permanent implants. Biodegradation tests in complex biological environments like the NaCl/FBS medium are more pertinent to predict the *in vivo* behavior of biocompatible films used for encapsulating implantable medical micro devices.

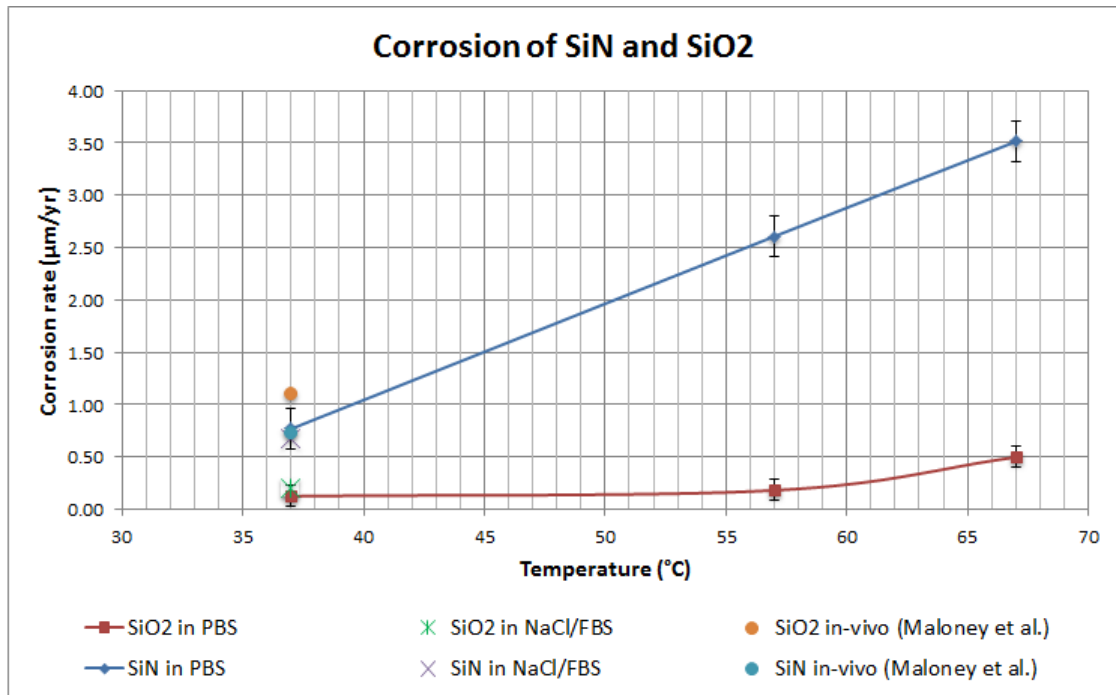


Figure 67: Corrosion rates of SiN and SiO₂ films in PBS and *in vivo* environments.

Conclusion

Six thin films (BN, DLC, HfO₂, SiC, SiOC, and TiO₂) were chemically stable after standard biomedical procedures of cleaning, sterilization with EtO and biodegradation tests in NaCl/FBS. Other four films were not stable in NaCl/FBS and had average dissolution rates of 8 µm/yr for ZnO, 0.7 µm/yr for SiN, 0.3 µm/yr for Al₂O₃, and 0.2 µm/yr for SiO₂. These *in vitro* dissolution rates are in good agreement with values reported for *in vivo* degradation tests [146], [152].

Al₂O₃ films were stable in PBS, but they were not stable and dissolved in the NaCl/FBS medium, which is in good agreement with the response *in vivo* of aluminum oxide implants [75, p. 95] and studies reporting the dissolution over time of Al₂O₃ films on silver [153] and stainless steel substrates [154].

3.3. Biocompatibility tests

Some materials are well known for their biocompatibility in the scientific literature. Nonetheless, biochemical contamination or different manufacturing processes can turn materials *a priori* biocompatible into materials not suitable for medical implantation. For this reason, novel packaging materials must be tested at first *in vitro* to assess their effects on cell viability and cellular morphology. The guideline ISO 10993-5 establishes that materials subject to *in vitro* cytotoxicity tests ought to be evaluated with a standard fibroblast cell culture (L929). A fibroblast is a type of cell that synthesizes the extracellular matrix and collagen, and plays a critical role in wound healing.

Silicon coupons with a full sheet of packaging layer were sterilized by immersion in ethanol at 70°C and irradiation with UV light (250 nm). Then, *in vitro* cytotoxicity tests were performed by the extraction method (Figure 68). The packaging layer was placed in contact with a typical cell culture medium supplemented with serum for 24h at 37°C in an incubator. Each condition produces 3 mL of extract (resulting in a ratio of 3 cm² per mL of extract). Afterward, 100 µL of extract are placed in contact with L929 cells for 24h at 37°C. Every material was evaluated twice by the cytotoxicity test with three points of measure per test (9 samples) and then submitted to the test of morphology (3 samples). In total, 12 coupons or more need to be measured per material.

Positive control for cell viability assays was polyether urethane (PU) film containing 0.1% zinc diethyldithiocarbamate (ZDEC). Negative control was high density polyethylene (HDPE). The cell viability was evaluated with the help of an indicator of metabolic activity called MTS. MTS is yellow colored and water soluble. It is metabolically reduced by viable cells to formazan, which is blue/violet colored and has a maximum of light absorption at 490–500 nm. The color intensity determined by photometric measurements at 492 nm correlates with the number of viable cells.

In parallel, the cellular morphology produced by contact with the different materials was evaluated by observation under a microscope with fluorescent markers that target the nucleus and cellular cytoplasm.

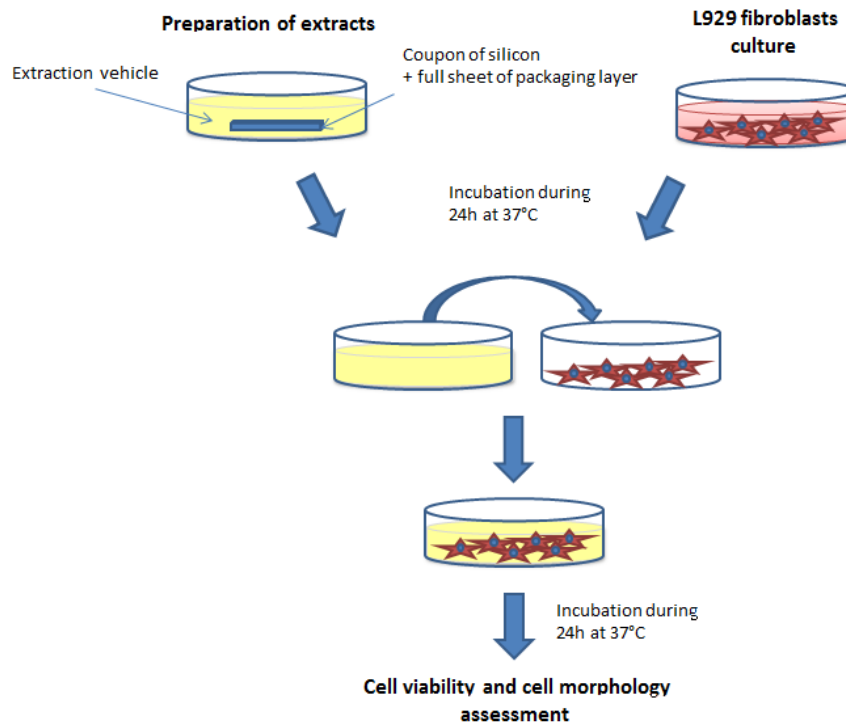


Figure 68: Scheme of the cytotoxicity test by the extraction method of ISO 10993-5.

Results and discussion

A material is considered to be non-cytotoxic when the cell viability of its pure extract is $>70\%$. Pure extracts of all films, except for DLC and ZnO, were found to be non-cytotoxic to L929 cells (Table 16). If pure extracts of DLC and ZnO are respectively diluted to a concentration of 50% and 10%, these films do not pose a cytotoxic risk. This means that if the exposed areas of ZnO and DLC are 3 cm^2 or larger, there is a high risk of cytotoxicity in your device. But if the exposed area is $<1.5 \text{ cm}^2$ for DLC and $<0.3 \text{ cm}^2$ for ZnO, these materials can be considered non-cytotoxic according to the norm ISO 10993-5.

Biocompatibility will depend on how much area of your device is made of these materials and is exposed to the external environment. For miniaturized medical devices with total volumes smaller than 1 cm^3 , it might be OK to use DLC and ZnO. That is assuming that these materials are biologically stable and do not degraded in physiological environments. DLC films are probably safe to use if their exposed area in your device is smaller than 1.5 cm^2 .

However, ZnO films should be avoided whenever possible because they corrode in water (Figure 62). This corrosion produces free ionic zinc (Zn^{2+}) that is known to be toxic for

eukaryotic cells above concentrations of 60 ng/L [155, p. 801]. A 20 nm film of ZnO deposited on a surface of 3.0 cm² contains, if fully dissolved to Zn²⁺, as much as 25 500 ng of Zn²⁺, which is well above the previous limit of toxicity for eukaryotic cells such as the L929 cell line. In fact, free ionic zinc is so toxic that compounds containing Zn²⁺ (e.g., ZDEC and ZDBC) are used as positive controls for various cytotoxicity tests [156].

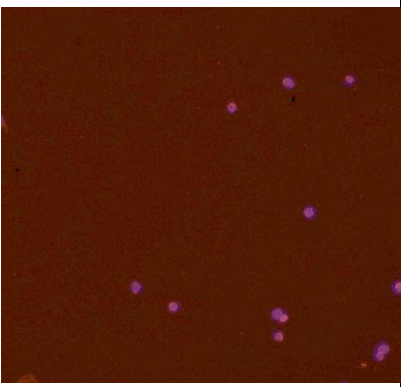
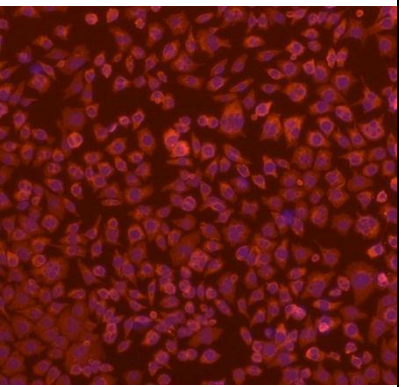
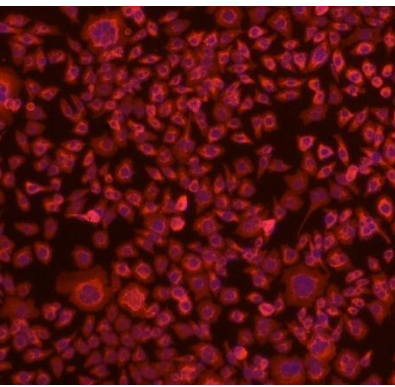
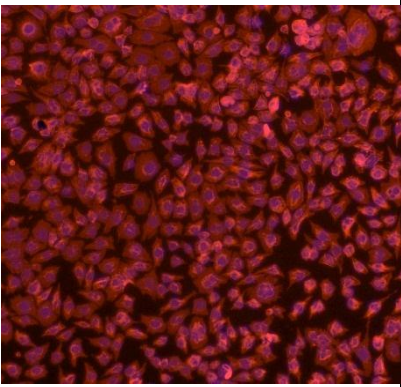
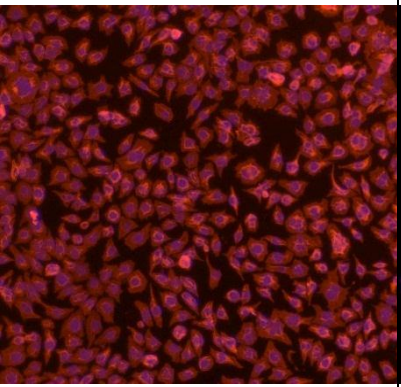
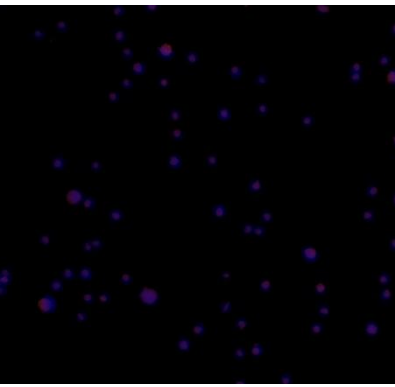
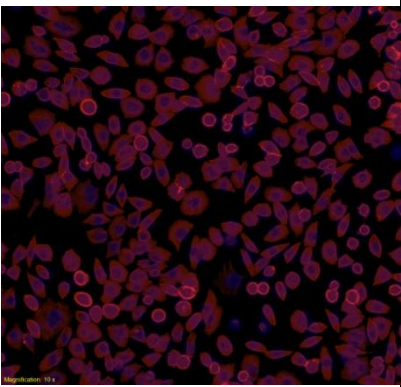
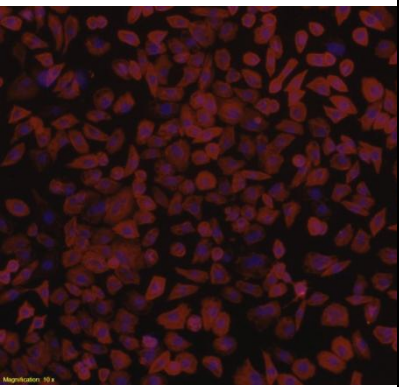
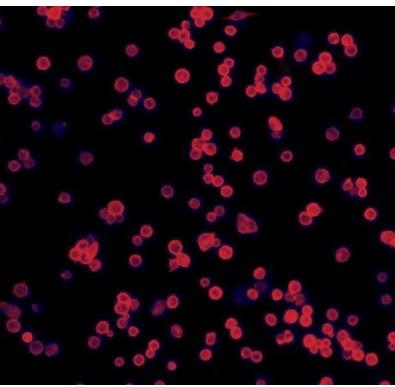
On the other hand, it was surprising to find DLC films were cytotoxic. Alas, it is known that DLC and carbon nanotubes containing amorphous sp² carbon are potentially cytotoxic because they produce Reactive Oxide Species (ROS) [123], [157]. Although deposited DLC films contain a high percentage of saturated sp³ carbon (see XPS analysis of DLC in page 78), the remaining percentage of unsaturated amorphous sp² carbons induce ROS such as peroxynitrite (ONOO⁻), superoxide anion (O₂^{•-}) and other free radicals. Such radical species render toxic the extracts collected from silicon coupons coated with DLC (a-CH) films.

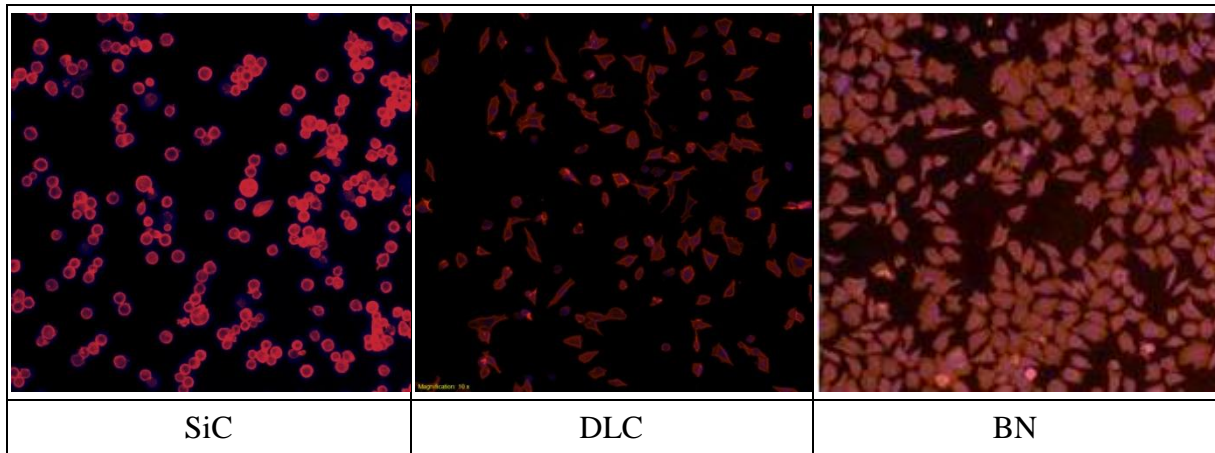
Table 16: Cell viability of pure extracts collected from Si coupons coated with various films.

Film	Cell viability (%)	Cytotoxic potential
Positive control (PU-ZDEC)	8.6	Cytotoxic
Negative control (HDPE)	100	No cytotoxic
20 nm Al ₂ O ₃ 250°C (pure extract)	97.4	No cytotoxic
20 nm HfO ₂ 250°C (pure extract)	100	No cytotoxic
20 nm TiO ₂ 250°C (pure extract)	97.7	No cytotoxic
50 nm BN 400°C (pure extract)	100	No cytotoxic
100 nm SiN 400°C (pure extract)	100	No cytotoxic
100 nm SiO ₂ 400°C (pure extract)	96.1	No cytotoxic
100 nm SiOC 400°C (pure extract)	99.0	No cytotoxic
100 nm SiC 350°C (pure extract)	100	No cytotoxic
100 nm DLC 400°C (pure extract)	48.0	Cytotoxic
100 nm DLC 400°C (50% extract)	73.1	No cytotoxic
100 nm DLC 400°C (10% extract)	93.6	No cytotoxic
100 nm DLC 400°C (1% extract)	93.9	No cytotoxic
20 nm ZnO 250°C (pure extract)	6.1	Cytotoxic
20 nm ZnO 250°C (50% extract)	10.2	Cytotoxic
20 nm ZnO 250°C (10% extract)	100	No cytotoxic
20 nm ZnO 250°C (1% extract)	100	No cytotoxic

Cell morphology tests in parallel showed that deposited packaging layers of alumina, titania, hafnia, silicon nitride, silicon dioxide, silicon oxycarbide, silicon carbide and boron nitride do not induce adverse biocompatibility effects (Table 17). There was no alteration of the cell morphology for these deposited films. This is in good agreement with reported literature on the biocompatibility of these materials.

Table 17: Cell morphology caused by various films deposited on silicon coupons.

		
Positive control	Negative control	Al ₂ O ₃
		
HfO ₂	TiO ₂	ZnO
		
SiN	SiO ₂	SiOC



3.4. Diffusion Barrier tests

There are many toxic elements that can diffuse out of silicon devices and have disastrous effects on living organisms. Copper is one of such elements. It is essential for all living forms in small concentrations. But, it is harmful at concentrations higher than 1.3 mg/L in drinking water and 4–8 μg Cu per gram of soft tissue [158], [159, p. 523].

As copper can rapidly diffuse (at $\sim 2 \mu\text{m/s}$) through crystalline silicon wafers at 37°C [160, p. 259], silicon coupons containing toxic copper are good test vehicles to assess the efficiency of a given encapsulant as diffusion barrier.

Fibroblast cells like the L929 are very sensitive to the presence of toxic substances such as zinc and copper ions, so it was decided to evaluate the efficiency of selected deposited films against thermal diffusion of copper ions by means of *in vitro* cytotoxicity tests. The test protocol and materials used were explained previously. The only difference is that prepared silicon substrates were coated with $1.5 \mu\text{m}$ of copper deposited by Physical Vapor Deposition. Then, films of Al_2O_3 , HfO_2 , SiO_2 and TiO_2 were deposited on these coupons because they were already known to be relatively stable in PBS (p.90) and dense (p.72). Multilayers of Al_2O_3 and TiO_2 were also tried as diffusion barriers because it has been reported they are good coatings to prevent corrosion of copper substrates [161].

Results and discussion

The viability of L929 cells cultivated for 24h at 37°C with pure and diluted extracts collected from copper coupons encapsulated with various packaging films are shown in Table 18. None of the pure extracts collected from coated samples passed the non-cytotoxicity criteria of cell

viability larger >70%. Nonetheless, barriers of Al₂O₃+TiO₂ deposited by 200°C ALD were relatively better to prevent copper diffusion. Better results can be expected by increasing the thickness of all deposited barriers.

Table 18: Cell viability of extracts collected from copper coupons coated with various barriers.

Barrier	Cell viability (%)	Cytotoxic potential
20 nm Al ₂ O ₃ 250°C (pure extract)	1.8	Cytotoxic
20 nm Al ₂ O ₃ 250°C (50% extract)	0.5	Cytotoxic
20 nm Al ₂ O ₃ 250°C (10% extract)	4.6	Cytotoxic
20 nm Al ₂ O ₃ 250°C (1% extract)	100	No cytotoxic
20 nm HfO ₂ 250°C (pure extract)	0	Cytotoxic
20 nm HfO ₂ 250°C (50% extract)	0	Cytotoxic
20 nm HfO ₂ 250°C (10% extract)	35.2	Cytotoxic
20 nm HfO ₂ 250°C (1% extract)	92.7	No cytotoxic
100 nm SiO ₂ 400°C (pure extract)	16.7	Cytotoxic
100 nm SiO ₂ 400°C (50% extract)	29.9	Cytotoxic
100 nm SiO ₂ 400°C (10% extract)	57.3	Cytotoxic
100 nm SiO ₂ 400°C (1% extract)	86.2	No cytotoxic
20 nm TiO ₂ 250°C (pure extract)	1.0	Cytotoxic
20 nm TiO ₂ 250°C (50% extract)	0	Cytotoxic
20 nm TiO ₂ 250°C (10% extract)	36.3	Cytotoxic
20 nm TiO ₂ 250°C (1% extract)	87.7	No cytotoxic
20 nm Al ₂ O ₃ + 20 nmTiO ₂ 200°C (pure extract)	25	Cytotoxic
20 nm Al ₂ O ₃ + 20 nmTiO ₂ 200°C (50% extract)	31	Cytotoxic
20 nm Al ₂ O ₃ + 20 nmTiO ₂ 200°C (10% extract)	78	No cytotoxic
20 nm Al ₂ O ₃ + 20 nmTiO ₂ 200°C (1% extract)	96	No cytotoxic
(2 nm Al ₂ O ₃ + 2 nmTiO ₂) ¹⁰ 250°C (pure extract)	0	Cytotoxic
(2 nm Al ₂ O ₃ + 2 nmTiO ₂) ¹⁰ 250°C (50% extract)	0	Cytotoxic
(2 nm Al ₂ O ₃ + 2 nmTiO ₂) ¹⁰ 250°C (10% extract)	10.9	Cytotoxic
(2 nm Al ₂ O ₃ + 2 nmTiO ₂) ¹⁰ 250°C (1% extract)	100	No cytotoxic

3.5. Helium permeability tests

The hermeticity provided to packages by encapsulants is function of the permeation rates of Oxygen, Water Vapor and Helium across them. As the measurements of OTR and WVTR are time-consuming and far too complicated for the purpose of screening packaging layers, alternative methods using Helium gas and UHV mass spectrometers have been proposed [162], [163]. The rationale behind this method is that packaging layers which are a bad barrier against helium gas are typically bad barriers against oxygen and water vapor as well. Therefore, Helium Transmission Rates (HeTR) are correlated with WVTR and OTR for choosing best packaging materials.

Permeation rates of helium through a material are especially interesting because they are related to helium leaks of hermetic packages sealed with organic adhesives. According to the mathematical model proposed by Traeger [22], [67], the time needed by a hermetic package sealed with a polymeric lid sealant is given by:

$$t = \frac{Vl}{KART} \ln \left(\frac{p_0 - p_1}{p_0 - p_2} \right) \quad \text{Eq. 13}$$

Where t is the time needed to reach pressure p_2 in seconds

V is the free volume of the container in cm^3

l is the length of the diffusion path presented by the sealant in cm

K is the permeability of the sealant in $\text{g cm} / \text{cm}^2 \text{ s torr}$

A is the area of the seal exposed to the permeant in cm^2

R is the gas constant = $82.05746 \text{ atm cm}^3 / \text{K mol}$

T is the temperature in K

p_0 is the external gas pressure in torr

p_1 is the initial, internal gas pressure in torr

p_2 is the final, internal gas pressure in torr

This equation can be used to calculate the package lifetimes offered by different materials to hermetically sealed cavities. Figure 5 of page 31 is one example. There, Eq. 13 was used to

plot the time needed for a cavity of 1.81 cm³ and seal area of 17.5 mm² to reach 50% of exterior humidity as function of the length and permeability of the sealant at *standard* ambient conditions of 25°C and 1 atm. The molar permeability of a material is defined by:

$$K = \left(\frac{q}{\Delta p}\right) \frac{l}{A} \quad \text{Eq. 14}$$

Where q is the molar flux of gas through a membrane of area A and length l under a partial pressure gradient Δp across the membrane [164]. Inserting Eq. 14 in Eq. 13 and assuming there is no gas initially present in the cavity so $\Delta p = p_0 - p_1 = p_0$,

$$t = \frac{Vp_0}{qRT} \ln\left(\frac{p_0}{p_0 - p_2}\right) \quad \text{Eq. 15}$$

Eq. 15 can be reorganized into,

$$t = -\frac{Vp_0}{qRT} \ln\left(1 - \frac{p_2}{p_0}\right) \quad \text{Eq. 16}$$

The flux of gas through the membrane in atm-cm³/s can be defined as,

$$L = qRT \quad \text{Eq. 17}$$

Where q is the molar flux of gas through the material, R is the gas constant and T is the temperature. Inserting Eq. 17 in Eq. 16,

$$t = -\frac{Vp_0}{L} \ln\left(1 - \frac{p_2}{p_0}\right) \quad \text{Eq. 18}$$

Eq. 18 is closely related to the mathematical relationship given by Eq. 19 between the amount of gas leaving a package and the package lifetime [25, p. 249],

$$t = -\frac{VP_0}{L_{H_2O}} \ln\left(1 - \frac{Q_{H_2O}}{\Delta p_{i,H_2O}}\right) \quad \text{Eq. 19}$$

Where t is the package lifetime in seconds

$$L_{H_2O} \text{ is the standard water leak rate} = L_{He} \cdot \sqrt{\frac{M_{He}}{M_{H_2O}}} = 0.471 * L_{He} \text{ in atm-cm}^3/\text{s}$$

V is the available internal volume of the cavity in cm^3

P_0 is the standard atmospheric pressure = 1 atm

Q_{H_2O} is the water that has leaked in the cavity

$\Delta p_{i,H_2O}$ is the initial difference in water partial pressure between the outside and the internal cavity.

Eq. 19 can be used to calculate, for example, the helium leak rate (L_{He}) needed to ensure a package lifetime of 10 years in the human body. The water partial pressure in the human body (at 37°C) is 0.062 atm according to Antoine's Eq. 1. Assuming there is no water present inside the package at time zero (thus $\Delta p_{i,H_2O} = 0.062$ atm) and defining 5000 ppm as the moisture limit inside the internal cavity (thus $Q_{H_2O} = 0.005$ atm), a package with available internal volume of 0.1 cm^3 (which is a reasonable value for miniaturize medical devices) must have a helium leak rate smaller than $5.7 \times 10^{-11} \text{ atm-cm}^3/\text{s}$ to ensure a package lifetime of 10 years in the human body.

Now, let us assume a geometrical configuration for a miniaturized medical device. Souriau *et al.* reported a seal area of $8.0 \times 10^{-4} \text{ cm}^2$ and seal length of $1.0 \times 10^{-2} \text{ cm}$ for a miniaturized physiological monitor of the cardiac activity called VTC [60]. Inserting these values in Eq. 14,

$$K_{He} = \left(\frac{L_{He}}{RT\Delta p}\right) \frac{l}{A} \quad \text{Eq. 20}$$

$$K_{He} = \frac{5.7 \times 10^{-11} \frac{\text{atm cm}^3}{\text{s}} \times 1.0 \times 10^{-2} \text{cm} \times 4.0026 \frac{\text{g}}{\text{mol}}}{82.05746 \frac{\text{atm cm}^3}{\text{mol K}} \times 310.15 \text{K} \times 1 \text{atm} \times 8.0 \times 10^{-4} \text{cm}^2}$$

$$K_{He} = 1.1 \times 10^{-13} \frac{\text{g cm}}{\text{cm}^2 \text{s atm}} = 6.1 \frac{\text{cm}^3 \text{mm}}{\text{m}^2 \text{day atm}}$$

This is the helium permeability needed from a polymer lid sealant to ensure a package lifetime of ten years for such miniaturized medical device. It would be explored with a state of the art gas permeameter if such values can be obtained with polymer substrates coated with gas barrier thin films.

A permeable polymer is needed as a substrate to perform helium permeation measurements. Typically, PET is used for this task but as our deposition processes occur at temperatures as high as 400°C, Kapton 200HN™ was chosen as substrate. Kapton substrates of thickness 50.8 μm were used as provided by the supplier (DuPont©) and cut inside a clean room with clean scissors to a 65 mm diameter required by the gas permeameter (Figure 69).

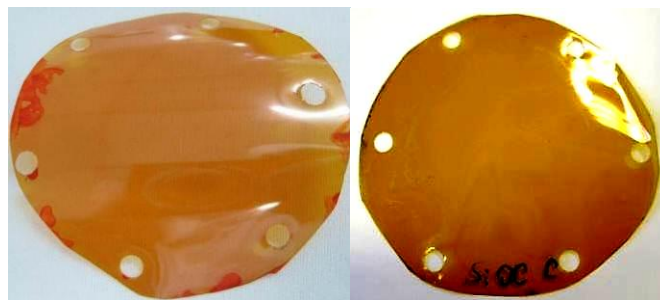


Figure 69: Al₂O₃ (Left) and SiOC (Right) films deposited on Kapton substrates.

Helium permeation measurements were performed with a patented permeameter of INES (French National Solar Energy Institute) which consists of a cell containing the sample in which the upstream side is filled with the gas of which the permeability is to be measured and the downstream side is an ultra-high vacuum chamber encasing a quadrupole analyzer with ionic trap detector and mass spectrometer from MKS E-Vision+. This cell is connected to a gas bench equipped with different permeating gas reserves and a primary vacuum unit,

allowing control of the upstream side atmosphere (Figure 70) [165]. Four samples of each packaging layer were measured in the gas permeameter at 38°C and 0% Relative Humidity.

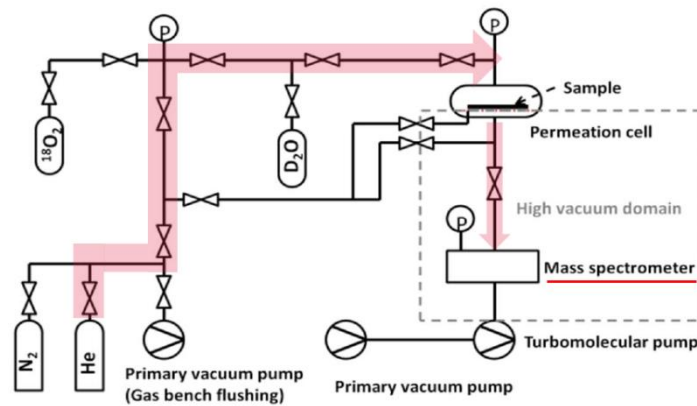


Figure 70: Scheme of the gas permeameter developed by S. Cros et al. [165]

Results and discussion

Results of the helium gas permeability measurements are shown in Table 19 (page 117). Samples with best values of permeability are listed there. The permeability coefficient K is $K=D \cdot S$, where S is the solubility of the gas in the material and D is the diffusion coefficient of the gas. Solubility coefficients are dimensionless and in the range of 10^{-2} – 10^{-3} cm^3 of gas per cm^3 of solid for glass and ceramics [25, p. 234]. D has units of $\text{length}^2/\text{time}$ and was calculated in Table 19 from the lag-time (t) as $D=l^2/6t$, where l is the length of the barrier and the lag-time is the time it takes for the gas to break through the diffusion barrier and approach its steady state leak rate [166].

Barrier Improvement Factor (BIF) is defined as the ratio by which the barrier gas permeability is improved compared to the barrier reference material, which is calculated for example as $123/1.43$ for the second row of Table 19. A BIF of >20 means that such a barrier typically has a WVTR $<10^{-3}$ $\text{g}/\text{m}^2/\text{day}$ and is therefore a good candidate for the packaging of Organic Solar Cells and Implantable Devices [162], [163]. On the contrary, a BIF value close to 1 has two possible meanings. First one is that the deposited packaging film is not dense enough to reduce the permeability of the substrate against the flow of helium gas. Second possible meaning is that the coating has large defects, pinholes or cracks due to an imperfect coating process or cracking of the rigid inorganic layer on the flexible substrate [163]. Indeed, Kapton

is highly flexible and materials like SiC and DLC are known for their hardness and brittleness. But the density of SiC and DLC films deposited on silicon substrates is close to 1.3 g/cm^3 , which is smaller than the density of the Kapton substrate (1.42 g/cm^3) [167]. As density is defined as mass per volume, films of SiC and DLC deposited on relatively porous Kapton substrates have probably a density lower than 1.3 g/cm^3 . Thus, deposited films of SiC and DLC do not improve the gas permeability of Kapton substrates due to their low density. A similar argument explains the small BIF values obtained from BN films (density 1.6 g/cm^3 on Si) deposited on Kapton.

Table 19: Helium Permeability of different packaging layers deposited on Kapton substrates.

Helium Gas Barrier	Permeability ($\text{cm}^3 \text{ mm m}^{-2} \text{ d}^{-1} \text{ atm}^{-1}$)	Diffusion (cm^2/s)* 10^{-7}	He BIF
Kapton (Reference)	123	8.7	1.0
+ 20 nm Al_2O_3 250°C	1.43	0.2	86.0
+ 20 nm HfO_2 250°C	2.56	3.0	48.0
+ (2 nm Al_2O_3 +2 nm TiO_2) ¹⁰ 250°C	3.07	3.2	40.1
+ 100 nm SiO_2 400°C	3.95	5.3	31.1
+ 100 nm SiN 400°C	4.98	5.8	24.7
+ 20 nm TiO_2 250°C	5.07	5.8	24.3
+ 20 nm ZnO 250°C	21.2	7.7	5.8
+ 100 nm SiOC 400°C	103	8.7	N/A
+ 100 nm SiC 350°C	112	8.7	1.1
+ 90 nm BN 400°C	112	8.7	1.1
+ 100 nm DLC 400°C	112	8.7	1.1

SiOC films have also low density ($\sim 2.2 \text{ g/cm}^3$), but in this case there are large defects visible on the Kapton substrates after deposition (Figure 69). This might be due to chemical reactions between SiOC gas precursors SiMe_4 , O_2 , He and carbon atoms in the polyimide structure that destroy the polymer structure [168], [169]. So, it was not possible to determine the helium gas permeability of SiOC by depositing it on Kapton, a polyimide polymer. But judging from the density of the film, a BIF similar to the one obtained for SiO_2 is expected.

It can be seen in Table 19 that Kapton substrates coated with TiO_2 , SiN , SiO_2 , HfO_2 and Al_2O_3 have helium permeability lower than $6.1 \text{ cm}^3 \text{ mm m}^{-2} \text{ day}^{-1} \text{ atm}^{-1}$, which is necessary for a package lifetime of 10 years for a miniaturized medical device with 0.1 cm^3 of available internal volume and dimensions like those of the VTC (Eq. 20). Moreover, a film of 50 nm Al_2O_3 on Kapton would be enough to ensure the same package lifetime for an internal volume of 0.01 cm^3 , which is typical for Micro Systems and MEMS.

Micro Systems and Micro Electro Mechanical Systems (MEMS) have internal cavities as small as 0.001 cm^3 [20]. A cavity of that size would need a true helium leak rate $<5.7 \times 10^{-13} \text{ atm-cm}^3/\text{s}$ to ensure a package lifetime of 10 years. However, most helium leak detectors for quality control during production have a detection limit of $1 \times 10^{-9} \text{ atm-cm}^3/\text{s}$ [20], [59]. In order to assure long package lifetimes, manufacturers of hermetic packages employ getter materials that can absorb a variety of contaminant gaseous species such as hydrogen, water or oxygen and therefore increase the apparent internal volume of the package. For example, 0.001 cm^3 of anhydrous magnesium sulfate can absorb $>1 \text{ cm}^3$ of water vapor [59]. If the apparent internal volume of the MEMS device is increased to 0.1 cm^3 by filling 10% of the cavity with 0.0001 cm^3 of MgSO_4 , such device would need a true He-leak rate of $5.7 \times 10^{-11} \text{ atm-cm}^3/\text{s}$ to ensure a package lifetime of 10 years. This helium leak rate corresponds to a permeability of $6.1 \text{ cm}^3 \text{ mm m}^{-2} \text{ day}^{-1} \text{ atm}^{-1}$ (Eq. 20) and it can be provided by polymer Kapton substrates coated with ceramic thin films listed in Table 19. And it is also measurable by modern helium leak detectors [60].

3.6. Conclusion

Table 20 resumes results obtained for different packaging films from different evaluation tests.

Table 20: Summary of evaluation tests performed on different packaging films.

Barrier film	Width (nm)	Deposit. Temp.	<i>In vitro</i> cytotoxic.	Gas hermetic.	Stability PBS	Stability NaCl/FBS	Diffusion barrier
Al ₂ O ₃ •TiO ₂	40	250°C	good	very good	excellent	excellent	poor
TiO ₂	20	250°C	good	good	excellent	excellent	poor
HfO ₂	20	250°C	good	very good	good	good	poor
Al ₂ O ₃	20	250°C	good	excellent	good	poor	poor
SiOC	100	400°C	good	-	excellent	excellent	poor
DLC (a- CH)	100	400°C	fair	poor	excellent	excellent	poor
SiC	100	350°C	good	poor	good	good	poor
SiN	100	400°C	good	good	poor	fair	poor
SiO ₂	100	400°C	good	good	fair	fair	poor
BN	50	400°C	good	poor	fair	fair	poor
ZnO	20	250°C	poor	poor	very poor	very poor	very poor

Pure extracts of Al₂O₃, BN, HfO₂, SiC, SiN, SiO₂, SiOC and TiO₂ films were confirmed to be non-cytotoxic according to *in vitro* elution tests outlined by the norm ISO 10993-5. There was also no alteration of the cell morphology for these films.

The best deposited encapsulation films in terms of helium gas permeability are in decreasing order: Al₂O₃, HfO₂, SiN, SiO₂ and TiO₂. Combination of these films should provide an effective hermetic packaging.

Packaging layers widely used in microelectronics such as SiN and SiO₂ are corroded by PBS and NaCl/FBS at 37°C. Corrosion rates of these films in both solutions and *in vivo* are given in page 105. Deposited SiO₂ and SiN films are relatively good gas barriers and have corrosion rates of 0.2–1.0 µm per year in 37°C NaCl/FBS. Therefore, for certain applications where

SiO₂ and SiN are not in direct contact with biofluids or the duration of contact is not permanent (>30 days), the usage of these packaging films could be practical.

Packaging films of Al₂O₃ and ZnO as deposited here are not recommended to be used in direct contact with biofluids. If they are used in medical devices, their large degradation rates should be noticed early on in the phase of design and preventive measures should be adopted.

Biological mediums such NaCl/FBS are more relevant than PBS to predict *in vivo* degradation rates of packaging materials intended for human implantation. Packaging layers of a-CH, HfO₂, SiC, SiOC, and TiO₂ have good chemical stability as proved by a film thickness variation below 2 nm after 4 weeks of degradation tests in NaCl/FBS at 37°C. They are therefore good packaging layers for biocompatible encapsulation of medical micro devices that are in contact with chemically aggressive physiological environments.

However, none of deposited packaging films of Table 20 passed the copper diffusion barrier tests designed after the elution test protocol of ISO 10993-5. Yet, 40 nm of Al₂O₃+TiO₂ deposited by 200°C ALD had the best performance as copper diffusion barrier. Better results can be expected by increasing the thickness of deposited barrier films. However, it is extremely time consuming to deposit thicker films of Al₂O₃ and TiO₂ with traditional temporal ALD reactors [113]. Therefore, thicker barriers of PECVD SiO₂ and SiN may be economically interesting to prevent external leaking of toxic substances from silicon devices during implantation. However, such thick PECVD barriers must be protected with biocompatible and biostable films such as HfO₂, SiOC and TiO₂ to prevent early failure of the packaging in biological environments.

Chapter 4: Test Vehicles

Various Test Vehicles were employed during this thesis to develop the technology bricks needed for packaging medical micro devices.

The first one is called VTB1 and contained Redistribution Layers¹ of Copper and other topological features such as metallic pads. Its purpose was to help select best encapsulants for the corrosion protection of Cu RDL in saline solution.

The second one is called VTB2 and served to assess the efficiency of the encapsulants to protect damascene Cu RDL from the chemical attack of saline solutions. In this case, the copper RDL was integrated within a passive layer of silicon oxide and there were no topological features present. Its purpose was to find out if this type of damascene architecture without topology was better for protecting silicon devices from corrosion by saline environments.

The purpose of the third Test Vehicle (VTB3) was to evaluate the ability of selected encapsulants to protect metallic substrates that are easily corroded by saline solutions, like for example tungsten nitride.

The fourth one (VTB4) consisted in developing dicing and etching techniques for the fabrication of unsharpened silicon devices; which help to reduce the reaction of rejection (Foreign Body Reaction) after human implantation.

Analysis and discussion are given for each Test Vehicle and there is a general conclusion about them at the end of this chapter.

¹ A Redistribution Layer (RDL) is an additional metal layer on top of a finished chip that relocates the original pads to another location for advanced packaging features such as flip chip bumping.

4.1. Test Vehicle VTB1

This vehicle test consisted of Copper Redistribution Layers of 1.8 μm fabricated by Electrochemical Deposition (ECD) on a silicon substrate (Figure 71). Copper is known to easily corrode in saline solutions and being toxic at concentrations larger than 4 ppm in soft tissue [159]. So, it was interesting to test the ability of selected packaging layers to prevent copper from diffusing outside the test vehicle.

Test vehicle VTB1 was fabricated by standard photolithography, electrochemical deposition and chemical etching of copper on silicon wafers of 8 inches. Fabrication details can be found elsewhere [64]. Figure 71 shows a cross section view and top view of a VTB1 coupon (size 12x16 mm²).

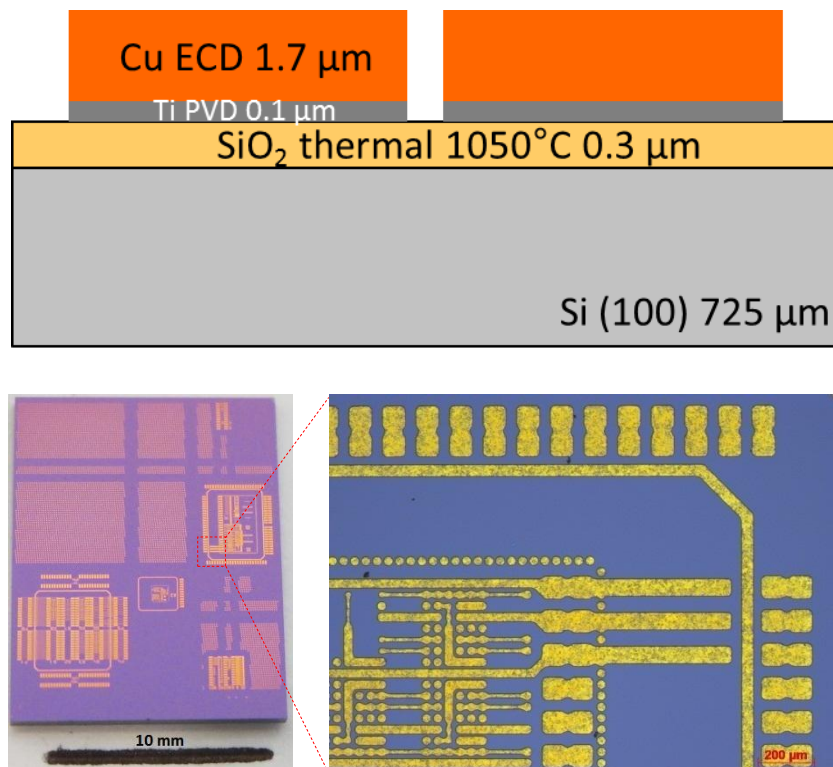


Figure 71: Cross section scheme of test vehicle VTB1 (Top) and upper view (Bottom).

Thin films of 20–100 nm of different encapsulants were deposited on VTB1 test vehicles. Before deposition of films, sample coupons were cleaned by rinsing sequentially with DI

water, acetone, isopropyl alcohol and DI water. Then, a nitrogen blow gun was used to remove the excess of water from coupons, before being dehydrated at 200°C for 10 min.

Coated samples were soaked for several days in PBS solution heated inside a convection oven to 67.0±0.1°C (Figure 72). They were examined during aging tests by photo camera, microscope, and profilometer measurements.

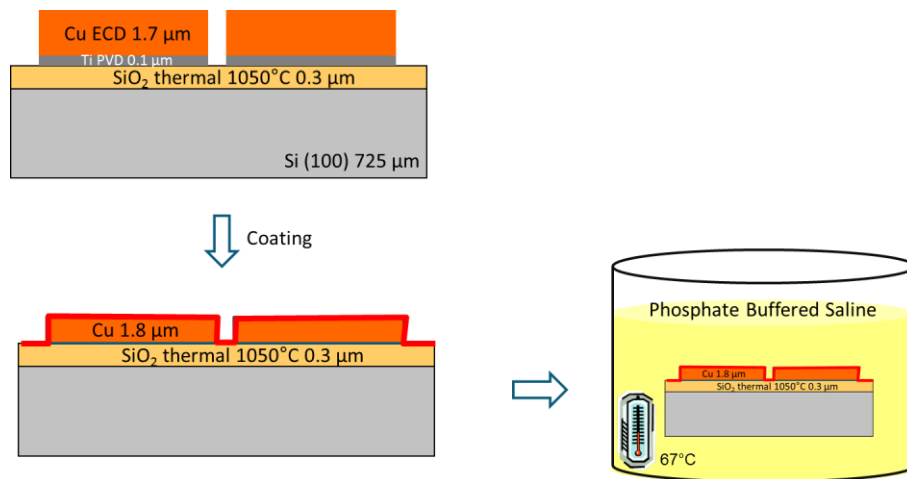


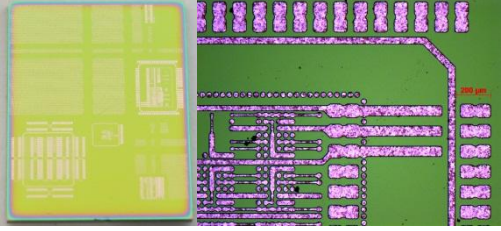
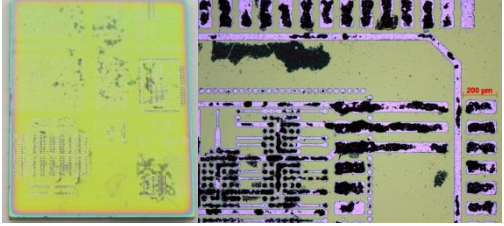
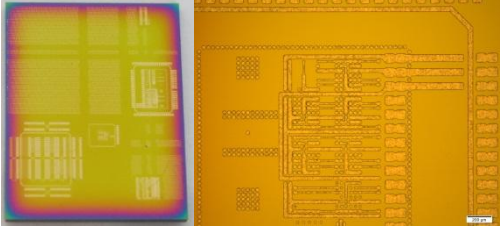
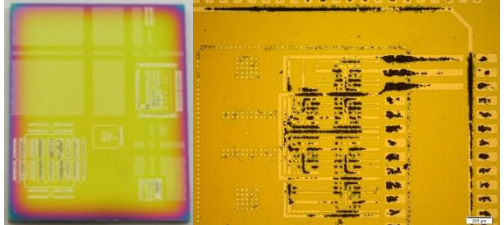
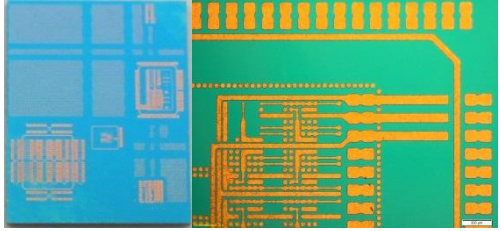
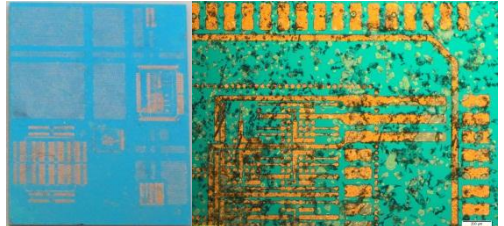
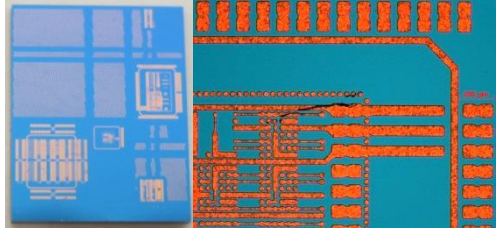
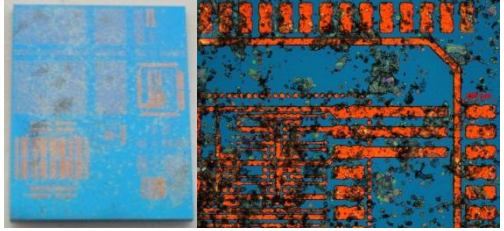
Figure 72: Scheme of accelerated aging tests of VTB1 coupons.

Results and discussion

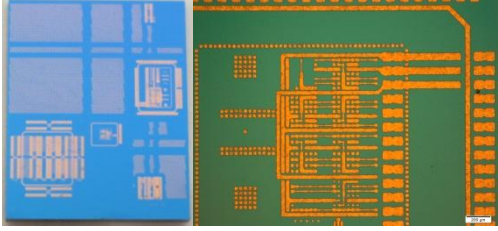
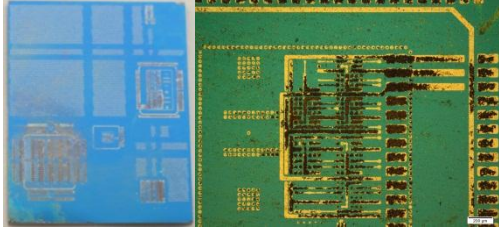
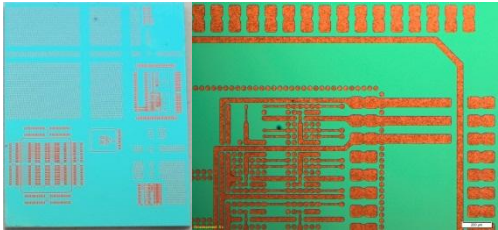
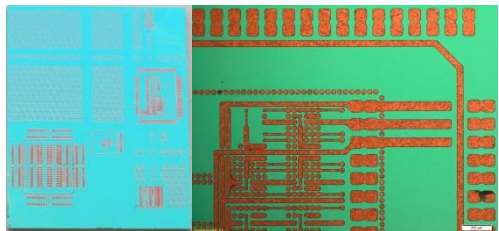
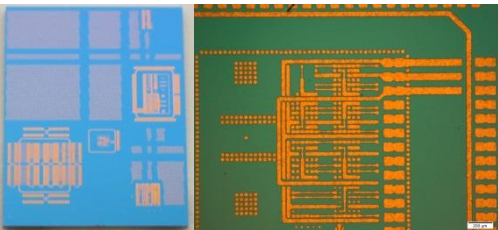
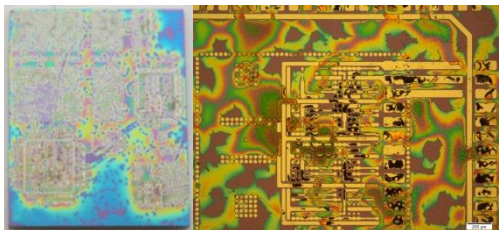
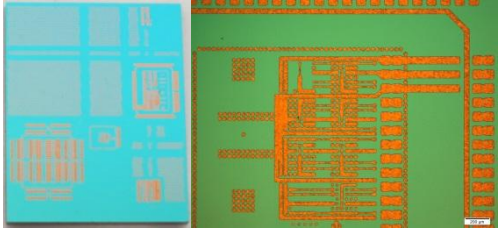
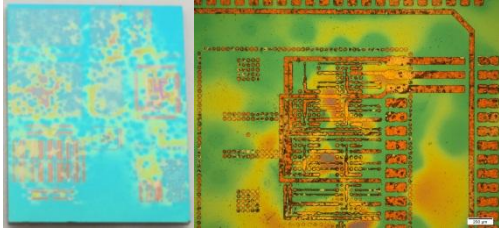
Camera, microscope and profilometer observations of VTB1 test vehicles coated with various encapsulant films before and after 7 days of soaking in 67°C PBS are shown in Table 21.

Table 21: Aging of VTB1 protected with different coatings after 7 days in 67°C PBS.

Coating	Initial	After 7 days in 67°C PBS	Remark
Al ₂ O ₃ 20 nm 250°C			Cu RDL absent
			Cu RDL absent

<p>SiC 100 nm 350°C</p>			<p>Cu RDL absent</p>
<p>DLC 100 nm 400°C</p>			<p>Cu RDL absent</p>
<p>HfO₂ 20 nm 250°C</p>			<p>Cu RDL present</p>
<p>HfO₂ 20 nm 200°C</p>			<p>Cu RDL present</p>

			Cu RDL present
SiN 100 nm 400°C			Cu RDL absent
			Cu RDL absent
SiO ₂ 100 nm 400°C			Cu RDL absent
			Cu RDL absent
SiOC 100 nm 400°C			Cu RDL absent
			Cu RDL absent

<p>TiO₂ 20 nm 250°C</p>			<p>Cu RDL absent</p>
<p>TiO₂ 20 nm 200°C</p>			<p>Cu RDL present</p>
<p>*2A2T¹⁰ 40 nm 250°C</p>			<p>Cu RDL absent</p>
<p>20A20T 40 nm 250°C</p>			<p>Cu RDL corroded through pits</p>

			Cu RDL corroded through pits
2A2T ¹⁰ 40 nm 200°C			Cu RDL present
			Cu RDL present
20A20T 40 nm 200°C			Cu RDL present
			Cu RDL present

* 2A2T¹⁰ means 10 times 2 nm Al₂O₃ plus 2 nm TiO₂. 20A20T means 20 nm Al₂O₃ plus 20 nm TiO₂.

Corrosion deposits of black color and organic contamination are visible on most coupons after soaking in the hot saline bath for one week. Best protective single layers were TiO₂ deposited at 200°C and HfO₂ deposited at 200/250°C, as indicated by a final RDL height of ~1.8 μm. Films of Al₂O₃, SiO₂, SiOC and SiN partially protect VTB1s from corrosion, as indicated by RDL heights of ~0.2 μm after one week of soaking at 67°C.

The initial RDL of ~1.8 μm virtually disappeared for VTB1s coated with packaging layers of SiC, DLC and TiO₂ 250°C. The low density of deposited SiC and DLC films (page 72) explains such poor corrosion protection behavior. But it was rather unexpected similar behavior from layers of TiO₂. This can be explained when it is remarked that TiO₂ films

deposited at 250°C have more defects than films deposited at 200°C, as indicated by the micro-blisters registered by AFM (page 69).

E. Marin *et al.* reported also micro-blisters on samples containing TiO₂ layers (deposited by 120°C ALD from TiCl₄ and H₂O precursors) and poorer corrosion protection compared to Al₂O₃ films [110]. As Al₂O₃ layers dissolve in saline solutions (page 101), a good way to improve corrosion protection of substrates is depositing multilayers of alumina and titania. Results from this multilayer approach are shown in the bottom of Table 21

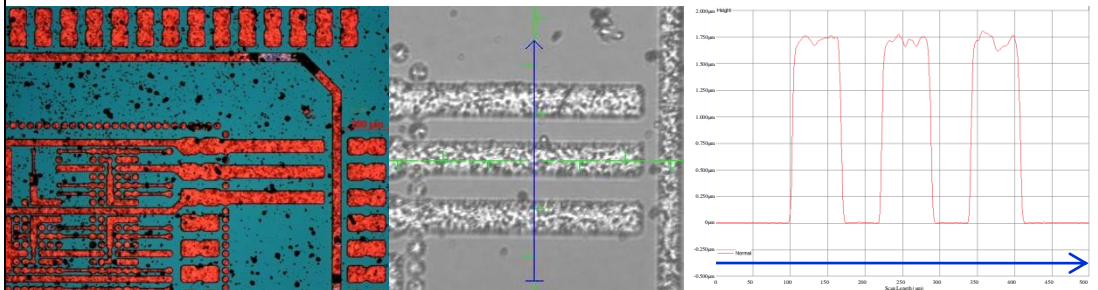
It can be seen that samples coated with 20A20T (i.e. 20 nm Al₂O₃ plus 20 nm TiO₂) had better corrosion protection than those coated with 2A2T¹⁰ (i.e. 10 times 2 nm Al₂O₃ plus 2 nm TiO₂). This is consistent with ALD studies showing that the residual porosity of films is reduced as their thickness is increased [111], [154].

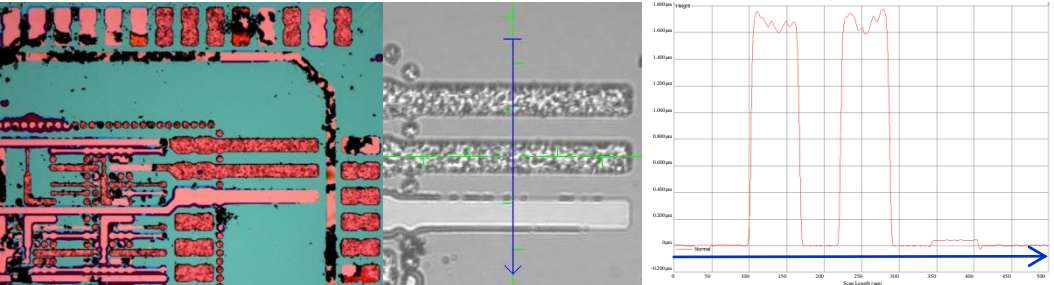
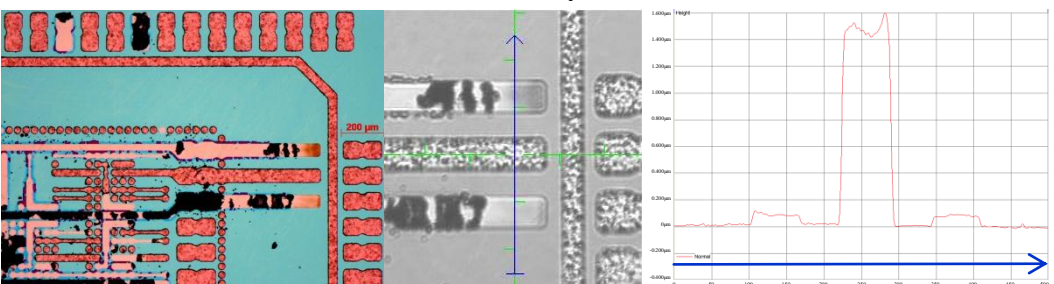
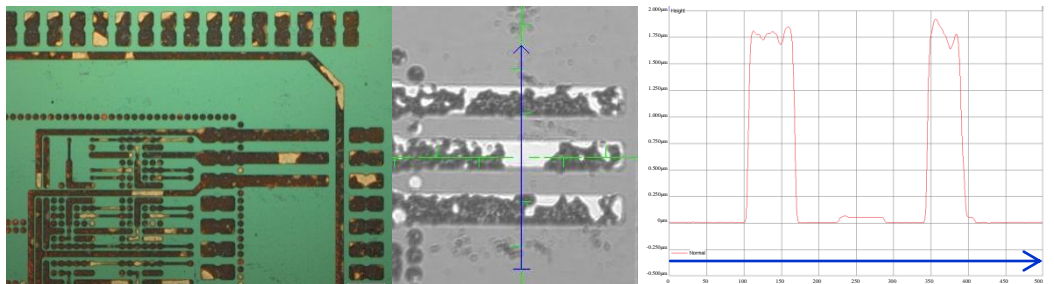
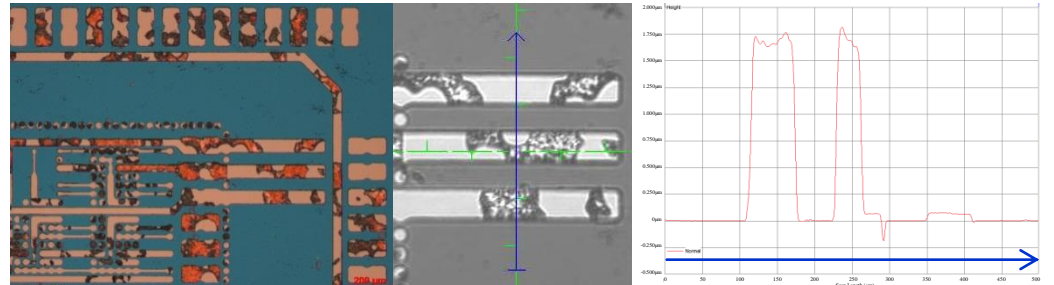
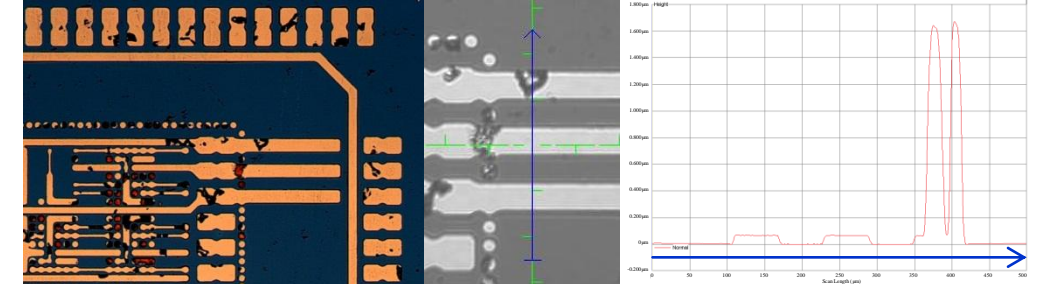
HfO₂ films did not show good protection against corrosion beyond 60 days of aging tests in PBS at 67°C, whereas TiO₂ 200°C showed good protection of VTB1 up to almost 120 days (Table 22).

Combinations of TiO₂ and Al₂O₃ deposited at 200°C showed remarkable corrosion protection of copper in PBS (Table 22). Here as well, 20A20T films protected better the copper substrates than those coated with 2A2T¹⁰. This suggests that residual porosity of ALD multilayers is indeed reduced as the thickness is increased, and as consequence their corrosion protection is increased.

Best corrosion protection results were obtained for coatings of 10A20T deposited at 200°C. Longer precursor exposure times were used for this coating, which is known for producing ALD layers of higher quality [161], [170] .

Table 22: Best protective films of VTB1 after aging test in 67°C PBS.

Coating	Time in 67°C PBS	Remark
2A2T ¹⁰ 40 nm 200°C	<p style="text-align: center;">+30 days</p> 	Cu RDL present

<p>20A20T 40 nm 200°C</p>	<p style="text-align: center;">+60 days</p> 	<p>>50% RDL absent</p>
<p>10A20T 30 nm 200°C</p>	<p style="text-align: center;">+166 days</p> 	<p>~33% RDL absent</p>
<p>TiO₂ 20 nm 200°C</p>	<p style="text-align: center;">+120 days</p> 	<p>Cu RDL absent</p>
<p>HfO₂ 20 nm 250°C</p>	<p style="text-align: center;">+60 days</p> 	<p>>90% RDL absent</p>
<p>HfO₂ 20 nm 200°C</p>	<p style="text-align: center;">+60 days</p> 	<p>>99% RDL absent</p>

4.2. Test Vehicle VTB2

Topological features such as copper RDL layers of few microns are difficult to perfectly coat by standard packaging layers and as consequence there is a high risk of infiltration of saline solution at the lower corners of the RDL (Figure 73).

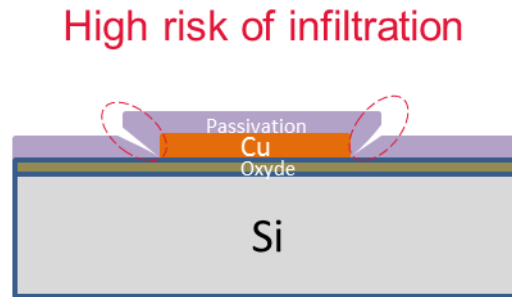


Figure 73: Risk of saline solution infiltration between passive layer and RDL.

In order to reduce this risk, a test vehicle called VTB2 was fabricated with copper RDL layers of 1.0 μm integrated inside a dielectric layer of PECVD SiO_2 (Figure 74). This type of RDL configuration is called damascene RDL and consists in first depositing the dielectric onto the substrate and then patterning by photolithography. The opened trenches are then filled by metal deposition.

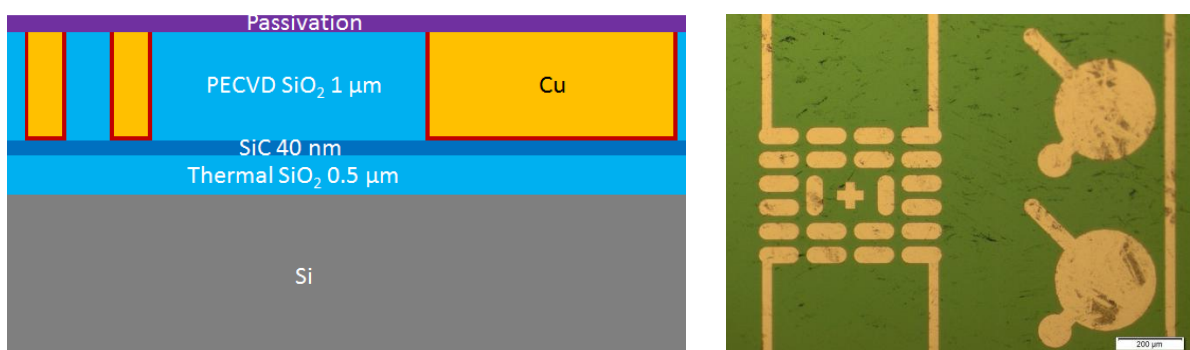


Figure 74: Scheme of cross section (Left) and upper view (Right) of test vehicle VTB2.

The purpose of VTB2 was to test if the absence of topological features was better to prevent corrosion of RDL layers during soaking tests.

Different packaging layers (Table 23) were deposited on top of 8-inch wafers containing VTB2 dices of size $5 \times 5 \text{ mm}^2$. Afterwards, VTB2 samples were cut from wafers by dicing and immersed for several days in PBS solution heated to $67.0 \pm 0.1^\circ\text{C}$ in a convection oven.

Table 23: Coating films deposited on VTB2 samples.

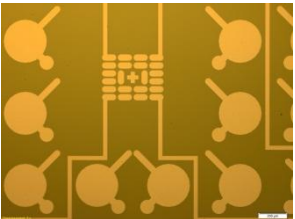
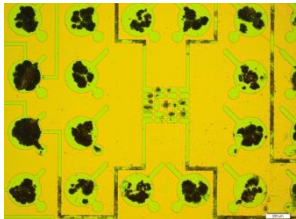
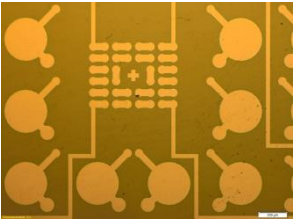
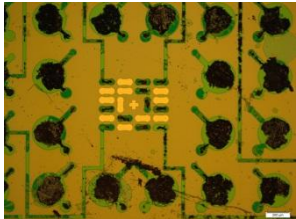
Coating	Avg. thickness (nm)	Fabrication
TiO ₂	40	ALD 200°C
Al ₂ O ₃ + TiO ₂	40	ALD 200°C
SiN	200	PECVD 400°C
SiO ₂	200	PECVD 400°C
SiOC	200	PECVD 400°C
SiC	200	PECVD 350°C
DLC	200	PECVD 400°C

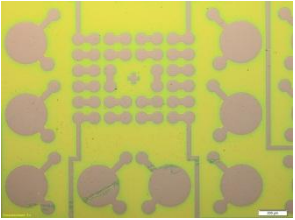
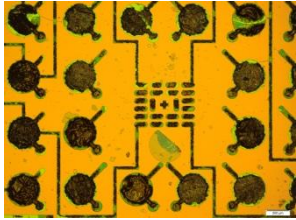
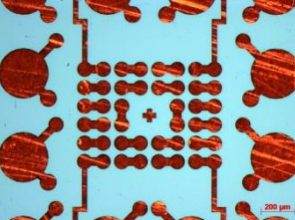
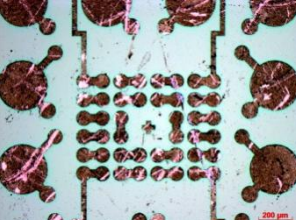
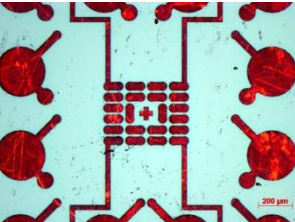
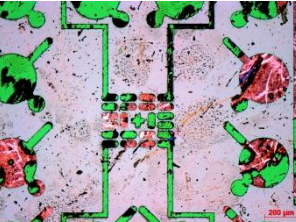
VTB2 samples were examined during aging tests by photo camera, microscope, and profilometer measurements.

Results and discussion

Table 24 shows results of various VTB2 coated samples before and after soaking in PBS.

Table 24: VTB2 protected with different coatings before and after soaking in 67°C PBS.

Coating	Initial aspect at T0	T0 + time 1	Comments
SiN 200 nm 400°C		 T0+7 days	RDL corroded within 7 days
SiC 200 nm 350°C		 T0+7 days	RDL corroded within 7 days

DLC 200 nm 400°C		 T0+7 days	RDL corroded within 7 days
TiO ₂ 40 nm 200°C		 T0+7 days	RDL corroded within 14 days
20A20T 40 nm 200°C		 T0+7 days	>75% RDL corroded within 7 days

* 20A20T means 20 nm Al₂O₃ plus 20 nm TiO₂.

None of the coatings listed in Table 23 was able to protect fabricated damascene Cu RDLs for more than 2 weeks in hot saline solution at 67°C.

The metal deposition process produced porous copper layers (Figure 75). As water can rapidly condensate inside micro cavities [18], corrosion processes can easily occur once liquid water is present inside the copper RDL.

Another cause of poor corrosion protection was the higher roughness of copper layers in VTB2, which was about two times larger than the RMS roughness measured for RDLs of VTB1 (~20 nm). Although the purpose of damascene process is to produce a flat surface with no topological features present, this fabrication process of damascene RDL was not efficient and metallic layers of significant roughness were produced (Figure 76). It is known that the adhesion of ALD films on substrates is negatively affected by the roughness of substrates [171], [172].

These two causes would explain the worse results of corrosion protection obtained for VTB2 coated samples compared to VTB1.

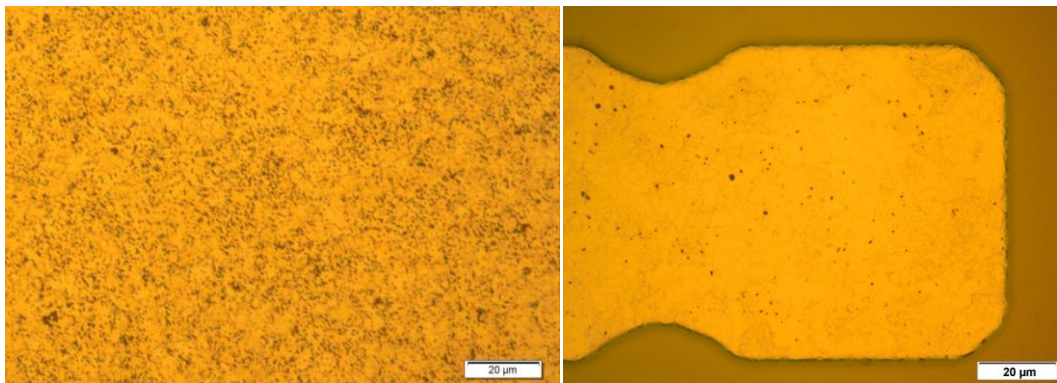


Figure 75: Micro photos of fabricated copper layers in VTB2 (Left) and VTB1 (Right).

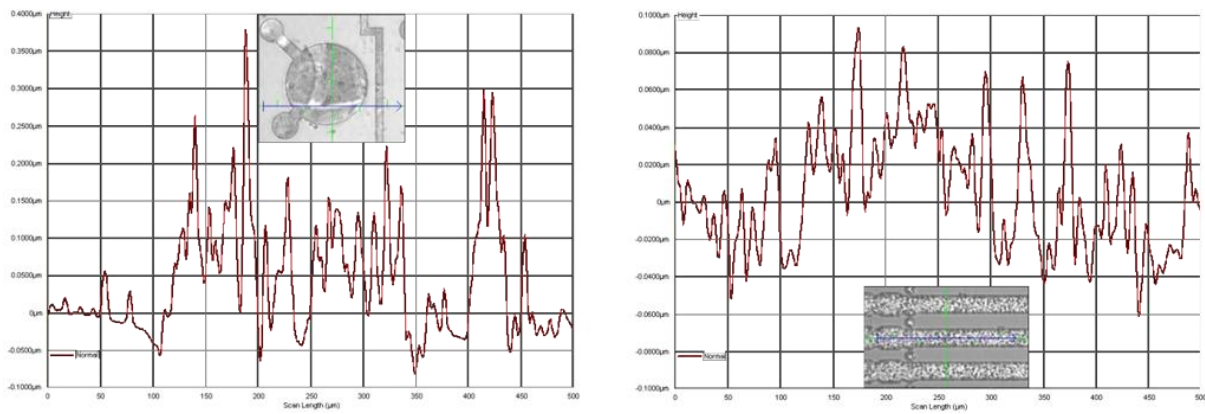


Figure 76: Roughness of fabricated copper layers in VTB2 (Left) and VTB1 (Right).

4.3. Test Vehicle VTB3

This vehicle test contained metallic pads with a total surface area of $\sim 1 \text{ cm}^2$ on a silicon substrate. The height of the metallic layer was 100 nm and was made of metals known to be easily corroded by saline solutions such as WN and TiN [77], [173]–[175]. Tungsten nitride and titanium nitride are especially interesting for testing because they are widely used in the microelectronics industry as diffusion barriers for copper and gold [64]. Besides, it is been reported problems of stability of neural microelectrodes containing tungsten nitride [174].

Test vehicle VTB3 was fabricated by standard photolithography, physical vapor deposition and chemical etching on crystalline silicon wafers of 200 mm. Details of the fabrication process of microelectronics are explained extensively elsewhere [64]. Metals layers of WN and TiTiN were deposited and patterned on silicon wafer. Figure 77 shows a schema of the cross-section view of test vehicle VTB3 as well a top view of the actual test vehicle. The size of a metallic pad is $5350 \times 1480 \text{ }\mu\text{m}^2$ and is separated from other pads by dicing streets of $90 \text{ }\mu\text{m}$. The size of one coupon is $10.7 \times 9.2 \text{ mm}^2$, or 0.98 cm^2 .

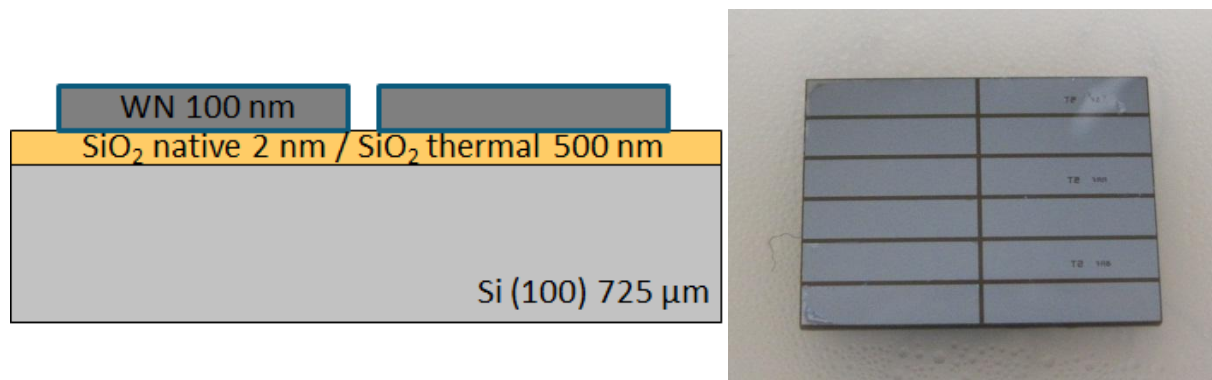


Figure 77: Scheme illustrating the cross section of test vehicle VTB3 (Left). Top view of a VTB3 containing 12 metallic pads of sputtered WN (Right). Pad length is $\sim 5 \text{ mm}$.

Stability of packaging films was tested on these coupons by soaking in Phosphate Buffer Saline (PBS) at 67°C . PBS solution was used to simulate the ionic concentrations of blood plasma.

Aging tests in PBS were performed on coupons containing metallic pads deposited on bulk Si and coated with different encapsulants of 20–40 nm deposited by ALD (Figure 78). Before

deposition of packaging layers, sample coupons were cleaned with the same cleaning sequence used for VTB1: DI water, acetone, isopropyl alcohol, DI water, nitrogen blow gun and dehydration at 200°C for >10 min.

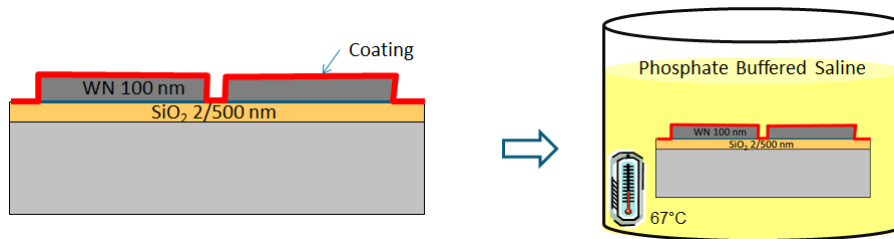


Figure 78: Accelerated aging tests of coated VTB3 coupons in hot saline solution.

ALD films are very conformal and uniform, so they were preferred for this study. Moreover, Al_2O_3 and TiO_2 were selected because they are well known for being biocompatible and widely used in implantable devices.

The thickness of metallic layers was measured by profilometer before and during the test. Coupons were removed from the PBS solution and cleaned with DI water before measurements. Samples were examined by photo camera, microscope, profilometer and TOF-SIMS measurements.

TOF-SIMS measurements were performed using a standard commercial TOF .SIMS 5 from ION-TOF GmbH. The sputtering gun consisted of ions of Cs^+ with a kinetic energy of 2 keV and raster size of 250 μm . The primary ion source for analysis was a Bismuth Liquid Metal Ion Gun (LMIG) that delivers cluster ions of Bi_n^{q+} with $n = 1-7$ and $q = 1-2$. The kinetic energy of these ions is 25 keV for singly charged ions and 50 keV for doubly charged ions. Its cycle time was 50 μs and raster size 90 μm . The spectrometer was set to detect negative ions in M- modes.

Results and discussion

First material tested was WN and it was observed that 100 nm of WN were totally dissolved after ~4 hours in 67°C PBS. Photos of a coupon with WN pads are shown in Figure 79.

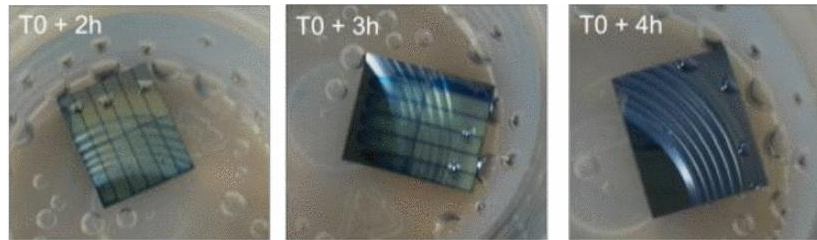
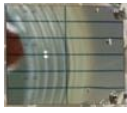



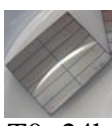


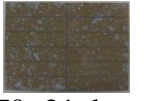
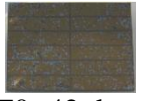










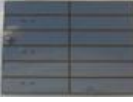


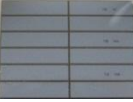


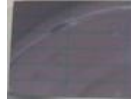
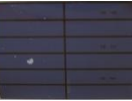
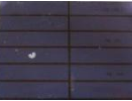

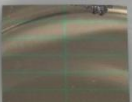


Figure 79: WN layer of 100 nm after 2, 3 and 4 hours of soaking in 67°C PBS.

An increase of measured RDL thickness >100 nm was observed for coupons of TiTiN deposited on $0.5 \mu\text{m}$ of thermal SiO_2 after 23 weeks of soaking in 67°C PBS. This can be explained by dissolution of SiO_2 in PBS (page 105). Under the assumption that TiTiN do not dissolve in PBS, the average dissolution rate of thermal SiO_2 in PBS would be $0.23 \pm 0.10 \mu\text{m}$ per year at 67 °C.

Different coatings deposited on VTB3 containing 100 nm layers of WN were evaluated in PBS solution at 67°C. Samples were observed during aging tests and results are presented in Table 25. Compared to results of coupons without encapsulation, the benefit of ALD coatings is clearly demonstrated.

Table 25: Photos of WN coupons with various coatings during soaking in PBS at 67°C.

#	Coating	Deposit. Temp.	Initial aspect T0	T0 + time 1	T0 + time 2	Remark
1	20 nm Al_2O_3	90°C		 T0+8h	 T0+10h	WN corroded in 10h
2	20 nm Al_2O_3	250°C		 T0+24h	 T0+50h	WN corroded in 50h
3	20 nm TiO_2	200°C		 T0+21 days	 T0+42 days	WN corroded in 21 days
4	20 nm TiO_2	250°C		 T0+50h	 T0+100h	WN corroded in 100h

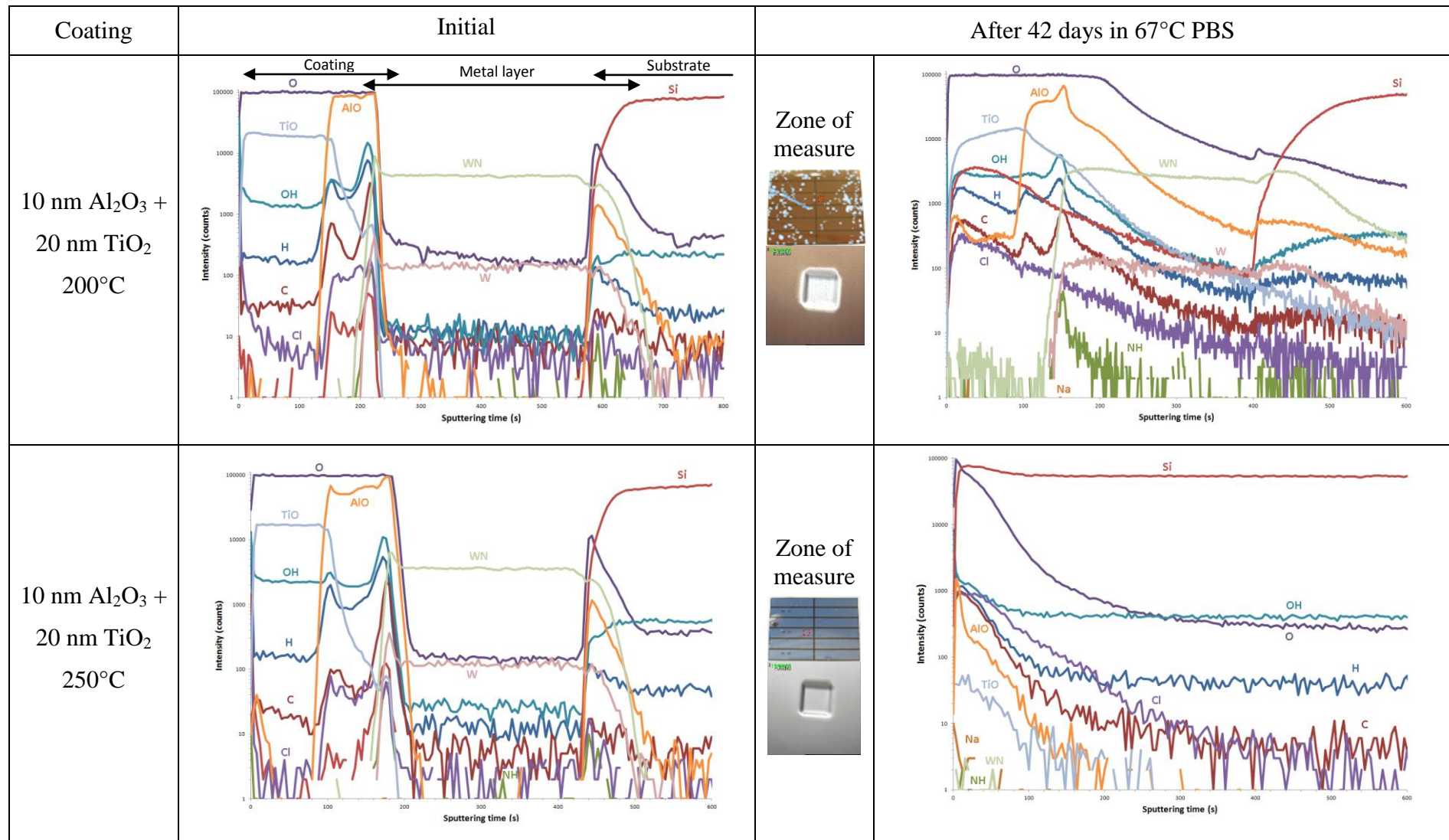
5	10 nm Al ₂ O ₃ + 20 nm TiO ₂	200°C		 T0+14 days	 T0+42 days	WN resists >42 days
6	10 nm Al ₂ O ₃ + 20 nm TiO ₂	250°C		 T0+14 days	 T0+42 days	WN corroded in 14 days
7	(2 nm Al ₂ O ₃ + 2 nm TiO ₂) ¹⁰	200°C		 T0+14 days	 T0+42 days	WN corroded in 21 days
8	(2 nm Al ₂ O ₃ + 2 nm TiO ₂) ¹⁰	250°C		 T0+7 days	 T0+35 days	WN corroded in 14 days
9	20 nm Al ₂ O ₃ + 20 nm TiO ₂	200°C		 T0+14 days	 T0+42 days	WN resists >42 days
10	20 nm Al ₂ O ₃ + 20 nm TiO ₂	250°C		 T0+7 days	 T0+42 days	WN corroded in 14 days

It was observed that the deposition temperature influences the corrosion protection of coatings. Al₂O₃ deposited at 250°C is a better barrier than Al₂O₃ deposited at 90°C. And TiO₂ deposited at 200°C shows significant improvement compared with deposition at 250°C. Consequently, best coatings were obtained using multilayer of Al₂O₃/TiO₂ of 10–20 nm deposited at 200°C.

Table 26 shows ToF-SIMS measurements of coatings 5 (200°C) and 6 (250°C) before and after saline soaking. Gray color zones seen in coating 6 (250°C) after soaking indicate that the original WN layer has disappeared because virtually no counts of WN⁻ and WO⁻ ions are detected there. Conversely, large counts of AlO⁻ and TiO⁻ ions in such zones suggest that the coating layer is still present on top of the coupon. It is therefore assumed that the WN layer has been corroded by infiltration of water and saline ions through coating 6.

On the other hand, coating 5 (200°C) protects better the WN layer after soaking as indicated by high counts of WN⁻ and WO⁻ ions. Although depth profile resolution was lost due to an increase of surface roughness after soaking, it can be inferred that ALD coatings of Al₂O₃/TiO₂ deposited at 200°C offer superior corrosion protection in saline solution.

Table 26: ToF-SIMS depth profiles of Al₂O₃+TiO₂ coatings deposited on Si + 100 nm WN.



Judging from photos in Table 25, one could infer that coating 3 (TiO_2 200°C) offers as good corrosion protection as coating 5 ($\text{Al}_2\text{O}_3+\text{TiO}_2$ 200°C). However, profilometer and TOF-SIMS measurements of VTB3 coated with 20 nm of TiO_2 200°C (Figure 80) showed that WN layer was corroded and mixed with other substances (-Cl, -OH, -Na) after 21 days of soaking.

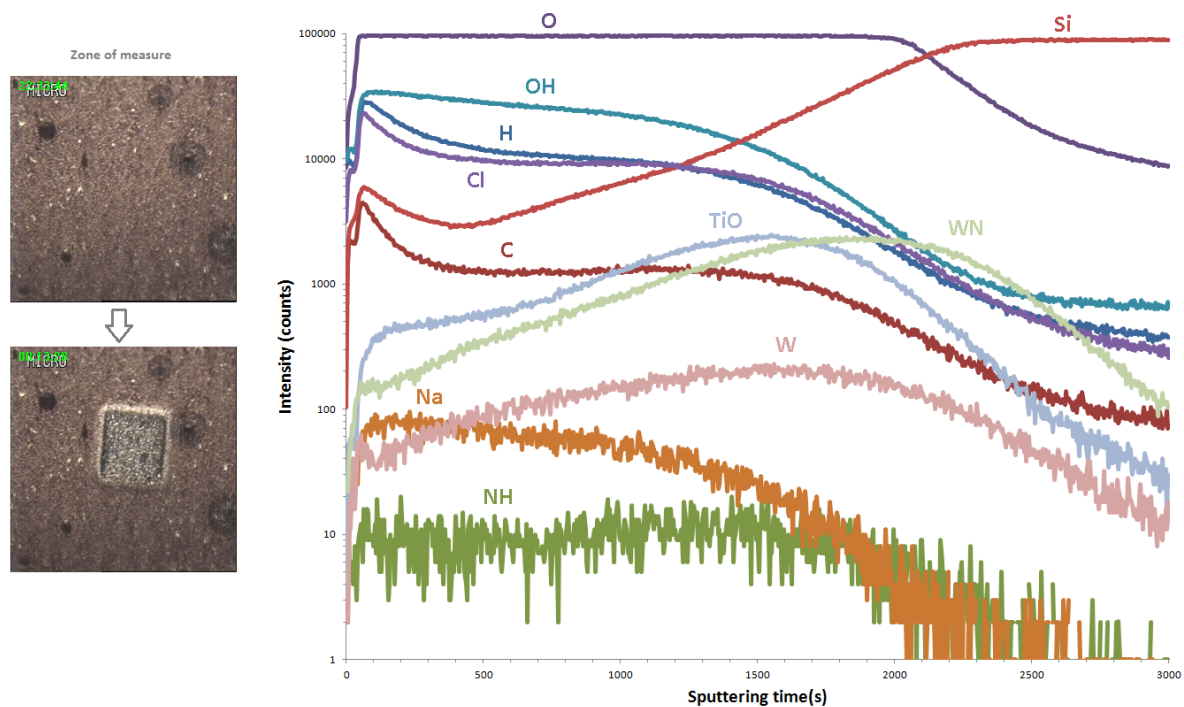


Figure 80: ToF-SIMS of VTB3 coated with 20 nm TiO_2 200°C after 21 days in 67°C PBS.

Encapsulated VTB3s revealed also that multilayers of Al_2O_3 and TiO_2 of 10–20 nm offer better corrosion protection than multilayers of 2 nm (Table 25). This is similar to results obtained with VTB1 (page 123), and consistent with research papers reporting that the residual porosity of ALD films is reduced as their thickness is increased [111], [154].

Finally, it was observed that TiO_2 layer was more stable in saline solution than Al_2O_3 layer. Best corrosion protection results were obtained with multilayers containing TiO_2 deposited at 200°C as top layer. However, these coatings did not protect completely the underlying substrate. It is assumed that dust particles and dicing fragments present on the surface are coated by the ALD layer and removed later on by soaking in PBS, which leaves behind infiltration pits (Figure 81). Profilometer and ToF-SIMS (Figure 82) measurements confirmed that the WN layer had disappeared below such infiltration pits.

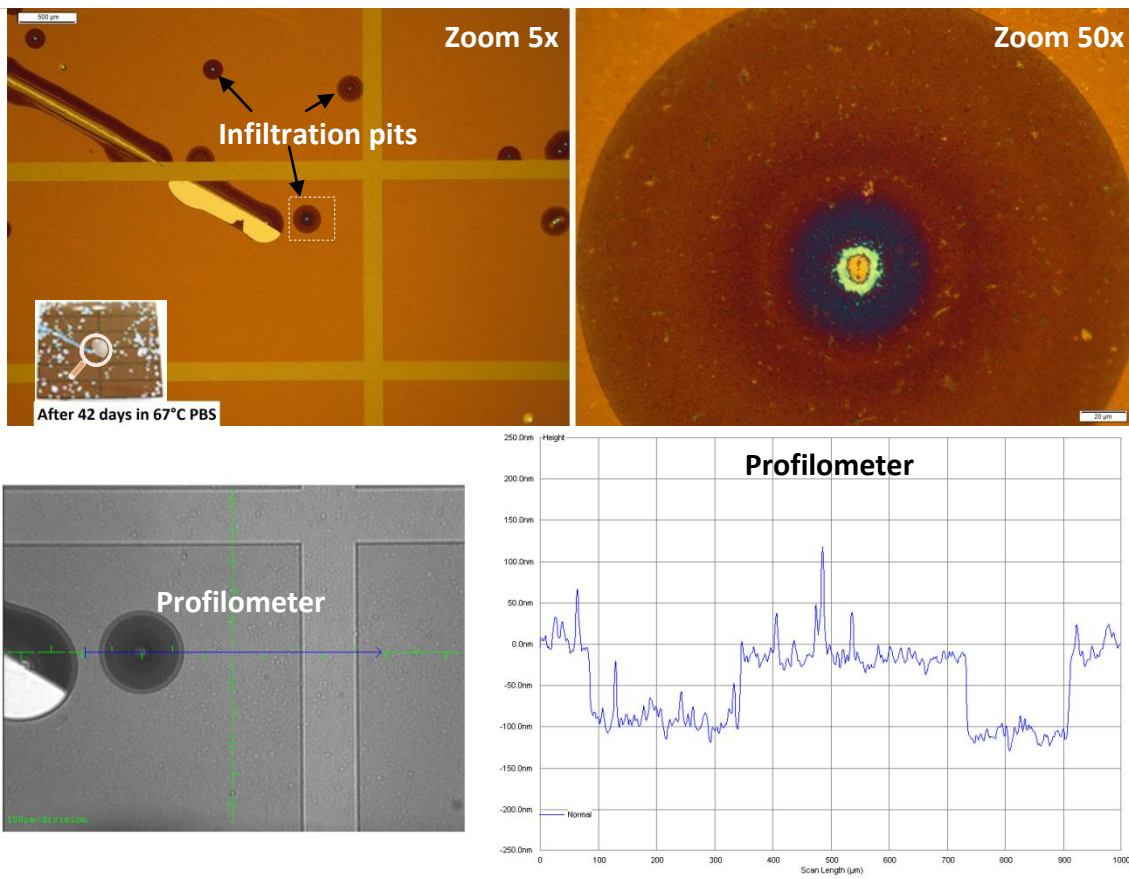


Figure 81: Infiltration pits of VTB3 coated with 10 nm Al_2O_3 + 20 nm TiO_2 200°C.

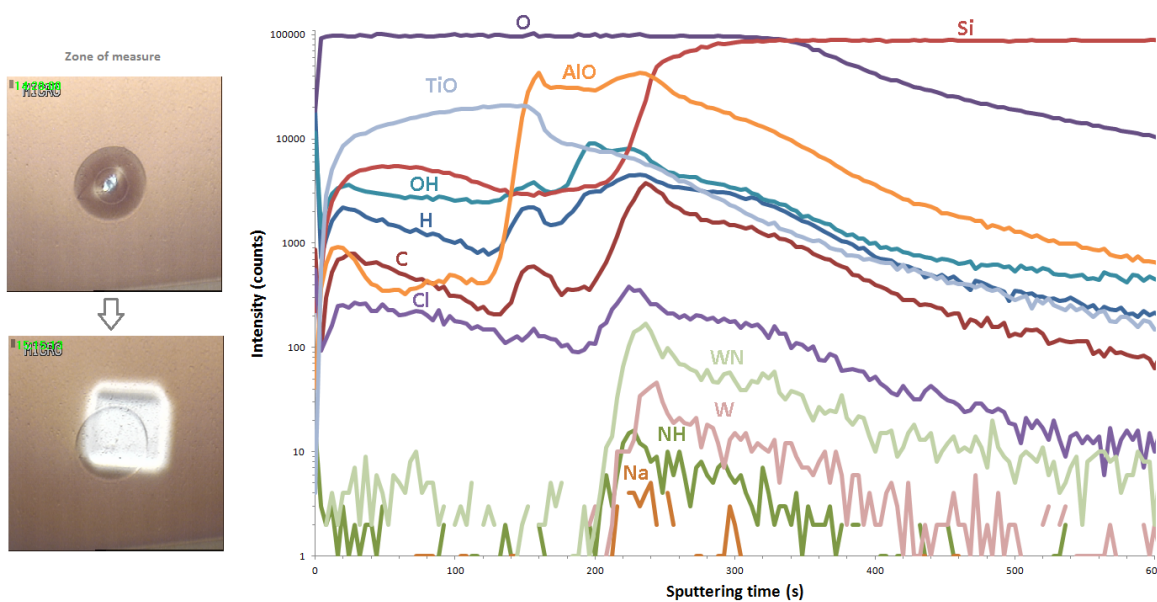


Figure 82: ToF-SIMS over infiltration pit of VTB3 coated with 10 nm Al_2O_3 + 20 nm TiO_2 200°C after 42 days in 67°C PBS. Metal layer of WN has disappeared in the pit.

For that reason, cleaning of substrates before ALD deposition is a key element to achieve excellent corrosion protection. For example, ALD coatings were deposited on VTB3 samples that were not cleaned with acetone and isopropyl alcohol. A photo of unclean coatings after 5 days of soaking in PBS at 67°C is shown in Figure 83.

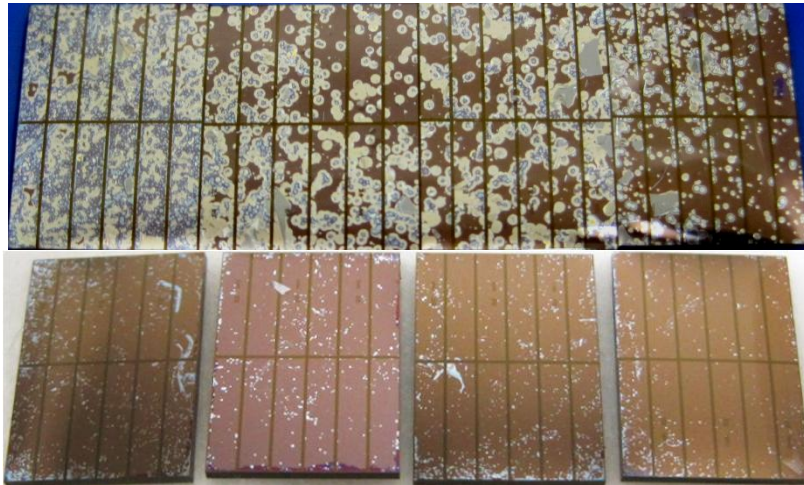


Figure 83: Photos of unclean (Top) and clean (Bottom) VTB3 coupons protected with multilayer of $(5 \text{ nm Al}_2\text{O}_3 + 5 \text{ nm TiO}_2)^4$ deposited at 200°C after 5 days in 67°C PBS.

Excellent corrosion protection with ALD coatings can be obtained by improving the cleaning protocol of substrates and fine tuning the parameters of deposition (Figure 84).

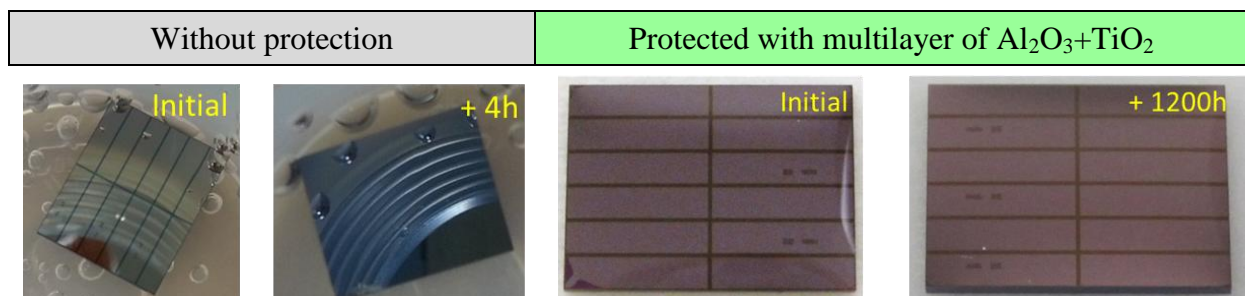


Figure 84: Photos of VTB3s before and after soaking in Phosphate Buffered Saline at 67°C.

4.4. Test Vehicle VTB4

Wafer dicing is normally done using conventional blade technology, which can cause chipping and cracking of the silicon device. The problem of sharpness of the implanted microelectronic device can be solved in some cases by embedding it in a soft biomaterial that resembles the mechanical properties of human tissue [46]. However, silicon dice sharp edges are problematic even when embedded in a soft biocompatible polymer because there is incomplete covering over the edges (Figure 6 in page 34), which leads to local problems in biocompatibility [176]. In the interest of minimizing the FBR of implantable miniature medical devices, a dicing method to obtain rounder or softer edges ought to be perfected. This Test Vehicle's goal was to optimize the fabrication of unsharpened silicon dices by means of physicochemical etching and sequential blade dicing techniques.

Polished Si(100) p-type 1–50 $\Omega\cdot\text{cm}$ wafers of diameter 200 mm and thickness 725 μm were used for etching and dicing essays as supplied by the provider (MEMC Korea Company). The generic process used to create thin unsharpened silicon devices is shown in Figure 85.

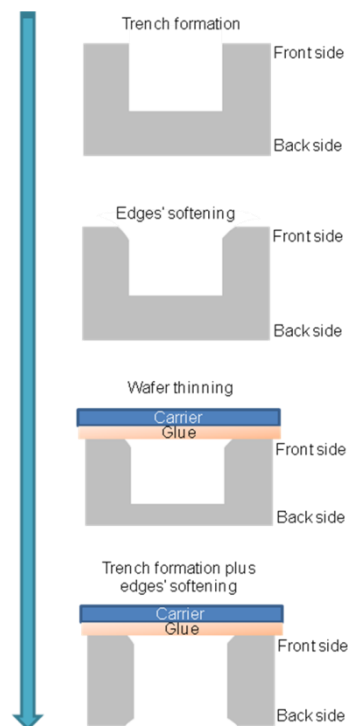


Figure 85: Generic process flow to create thin unsharpened silicon devices.

Trenches in silicon were created by blade dicing or Deep Reactive Ion Etching (DRIE). DRIE technique was chosen because it is known for producing soft surfaces without chipping [45], whereas blade dicing has the advantage of cutting through all kind of materials, even metals.

The softening of edges was done by doing a lateral chemical etching under a hard mask before the DRIE step (Physicochemical etching method), or by using a V-shaped dicing blade after formation of partial trenches (Sequential blade dicing method).

Scanning Electron Microscope (SEM) images of each method were taken with a Hitachi S-4000 microscope. Experimental errors of 10% can be expected for these length measurements.

1. Physicochemical etching method

The process flow of this method is illustrated in Figure 86. First step consisted in depositing a hard mask of 1 μm PECVD SiO_2 (SiH_4 200°C) on the front side of the wafer. Then, a 3 μm resin with square patterns of $6500 \times 0 \mu\text{m}^2$ and open streets of 90 μm (total area exposed of 5.09%) was spin-coated on top, and lateral chemical etching was performed with a bath in Buffered Oxide Etch (BOE) for 900 seconds. Afterward, a DRIE with SF_6 and C_4F_8 was performed for 570 seconds in order to etch about 40 μm of silicon. The photolithographic resin was then stripped and isotropic plasma etching with pure SF_6 was performed for 1-8 min to soften the dicing street edges.

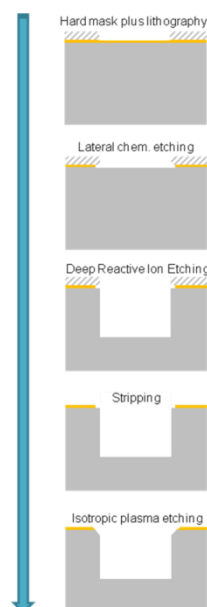


Figure 86: Process flow of the physicochemical etching method followed to soften die edges.

The front side of the wafer was then glued to a carrier glass wafer and its back-side was thinned down to 100 μm . And the same steps previously described for the front side of the wafer were performed on the back-side.

Anisotropic DRIE and isotropic plasma etching essays were performed using an etching machine of Surface Technology Systems Plc. (STS).

2. Sequential blade dicing method

The process flow of the sequential blade dicing method is illustrated in Figure 87. First, a partial standard dicing was performed for a depth of 150-300 μm measured from the top of the wafer. The thickness of the standard nickel bond blades was 40 μm (ref. S1435-Q500 of Kulicke and Soffa Industries, Inc.). Next, a partial chamfered dicing of depth 10-20 μm was performed using a resin bond blade. The tip of the resin bond blade had the shape of a 30° trapezoid with an upper base of 500 μm and lower base of 50.8 μm (ref. 2.187A-20A-9R3 of Thermocarbon Inc.). Standard and chamfered dicing was performed in machines of DISCO Corporation.

The front face of the wafer was then glued to a carrier polymer film and the same process depicted in Figure 87 was performed on the back-side of the wafer to obtain softer edges.

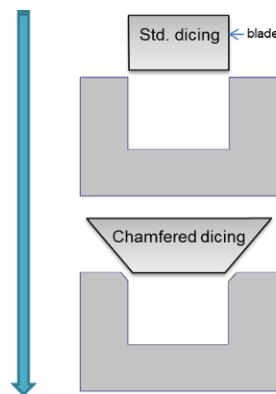


Figure 87: Process flow of our sequential dicing method for softening die edges.

Results and discussion

1. Physicochemical etching method

The dicing streets obtained for the front-side of the wafer after the steps depicted in Figure 86 were much larger than openings of the photo-mask (+ 20 μm). Moreover, the dicing street

edges were sharp and rugged, as confirmed by SEM inspection after plasma etching with pure SF_6 for 3 minutes and removal of the hard mask with a 30 seconds bath in HF 40% (Figure 88a).

Here, we decided to increase the isotropic plasma etching time with the intention of obtaining softer edges. Figure 88b shows the edges obtained after 6 min of isotropic plasma etching and subsequent hard mask removal. Thanks to this, the angle of the dicing street edges was decreased from 64° (Figure 88a) to 58° (Figure 88b) and the dicing street upper edges became less acute. However, during this process about $10\ \mu\text{m}$ of bulk silicon were also etched laterally, widening the width of the dicing street to more than $120\ \mu\text{m}$. In total, $30\text{-}40\ \mu\text{m}$ of bulk silicon were over-etched laterally by this method. Isotropic etching with pure SF_6 for 8 min increased further the width of the dicing street without significantly decreasing the angle of the edges. Thus, it was decided to continue the process flow depicted in Figure 85 with wafers that had 6 min of isotropic plasma etching.

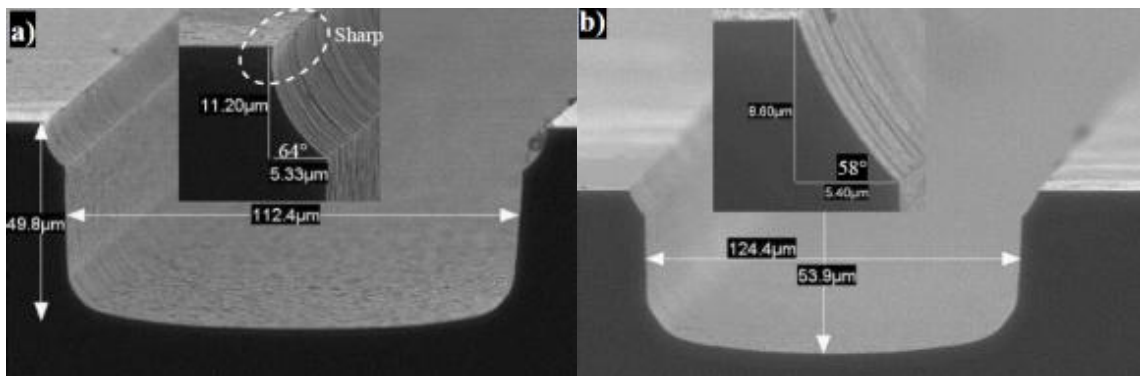


Figure 88: Profile obtained after isotropic etching with pure SF_6 for a) 3 min (Top) and b) 6 min (Bottom) and hard mask removal.

The front side of the wafer was then glued to a carrier glass wafer and the back-side of the wafer was ground down to $100\ \mu\text{m}$ (Figure 89). In the upper part of Figure 89, the location of the dicing street of the back-side of the wafer can be seen delineated by the lithographic mask; and below it, the glass carrier wafer is seen glued to the front-side of the silicon wafer. The front-side dicing street seems to be smaller than it is due to the presence of $20\ \mu\text{m}$ of glue attached to its walls.

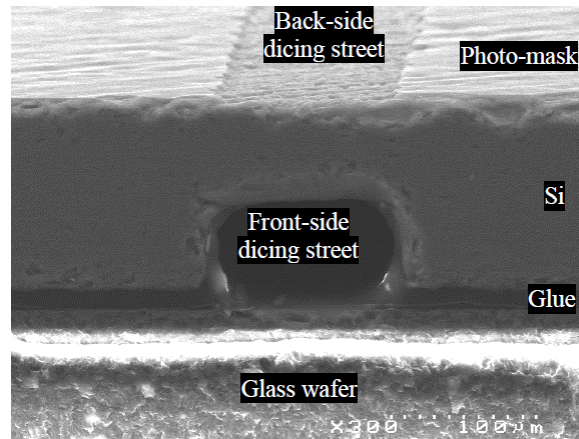


Figure 89: Thin silicon wafer glued to a glass carrier wafer.

Afterwards, the process flow depicted in Figure 86 was applied on the back side of the thin silicon wafer. Lateral chemical etching with Buffered Oxide Etch (BOE) for 900 seconds was followed by DRIE with SF_6 and C_4F_8 for 720 seconds. DRIE etching time was increased from 570 to 720 seconds for the back-side with the purpose of fully dicing through the thickness of the silicon wafer ($100\ \mu\text{m}$). However, this method was penalized for over-etching laterally more than $30\ \mu\text{m}$ of silicon during the front-side processing steps; so the resulting dicing street of the back-side was smaller than the dicing street of the front-side (Figure 90). It can be seen in Figure 90 that DRIE was done not along the lines of the hard photo-mask. This is probably due to the lateral chemical etching performed before the DRIE step. It was decided not to perform the step of isotropic plasma etching as it would not change the difference in width between the back and front side dicing streets.

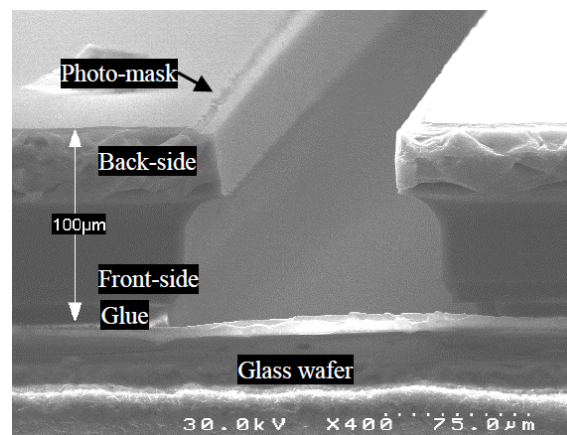


Figure 90: Etch profile obtained after $50\ \mu\text{m}$ of DRIE. Front-side was glued to a glass carrier.

If a different lithography mask with larger dicing streets is used for the back-side of the silicon wafer, it should be possible to obtain a proper thin rounded silicon dice. Another option is to decrease the lateral chemical etching time. Nevertheless, the physicochemical etching method as explained here consumes considerable amounts of silicon laterally and this might exclude its application in wafers with small distances between dices. Moreover, plasma etching may be blocked by the presence of materials other than silicon in the dicing street (e.g. metallic pads placed for identification, or to prevent dishing during steps of Chemical Mechanical Polishing).

2. Sequential blade dicing method

Blade dicing techniques commonly used in the microelectronics industry produce sharp and irregular edges due to die chipping and cracking [44],[45]. One example of blade dicing is shown in Figure 91, where the 40 μm thick nickel bond blade previously described with rotational speed of 30000 rpm and displacement of 7 mm/s was used.

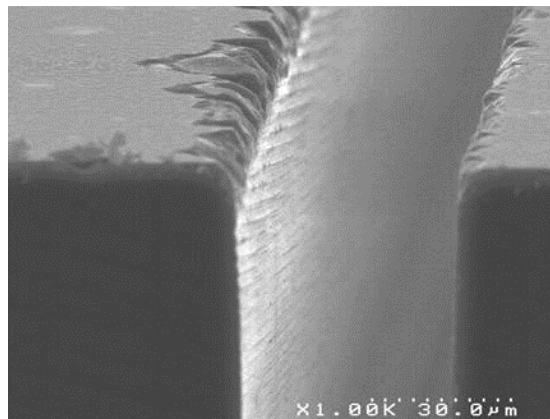


Figure 91: Die chipping caused by blade dicing on a silicon wafer.

The goal of our sequential blade dicing method was to obtain unsharpened chamfered edges, unlike the irregular and broken edges shown in Figure 91. The first part of this method consisted in calibrating the use of the V-shaped resin bond blade. It was necessary to control the depth of dicing in order to control the width of the dicing street. Figure 92 shows a dicing street about 20 μm deep created with the V-shaped blade.

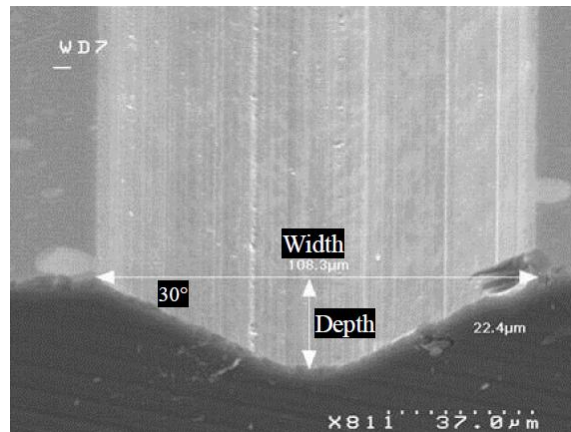


Figure 92: Dicing street obtained with V-shaped blade when a depth of 20 μm was intended.

The width of the dicing street is ~100 μm, which is in good agreement with the trigonometric formula for the height of a trapezoid with lower base of 50.8 μm and upper base of 500 μm (i.e. the shape of the resin bond blade's tip) plus a correction term of 5 μm (Eq. 21).

$$\text{Depth} = 0.5 \cdot \tan 30^\circ \cdot (\text{Width} - 50.8) + 5 \quad \text{Eq. 21}$$

Next, a partial standard dicing of 150 μm followed by a chamfered dicing of depth 10 μm and 20 μm were performed on silicon wafers. Smooth and homogenous edges were obtained this way (Figure 93). Overall, the smoothness and reproducibility of the die edges obtained by this sequential blade dicing method were remarkable.

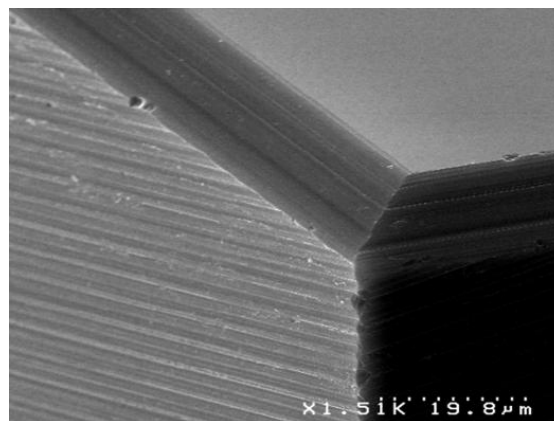


Figure 93: Chamfered edges obtained by partial standard dicing followed by chamfered dicing (depth 20 μm) with a 30° V-shaped blade.

The front side of the wafer was then glued to a carrier polymer film in order to dice the back side of the wafer. Next, full dicing (depth $\sim 500 \mu\text{m}$) followed by chamfered dicing (depth $20 \mu\text{m}$) were performed on the back side of the wafer. However, unlike the smooth and homogeneous edges obtained for the front side of the wafer, the back-side edges were not different from those obtained by standard dicing (Figure 94). This was probably due to a defective alignment between the back and front side's dicing streets.

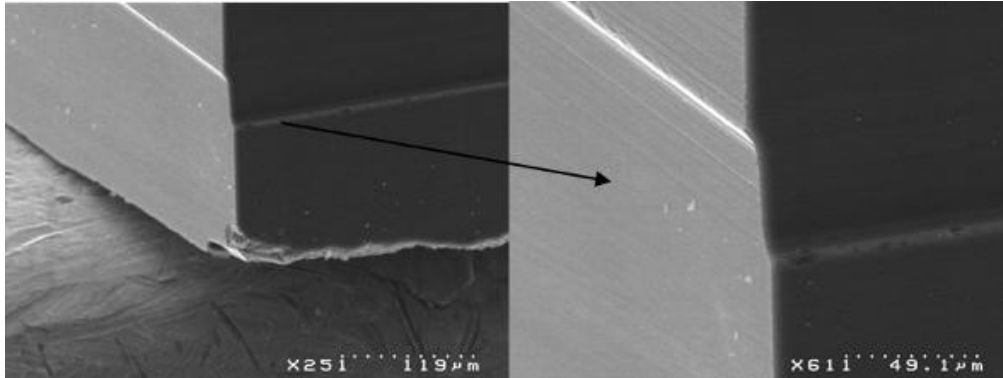


Figure 94: Problem of alignment that occurred during the sequential blade dicing method.

In summary, fabrication of *unsharpened* silicon devices is viable and compatible with the process flow of back-end packaging of silicon devices. Lithographic masks for correct alignment of the back-side with the front-side of the wafer are a key component in both methods tried here: physicochemical etching and sequential blade dicing.

The physicochemical etching method (Figure 86) has several advantages over the sequential blade dicing method (Figure 87) such as absence of die chipping, simultaneous etching of all dicing streets and the possibility of creating non-rectangular shapes and thinner dicing streets with appropriate lithographic masks. Moreover, the sequential blade dicing method has an increased risk of chipping and cracking with thin silicon wafers. On the other hand, the physicochemical etching method is potentially more expensive due to the use of techniques such as DRIE and isotropic plasma etching. The sequential blade dicing method should be cheaper and easier to implement than the physicochemical etching method, and it is also useful when there are materials other than silicon (e.g. metals) present on the dicing street. Conversely, V-shaped blades are rather fragile. This might impose limits on the speed and economy of the sequential blade dicing method.

4.5. Conclusion

The development of packaging layers of silicon devices for biomedical applications was presented. Aging tests showed the benefit of barriers such as HfO_2 , TiO_2 and Al_2O_3 to protect silicon and metallic substrates from corrosion in saline solution. Although the effect of deposition temperature on film quality was explored for these three materials, other deposition parameters and cleaning protocols have to be further optimized for industrial applications.

Although the purpose of damascene process is to produce a flat surface with no topological features present, this fabrication process of damascene RDL was not efficient and metallic layers of significant roughness were produced. It is known that the adhesion of thin films on substrates is negatively affected by the roughness of substrates. Besides, the metal deposition process produced porous copper layers. As water can rapidly condensate inside small cavities, corrosion processes can easily occur once liquid water is present inside the copper RDL. These two causes would explain the worse results of corrosion protection obtained for coated damascene samples compared to samples with topological RDL.

Due to large corrosion rates of crystalline silicon *in vivo*, semiconductor devices intended for biomedical applications must be coated with a biocompatible, biostable and hermetic coating such as SiO_2/SiOC and $\text{Al}_2\text{O}_3/\text{TiO}_2$.

Multilayers of Al_2O_3 and TiO_2 deposited by ALD at 200°C from TMA and TDMAT precursors constitute a promising encapsulant of medical micro devices for permanent implantation. Even better results can be expected for multilayers of $\text{Al}_2\text{O}_3/\text{TiO}_2$ isolated from aqueous solution with inert polymers such as silicone, epoxy and parylene (page 37).

In order to improve biocompatibility, plasma or sequential blade dicing methods can be used to fabricate unsharpened silicon devices. Silicon devices unsharpened by these methods should have an improved biological response post-implantation. Pertinent biological evaluation tests should be conducted to test this hypothesis.

General Conclusion and Outlook

A biocompatible material ought to coexist with the biological environment of the patient without causing undesirable effects to the patient and the device in the frame of a specific application. As there are many different types of biomaterials, various norms have been created to homogenize their evaluation and testing. The most relevant in Europe is the guideline ISO 10993 for the biological evaluation and testing of medical devices that have direct or indirect contact with patients. The guideline ISO 10993 is called guideline because it does not provide a rigid set of tests methods as this might result in unnecessary constraints on the development and use of novel medical devices. It does stipulate, however, that whenever novel materials or devices are manufactured, they must be characterized regarding chemical composition and morphology, and to undergo biological tests to assess their toxicological risk.

Packaging materials intended for the encapsulation of medical micro devices have additional material requirements that are not defined by international guidelines such as ISO 10993. An ideal biocompatible packaging layer of implantable electronic micro devices should be not be degraded during implantation and its thickness should remain stable over time. It should be also compatible with micro fabrication in clean rooms, to be impermeable to moisture and toxic elements like copper and tungsten, to be compatible with sterilization, and to have good adhesion on silicon substrates.

Taking into account the ISO guideline and previous requirements, ten packaging layers deposited by Chemical Vapor Deposition (BN, DLC, SiC, SiOC, SiN, SiO₂) or Atomic Layer Deposition (Al₂O₃, HfO₂, TiO₂, ZnO) were selected and evaluated in this thesis. Deposited layers were characterized by various techniques such as XPS and XRD to study their chemical composition and morphology; and their toxicological risk was assessed by means of *in vitro* cytotoxicity tests outlined by the guideline ISO 10993-5.

Table 27 shows selected packaging films and the results obtained from different evaluation tests.

Table 27: Summary of evaluated barrier films for biocompatible packaging of silicon devices.

Barrier film	Width (nm)	Deposit. Temp.	Deposit. Time	<i>In vitro</i> cytotoxic.	Gas hermetic.	Stability NaCl/FBS	Diffusion barrier	Corrosion protection
Al ₂ O ₃ +TiO ₂	20+20	200°C	4h30	good	very good	excellent	fair	very good
TiO ₂	20	250°C	2h30	good	good	excellent	poor	fair
HfO ₂	20	250°C	1h15	good	very good	good	poor	fair
Al ₂ O ₃	20	250°C	1h15	good	excellent	poor	poor	fair
SiOC	100	400°C	0h15	good	-	excellent	-	poor
DLC (a- CH)	100	400°C	0h15	fair	poor	excellent	-	poor
SiC	100	350°C	0h15	good	poor	good	-	poor
SiN	100	400°C	0h15	good	good	fair	-	poor
SiO ₂	100	400°C	0h15	good	good	fair	poor	poor
BN	50	400°C	0h30	good	poor	fair	-	poor
ZnO	20	250°C	1h15	poor	poor	very poor	-	-

Pure extracts of Al₂O₃, BN, HfO₂, SiC, SiN, SiO₂, SiOC and TiO₂ were confirmed to be non-cytotoxic (i.e. cell viability >70%) according to the guideline ISO 10993-5. There was also no alteration of the cell morphology for these films. Pure extracts of DLC and ZnO films produced L929 cell viabilities of 48% and 6%, respectively.

Best deposited encapsulation films in terms of helium gas permeability are in decreasing order: Al₂O₃, HfO₂, SiO₂, SiN and TiO₂. These films or combinations of them should provide an effective hermetic packaging barrier against moisture and other gases.

Biological mediums such as NaCl/FBS are more relevant than PBS to predict *in vivo* degradation rates of packaging materials intended for human implantation. On one hand, PBS overestimates greatly the degradation rates of some films like SiN compared to *in vivo* degradation rates. On the other hand, it fails to predict the decomposition of films like Al₂O₃

and it underestimates by a factor of >4 the dissolution rates of SiO_2 films [146], [152] and crystalline Si [18], [143].

Packaging layers of DLC, HfO_2 , SiC, SiOC and TiO_2 have good chemical stability as proved by a film thickness variation below 2 nm after 4 weeks of degradation tests in NaCl/FBS at 37°C . They are therefore good packaging layers for biocompatible encapsulation of medical micro devices that are in contact with chemically aggressive physiological environments.

Conversely, packaging layers of PECVD SiN and SiO_2 have corrosion rates of 0.68 ± 0.15 $\mu\text{m}/\text{yr}$ and 0.20 ± 0.15 $\mu\text{m}/\text{yr}$ in NaCl/FBS at 37°C , respectively. But they are relatively good hermetic barriers and can be readily deposited in thick coatings of several microns in standard clean rooms. Therefore, for certain applications where PECVD SiO_2 and SiN are not in direct contact with the body or the duration of contact is not permanent (>30 days), the usage of these packaging films could be practical.

Dissolution rates of SiN in NaCl/FBS are in good agreement with *in vivo* rates reported by J. Maloney and H. Hämmerle [146], [152], however they reported larger *in vivo* dissolution rates for PECVD SiO_2 . Although NaCl/FBS is more pertinent than PBS to predict the *in vivo* behavior of implanted materials, it does not simulate perfectly *in vivo* environments. Materials that are stable in NaCl/FBS should be tested as well *in vivo* to estimate their corrosion rates in the targeted service environment. This is especially important for packaging materials intended for implants of several years.

None of deposited packaging films passed the copper diffusion barrier tests (i.e. cell viability $>70\%$) designed after the elution test protocol of ISO 10993-5. This is probably due to insufficient thickness of deposited layers. Better diffusion barriers should be obtained by increasing the thickness of deposited films. As it is expensive and time consuming to deposit ALD films thicker than 50 nm with traditional temporal ALD reactors, PECVD films of >200 nm could act as good diffusion barriers to prevent external leaking of toxic substances from silicon devices during implantation. Thick PECVD diffusion barriers should be coated with biocompatible and biostable layers such as HfO_2 , SiC, SiOC and TiO_2 to extend the packaging lifetime of silicon devices in targeted biological environments.

Aging tests of fabricated test vehicles showed the benefit of barrier films of HfO_2 and $\text{Al}_2\text{O}_3+\text{TiO}_2$ to protect silicon and metallic substrates from corrosion in hot saline solution. The effect of deposition temperature on corrosion protection was explored and adjusted for these three materials. However, other parameters of deposition and preparation of substrates (e.g., cleaning, RDL planarization, surface activation) have to be further optimized for industrial applications.

As silicon corrodes at rates of $\sim 1 \mu\text{m}$ per month in biological environments, silicon devices intended for medical implants of >10 years should be coated with a biocompatible, biostable and hermetic coating such as $\text{Al}_2\text{O}_3+\text{TiO}_2$ or $\text{Al}_2\text{O}_3+\text{HfO}_2$. Afterwards, reactive ion etching or sequential blade dicing methods could be used to create unsharpened silicon devices from the wafer. A second biocompatible, conformal and relatively inert coating that resembles the mechanical properties of the surrounding tissue (e.g., parylene, silicone and chitosan) should be applied lastly to further improve biocompatibility and corrosion protection. These devices should have an improved biological response post-implantation. Pertinent biological evaluation tests should be conducted to validate these biocompatible packaging technologies for medical micro devices.

Bibliography

- [1] R. Freitas, *Nanomedicine, Volume IIA: Biocompatibility*. Georgetown: S. Karger AG, 2003.
- [2] “Medical devices - European Commission.” [Online]. Available: http://ec.europa.eu/growth/sectors/medical-devices/index_en.htm. [Accessed: 01-Sep-2015].
- [3] J. Black, *Biological Performance of Materials: Fundamentals of Biocompatibility*,. New York: Marcel Dekker, 1999.
- [4] D. F. Williams, *The Williams Dictionary of Biomaterials*. Liverpool: Liverpool University Press, 1999.
- [5] L. Yang, “Regulatory Requirement for Biocompatibility Tests on Medical Device,” Singapore, 24-Mar-2014.
- [6] International Standards Organization, “ISO 10993-1:2009 - Biological evaluation of medical devices -- Part 1: Evaluation and testing within a risk management process.” 2009.
- [7] J. W. Carraway and E. M. Daniel, “Study Design and Methodologies for Study of Ocular Medical Devices,” in *Ocular Pharmacology and Toxicology*, Springer, 2014, pp. 243–265.
- [8] International Standards Organization, “ISO/IEC 17025:2005 - General requirements for the competence of testing and calibration laboratories.” 2005.
- [9] International Standards Organization, “ISO 10993-9:2009 - Biological evaluation of medical devices -- Part 9: Framework for identification and quantification of potential degradation products.” 2009.
- [10] K. Moyer, “EXTRACTABLES AND LEACHABLES FOR MEDICAL DEVICES: MEETING THE 510 (k) REQUIREMENTS,” 2012. [Online]. Available: http://www.nsf.org/newsroom_pdf/NSF_Pharmalytica_EL_white_paper_Feb_2012.pdf. [Accessed: 23-Feb-2015].
- [11] R. L. Williams, S. A. Brown, and K. Merritt, “Electrochemical studies on the influence of proteins on the corrosion of implant alloys,” *Biomaterials*, vol. 9, no. 2, pp. 181–186, Mar. 1988.
- [12] European Communities, “Council Directive 90/385/EEC,” *Off. J. Eur. Communities*, vol. 33, no. 189, 1990.
- [13] BCC Research, “Microelectronic Medical Implants: Products, Technologies & Opportunities,” May-2011. [Online]. Available: <http://www.bccresearch.com/market-research/healthcare/microelectronic-medical-implants-produts-hlc016d.html>. [Accessed: 24-Mar-2015].
- [14] J. Banke, “Technology Readiness Levels Demystified,” *NASA*, 07-Jun-2013. [Online]. Available: http://www.nasa.gov/topics/aeronautics/features/trl_demystified.html. [Accessed: 21-Feb-2015].
- [15] Heterogeneous Technology Alliance, “Position papers 2014.” [Online]. Available: <http://www.hta->

- online.eu/fileadmin/MEDIA/Press_and_Media/HTA_Positions_Papers_12_2014_WEB.pdf. [Accessed: 21-Feb-2015].
- [16] “Regulators had not approved most PIP implants: lawyer,” *Reuters*, 27-Dec-2011.
- [17] A. Vanhoostenberghe and N. Donaldson, “The Limits of Hermeticity Test Methods for Micropackages,” *Artif. Organs*, vol. 35, no. 3, pp. 242–244, Mar. 2011.
- [18] A. Vanhoostenberghe and N. Donaldson, “Corrosion of silicon integrated circuits and lifetime predictions in implantable electronic devices,” *J. Neural Eng.*, vol. 10, no. 3, p. 031002, Jun. 2013.
- [19] P. Roberge, “Periodic Table of Toxic Elements.” [Online]. Available: <http://corrosion-doctors.org/Elements-Toxic/Elements.htm>. [Accessed: 21-Feb-2015].
- [20] G. Jiang and D. Zhou, “Technology Advances and Challenges in Hermetic Packaging for Implantable Medical Devices,” in *Implantable Neural Prostheses 2 - Techniques and Engineering Approaches, Biological and Medical Physics, Biomedical Engineering*, New York: Springer, 2009, pp. 27–61.
- [21] R. Tummala and E. Rymaszewski, *Microelectronics Packaging Handbook*. New York: Van Nostrand Reinhold, 1989.
- [22] R. K. Traeger, “Hermeticity of polymeric lid sealants,” in *Proceedings 25th Electronics Components conference*, Delft, 1976.
- [23] P. E. Garrou, *Multichip Module Technology Handbook*. McGraw-Hill, 1998.
- [24] United States Department of Defense, “MIL-STD-883J w/ CHANGE4,” 03-Jul-2014. [Online]. Available: <http://www.landandmaritime.dla.mil/Downloads/MilSpec/Docs/MIL-STD-883/std883.pdf>. [Accessed: 15-Feb-2015].
- [25] H. Greenhouse, R. Lowry, and B. Romenesko, *Hermeticity of Electronic Packages*, 2nd ed. Oxford: Elsevier, 2012.
- [26] C. Antoine, “Tensions des vapeurs; nouvelle relation entre les tensions et les températures,” *Comptes rendus de l’Académie des sciences*, no. 107, pp. 681–684, 1888.
- [27] UCLA Department of Epidemiology, “Definitions.” [Online]. Available: http://www.ph.ucla.edu/epi/bioter/anthapha_def_a.html. [Accessed: 22-Feb-2015].
- [28] 3M Company, “3M™ Steri-Vac™ Ethylene Oxide Sterilization Systems,” 10-May-2010. [Online]. Available: <http://multimedia.3m.com/mws/media/6531190/steri-vac-ethylene-oxide-sterilization-systems.pdf>. [Accessed: 22-Feb-2015].
- [29] J. Bommer and E. Ritz, “Ethylene oxide (ETO) as a major cause of anaphylactoid reactions in dialysis (a review),” *Artif. Organs*, vol. 11, no. 2, pp. 111–117, Apr. 1987.
- [30] J. van Doornmalen and K. Kopinga, “Review of surface steam sterilization for validation purposes,” *Am. J. Infect. Control*, vol. 36, no. 2, pp. 86–92, Mar. 2008.
- [31] P. Dvorak, “Designing For Sterilization,” 2005. [Online]. Available: <http://medicaldesign.com/contract-manufacturing/designing-sterilization>. [Accessed: 22-Feb-2015].
- [32] M. Vert, Y. Doi, K.-H. Hellwich, M. Hess, P. Hodge, P. Kubisa, M. Rinaudo, and F. Schué, “Terminology for biorelated polymers and applications (IUPAC Recommendations 2012),” *Pure Appl. Chem.*, vol. 84, no. 2, Jan. 2012.
- [33] International Standards Organization, “ISO 2409:2013 - Paints and varnishes -- Cross-cut test.” 2013.
- [34] J. W. Osenbach and W. R. Knolle, “Behavior of a - SiN : H and a - SiON : H Films in Condensed Water,” *J. Electrochem. Soc.*, vol. 139, no. 11, pp. 3346–3351, Nov. 1992.

- [35] J. W. Osenbach, “Corrosion-induced degradation of microelectronic devices,” *Semicond. Sci. Technol.*, vol. 11, no. 2, p. 155, Feb. 1996.
- [36] J. S. Osenbach and J. L. Zell, “Corrosion of thin film aluminum metallization: conformal coating materials,” *IEEE Trans. Compon. Hybrids Manuf. Technol.*, vol. 16, no. 3, pp. 350–359, May 1993.
- [37] J. W. Osenbach, “Water-Induced Corrosion of Materials Used for Semiconductor Passivation,” *J. Electrochem. Soc.*, vol. 140, no. 12, pp. 3667–3675, Dec. 1993.
- [38] K. Kendall, “Adhesion: Molecules and Mechanics,” *Science*, vol. 263, no. 5154, pp. 1720–1725, Mar. 1994.
- [39] J. L. Bologna, J. L. Jorizzo, and J. V. Schaffer, *Dermatology*, 3th ed. Saunders, 2012.
- [40] R. O. Darouiche, “Treatment of Infections Associated with Surgical Implants,” *N. Engl. J. Med.*, vol. 350, no. 14, pp. 1422–1429, Apr. 2004.
- [41] B. F. Matlaga, L. P. Yasenachak, and T. N. Salthouse, “Tissue response to implanted polymers: The significance of sample shape,” *J. Biomed. Mater. Res.*, vol. 10, no. 3, pp. 391–397, May 1976.
- [42] P. Moshayedi, G. Ng, J. C. F. Kwok, G. S. H. Yeo, C. E. Bryant, J. W. Fawcett, K. Franze, and J. Guck, “The relationship between glial cell mechanosensitivity and foreign body reactions in the central nervous system,” *Biomaterials*, vol. 35, no. 13, pp. 3919–3925, Apr. 2014.
- [43] J. Hilborn and L. M. Bjursten, “A new and evolving paradigm for biocompatibility,” *J. Tissue Eng. Regen. Med.*, vol. 1, no. 2, pp. 110–119, Mar. 2007.
- [44] DISCO Corporation, “Laser Full Cut Dicing.” [Online]. Available: <http://www.disco.co.jp/eg/solution/library/laser.html>. [Accessed: 25-Mar-2015].
- [45] SPTS Technologies, “Plasma dicing to improve yield.” [Online]. Available: <http://www.spts.com/banners/wafer-dicing>. [Accessed: 25-Mar-2015].
- [46] L. Yu, B. J. Kim, and E. Meng, “Chronically Implanted Pressure Sensors: Challenges and State of the Field,” *Sensors*, vol. 14, no. 11, pp. 20620–20644, Oct. 2014.
- [47] C. Hierold, B. Clasbrumme, D. Behrend, T. Scheiter, M. Steger, K. Oppermann, H. Kapels, E. Landgraf, D. Wenzel, and D. Etuodt, “Implantable low power integrated pressure sensor system for minimal invasive telemetric patient monitoring,” in *The Eleventh Annual International Workshop on Micro Electro Mechanical Systems, 1998. MEMS 98. Proceedings*, 1998, pp. 568–573.
- [48] APCMAG, “How a chip is made.” [Online]. Available: <http://apcmag.com/picture-gallery-how-a-chip-is-made.htm/>. [Accessed: 28-Jun-2015].
- [49] O. Aquilina, “A brief history of cardiac pacing,” *Images Paediatr. Cardiol.*, vol. 8, no. 2, pp. 17–81, 2006.
- [50] Y. Lamy and G. Simon, “Electronic and ultra miniaturization : towards smart biomedical devices,” 16-Apr-2013. [Online]. Available: http://www-leti.cea.fr/en/content/download/1806/23891/file/8_Electronique%20et%20syst%C3%A8mes%20ultra-miniaturis%C3%A9e.pdf. [Accessed: 21-Feb-2015].
- [51] Business Wire, “St. Jude Medical Announces Start of European Post-Approval Trial for Nanostim Leadless Pacemaker.” [Online]. Available: <http://www.businesswire.com/multimedia/home/20140318005184/en/#.VXxhR0Yw81c>. [Accessed: 13-Jun-2015].
- [52] E. Jung, “Medical Device Innovations by Miniaturization,” 11-Dec-2014. [Online]. Available:

- http://thor.inemi.org/webdownload/2014/Med_Device_Innovations_121114.pdf. [Accessed: 21-Feb-2015].
- [53] St. Jude Medical, Inc., “Leadless Pacing Nanostim™.” [Online]. Available: <http://www.sjm.com/leadlesspacing/intl/options/leadless-pacing>. [Accessed: 28-Jun-2015].
- [54] Medigus Ltd, “micro ScoutCam™ 1.2.” [Online]. Available: <http://www.microscoutcam.com/medigus-products/micro-scoutcam-cameras-for-medical-applications/121-1-2mm-camera>. [Accessed: 08-May-2015].
- [55] Noviosense, “Tear Glucose Sensor.” [Online]. Available: <http://noviosense.com/>. [Accessed: 13-Jun-2015].
- [56] Sensimed AG, “Triggerfish®.” [Online]. Available: <http://www.sensimed.ch/en/sensimed-triggerfish/sensimed-triggerfish.html>. [Accessed: 13-Jun-2015].
- [57] P. E. K. Donaldson, “The Encapsulation of Microelectronic Devices for Long-Term Surgical Implantation,” *IEEE Trans. Biomed. Eng.*, vol. BME-23, no. 4, pp. 281–285, Jul. 1976.
- [58] F. Graichen, R. Arnold, A. Rohlmann, and G. Bergmann, “Implantable 9-channel telemetry system for in vivo load measurements with orthopedic implants,” *IEEE Trans. Biomed. Eng.*, vol. 54, no. 2, pp. 253–261, Feb. 2007.
- [59] G. E. Loeb and F. J. Richmond, “BION™ Implants for Therapeutic and Functional Electrical Stimulation,” in *Neural Prostheses for Restoration of Sensory and Motor Function*, Boca Raton: CRC, 2000, pp. 75–99.
- [60] J.-C. Souriau, L. Castagne, G. Parat, G. Simon, K. Amara, P. D’hiver, and R. Dal Molin, “Implantable device including a MEMS accelerometer and an ASIC chip encapsulated in a hermetic silicon box for measurement of cardiac physiological parameter,” in *Electronic Components and Technology Conference (ECTC), 2014 IEEE 64th*, 2014, pp. 1198–1203.
- [61] J. F. Rizzo, J. Wyatt, M. Humayun, E. de Juan, W. Liu, A. Chow, R. Eckmiller, E. Zrenner, T. Yagi, and G. Abrams, “Retinal prosthesis,” *Ophthalmology*, vol. 108, no. 1, pp. 13–14, Jan. 2001.
- [62] D. C. Ng, S. Bai, J. Yang, N. Tran, and E. Skafidas, “Wireless technologies for closed-loop retinal prostheses,” *J. Neural Eng.*, vol. 6, no. 6, p. 065004, Dec. 2009.
- [63] H. Gerding, “A new approach towards a minimal invasive retina implant,” *J. Neural Eng.*, vol. 4, no. 1, pp. S30–S37, Mar. 2007.
- [64] S. Franssila, *Introduction to Microfabrication*. John Wiley & Sons, 2010.
- [65] D. Godlewski, “Reliability Requirements for Implantable Medical Devices | iNEMI.” [Online]. Available: <http://www.inemi.org/project-page/defining-requirements-development-medical-electronics-reliability-specifications>. [Accessed: 19-Feb-2015].
- [66] J. Neteler, “Clean Room ESD Packaging Overview,” in *Electrical Overstress/Electrostatic Discharge Symposium, 1997. Proceedings*, 1997, pp. 263–270.
- [67] R. K. Traeger, “Nonhermeticity of Polymeric Lid Sealants,” *IEEE Trans. Parts Hybrids Packag.*, vol. 13, no. 2, pp. 147–152, Jun. 1977.
- [68] D. G. Munoz and H. Feldman, “Causes of Alzheimer’s disease,” *Can. Med. Assoc. J.*, vol. 162, no. 1, pp. 65–72, Jan. 2000.
- [69] M. N. Helmus, D. F. Gibbons, and D. Cebon, “Biocompatibility: Meeting a Key Functional Requirement of Next-Generation Medical Devices,” *Toxicol. Pathol.*, vol. 36, no. 1, pp. 70–80, Jan. 2008.

- [70] D. E. Clark and B. K. Zaitos, *Corrosion of Glass, Ceramics and Ceramic Superconductors: Principles, Testing, Characterization and Applications*, 1 edition. Park Ridge, N.J: William Andrew, 1993.
- [71] R. Zhuo, P. Colombo, C. Pantano, and E. A. Vogler, “Silicon oxycarbide glasses for blood-contact applications,” *Acta Biomater.*, vol. 1, no. 5, pp. 583–589, Sep. 2005.
- [72] S. K. Arya, S. Saha, J. E. Ramirez-Vick, V. Gupta, S. Bhansali, and S. P. Singh, “Recent advances in ZnO nanostructures and thin films for biosensor applications: Review,” *Anal. Chim. Acta*, vol. 737, pp. 1–21, Aug. 2012.
- [73] S. Lousinian, N. Kalfagiannis, and S. Logothetidis, “Optical and surface characterization of amorphous boron nitride thin films for use as blood compatible coatings,” *Solid State Sci.*, vol. 11, no. 10, pp. 1801–1805, Oct. 2009.
- [74] E. Salgueiredo, M. Vila, M. A. Silva, M. A. Lopes, J. D. Santos, F. M. Costa, R. F. Silva, P. S. Gomes, and M. H. Fernandes, “Biocompatibility evaluation of DLC-coated Si₃N₄ substrates for biomedical applications,” *Diam. Relat. Mater.*, vol. 17, no. 4–5, pp. 878–881, Apr. 2008.
- [75] D. F. Williams, *Fundamental aspects of biocompatibility / editor, David F. Williams*. Boca Raton, Fla. : CRC Press, c1981., 1981.
- [76] Y. Hedberg, “Stainless Steel in Biological Environments – Relation between Material Characteristics, Surface Chemistry and Toxicity,” 2012.
- [77] D. M. Brunette, P. Tengvall, M. Textor, and P. Thomsen, *Titanium in Medicine: Material Science, Surface Science, Engineering, Biological Responses and Medical Applications*. Springer Science & Business Media, 2012.
- [78] B. D. Ratner, A. S. Hoffman, F. J. Schoen, and J. E. Lemons, *Biomaterials Science, Third Edition: An Introduction to Materials in Medicine*, 3 edition. Amsterdam ; Boston: Academic Press, 2012.
- [79] G. Jiang and G. Jiang, “Design challenges of implantable pressure monitoring system,” *Neuroprosthetics*, vol. 4, p. 29, 2010.
- [80] J. C. Scully, *The fundamentals of corrosion*. Pergamon Press, 1975.
- [81] Stacy Gleixner, “The Characterization of Particulate Ti Debris: Ch. 5.” [Online]. Available: <http://www.engr.sjsu.edu/WofMatE/projects/srproject/srproj5.html>. [Accessed: 23-Jun-2015].
- [82] M. Textor, C. Sittig, V. Frauchiger, S. Tosatti, and D. M. Brunette, “Properties and Biological Significance of Natural Oxide Films on Titanium and Its Alloys,” in *Titanium in Medicine*, Springer Berlin Heidelberg, 2001, pp. 171–230.
- [83] G. L. Humphrey, “Heats of Formation of Hafnium Oxide and Hafnium Nitride,” *J. Am. Chem. Soc.*, vol. 75, no. 12, pp. 2806–2807, Jun. 1953.
- [84] W. L. Masterton, E. J. Slowinski, and C. L. Stanitski, *Chemical principles: alternate edition with a qualitative analysis supplement*. Philadelphia: Saunders College Pub, 1983.
- [85] Charles Kittel, *Introduction to Solid State Physics*, 8th ed. Hoboken, NJ: Wiley, 2004.
- [86] D. R. Lide and CRC Press, Eds., *CRC handbook of chemistry and physics: a ready-reference book of chemical and physical data*, 87. ed., 2006-2007. Boca Raton, Fla.: CRC, Taylor & Francis, 2006.
- [87] A. J. Bard, R. Parsons, and J. Jordan, *Standard Potentials in Aqueous Solution*. CRC Press, 1985.

- [88] Aluminium Design .Net, “Aluminium Corrosion Resistance.” [Online]. Available: <http://www.aluminiumdesign.net/design-support/aluminium-corrosion-resistance/>. [Accessed: 20-Aug-2015].
- [89] “Aluminum E-pH (Pourbaix) diagram.” [Online]. Available: <http://corrosion-doctors.org/Corrosion-Thermodynamics/Potential-pH-diagram-aluminum.htm>. [Accessed: 12-Aug-2015].
- [90] M. Long and H. J. Rack, “Titanium alloys in total joint replacement—a materials science perspective,” *Biomaterials*, vol. 19, no. 18, pp. 1621–1639, Sep. 1998.
- [91] E. Gultepe, D. Nagesha, S. Sridhar, and M. Amiji, “Nanoporous inorganic membranes or coatings for sustained drug delivery in implantable devices,” *Adv. Drug Deliv. Rev.*, vol. 62, no. 3, pp. 305–315, Mar. 2010.
- [92] S. G. Steinemann, “Titanium — the material of choice?,” *Periodontol. 2000*, vol. 17, no. 1, pp. 7–21, Jun. 1998.
- [93] G. Schmalz and D. A. Bindslev, *Biocompatibility of Dental Materials*. Springer Science & Business Media, 2008.
- [94] D. Zhou and B. Mech, “Accelerated corrosion tests on Silicon wafers for implantable medical devices,” in *Proceedings of 198th Electrochemical Society Meeting*, Phoenix, p. 363.
- [95] G. Kotzar, M. Freas, P. Abel, A. Fleischman, S. Roy, C. Zorman, J. M. Moran, and J. Melzak, “Evaluation of MEMS materials of construction for implantable medical devices,” *Biomaterials*, vol. 23, no. 13, pp. 2737–2750, Jul. 2002.
- [96] R. Matero, M. Ritala, M. Leskelä, T. Salo, J. Aromaa, and O. Forsén, “Atomic layer deposited thin films for corrosion protection,” *J. Phys. IV*, vol. 09, no. PR8, pp. Pr8–493–Pr8–499, Sep. 1999.
- [97] V. Miikkulainen, M. Leskelä, M. Ritala, and R. L. Puurunen, “Crystallinity of inorganic films grown by atomic layer deposition: Overview and general trends,” *J. Appl. Phys.*, vol. 113, no. 2, p. 021301, Jan. 2013.
- [98] A. I. Abdulagatov, Y. Yan, J. R. Cooper, Y. Zhang, Z. M. Gibbs, A. S. Cavanagh, R. G. Yang, Y. C. Lee, and S. M. George, “Al₂O₃ and TiO₂ Atomic Layer Deposition on Copper for Water Corrosion Resistance,” *ACS Appl. Mater. Interfaces*, vol. 3, no. 12, pp. 4593–4601, Dec. 2011.
- [99] H. Marsh and F. R. Reinoso, *Activated Carbon*. Elsevier, 2006.
- [100] Sandia National Labs, “What is CVD?” [Online]. Available: <http://www.sandia.gov/pcnsc/departments/cvd/whatis.html>. [Accessed: 08-Jul-2015].
- [101] T. Kääriäinen, D. Cameron, M.-L. Kääriäinen, and A. Sherman, “Fundamentals of Atomic Layer Deposition,” in *Atomic Layer Deposition*, John Wiley & Sons, Inc., 2013, pp. 1–31.
- [102] J.-O. Carlsson and P. M. Martin, “Chapter 7 - Chemical Vapor Deposition,” in *Handbook of Deposition Technologies for Films and Coatings (Third Edition)*, P. M. Martin, Ed. Boston: William Andrew Publishing, 2010, pp. 314–363.
- [103] Frank Muscolino, Scotten W. Jones, “IC Packaging Report.” [Online]. Available: <http://www.icknowledge.com/products/packaging.html>. [Accessed: 31-Jul-2015].
- [104] G. N. Strauss, “Mechanical Stress in Optical Coatings,” in *Optical Interference Coatings*, D. N. Kaiser and D. H. K. Pulker, Eds. Springer Berlin Heidelberg, 2003, pp. 207–229.

- [105] H. Kupfer, T. Flügel, F. Richter, and P. Schlott, “Intrinsic stress in dielectric thin films for micromechanical components,” *Surf. Coat. Technol.*, vol. 116–119, pp. 116–120, Sep. 1999.
- [106] R. L. Puurunen, “A Short History of Atomic Layer Deposition: Tuomo Suntola’s Atomic Layer Epitaxy,” *Chem. Vap. Depos.*, vol. 20, no. 10–11–12, pp. 332–344, Dec. 2014.
- [107] M. D. Groner, F. H. Fabreguette, J. W. Elam, and S. M. George, “Low-Temperature Al₂O₃ Atomic Layer Deposition,” *Chem. Mater.*, vol. 16, no. 4, pp. 639–645, Feb. 2004.
- [108] D. J. Monsma and J. Becker, “Savannah ALD Systems: Enabling Quick Results,” *ECS Trans.*, vol. 11, no. 7, pp. 39–44, Sep. 2007.
- [109] Cambridge NanoTech Inc., “A Tutorial of Atomic Layer Deposition.” 08-Jan-2006.
- [110] E. Marin, L. Guzman, A. Lanzutti, W. Ensinger, and L. Fedrizzi, “Multilayer Al₂O₃/TiO₂ Atomic Layer Deposition coatings for the corrosion protection of stainless steel,” *Thin Solid Films*, vol. 522, pp. 283–288, Nov. 2012.
- [111] A. Marquardt, E. M. Breitung, T. Drayman-Weisser, G. Gates, G. W. Rubloff, and R. J. Phaneuf, “Characterization of Atomic Layer Deposited Films as Diffusion Barriers for Silver Art Objects,” *ECS Trans.*, vol. 58, no. 10, pp. 277–286, Aug. 2013.
- [112] J. Kools, “High Throughput Atomic Layer Deposition for Encapsulation of Large Area Electronics,” 2011, pp. 195–201.
- [113] T. Kääriäinen, D. Cameron, M.-L. Kääriäinen, and A. Sherman, “ALD Applications and Industry,” in *Atomic Layer Deposition*, John Wiley & Sons, Inc., 2013, pp. 215–242.
- [114] PlasticsToday.com, “PTFE delamination plagues medical device manufacturers.” [Online]. Available: <http://www.plasticstoday.com/articles/PTFE-delamination-plagues-medical-device-manufacturers-140926>. [Accessed: 19-Sep-2015].
- [115] *Materials and Coatings for Medical Devices: Cardiovascular*. ASM International, 2009.
- [116] Y.-S. Lin, “Fiji Thermal and Plasma Atomic Layer Deposition System (ALD) By Ultratech (Cambridge),” 30-Jul-2013. [Online]. Available: http://www.nanolab.ucla.edu/pdf/ALD_Fiji.pdf.
- [117] David Leadley, “X-ray Reflectivity.” [Online]. Available: <http://www2.warwick.ac.uk/fac/sci/physics/current/postgraduate/regs/mpags/ex5/techniques/structural/gixrd/>. [Accessed: 04-Aug-2015].
- [118] T. Matsubara, T. Oishi, and A. Katagiri, “Determination of Porosity of TiO₂ Films from Reflection Spectra,” *J. Electrochem. Soc.*, vol. 149, no. 2, pp. C89–C93, Feb. 2002.
- [119] T. M. Besmann, *Proceedings of the Thirteenth International Conference on Chemical Vapor Deposition*. The Electrochemical Society, 1996.
- [120] Renju Zacharia, “Desorption of gases from graphitic and porous carbon surfaces.”
- [121] A. Barinov, O. B. Malcioğlu, S. Fabris, T. Sun, L. Gregoratti, M. Dalmiglio, and M. Kiskinova, “Initial Stages of Oxidation on Graphitic Surfaces: Photoemission Study and Density Functional Theory Calculations,” *J. Phys. Chem. C*, vol. 113, no. 21, pp. 9009–9013, May 2009.
- [122] F. Atamny, J. Blöcker, A. Dübotzky, H. Kurt, O. Timpe, G. Loose, W. Mahdi, and R. Schlögl, “Surface chemistry of carbon: activation of molecular oxygen,” *Mol. Phys.*, vol. 76, no. 4, pp. 851–886, Jul. 1992.

- [123] K. Pulskamp, J. M. Wörle-Knirsch, F. Hennrich, K. Kern, and H. F. Krug, “Human lung epithelial cells show biphasic oxidative burst after single-walled carbon nanotube contact,” *Carbon*, vol. 45, no. 11, pp. 2241–2249, Oct. 2007.
- [124] Thermo Fisher Scientific Inc., “What is XPS.” [Online]. Available: <http://xpssimplified.com/whatisxps.php>. [Accessed: 22-Jul-2015].
- [125] “NIST XPS Database, Selected Element Search Result.” [Online]. Available: http://srdata.nist.gov/xps/EngElmSrChQuery.aspx?EType=PE&CSOpt=Retri_ex_dat&Elm=C. [Accessed: 05-Aug-2015].
- [126] Thermo Fisher Scientific Inc., “XPS Interpretation of Silicon.” [Online]. Available: <http://xpssimplified.com/elements/silicon.php>. [Accessed: 05-Aug-2015].
- [127] Thermo Fisher Scientific Inc., “XPS Interpretation of Carbon.” [Online]. Available: <http://xpssimplified.com/elements/carbon.php>. [Accessed: 05-Aug-2015].
- [128] S. S. Block, *Disinfection, Sterilization, and Preservation*. Lippincott Williams & Wilkins, 2001.
- [129] C. S. Hwang, *Atomic Layer Deposition for Semiconductors*. Springer Science & Business Media, 2013.
- [130] Thermo Fisher Scientific Inc., “XPS Interpretation of Oxygen.” [Online]. Available: <http://xpssimplified.com/elements/oxygen.php>. [Accessed: 06-Aug-2015].
- [131] Thermo Fisher Scientific Inc., “XPS Interpretation of Hafnium.” [Online]. Available: <http://xpssimplified.com/elements/hafnium.php>. [Accessed: 05-Aug-2015].
- [132] Thermo Fisher Scientific Inc., “XPS Interpretation of Nitrogen.” [Online]. Available: <http://xpssimplified.com/elements/nitrogen.php>. [Accessed: 06-Aug-2015].
- [133] Thermo Fisher Scientific Inc., “XPS Interpretation of Titanium.” [Online]. Available: <http://xpssimplified.com/elements/titanium.php>. [Accessed: 07-Aug-2015].
- [134] Thermo Fisher Scientific Inc., “XPS Interpretation of Zinc.” [Online]. Available: <http://xpssimplified.com/elements/zinc.php>. [Accessed: 07-Aug-2015].
- [135] D. W. L. Hukins, A. Mahomed, and S. N. Kukureka, “Accelerated aging for testing polymeric biomaterials and medical devices,” *Med. Eng. Phys.*, vol. 30, no. 10, pp. 1270–1274, Dec. 2008.
- [136] P. Viswanadham and P. Singh, *Failure Modes and Mechanisms in Electronic Packages*. Springer Science & Business Media, 1998.
- [137] William J. Vigrass, “Calculation of Semiconductor Failure Rates.” [Online]. Available: http://www.intersil.com/content/dam/Intersil/quality/rel/calculation_of_semiconductor_failure_rates.pdf. [Accessed: 30-Jul-2015].
- [138] W. W. Weick, “Acceleration Factors for IC Leakage Current in a Steam Environment,” *IEEE Trans. Reliab.*, vol. R-29, no. 2, pp. 109–115, Jun. 1980.
- [139] Karl J. Hemmerich, “General Aging Theory and Simplified Protocol for Accelerated Aging of Medical Devices.” [Online]. Available: <http://www.mddionline.com/article/general-aging-theory-and-simplified-protocol-accelerated-aging-medical-devices>. [Accessed: 29-Jun-2015].
- [140] NASA, “CORROSION CONTROL AND TREATMENT MANUAL,” 01-Nov-1994. [Online]. Available: <http://corrosion.ksc.nasa.gov/pubs/tm584c.pdf>. [Accessed: 21-Feb-2015].
- [141] Dissemination of IT for the Promotion of Materials Science (DoITPoMS), “The Nernst Equation and Pourbaix Diagrams.” [Online]. Available:

- http://www.doitpoms.ac.uk/tlplib/pourbaix/pourbaix_example.php. [Accessed: 20-Aug-2015].
- [142] VITLAB GmbH, “Sample vials, PFA.” [Online]. Available: <http://www.vitlab.com/en/product/sample-vials-pfa/>. [Accessed: 12-May-2015].
- [143] D. J. Edell, “INSULATING BIOMATERIALS,” in *Neuroprosthetics*, vol. 2, WORLD SCIENTIFIC, 2004, pp. 517–579.
- [144] The Engineering ToolBox, “Densities of Miscellaneous Solids.” [Online]. Available: http://www.engineeringtoolbox.com/density-solids-d_1265.html. [Accessed: 21-Aug-2015].
- [145] D. Zhou and E. Greenbaum, *Implantable Neural Prostheses 1: Devices and Applications*. Springer Science & Business Media, 2009.
- [146] J. M. Maloney, S. A. Lipka, and S. P. Baldwin, “In Vivo Biostability of CVD Silicon Oxide and Silicon Nitride Films,” in *Symposium J – Micro- and Nanosystems—Materials and Devices*, 2005, vol. 872.
- [147] *Corrosion Engineering: Principles and Practice*, 1 edition. New York: McGraw-Hill Education, 2008.
- [148] M. Morita, T. Sasada, I. Nomura, Y. Q. Wei, and Y. Tsukamoto, “Influence of low dissolved oxygen concentration in body fluid on corrosion fatigue behaviors of implant metals,” *Ann. Biomed. Eng.*, vol. 20, no. 5, pp. 505–516, 1992.
- [149] S. Lousinian, N. Kalfagiannis, and S. Logothetidis, “Albumin and fibrinogen adsorption on boron nitride and carbon-based thin films,” *Mater. Sci. Eng. B*, vol. 152, no. 1–3, pp. 12 – 15, 2008.
- [150] C. E. Housecroft and A. G. Sharpe, *Inorganic Chemistry*. Pearson Education, 2005.
- [151] J. A. Woollam Co., “Optical Characterization By Spectroscopic Ellipsometry,” Dec-2010. [Online]. Available: http://www.jawoollam.com/tutorial_1.html.
- [152] H. Hämmerle, K. Kobuch, K. Kohler, W. Nisch, H. Sachs, and M. Stelzle, “Biostability of micro-photodiode arrays for subretinal implantation,” *Biomaterials*, vol. 23, no. 3, pp. 797–804, Feb. 2002.
- [153] L. G. L. Paussa, “Protection of silver surfaces against tarnishing by means of alumina/titania-nanolayers,” *Surf. Amp Coat. Technol. - SURF COAT TECH*, vol. 206, no. 5, pp. 976–980, 2011.
- [154] B. Díaz, J. Światowska, V. Maurice, A. Seyeux, B. Normand, E. Härkönen, M. Ritala, and P. Marcus, “Electrochemical and time-of-flight secondary ion mass spectrometry analysis of ultra-thin metal oxide (Al₂O₃ and Ta₂O₅) coatings deposited by atomic layer deposition on stainless steel,” *Electrochimica Acta*, vol. 56, no. 28, pp. 10516–10523, Dec. 2011.
- [155] J. O. Nriagu, *Encyclopedia of environmental health*. Amsterdam [u.a.: Elsevier, 2011.
- [156] T. Tsuchiya, Y. Ikarashi, H. Hata, K. Toyoda, M. Takahashi, T. Uchima, N. Tanaka, T. Sasaki, and A. Nakamura, “Comparative studies of the toxicity of standard reference materials in various cytotoxicity tests and in vivo implantation tests,” *J. Appl. Biomater. Off. J. Soc. Biomater.*, vol. 4, no. 2, pp. 153–156, 1993.
- [157] M. S. Muthu, A. Abdulla, and B. L. Pandey, “Major toxicities of carbon nanotubes induced by reactive oxygen species: should we worry about the effects on the lungs, liver and normal cells?,” *Nanomed.*, vol. 8, no. 6, pp. 863–866, Jun. 2013.
- [158] Agency for Toxic Substances and Disease Registry (ATSDR), “Toxicological Profile for Copper.” [Online]. Available:

- <http://www.atsdr.cdc.gov/toxprofiles/tp.asp?id=206&tid=37#bookmark16>. [Accessed: 04-Sep-2015].
- [159] P. Collery, *Metal Ions in Biology and Medicine*. John Libbey Eurotext, 1996.
- [160] C. L. Claeys, *High Purity Silicon VI: Proceedings of the Sixth International Symposium*. The Electrochemical Society, 2000.
- [161] A. I. Abdulagatov, Y. Yan, J. R. Cooper, Y. Zhang, Z. M. Gibbs, A. S. Cavanagh, R. G. Yang, Y. C. Lee, and S. M. George, “Al₂O₃ and TiO₂ Atomic Layer Deposition on Copper for Water Corrosion Resistance,” *ACS Appl. Mater. Interfaces*, vol. 3, no. 12, pp. 4593–4601, Dec. 2011.
- [162] A. Hogg, T. Aellen, S. Uhl, B. Graf, H. Keppner, Y. Tardy, and J. Burger, “Ultra-thin layer packaging for implantable electronic devices,” *J. Micromechanics Microengineering*, vol. 23, no. 7, p. 075001, Jul. 2013.
- [163] A. Morlier, S. Cros, J.-P. Garandet, and N. Alberola, “Gas barrier properties of solution processed composite multilayer structures for organic solar cells encapsulation,” *Sol. Energy Mater. Sol. Cells*, vol. 115, pp. 93–99, Aug. 2013.
- [164] S. A. Stern, “The ‘barrer’ permeability unit,” *J. Polym. Sci. Part -2 Polym. Phys.*, vol. 6, no. 11, pp. 1933–1934, Nov. 1968.
- [165] M. Firon, S. Cros, and P. Trouslard, “Method and device for measurement of permeation,” US20070186622 A1, 16-Aug-2007.
- [166] G. L. Graff, R. E. Williford, and P. E. Burrows, “Mechanisms of vapor permeation through multilayer barrier films: Lag time versus equilibrium permeation,” *J. Appl. Phys.*, vol. 96, no. 4, p. 1840, 2004.
- [167] Mark Mcalees, “Pressure Sensitive Tape.” [Online]. Available: <http://www.pstc.org/i4a/pages/index.cfm?pageid=3540>. [Accessed: 24-Aug-2015].
- [168] C.-Y. Yang, J. S. Chen, and S. L.-C. Hsu, “Effects of O₂ and N₂ Plasma Treatment on 6FDA-BisAAF Fluorine-Contained Polyimide,” *J. Electrochem. Soc.*, vol. 153, no. 6, p. F120, 2006.
- [169] S. B. Lee and Y.-K. Kim, “Adhesion Improvement of Polyimide/Metal Interface by He/O₂/NF₃ Atmospheric Pressure Plasma,” *Plasma Process. Polym.*, vol. 6, no. S1, pp. S525–S529, Jun. 2009.
- [170] A. W. Ott, J. W. Klaus, J. M. Johnson, and S. M. George, “Al₂O₃ thin film growth on Si(100) using binary reaction sequence chemistry,” *Thin Solid Films*, vol. 292, no. 1–2, pp. 135–144, Jan. 1997.
- [171] H. C. Barshilia, A. Ananth, J. Khan, and G. Srinivas, “Ar + H₂ plasma etching for improved adhesion of PVD coatings on steel substrates,” *Vacuum*, vol. 86, no. 8, pp. 1165–1173, Feb. 2012.
- [172] J. N. Ding, X. F. Wang, N. Y. Yuan, C. L. Li, Y. Y. Zhu, and B. Kan, “The influence of substrate on the adhesion behaviors of atomic layer deposited aluminum oxide films,” *Surf. Coat. Technol.*, vol. 205, no. 8–9, pp. 2846–2851, Jan. 2011.
- [173] H. P. Kattelus, E. Kolawa, K. Affolter, and M.-A. Nicolet, “Sputtered W–N diffusion barriers,” *J. Vac. Sci. Technol. A*, vol. 3, no. 6, pp. 2246–2254, Nov. 1985.
- [174] E. Patrick, M. E. Orazem, J. C. Sanchez, and T. Nishida, “Corrosion of Tungsten Microelectrodes used in Neural Recording Applications,” *J. Neurosci. Methods*, vol. 198, no. 2, pp. 158–171, Jun. 2011.
- [175] M. Op de Beeck, K. Qian, P. Fiorini, K. Malachowski, and C. Van Hoof, “Design and characterization of a biocompatible packaging concept for implantable electronic devices,” *J. Microelectron. Electron. Packag.*, vol. 9, no. 1, pp. 43–50, Jan. 2012.

- [176] C. Hierold, B. Clasbrumme, D. Behrend, T. Scheiter, M. Steger, K. Oppermann, H. Kapels, E. Landgraf, D. Wenzel, and D. Etuodt, “Implantable low power integrated pressure sensor system for minimal invasive telemetric patient monitoring,” in *The Eleventh Annual International Workshop on Micro Electro Mechanical Systems, 1998. MEMS 98. Proceedings*, 1998, pp. 568–573.
- [177] G. Woan, *The Cambridge handbook of physics formulas*. Cambridge; New York: Cambridge University Press, 2000.
- [178] H. Fujiwara, “Principles of Spectroscopic Ellipsometry,” in *Spectroscopic Ellipsometry*, John Wiley & Sons, Ltd, 2007, pp. 81–146.
- [179] H. Fujiwara, “Data Analysis,” in *Spectroscopic Ellipsometry*, John Wiley & Sons, Ltd, 2007, pp. 147–207.
- [180] M. A. Green, “Self-consistent optical parameters of intrinsic silicon at 300 K including temperature coefficients,” *Sol. Energy Mater. Sol. Cells*, vol. 92, no. 11, pp. 1305–1310, Nov. 2008.
- [181] P. Nayar, A. Khanna, D. Kabiraj, S. R. Abhilash, B. D. Beake, Y. Losset, and B. Chen, “Structural, optical and mechanical properties of amorphous and crystalline alumina thin films,” *Thin Solid Films*, vol. 568, pp. 19–24, Oct. 2014.
- [182] A. Abdellaoui, A. Bath, B. Bouchikhi, and O. Baehr, “Structure and optical properties of boron nitride thin films prepared by PECVD,” *Mater. Sci. Eng. B*, vol. 47, no. 3, pp. 257–262, Jun. 1997.
- [183] J.-M. Hsu, P. Tathireddy, L. Rieth, A. R. Normann, and F. Solzbacher, “Characterization of a-SiCx:H thin films as an encapsulation material for integrated silicon based neural interface devices,” *Thin Solid Films*, vol. 516, no. 1, pp. 34–41, Nov. 2007.
- [184] J. Robertson, “Diamond-like amorphous carbon,” *Mater. Sci. Eng. R Rep.*, vol. 37, no. 4–6, pp. 129–281, May 2002.
- [185] M. C. Cheynet, S. Pokrant, F. D. Tichelaar, and J.-L. Rouvière, “Crystal structure and band gap determination of HfO₂ thin films,” *J. Appl. Phys.*, vol. 101, no. 5, p. 054101, Mar. 2007.
- [186] F. L. Martínez, M. Toledano-Luque, J. J. Gandía, J. Cárabe, W. Bohne, J. Röhrich, E. Strub, and I. Mártel, “Optical properties and structure of HfO₂ thin films grown by high pressure reactive sputtering,” *J. Phys. Appl. Phys.*, vol. 40, no. 17, p. 5256, Sep. 2007.
- [187] E. D. Palik, *Handbook of optical constants of solids*. Orlando: Academic Press, 1985.
- [188] T. Nakai, K. Yusu, Y. Satoh, and S. Ashida, “High-Speed Deposition of New Low-Refractive-Index Dielectric Film ‘SiOC’ for Rewritable HD DVD Media,” *Jpn. J. Appl. Phys.*, vol. 45, no. 2S, p. 1447, Feb. 2006.
- [189] H. J. Kim, Q. Shao, and Y.-H. Kim, “Characterization of low-dielectric-constant SiOC thin films deposited by PECVD for interlayer dielectrics of multilevel interconnection,” *Surf. Coat. Technol.*, vol. 171, no. 1–3, pp. 39–45, Jul. 2003.
- [190] M. Zhang, G. Lin, C. Dong, and L. Wen, “Amorphous TiO₂ films with high refractive index deposited by pulsed bias arc ion plating,” *Surf. Coat. Technol.*, vol. 201, no. 16–17, pp. 7252–7258, May 2007.
- [191] J. R. Devore, “Refractive Indices of Rutile and Sphalerite,” *J. Opt. Soc. Am.*, vol. 41, no. 6, p. 416, Jun. 1951.
- [192] S. Kasap and P. Capper, *Springer Handbook of Electronic and Photonic Materials*. Springer Science & Business Media, 2006.

Annexes

A1. Characterization of thin films by VASE

Spectroscopy Ellipsometry (SE) is an analytic optical technique employed to investigate the optical properties of thin films. It can be used to find the refractive index, thickness and dielectric constant of films. It is called ellipsometry because linearly polarized light is reflected as light with elliptical polarization after interaction with the sample. Figure 95 shows the schematic setup of a SE measurement. When light from different angles of incidence Φ is recorded, SE is called Variable Angle Spectroscopy Ellipsometry or VASE.

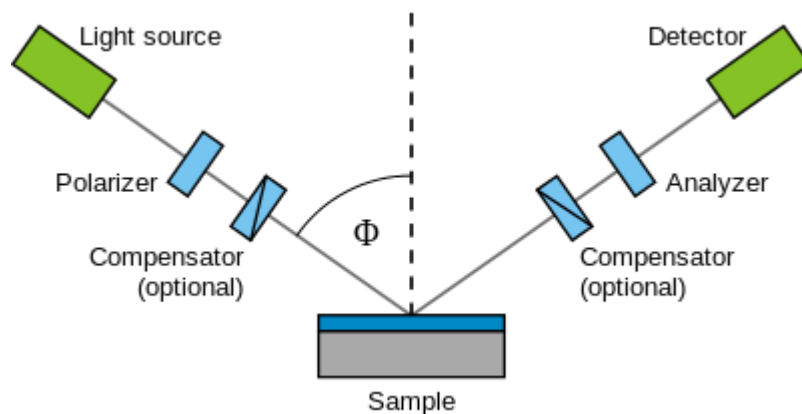


Figure 95: Schematic setup of a Variable Angle Spectroscopy Ellipsometry measurement.

Elliptically polarized light is very sensitive to changes induced by interactions with matter of the analyzed film. Figure 96A shows an example of a linearly polarized wave. Component waves are in phase with each other and the result is a linearly polarized wave. If for some reason, one of the component waves is delayed and becomes 90° out of phase with the other component wave, the result is a circularly polarized wave (Figure 96B). Actually, linear and circular polarizations are mathematical subsets of elliptical polarization. If light has component waves of arbitrary phase and amplitude with each other, the wave light is said to be elliptically polarized (Figure 96C) [151].

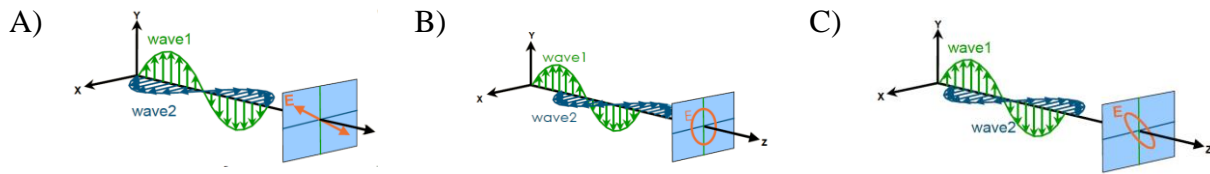


Figure 96: Orthogonal waves: A) linearly, B) circularly, C) elliptically polarized. [151]

Two numbers are required to define an ellipse: orientation and size (intensity). Spectroscopy Ellipsometry measures the change in polarization of light reflected from the surface of the sample, so it measures the orientation and intensity of the reflected light (Figure 97).

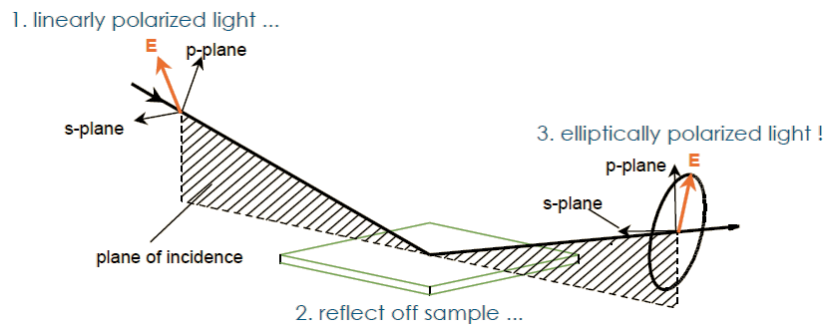


Figure 97: The principle of ellipsometry measurements. [151]

The polarized state of the incident light can be decomposed into the components s and p of, where the s -component is oscillating perpendicular to the plane of incidence and the p -component is oscillating parallel to the surface of the sample. The amplitudes of the s and p components after reflection and normalized to their initial value are respectively denoted by r_s and r_p . According to physicist Augustin-Jean Fresnel [177], the complex reflectance ratio (ρ) is defined as the ratio of r_p to r_s and equals:

$$\rho = \frac{r_p}{r_s} = \tan(\Psi) e^{i\Delta} = \tan(\Psi) \cdot \cos\Delta + i \cdot \tan(\Psi) \cdot \sin\Delta \quad \text{Eq. 22}$$

In Eq. 22, $\tan(\Psi)$ is the amplitude ratio after reflection and Δ is the phase shift or delay of the polarized light. Ellipsometry is very accurate and reproducible due to the fact that it measures the ratio of two physical values and not their absolute values. Thanks to this, no reference beam or standard samples are needed. And the sensitivity of the technique can be further

increased down to the sub nanometer regime by obtaining data from different angles of incidence.

The measured Ψ and Δ values cannot be directly converted to the optical constants of the sample, so data analysis has to be done. A mathematical model must be fitted to the experimental data using an iterative procedure of least-squares minimization to convert Ψ and Δ into the optical constants of the sample. It is therefore important to study the mathematical equations behind spectroscopic ellipsometry.

The refractive index of a material gives an idea of its “optical density”, or a notion of how much the speed of light is decreased inside the material. For bulk materials that absorb light, there is complete extinction of incoming light. For a thin film, the decay of the intensity (I) of the incoming light as a function of film thickness (z) is given by:

$$I(z)^\circ = I_{max}e^{-\alpha z} \quad \text{Eq. 23}$$

In Eq. 23, α is called the absorption coefficient of the material and is defined as:

$$\alpha^\circ = \frac{4\pi k(\lambda)}{\lambda} \quad \text{Eq. 24}$$

In Eq. 24, k is called the extinction coefficient and is function of the light wavelength (λ). The complex refractive index (\tilde{n}) is thus equal to:

$$\tilde{n}(\lambda) = n(\lambda) + ik(\lambda) = \sqrt{\varepsilon(\lambda)} = \sqrt{\varepsilon_1(\lambda) + i\varepsilon_2(\lambda)} \quad \text{Eq. 25}$$

$$\text{Thus, } \varepsilon_1 = n^2 - k^2 \text{ and } \varepsilon_2 = 2nk \quad \text{Eq. 26}$$

In Eq. 25, ε is the complex dielectric function of the material film and describes what the light wave does to the material, whereas the complex refractive index (\tilde{n}) describes what the material does to the light wave. In Eq. 26, ε_1 is called the volume polarization term of the dielectric function, and ε_2 is called the volume absorption term. ε_1 is influenced by the oscillating dipoles of the material, whereas ε_2 is influenced by heat losses produced by the

generation of charge carriers in the material. Optical absorption by a material can occur by four different mechanisms that take energy from the light wave:

1. Free electrons in the material absorb energy from the wave. This occurs only in metals and semiconductors.
2. The electron clouds of the material oscillate in resonance with the light and produce heat losses. This case is common in dielectrics where electrons are bound to atoms.
3. Electrons are broken free from their bound states by light with enough energy. This occurs mainly in semiconductors and dielectrics irradiated with UV light.
4. Atoms and molecules vibrate in resonance with the electromagnetic radiation. This occurs mainly with infrared (IR) light of wavelength $>2 \mu\text{m}$.

Each mechanism is considered separately by different types of spectroscopy. Figure 98 shows the optical response of the dielectric function of rutile TiO_2 on a spectral range from the ultra violet to the infrared light. It can be seen that rutile TiO_2 is transparent in a large region of the visible and IR spectrum (from ~ 0.1 to 3 eV). It is implied by “transparent” that the absorption coefficient is zero in this region and therefore the volume absorption term $\epsilon_2=2nk$ is also zero. For photon energies larger than 3 eV , there is absorption of UV light by rutile TiO_2 . There are also lattice vibrations and heat losses for infrared light of photon energy $<0.1 \text{ eV}$.

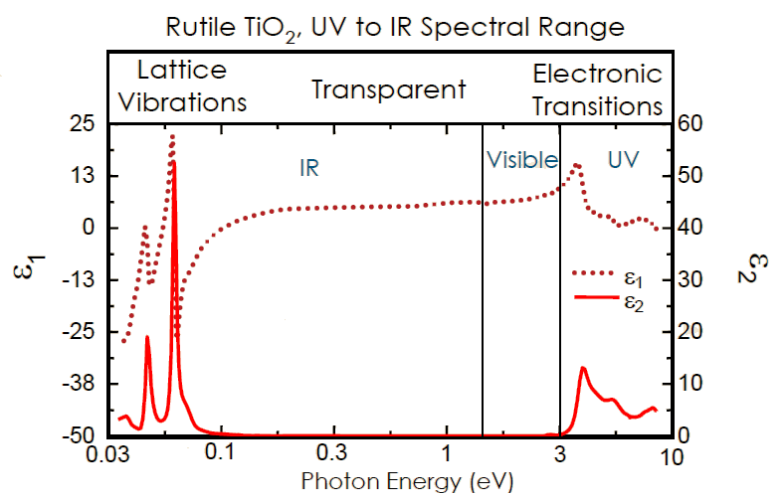


Figure 98: Dielectric function of rutile TiO_2 on a spectral range from UV to IR. [151]

Figure 99 shows the *normal dispersion* of a material transparent in the visible region (i.e. $k=0$ from 1.65–3.25 eV) like rutile TiO_2 . It is meant by *normal* that the refractive index increases toward shorter wavelengths and there is little light absorption. The opposite case is anomalous dispersion where there are peaks of light absorption (Figure 100). It can be seen in Figure 100 a dip of the refractive index n for wavelengths <450 nm. As the electrons clouds of dipoles enter in resonance with light of <450 nm and “bump” into each other, there is transformation of light energy as heat and the extinction coefficient k reaches a maximum value.

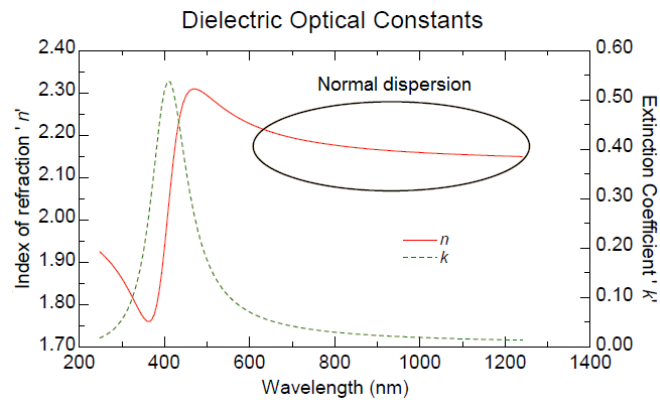


Figure 99: Normal dispersion of a transparent material. [151]

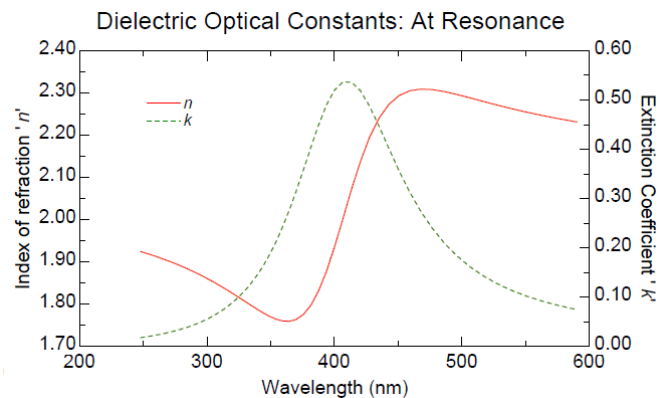


Figure 100: Anomalous dispersion of film in resonance with light of <450 nm. [151]

When sharp peaks are observed in the graph of the dielectric optical constants, it means there is transition of electrons from the valence band to the conduction band of the material [178]. This is often seen in the UV region (wavelengths <380 nm). These sharp absorption features are called *critical points* and they are not seen in amorphous materials. Figure 101 compares

the optical constants of crystalline and amorphous silicon in the UV and visible region of light. There are no sharp critical point transitions for amorphous silicon.

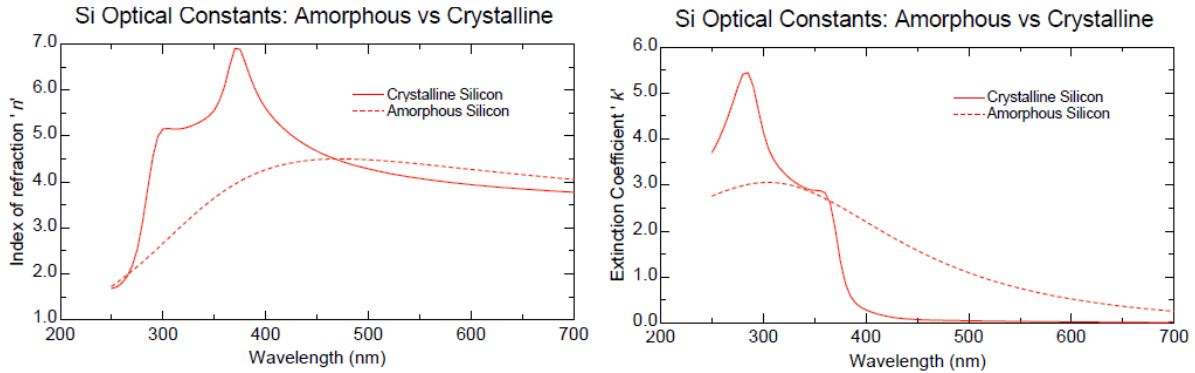


Figure 101: Optical constants of crystalline and amorphous Si in UV and visible region. [151]

For transparent thin films with normal dispersion along an interval of light wavelength (which is the case of films of Table 8), the mathematical model of Cauchy provides a simple and accurate method to calculate its optical constants from measured Ψ and Δ values. The Cauchy relationship is given by Eq. 27, where λ is the light wavelength and the constants A, B and C are adjusted to match the refractive index of the material [179]. For the Cauchy model to be consistent with curves of normal dispersion, constants A and B are generally positive.

$$n(\lambda) = A + \frac{B}{\lambda^2} + \frac{C}{\lambda^4} \tag{Eq. 27}$$

The Cauchy model could be applied, for example, to rutile TiO_2 to find its refractive index and thickness in the visible region (Figure 98). When fitting SE experimental data, the number of unknown properties should not exceed the number of known variables contained in the experimental data. A single-wavelength ellipsometer produces two data points (Ψ, Δ) which allows a maximum of two material properties to be determined (in this case, the refractive index and film thickness) [151], [179].

The data fitting procedure is conducted according to the flowchart shown in Figure 102. First, an optical model is constructed for the region of interest. Then, initial values are generated for the dielectrics functions. From these values, Ψ and Δ values are calculated and compared to the experimental data with help of Fresnel equations. This process continues until a minimum

fitting error is reached. Finally; the optical constant and thickness for the sample are determined and judged [179].

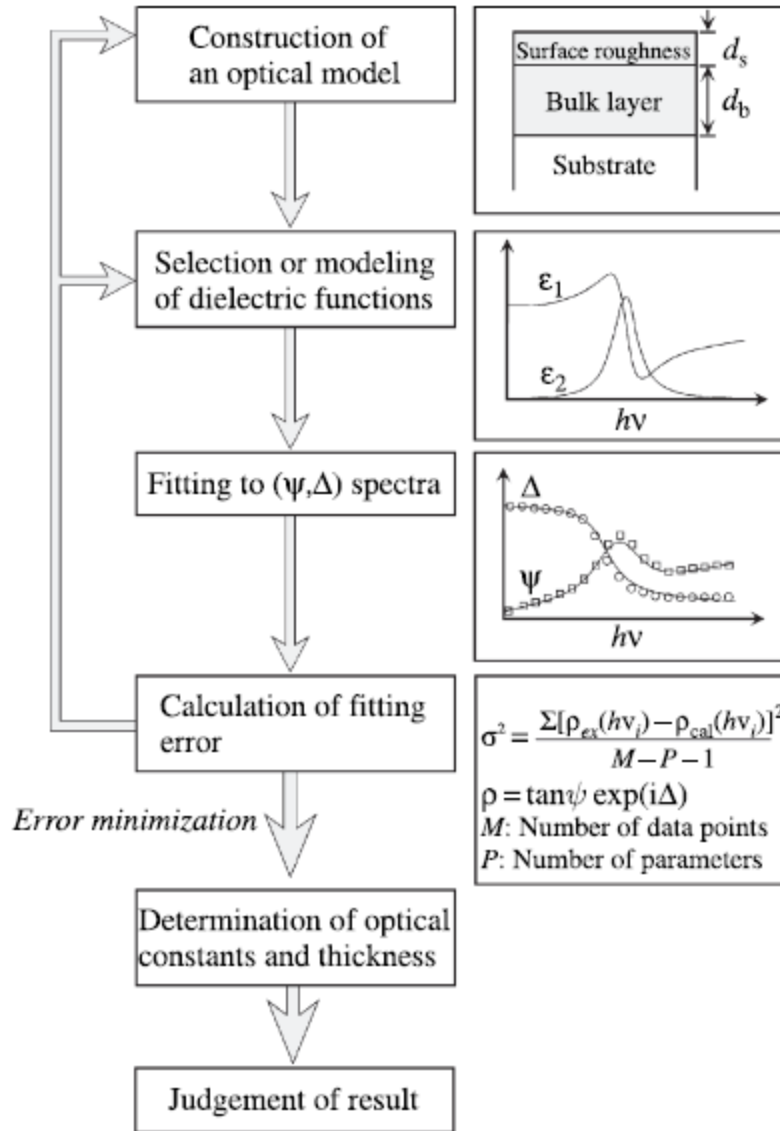


Figure 102: Flowchart of the data analysis procedure in spectroscopic ellipsometry. [179]

VASE measurements were performed with a computer-controlled variable angle of incidence spectroscopic ellipsometer of the rotating analyzer type M-2000DI® by J.A. Woollam Co., Inc. Spectroscopic measurements were made in the wavelength range of 190–1700 nm with 5 nm intervals at an incident angle of 55–75°. For data analysis, the software WVASE32 (version 3.774) was used. The Mean Squared Error (MSE) of thickness estimated by data fitting was smaller than 5.0 in most cases, which implies a very good fit.

Crystalline silicon

Figure 103 shows results of VASE analysis for a crystalline silicon coupon used as substrate of deposited thin films. A film of native silicon dioxide of 2.3 nm was present on this sample. Measurements done in five coupons had an average thickness of 2.3 nm. This value was used for the fitting models of other deposited films. Surface roughness of 0.10 nm was estimated for this substrate (MSE 1.5). The characteristic critical points of silicon in the UV region can be seen in Figure 103B. Generated optical constants ($n=3.87$ and $k=0.018$ at 633 nm) were in good agreement with those reported for crystalline silicon [180].

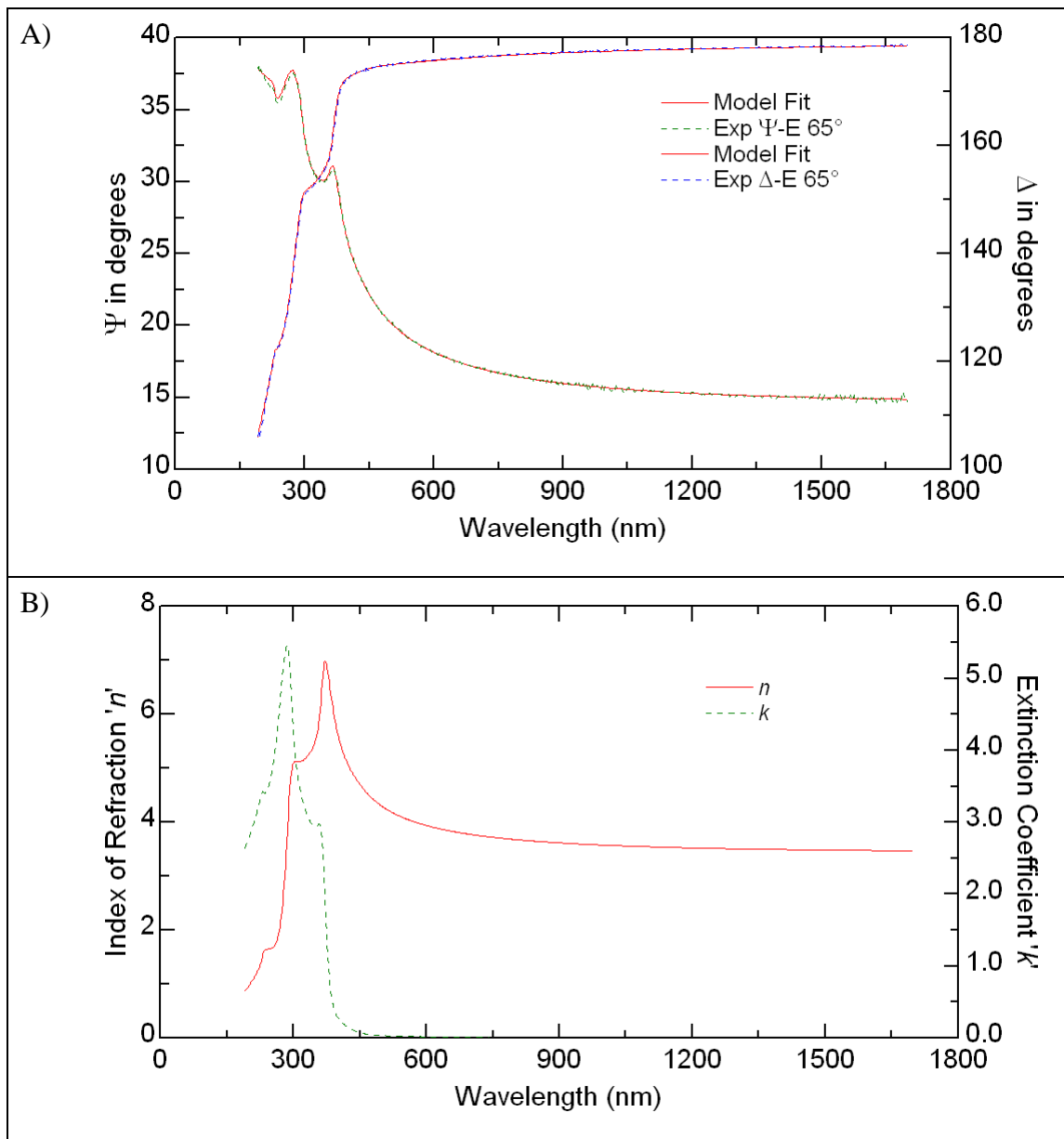


Figure 103: VASE analysis of crystalline silicon. A) Experimental and model-generated Ψ and Δ . B) Refractive index and extinction coefficient.

Al₂O₃

Figure 104 shows VASE analysis of a 19.6 nm Al₂O₃ film deposited by ALD 250°C on silicon. Surface roughness of 0.39 nm was estimated for this film (MSE 1.0). Unlike crystalline silicon and other dielectric films (e.g., BN, DLC, SiOC), this film of Al₂O₃ does not absorb UV light, so it was easily fitted with the Cauchy model in the whole measured spectral range. Hence, this film is a transparent material ($k=0$) on a wide spectral range. This makes it ideal for encapsulation of optical devices. Refractive index was 1.62 ± 0.05 at 633 nm, which is consistent with reported values for amorphous alumina films [181].

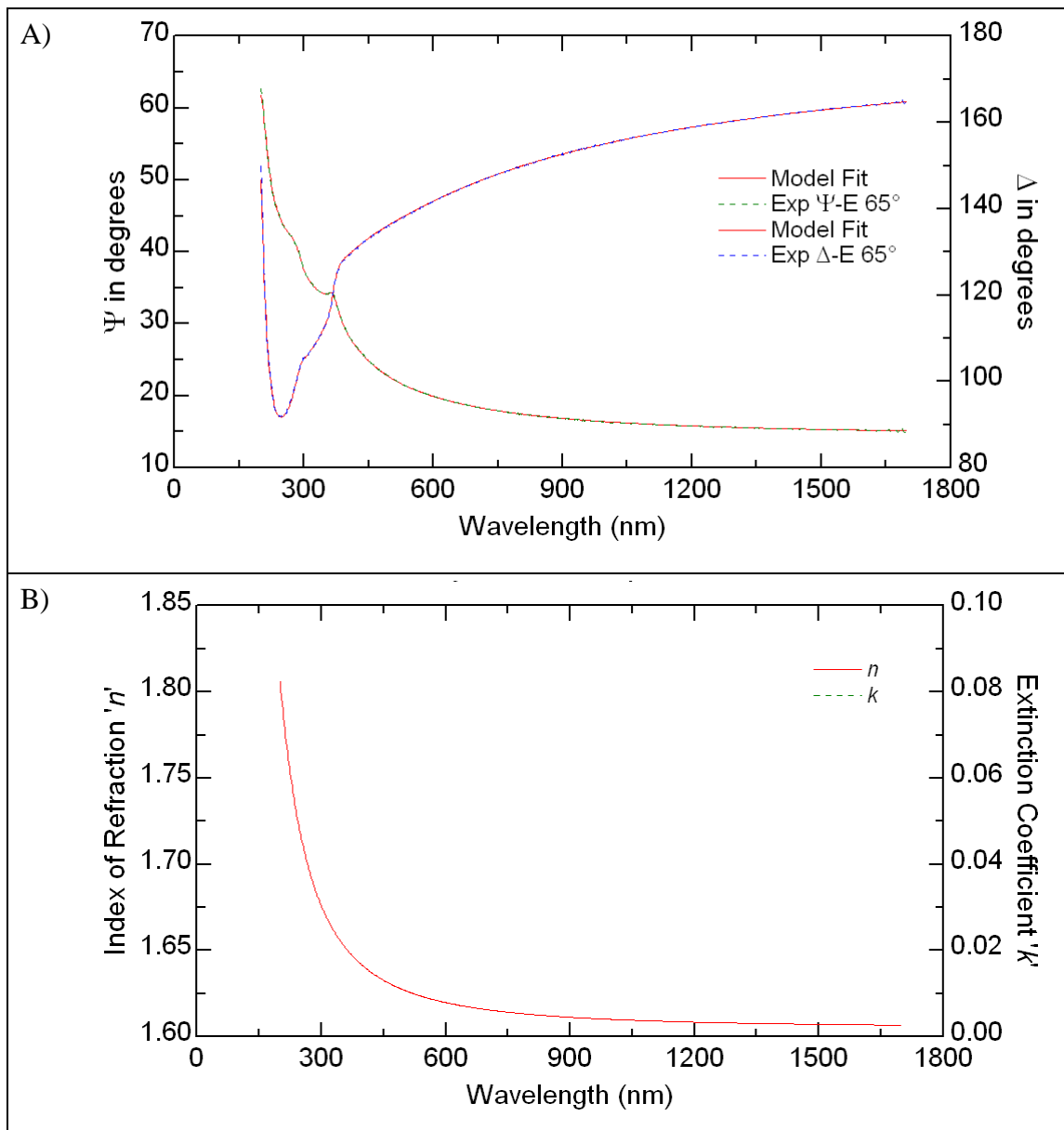


Figure 104: VASE analysis of 20 nm Al₂O₃ 250°C. A) Experimental and model-generated Ψ and Δ . B) Refractive index and extinction coefficient.

BN

The VASE analysis of a BN film deposited by PECVD 400°C is shown in Figure 105. A thickness and surface roughness of 47.2 nm and 0.30 nm (MSE 3.7) were respectively found for this film. Generated optical constants ($n=2.0$ and $k=0.022$ at 633 nm) are consistent with reported values for boron nitride films prepared by PECVD [182]. BN films absorb visible and near UV radiation. Especially, there is considerable absorption of light below wavelengths of 400 nm (Figure 105B).

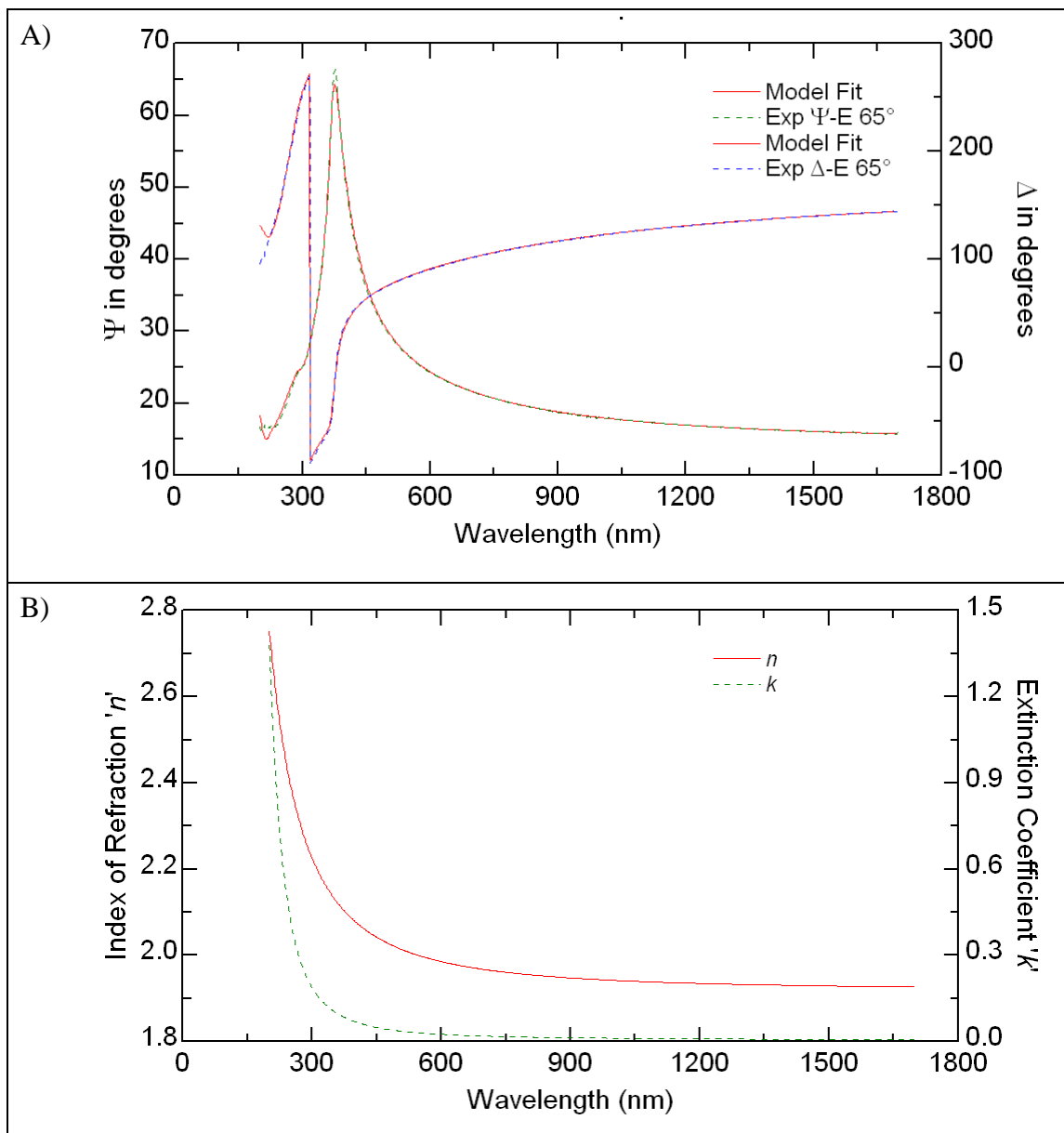


Figure 105: VASE analysis of 50 nm BN 400°C. A) Experimental and model-generated Ψ and Δ . B) Refractive index and extinction coefficient.

SiC

VASE results of a SiC film deposited by PECVD at 350°C are shown in Figure 106. Film thickness and average roughness of 98.6 nm and 0.79 nm (MSE 2.8) were respectively found. Equivalent results were found by XRR ($z=100.4$ nm) and AFM ($R_{\text{RMS}}=1.02$ nm). Generated optical constants ($n=1.84$ and $k=0$ at 633 nm) are consistent with those reported for hydrogenated amorphous silicon carbide films prepared by PECVD [183]. SiC films had strong absorption of light below wavelengths of 400 nm. It was not possible to fit the Cauchy model for light wavelengths inferior to such value.

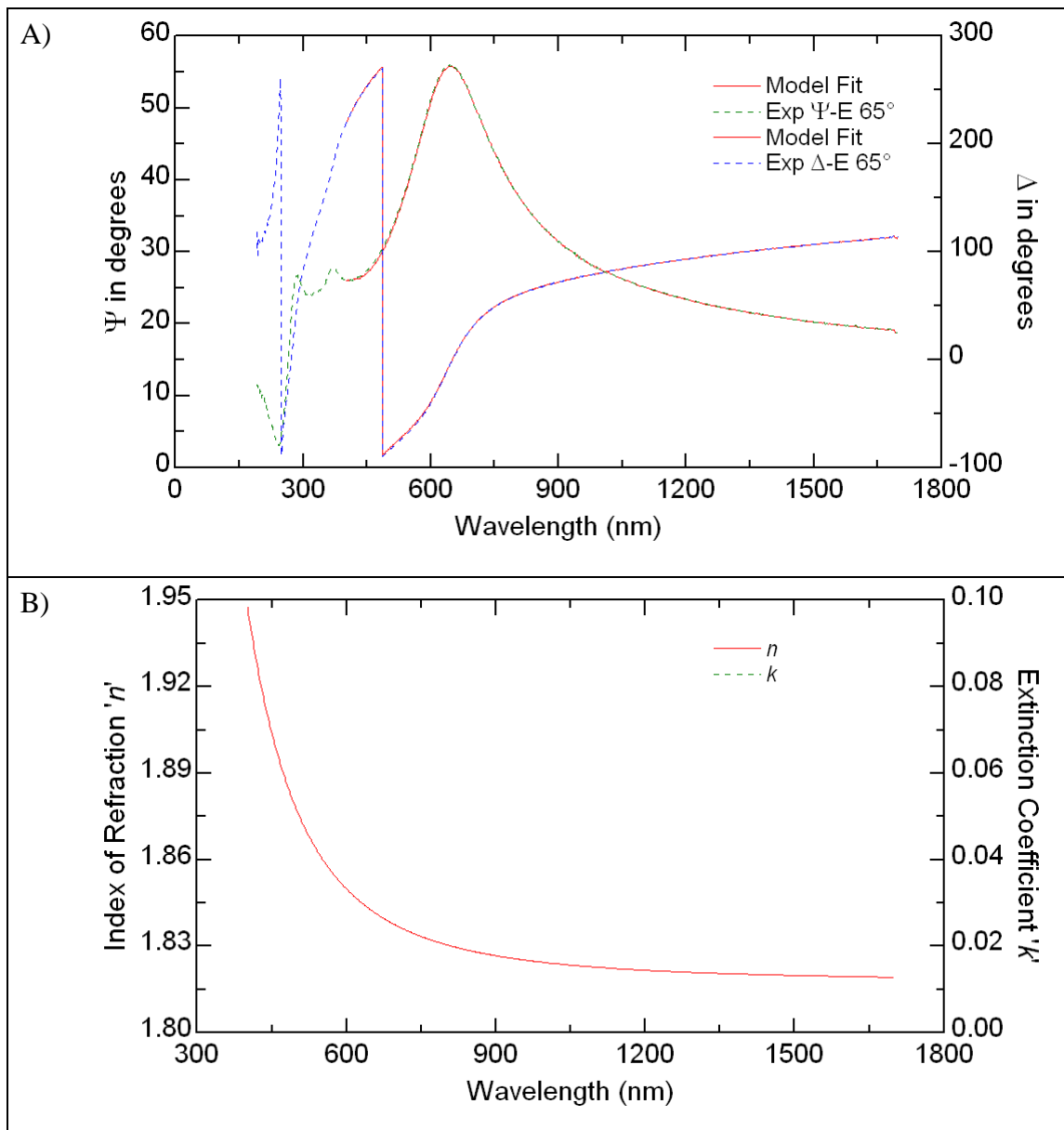


Figure 106: VASE analysis of 100 nm SiC 350°C. A) Experimental and model-generated Ψ and Δ . B) Refractive index and extinction coefficient.

DLC

Figure 107 shows VASE analysis of a DLC film deposited by PECVD at 400°C on silicon. A thickness and surface roughness of 111.1 nm and 6.3 nm (MSE 3.4) were respectively found for this film. Roughness measured by AFM was quite different ($R_{\text{RMS}}=0.38$ nm). This is probably due to imperfect data fitting with the Cauchy model because this film is not entirely transparent ($k>0$). Hence, it was not possible to fit the data for wavelengths below 400 nm. An absorption peak is expected in that region. Generated optical constants at 633 nm ($n=1.81$ and $k=0.12$) are similar to reported ones for amorphous soft a-CH films [184].

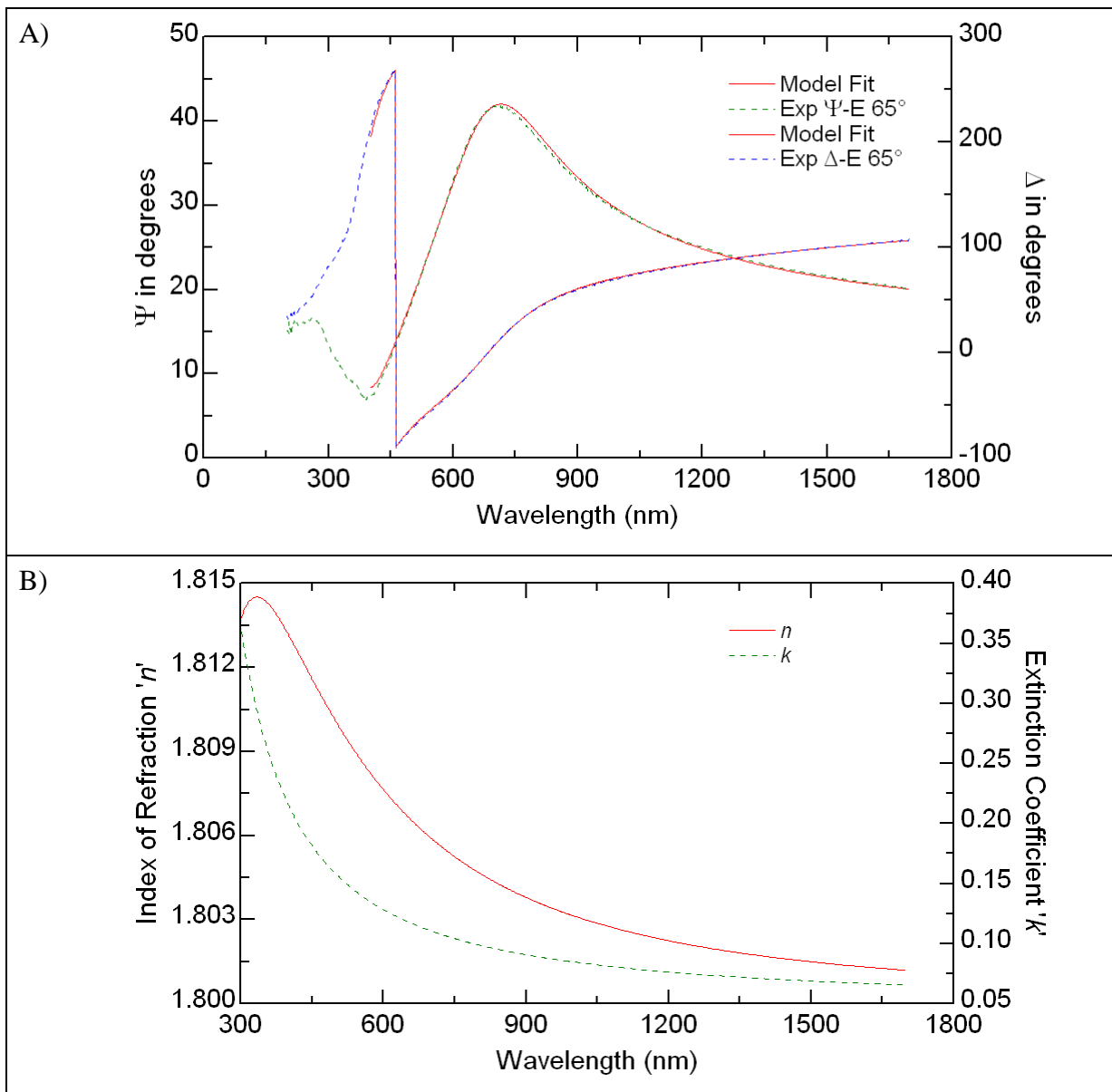


Figure 107: VASE analysis of 110 nm DLC 400°C. A) Experimental and model-generated Ψ and Δ . B) Refractive index and extinction coefficient.

HfO₂

Figure 108 shows the VASE analysis of HfO₂ film deposited by ALD at 250°C on silicon. Thickness and surface roughness of 19.9 nm and 0.10 nm (MSE 0.9) were respectively found for this film. This film is not transparent and shows strong absorption of light below 600 nm. An absorption peak is present in the UV region. An optical band gap of <5.9 eV can be expected for this HfO₂ film [185]. Generated optical constants at 633 nm ($n=2.03$ and $k=0.66$) are consistent with values reported for amorphous HfO₂ thin films of high density [186]. So, this amorphous film has a smooth and dense structure that is potentially a good encapsulant.

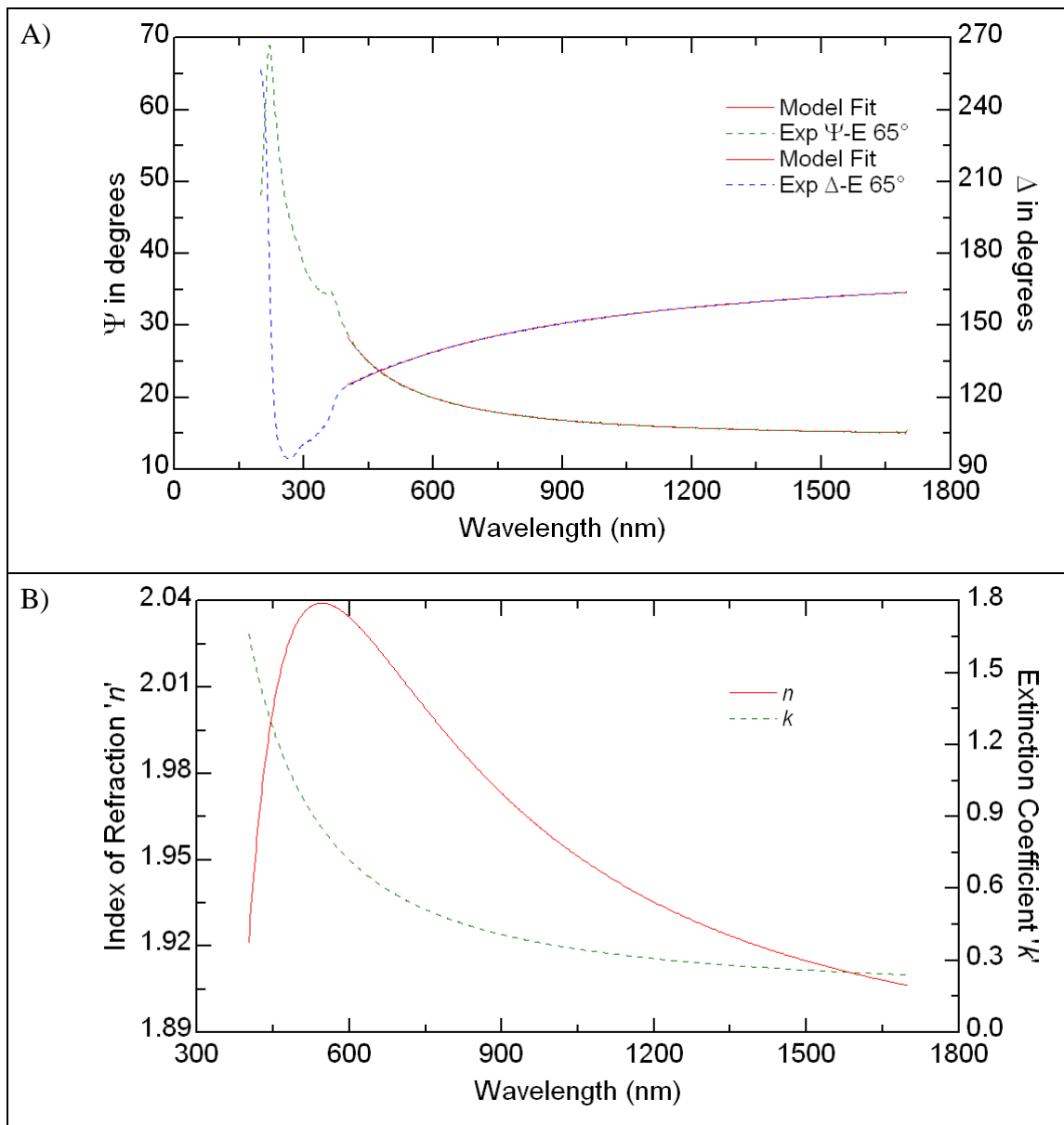


Figure 108: VASE analysis of 20 nm HfO₂ 250°C. A) Experimental and model-generated Ψ and Δ . B) Refractive index and extinction coefficient.

SiN

Thickness and surface roughness of 100.0 nm and 0.95 nm (MSE 2.6) were respectively found for a SiN film deposited by PECVD at 400°C (Figure 109). These results are equivalent to those found by XRR ($z=99.0$ nm) and AFM ($R_{\text{RMS}}=1.10$ nm). This film does not absorb UV light, so it was easily fitted with the Cauchy model in the whole measured spectral range. Generated optical constants ($n=1.87$ and $k=0.0037$ at 633 nm) are similar to those reported by Osenbach *et al.* for SiN films prepared by PECVD at 360°C from SiH_4 , NH_3 and N_2O [34].

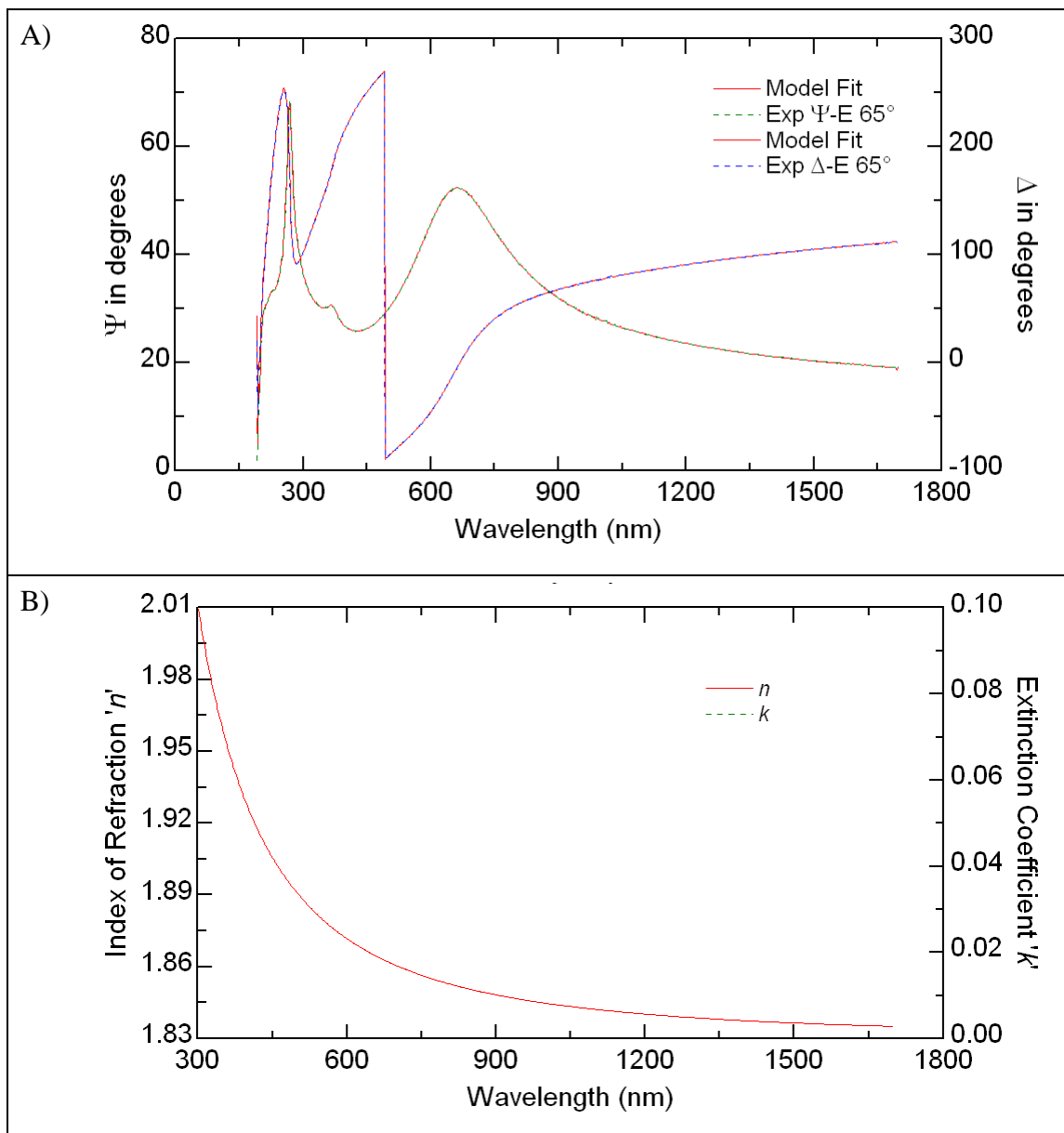


Figure 109: VASE analysis of 100 nm SiN 400°C. A) Experimental and model-generated Ψ and Δ . B) Refractive index and extinction coefficient.

SiO₂

VASE results of a SiO₂ film deposited by PECVD at 400°C are shown in Figure 110. Film thickness and surface roughness of 98.6 nm and 0.28 nm (MSE 2.9) were respectively found. Slightly different results obtained by XRR ($z=103.2$ nm) and AFM ($R_{\text{RMS}}=1.55$ nm) are probably due to imperfect data fitting. Generated optical constants ($n=1.46$ and $k=0.000$ at 633 nm) are similar to reported values for SiO₂ films [187]. This SiO₂ film had slight absorption ($k \sim 0.01$) of light below wavelengths of 300 nm.

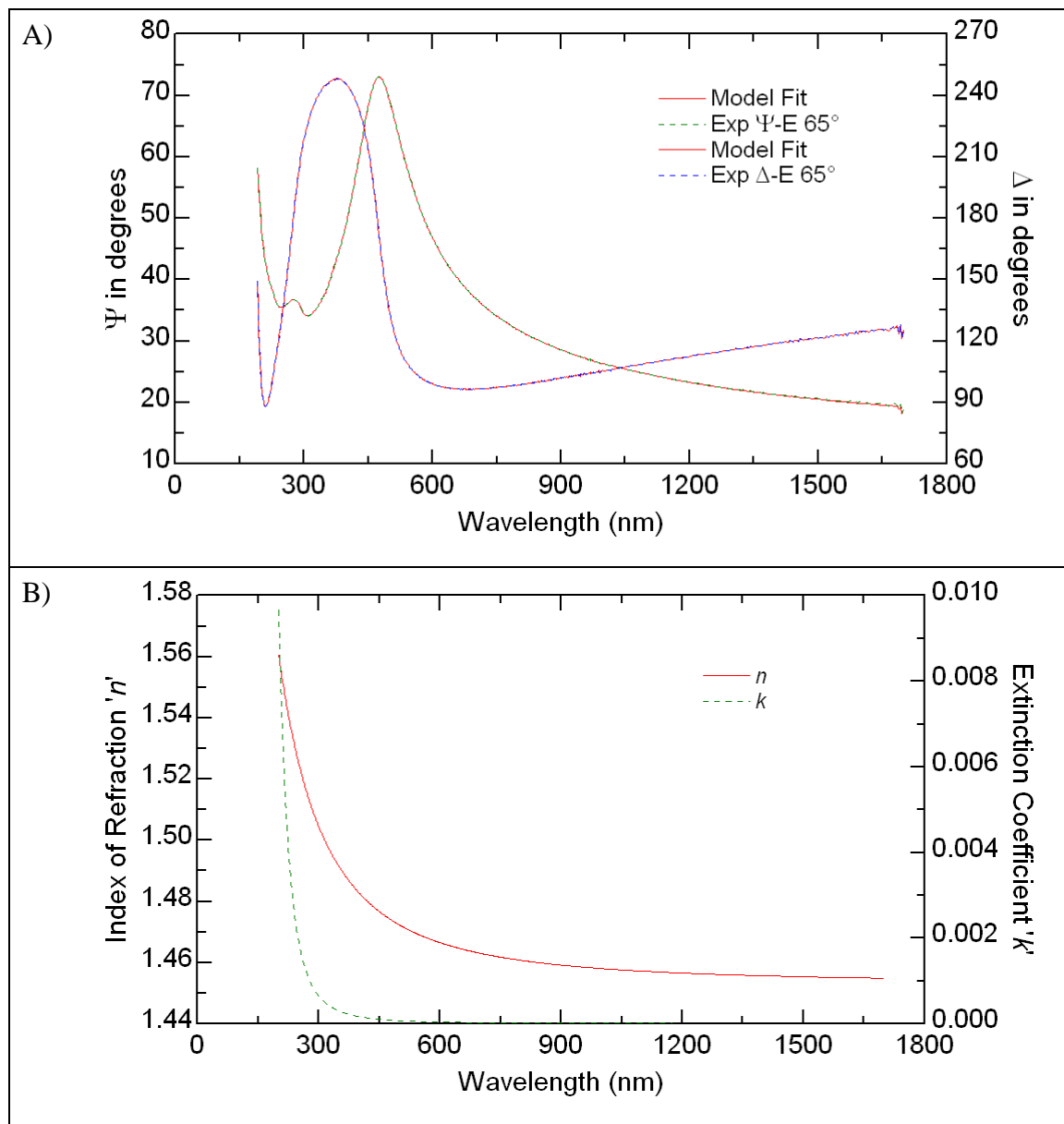


Figure 110: VASE analysis of 100 nm SiO₂ 400°C. A) Experimental and model-generated Ψ and Δ . B) Refractive index and extinction coefficient.

SiOC

The VASE analysis of a SiOC film deposited by PECVD 400°C is shown in Figure 111. A thickness and surface roughness of 98.1 nm and 0.20 nm (MSE 1.4) were respectively found for this film. Generated optical constants ($n=1.42$ and $k=0$ at 633 nm) are characteristic of low dielectric constant SiOC films [188], [189]. In fact, this film's dielectric constant is 2.9. This value suggests the presence of air pores, which has a refractive index of 1.000. The low density of this film was confirmed by XRR measurements ($\sim 2.2 \text{ g/cm}^3$). This SiOC film shows considerable absorption of light below wavelengths of 400 nm.

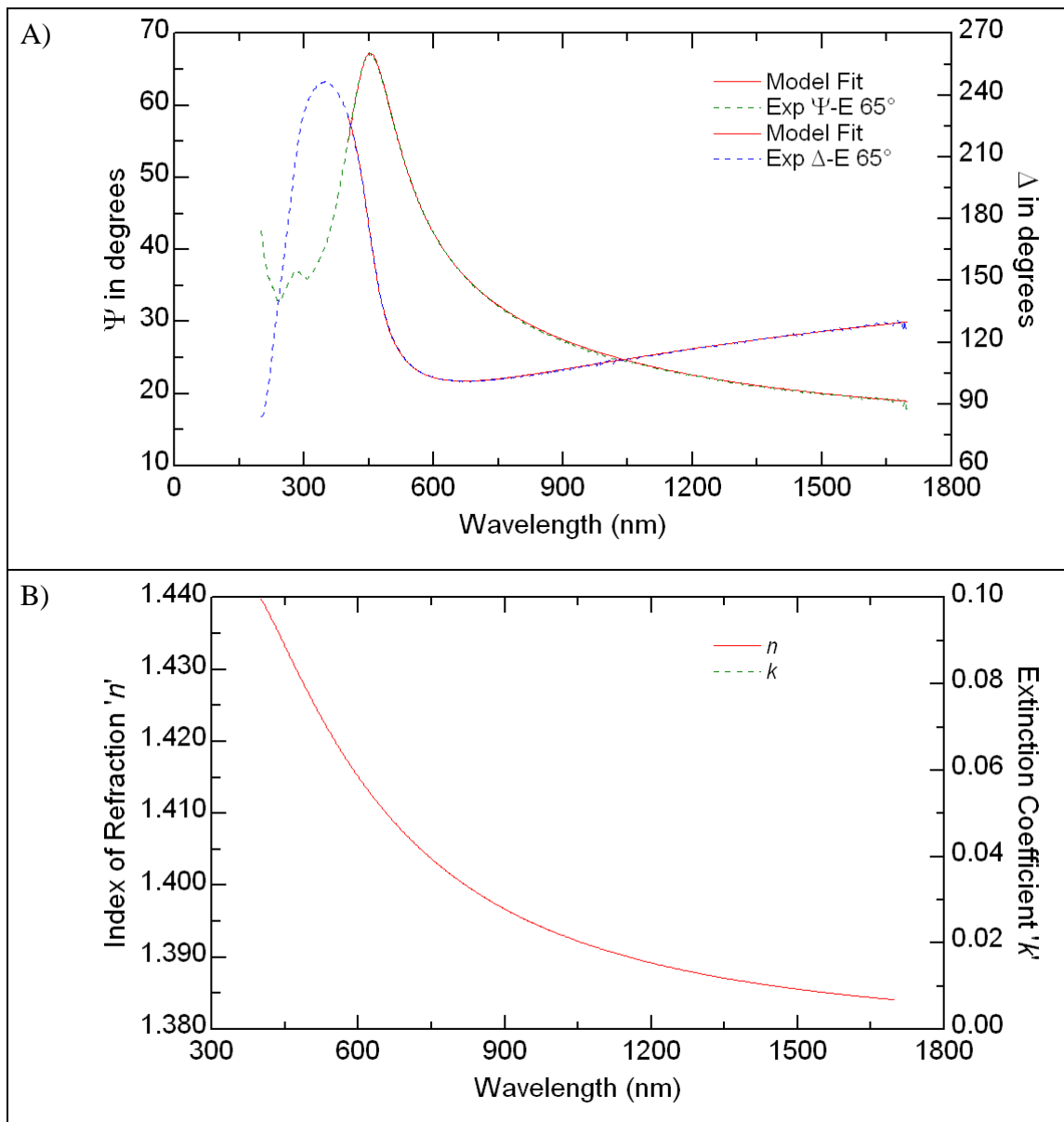


Figure 111: VASE analysis of 100 nm SiOC 400°C. A) Experimental and model-generated Ψ and Δ . B) Refractive index and extinction coefficient.

TiO₂

Figure 112 shows VASE analysis of a TiO₂ film deposited by ALD 250°C. Film thickness and surface roughness of 15.4 nm and 0.21 nm (MSE 2.3) were respectively found. Equivalent results were obtained by XRR ($z=16.2$ nm) and AFM ($R_{\text{RMS}}=0.30$ nm). Generated optical constants ($n=2.64$ and $k=0.25$ at 633 nm) are consistent for amorphous TiO₂ films with a density close to that of rutile, which has a $n=2.87$ [190], [191]. XRR confirmed the density of this film was close to that of rutile (4.3 g/cm³). This TiO₂ film has a non-negligible absorption ($k>0.25$) of visible and UV light, suggesting the presence of free electrons.

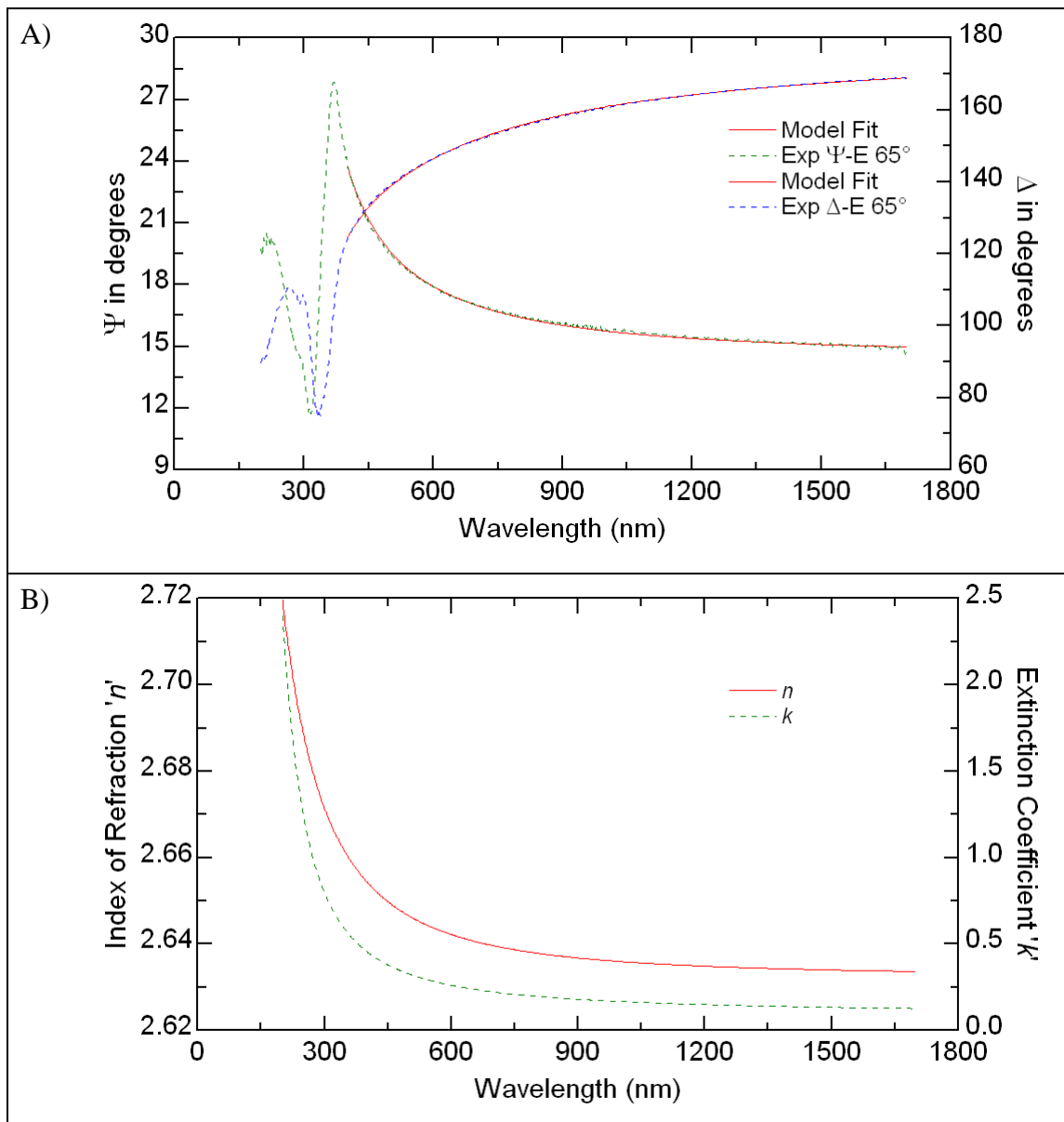


Figure 112: VASE analysis of 20 nm TiO₂ 250°C. A) Experimental and model-generated Ψ and Δ . B) Refractive index and extinction coefficient.

ZnO

Figure 113 shows results of VASE analysis of ZnO film deposited by ALD 250°C on silicon. A thickness and surface roughness of 20.6 nm and 1.14 nm (MSE 1.1) were respectively found for this film. Similar results were obtained by XRR ($z=22.1$ nm) and AFM ($R_{\text{RMS}}=1.31$ nm). Generated optical constants ($n=1.92$ and $k=0$ at 633 nm) are coherent with reported values for crystalline ZnO films [192, p. 328]. This film is transparent ($k=0$) on a wide spectral range (400–1700 nm), which is desirable for applications in electro-photonic devices.

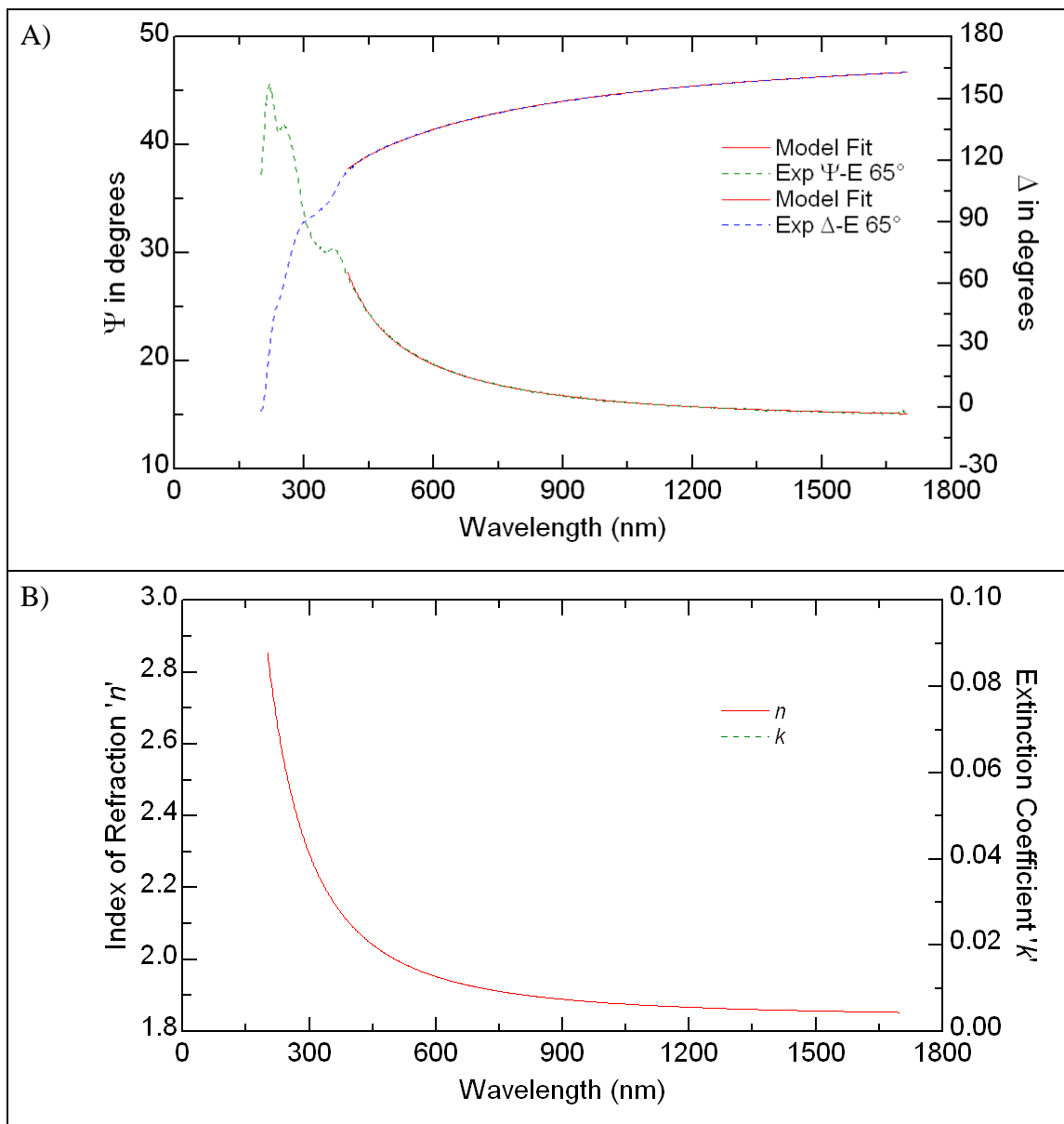


Figure 113: VASE analysis of 20 nm ZnO 250°C. A) Experimental and model-generated Ψ and Δ . B) Refractive index and extinction coefficient.

Résumé (français):

Les dispositifs médicaux miniaturisés sont de plus en plus répandus dans le monde médical, car ils offrent de nouvelles opportunités de traitement et de surveillance. La miniaturisation des systèmes permet notamment une chirurgie minimalement invasive, une portabilité améliorée et une facilité d'utilisation. Parmi les exemples on peut mentionner les micro-stimulateurs cardiaques, les micro-implants cochléaires et les micro-capteurs ex-situ de glucose. Cependant, les micro-dispositifs implantables qui utilisent des technologies d'assemblage autres que les boîtiers métalliques sont encore à découvrir. La surveillance de paramètres physiologiques à l'aide de capteurs in-situ de pression et BioMEMS pourraient bénéficier des progrès faits sur les études d'encapsulation en couche mince destinées à protéger les micro-dispositifs de silicium contre la corrosion. En effet, une barrière qui empêche la diffusion et la pénétration des substances nocives est indispensable pour protéger à la fois le patient et le micro-dispositif. Les couches minces céramiques déposées par des procédés chimiques en phase vapeur sont de bons candidats grâce à leurs faibles perméabilités aux gazes, faibles réactivités chimiques et conformités de dépôt élevées. Cependant, dans des milieux biologiques représentatifs du corps humain, peu d'études ont été réalisées dans le domaine de la protection des dispositifs microélectroniques contre la corrosion.

Au cours de cette thèse, dix matériaux, choisis à l'issue d'une étude bibliographique, ont été étudiés: Al_2O_3 , BN, DLC, HfO_2 , SiC, SiN, SiO_2 , SiOC, TiO_2 et ZnO. Des couches ultrafines de ces matériaux (de 5 à 100 nm) ont été déposées par voie chimique en phase vapeur assisté par plasma (PECVD) ou par couches atomiques (ALD) sur des substrats silicium recouverts de matériaux généralement présents dans des dispositifs microélectroniques tels que le silicium cristallin, le cuivre, le tungstène nitrure et le poly-imide. Des mesures de cytotoxicité ont été réalisées et des tests de vieillissement ont été effectués pendant plusieurs semaines à des températures différentes dans une solution saline phosphatée (PBS) mais aussi dans une solution à base de sérum de veau fœtale (NaCl/SVF). Les changements dans la composition chimique et l'épaisseur ont été suivies par VASE, XPS et spectroscopie de masse d'ions secondaires à temps de vol (TOF-SIMS). Il a été montré que les couches de SiO_2 et de SiN (généralement utilisées pour la protection dans l'industrie de la microélectronique) n'étaient pas stables dans le PBS et le NaCl/SVF à 37°C, même si en revanche elles offraient une bonne barrière aux gazes. L' Al_2O_3 a lui montré une très bonne tenue en milieu salin et une remarquable herméticité mais en revanche, il s'est corrodé rapidement dans le NaCl/SVF. Les couches de DLC, SiOC et TiO_2 ont donné les meilleurs résultats de stabilité dans le PBS et le sérum de veau. Enfin, il a aussi été montré dans cette thèse que l'empilement TiO_2 sur Al_2O_3 offrait la meilleure efficacité comme barrière hermétique et diffusive pour la protection des microsystèmes de silicium contre la corrosion dans les milieux salins.

Title :

Selecting and evaluating biocompatible barrier films for protecting medical micro devices

Abstract:

Miniaturized medical devices are becoming increasingly adopted by doctors and patients because they enable new treatment and monitoring capabilities, minimally invasive surgery, improved portability and ease of use. Recent examples include micro pacemakers, micro cochlear implants and ex-situ micro glucose sensors. However, implantable micro devices employing packaging technologies other than metallic enclosures are yet to be seen. Physiological monitors such as in-situ pressure sensors and BioMEMS could profit significantly from advances in thin barrier films for corrosion protection of silicon micro devices. Coating films that stop the diffusion and permeation of harmful substances are necessary to protect both the patient and the micro device. Ceramic films deposited by chemical vapor deposition techniques are good candidates for this task due to their low permeability to gases, low chemical reactivity and high conformality. However, few studies are available about the corrosion protection offered by biocompatible coatings to microelectronic devices in representative biological environments.

Ten materials were selected in this thesis after a bibliographic study: Al₂O₃, BN, DLC, HfO₂, SiC, SiN, SiO₂, SiOC, TiO₂ and ZnO. Ultra-thin films of these materials (5-100 nm) were deposited by plasma enhanced chemical vapor deposition (PECVD) or atomic layer deposition (ALD) on substrates commonly found in electronic micro devices: crystalline silicon, copper, tungsten nitride and polyimide. *In vitro* cytotoxicity tests and degradation tests were performed for several weeks at different temperatures in Phosphate Buffer Saline (PBS) and NaCl supplemented with 10% Fetal Bovine Serum (NaCl/FBS). Changes in thickness and chemical composition were monitored by VASE, XPS and time-of-flight secondary ion mass spectroscopy (TOF-SIMS). It was found that SiO₂ and SiN films (generally used for protection in the microelectronics industry) are not stable in PBS and NaCl/FBS at 37°C, even though they act as good hermetic barriers. Al₂O₃ showed very good stability in saline solution and excellent behavior as gas barrier, but it was rapidly dissolved in NaCl/FBS. In contrast, films of DLC, SiOC and TiO₂ showed very low chemical reactivity in both mediums. Finally, it was shown that multilayers of TiO₂ on Al₂O₃ offer the best performance as hermetic and diffusion barriers for corrosion protection of silicon micro systems in saline environments.

Mots clés (français):

Biocompatibilité - Corrosion – Couche Barrière - Dispositif Médical Microélectronique

Keywords:

Biocompatible – Biodegradation – Corrosion – Barrier Film – Microelectronic Medical Device